



<https://theses.gla.ac.uk/>

Theses Digitisation:

<https://www.gla.ac.uk/myglasgow/research/enlighten/theses/digitisation/>

This is a digitised version of the original print thesis.

Copyright and moral rights for this work are retained by the author

A copy can be downloaded for personal non-commercial research or study,
without prior permission or charge

This work cannot be reproduced or quoted extensively from without first
obtaining permission in writing from the author

The content must not be changed in any way or sold commercially in any
format or medium without the formal permission of the author

When referring to this work, full bibliographic details including the author,
title, awarding institution and date of the thesis must be given

Enlighten: Theses

<https://theses.gla.ac.uk/>
research-enlighten@glasgow.ac.uk

DETERMINATION OF PHYSICAL AND MAGNETIC MICROSTRUCTURE BY STEM

Ian Robson McFadyen

Thesis submitted for the degree of Ph.D.

at The University of Glasgow

Department of Physics and Astronomy

November 1986

ProQuest Number: 10948124

All rights reserved

INFORMATION TO ALL USERS

The quality of this reproduction is dependent upon the quality of the copy submitted.

In the unlikely event that the author did not send a complete manuscript and there are missing pages, these will be noted. Also, if material had to be removed, a note will indicate the deletion.



ProQuest 10948124

Published by ProQuest LLC (2018). Copyright of the Dissertation is held by the Author.

All rights reserved.

This work is protected against unauthorized copying under Title 17, United States Code
Microform Edition © ProQuest LLC.

ProQuest LLC.
789 East Eisenhower Parkway
P.O. Box 1346
Ann Arbor, MI 48106 – 1346

This book "is an indispensable companion to all those who are keen to make sense of life in an infinitely complex and confusing Universe, for though it cannot hope to be useful or informative on all matters, it does make the reassuring claim that where it is inaccurate, it is at least *definitively* inaccurate. In cases of major discrepancy it is always reality that's got it wrong."

from **The Hitch-Hikers Guide To The Galaxy**
by **Douglas Adams**

	Bright field imaging	27
	Asymmetric detector	29
	The effect of partial coherence	31
2.4	The Aharonov And Bohm Effect	32
2.5	Differential Phase Contrast Imaging	33
2.6	Microscope Operating Conditions For DPC	35
	Scherzer focus in the HB5	36
	Post specimen lens setting	37
2.7	Image Acquisition On The HB5	38
	Computer controlled image acquisition	39
	Zeroing the integrator	40
2.8	Electron Energy Loss And X-ray Spectra	42
	Electron energy loss spectra	43
	Measurement of specimen thickness	44
	X-ray spectra from thin specimens	46
	Estimation of volume analysed	48
	Operating conditions for spectrum acquisition	49
	Spectrum acquisition	50
<hr/>		
CHAPTER 3	LARGE GRAIN POLYCRYSTALLINE COBALT	52
3.1	Introduction	
3.2	Polycrystalline Cobalt	53
3.3	Theoretical Relationship Between Physical And Magnetic Structure	55
3.4	Experimental Measurements	57
	General observations	
	Edge effects	58
	Approximation to ideal single crystal	59
	Measurement of θ and Φ_0	60
	Comparison with figures 3.3 and 3.4	61
3.5	Domain Wall Profiles In Thin Crystal Cobalt	62
3.6	Summary	64

CHAPTER 4	MAGNETIC STRAY FIELD MAPPING	65
4.1	Introduction	
4.2	Stray Fields From A Cobalt Foil	66
	Production of vector maps from digitally acquired images	67
	Comparison with theory	68
	Sensitivity limit of technique	69
4.3	Stray Fields From Written Tracks On Magnetic Recording Material	70
4.4	Conclusions	73
CHAPTER 5	MAGNETIC AND PHYSICAL STRUCTURE OF CoCr FILM FOR MAGNETIC RECORDING	75
5.1	Introduction	
5.2	Co-Cr Artificial Superstructure Films	76
	Crystal structure	
	Magnetic structure	77
	Discussion	78
5.3	CoCr Thin Film Alloys	79
	C-axis texture	80
	Magnetic structure:	
	Films deposited at room temperature	81
	Films deposited at 200 and 250 ^o C	82
	Films deposited at 300 ^o C	83
5.4	Summary And Conclusions	84
	Co-Cr artificial superstructure films	
	CoCr alloy films	
CHAPTER 6	ELEMENTAL SEGREGATION IN CoCr PERPENDICULAR MAGNETIC RECORDING MEDIA	87
6.1	Introduction	
6.2	Specimen Preparation	89

6.3	General Observation Of CoCr Transverse Sections	90
6.4	Spectrum Acquisition Conditions	91
6.5	Results Of Microanalysis	93
	Raw data from x-ray spectra	
	Calculation of volume fraction, f	95
	Estimation of boundary width	97
	Effects of beam broadening and boundary width	98
6.6	Summary And Discussion	
CHAPTER 7	INVESTIGATION OF MAGNETIC STRUCTURE IN CROSS-SECTIONS OF PERPENDICULAR MAGNETIC RECORDING MEDIA	101
7.1	Introduction	
	Reasons for transverse sectioning of film	102
	The specimens investigated	103
	Requirements for preliminary investigation	104
7.2	Preliminary Observations In The CTEM	105
	Importance of specimen thickness	
	Physical microstructure	
	Preliminary investigation of magnetic structure	106
7.3	Investigation Of The Soft Magnetic Underlayers	107
	CoZrNb underlayer	
	NiFe underlayer	108
7.4	Stray Fields From Single And Double Layer Films	111
7.5	Magnetic Structure Within The CoCr Layer	113
7.6	Summary And Conclusion	114
CHAPTER 8	CONCLUSIONS AND FUTURE WORK	117
8.1	General Conclusions	
	High resolution without a magnetic field	118

	Simultaneous EELS and EDX	
	Novel detector response function	119
	Digital acquisition	120
8.2	Future Work	121
	Computer acquisition and analysis	
	CoCr recording material:	
	Artificial superstructure films	123
	Alloy films	
	Elemental segregation	124
APPENDIX A	STRAY FIELD MAPPING PROGRAMS	126
	VMAP	127
	DRAMAP	140
	LOG1	146
APPENDIX B	ALIGNMENT ROUTINES AND ASSOCIATED PROBLEMS	148
B.1	Introduction	
B.2	Alignment Of Well Defined Magnetic Domain Walls	
	Problems with covariance as an alignment test	149
B.3	Alignment Of Magnetic Domain Walls In Images With Strong Crystallite Contrast	150
	Median Filter	
	Spatial frequency filter	151
	Alignment to a standard pattern	
B.4	Implementation Of Alignment Techniques On The Toltec	152
APPENDIX C	JEOL 1200EX FREE LENS CONTROLLER - LOW MAG SETTINGS	153
	Introduction	
	Magnifications of > 1000x with the objective lens OFF	

	Obtaining a desired magnification	154
	Stigmating when using the FLC	
	Storing FLC settings in memory	155
APPENDIX D	HIGH FREQUENCY FILTERING OF DIGITAL IMAGES	156
D.1	Introduction	
D.2	Fourier Transforms On The Toltec Computer	
D.3	Frequency Filters Available	157
D.4	Relationship Between Fourier Space And Real Space	158

REFERENCES

AKNOWLEDGMENTS

I would like to express my appreciation of the help given to me by others during the three years of this work. Firstly I must thank my supervisor Dr J. N. Chapman for his help and encouragement throughout this work and Professor R. P. Ferrier for making the electron microscope facilities in the Solid State Group at Glasgow available to me. I am indebted to Dr G. R. Morrison for his help in operating the HB5 STEM at Glasgow, and would like to thank him, Dr Chapman and Professor Ferrier for many hours of helpful discussion on magnetic materials and electron microscopy. I am grateful to Dr G.W. Lorimer for providing the Monté Carlo program mentioned in Chapter 6, Mr A. McGibbon for running the program for me, and Mr S. McVitie for calculating the theoretical stray field distributions reported in Chapter 4.

I would also like to thank Mr J. Simms and Miss M. Low for maintaining, and for help in using, the conventional electron microscopes, Dr. W.A.P. Nicholson, Mr A. Khan and Mr A. Howie for maintaining the HB5 STEM, and Mr A. Young and Mr D. McDonald for maintaining and for help in using the carbon evaporators. Furthermore I would like to thank Mr A. Khan, Mr D. Dickson and Mr I. Smith, who have been of invaluable assistance in building and repairing much of the electronics used in this work.

As regards the preparation of this thesis, I am indebted to Miss M. Low for preparing diagrams, and Mr I. McVicar for producing the photographic prints. For the typing of the thesis I would like to thank all who kindly gave up the Apple Mac wordprocessor to allow me to use it, the High Energy Physics group for providing the Apple Mac and Mr L. Fairley for printing the thesis on the night shift.

In addition I would like to thank my wife, Alison, for proof reading all of the thesis, and for putting up with my late night and weekend working in the latter stages of this work. Finally I would like to thank the SERC for providing financial support and equipment.

DECLARATION

This thesis is a record of work carried out by me in the Department of Natural Philosophy (now Physics and Astronomy) at the University of Glasgow. The work described herein is my own with the exception of the manufacture and preparation of the electron microscope samples used. The cobalt foil investigated in Chapters 3 and 4 was provided by Dr J. N. Chapman, the FeCoCr film in Chapter 4 and the artificial superstructure films of Chapter 5 were provided by IBM* (the former through the kind offices of Professor R.P. Ferrier), and the CoCr alloy films discussed in Chapters 5, 6 and 7 were provided by Philips**.

Some of the work described in Chapter 3 has been published in the paper:

"Determination of Physical and Magnetic Microstructure by STEM", J. N. Chapman, J. P. Jakubovics and I. R. McFadyen, *Journal of Magnetism and Magnetic Materials*, 54-57 (1986) 847-848

A number of the results in Chapters 4 and 7 were reported at the International Colloquium on Magnetic Films and Surfaces, ICMFS-11, a satellite meeting of the International Conference on Magnetism 1985

The work reported in Chapter 6 is currently in press and will be published in the *Journal of Magnetism and Magnetic Materials*.

This thesis has not previously been submitted for a higher degree.

* IBM 5600 Cottle Road, San Jose, California

** Philips Research Laboratories, P.O. Box 80.000, 5600 JA Eindhoven, The Netherlands.

SUMMARY

This thesis is concerned with the use of a dedicated scanning transmission electron microscope (STEM) to investigate the physical and magnetic microstructure of thin film specimens. The materials investigated were ferromagnetic and some of them are considered as possible media for high density perpendicular magnetic recording. The first chapter introduces the concepts of ferromagnetism and the energy contributions which determine the domain structures in thin films. The requirements for magnetic recording media are also discussed in this chapter and the reasons for interest in perpendicular, rather than longitudinal recording, as a means of achieving high information storage densities are discussed.

Chapter 2 describes the STEM used in this work, which was an extended V.G. Microscopes HB5, and then goes on to explain image formation in a STEM. It is shown that the use of a non-standard detector with an asymmetric response function in the STEM allows direct information on magnetic structures within a thin film to be obtained (the differential phase contrast imaging mode). Furthermore it is seen that the very small source size of the field emission gun in the HB5 allows this information to be obtained with a high spatial resolution, and that the sequential nature of image formation in the STEM allows this information to be acquired digitally. The remainder of the chapter deals with the microscope conditions used for, and spatial resolution available with, x-ray and EELS microanalysis.

Chapter 3 demonstrates the use of the STEM to characterise fully the physical and magnetic microstructure of a large grain polycrystalline cobalt foil. In this chapter it is demonstrated that electron diffraction can be used to determine the crystallography of the foil, the thickness can be determined by measuring the deflection of the electron beam as it passes through the foil, and the magnetic structure and domain wall profile can be determined using differential phase contrast imaging in the STEM. In Chapter 4 the magnetic stray

fields from the cobalt foil of Chapter 3 are investigated, as are those from written tracks on a longitudinal magnetic recording medium. It is seen that the measured stray fields from the simple domain structure of the cobalt foil are in good agreement with theoretical calculations.

In Chapter 5 the techniques demonstrated in Chapter 3 are applied to planar polycrystalline Co-Cr films with artificial superstructures and to CoCr alloy films. Both materials were grown so as to have a preferential crystal orientation, with a c-axis texture, in the alloys and in the Co layers of the artificial superstructure films, along the film normal. The magnetic structure observed in these films indicated that this c-axis texture had given rise to a degree of perpendicular magnetic anisotropy.

In Chapters 6 and 7 cross-sections of single and double layer perpendicular magnetic recording films are investigated. In Chapter 6, elemental segregation of Cr to individual column boundaries within the columnar microstructure is demonstrated using x-ray microanalysis. When the effects of beam broadening are considered it is seen that the column boundaries are likely to be non-magnetic. In Chapter 7 the magnetic structure of the cross-sections is investigated. Although no unambiguous magnetic contrast is revealed in the CoCr layers, the magnetic structure in the backing layers, and the stray fields from the cross-sections show that there is very small scale magnetic structure within the CoCr layer.

Chapter 8 is a summary of the results obtained, and contains suggestions for future investigations of magnetic recording materials. Three of the four Appendices are concerned with computer processing of STEM images, and one explains the use of the free lens controller on the CTEM used in this work for preliminary investigations.

CHAPTER 1

FERROMAGNETISM AND MAGNETIC RECORDING

1.1 Introduction

Most of the samples studied in this work were ferromagnetic thin films which were either single crystal or polycrystalline. Therefore a brief summary of ferromagnetism, and in particular ferromagnetism in thin films, is given in this chapter. Furthermore some of the materials studied are intended for use as magnetic recording materials, and a summary of the properties required of a magnetic recording media is also given.

1.2 Ferromagnetic Materials

Atoms which have a non-zero electron orbital angular momentum or electron spin, have an intrinsic atomic magnetic moment. At finite temperatures, and in the absence of any interaction between atoms, thermal agitation acts to randomise the orientation of these magnetic moments, giving rise to zero net magnetisation. Ferromagnetic materials, however, have a net magnetisation even at finite temperatures and this is due to a strong coupling between individual atoms. In order to overcome thermal agitation and align the individual moments at room temperature, a magnetic field of the order of 10^9 Am^{-1} is required. In 1907, Weiss proposed that there existed in ferromagnetic materials what he called a molecular field, H_m , which was proportional to the magnetisation, M , of the ferromagnetic material; the constant of proportionality being the molecular field coefficient, λ . This molecular field, together with thermal agitation, gives rise to the idea that for a ferromagnet there will be a temperature, known as the Curie temperature T_c , below which an ordered ferromagnetic structure will prevail, and above which thermal randomisation will dominate. This temperature is given by:

$$T_c = \frac{N \mu^2 \lambda}{3k} \quad (1.1)$$

where N is the number of magnetic atoms per unit volume; μ is the magnetic moment of each of these atoms; and k is Boltzmann's constant.

From the measured values of T_c for materials such as iron and cobalt, it can be seen that λ is orders of magnitude too large for the origin of the molecular field to lie in magnetostatic interactions between neighbouring moments. The origin of the molecular field is in fact a quantum mechanical exchange force (Heisenberg 1928), where the potential energy between two atoms with spins \underline{S}_i and \underline{S}_j is given by:

$$U = -2J \underline{S}_i \cdot \underline{S}_j \quad (1.2)$$

Here J is an exchange integral and is often related to the overlap of the electron orbitals. If J is positive, then the condition of lowest energy is when \underline{S}_i and \underline{S}_j are parallel, and this is the case in ferromagnetic materials.

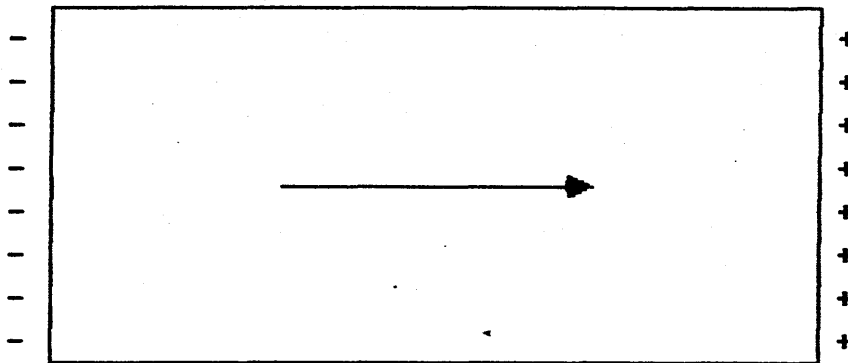
1.3 Magnetic Domains

The above theory predicts that for temperatures below the Curie temperature, a bar of ferromagnetic material should be uniformly magnetised in the one direction, as shown in figure 1.1 a), so as to minimise the exchange energy. However, the net magnetisation in most samples of ferromagnetic materials is close to zero. This is because the exchange energy is not the only energy term that has to be considered.

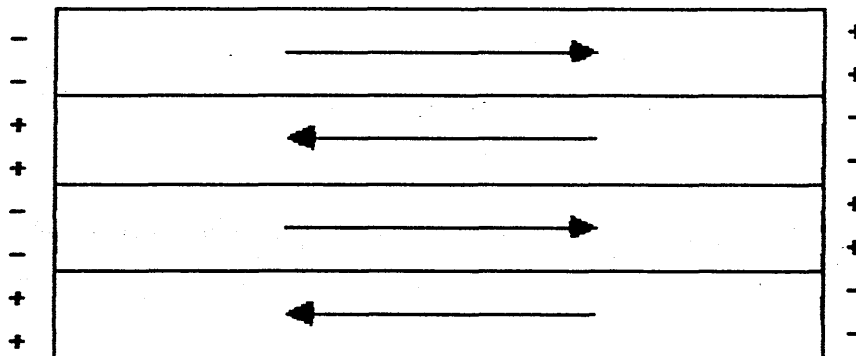
Magnetostatic energy and domain walls:

The magnetisation distribution shown in figure 1.1 a) has a high magnetostatic energy associated with the free poles at either end of the

a)



b)



c)

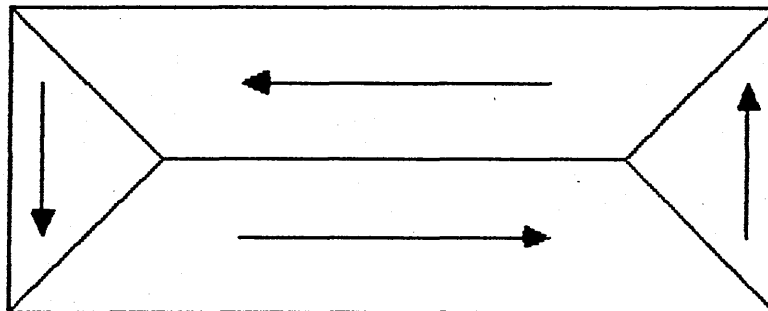


Figure 1.1: a) uniformly magnetised ferromagnetic sample; b) possible domain structure in a ferromagnetic sample with uniaxial anisotropy; c) possible domain structure in a ferromagnetic sample with cubic anisotropy.

bar. These free poles produce a field in the opposite direction to the internal magnetisation of the sample, known as a demagnetising field. This field is given by:

$$H_d = D M / \mu_0$$

where M is the magnetisation of the sample; μ_0 is the permeability of free space; and D is the demagnetising factor, which is dependent on the shape of the sample and on the direction of magnetisation within the sample.

The magnetostatic energy can be reduced by splitting the one large magnetic domain up into a number of smaller domains magnetised in opposite directions (Weiss 1907), as shown in figure 1.1 b). The magnetic fields generated by this distribution of magnetic free poles are mostly beyond the ends of the sample, therefore the sample is not subject to a large demagnetising field. The magnetostatic energy of the configuration in b) is lower than that in a) by a factor of the order of $1/n$, where n is the number of domains. This suggests that the energy of the sample would be minimised by it having a very large number of domains. However, the decrease in magnetostatic energy is counteracted by an increase in exchange energy in the regions between the domains, which are known as magnetic domain walls. Bloch (1932) showed that the interfaces between magnetic domains were not atomically sharp, and that the magnetisation rotated gradually from the direction in one domain to the direction in the next, as shown in figure 1.2. Since the moments of adjacent atoms within the domain wall are not parallel, the wall has associated with it an exchange energy per unit length. In some cases the wall can also have associated with it magnetostatic energy and a number of other energy terms which are discussed below. This wall energy is minimised by minimising the length of domain wall within the sample. The size of magnetic domains within a ferromagnetic sample is therefore determined by the relative contributions of exchange, magnetostatic and domain wall energies to the overall energy of the system.

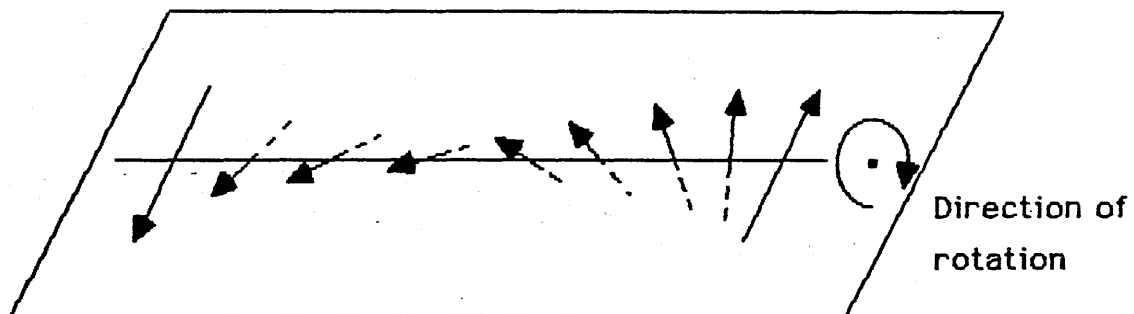


Figure 1.2: Pattern of rotation of magnetisation within a Bloch wall.

Magnetocrystalline energy:

For many crystalline ferromagnetic materials the internal energy is dependent on the direction of the magnetisation with respect to the crystal structure. The magnetocrystalline contribution to the internal energy of these materials is minimised when the magnetisation points along certain, prominent crystal axes, known as easy axes. For example, in hcp cobalt the easy axis of magnetisation is the c-axis, and cobalt is said to have a uniaxial magnetocrystalline anisotropy. In bulk samples

the magnetisation will lie parallel or anti-parallel to the easy axis of the material. Figure 1.1 c) shows the type of domain structure seen in a material, such as single crystal Fe cut along a [100] direction, which has cubic anisotropy, in this case there are no free poles at the surfaces and flux closure is achieved within the sample.

In an anisotropic magnetic material, not only does the magnetisation within the domains lie along specific easy axes, the domain walls tend to lie along specific crystal planes. This reduces the anisotropy energy associated with the walls. Therefore, although the size of domains within a bulk sample of ferromagnetic material is determined by the exchange, magnetostatic and wall energies if the sample has a strong magnetocrystalline anisotropy then this will determine the direction and shape of the domains.

Magnetostriction:

In some materials, magnetisation can induce a strain in the crystal lattice; this phenomenon is known as magnetostriction. A sample with a positive magnetostriction will extend along the direction in which it is magnetised, and contract in the perpendicular direction. This can lead to a deformation of the magnetic sample, and an increase in the internal elastic strain energy. Therefore, if possible, the domain structure within a material with a large magnetostriction will be such that the strain energy is minimised.

Another consequence of magnetostriction is that straining a

sample can induce an easy axis of magnetisation; i.e. the magnetisation will tend to lie along a direction which leads to a decrease in the stored elastic strain energy. This idea of introducing a strain into a sample to define an easy axis will be discussed, with regard to artificial superstructures, in chapter 5.

The domain structure in a magnetic material can, therefore, be seen to represent a potential energy minimum in which the exchange, magnetocrystalline, magnetostatic, magnetostrictive and wall energies all have to be considered. Calculation of the domain structure in an arbitrary sample is thus almost completely impossible. If however, one or two energy contributions dominate, the calculation of the general trend of the domain structure is greatly simplified. One such case in which the determination of the general domain structure is somewhat simplified is that of thin film magnetic materials.

Thin film domain structures:

The discussion so far has been about the basic principles of ferromagnetism, and the formation of domain structures, in a general ferromagnetic sample. However, the samples studied in this work were either thin films or cross-sections of thin films. Therefore, at least one lateral dimension of the sample (two in the case of the cross-sections) was very much smaller than the others; this leads to a strong shape anisotropy. For a thin film uniformly magnetised in-plane, the magnetostatic energy is very small because the free poles are very far apart, giving a low scalar magnetic potential. This gives rise to a demagnetising factor, D , of approximately zero. For the same film magnetised perpendicular to the plane of the film, the free poles are very close together giving a high scalar magnetic potential and therefore a high magnetostatic energy; In this case $D \sim 1$. This shape anisotropy therefore acts to keep the direction of magnetisation within the plane of the film so as to minimise the magnetostatic energy of the sample.

In materials in which the magnetostatic energy contribution

dominates, the magnetisation within the domains will lie in the plane of the film. This is typical of the domain structures in soft magnetic materials, such as permalloy. In a material which has a strong out of plane anisotropy, the magnetic structure is a compromise between the magnetostatic considerations trying to keep the magnetisation within the plane of the film and the out-of-plane anisotropy. In this case the magnetisation will generally lie at some angle between the easy axis and the film plane. The domain sizes are usually quite small to reduce the magnetostatic energy. The in-plane component of magnetisation generally lies along the projection of the easy axis in the film plane. If the magnetocrystalline anisotropy is strong enough, and oriented along the film normal, the film may be magnetised along the film normal, in which case the domain widths will be very small to try to minimise the magnetostatic energy. Most of the materials studied in this work had strong magnetocrystalline anisotropies. In chapters 3 and 4 the domain structures and stray fields from a large grain cobalt foil will be discussed. In this case the domain structure will be shown to be determined entirely by the orientation of the c-axis of the crystals with respect to the film normal. In chapters 5 to 7 the domain structure within materials intended for use as perpendicular magnetic recording materials will be investigated. These materials are designed to have a strong perpendicular anisotropy, and the presence and origin of this will be discussed.

1.4 Magnetic Recording

Longitudinal recording:

In a magnetic recording system, information is read from the magnetic recording medium by a play-back head which interacts with the magnetic fields above the medium as it moves past the head. Therefore, the information has to be written in such a way that the resulting domain structure produces a sufficiently strong magnetic field distribution for the play-back head to detect. The most common

way to achieve this is to write the information as a series of in-plane domains, with the magnetisation in adjacent domains being head-on, as shown in figure 1.3 a). This is called longitudinal magnetic recording, and is the system used in almost all commercial magnetic recording systems.

In order to sustain the head-on domain structure used in longitudinal recording, the recording medium usually has both of the following: 1) a high coercivity and 2) an in-plane easy axis running along the track direction. This is because the magnetic free poles from oppositely magnetised domains produce a strong demagnetising field which tries to rotate the magnetisation within the domains so that the magnetisation vector on either side of the magnetic transitions are anti-parallel, as shown in figure 1.4. A high coercivity prevents the demagnetising field rotating the magnetisation within the head-on domains. A strong in-plane anisotropy along the recording track direction locks the magnetisation in the domains along the track direction to minimise the anisotropy energy.

The required in-plane anisotropy can be produced by a number of different methods in different magnetic recording media: For instance, the most common magnetic recording medium, $\delta\text{-Fe}_2\text{O}_3$, is a particulate medium consisting of a series of needle shaped particles in a binder matrix. The long axis of the particles is aligned with the direction of the magnetic recording track, which is the direction in which the medium travels past the head, and these individual particles can be easily magnetised either parallel or anti-parallel to the track direction. Because of the shape anisotropy of the individual particles it is very difficult to magnetise them in any other direction. In more modern particulate media, the needles also have a magnetocrystalline anisotropy along their long axis (Berkowitz *et al* 1985).

Another type of material used for longitudinal magnetic recording is continuous thin film medium. An in-plane anisotropy can be introduced into this type of medium by depositing the thin film onto the disk or tape using oblique incident evaporation. Ferrier *et al* (1983)

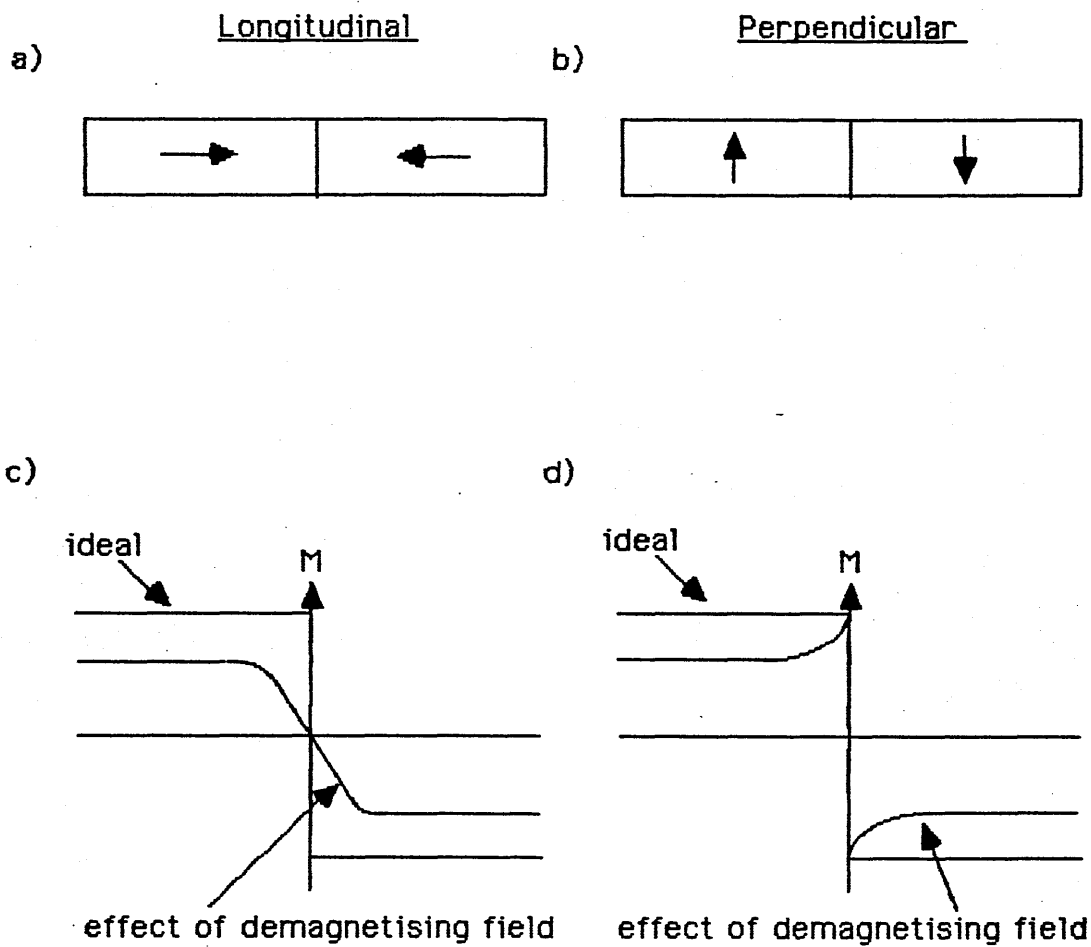


Figure 1.3: The effect of demagnetising fields on the magnetisation transitions in longitudinal and perpendicular recording media.

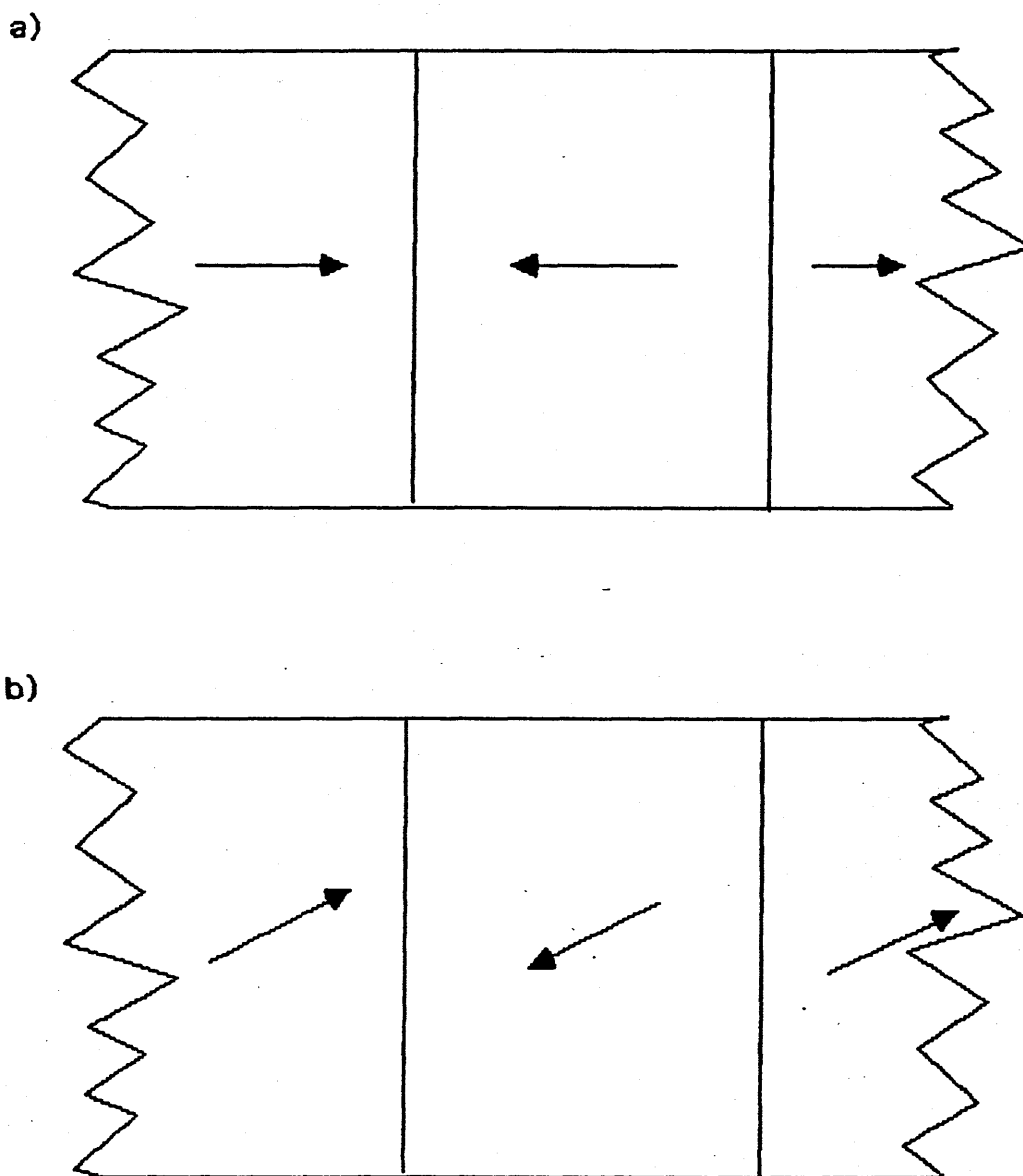


Figure 1.4: a) Ideal magnetisation in longitudinal recording
b) Effect of demagnetising field.

reported details of an FeCoCr disk produced in this way in which the anisotropy along the track direction was approximately seven times that in any other direction. The addition of grooves in the disk surface to improve the flying characteristics of recording head increased this ratio from seven to nine (Ferrier 1986).

At the time each individual magnetisation transition is written on a longitudinal recording medium, the magnetisation of the domains on either side of it equals the saturation magnetisation of the medium. However, once the medium moves past the recording head, the magnetic field from the domain no longer has an easy return path through the magnetic core of the head, and it acts to demagnetise the domain as described above (Suzuki 1984). The effect of this on the magnetisation within the recording medium is shown in figures 1.3 c). The ideal curve represents the magnetisation produced within the medium by the write head, the second curve represents the effect of the demagnetising field on the remanent magnetisation within the medium. The effect is strongest at the transition itself and smears the transition out. This demagnetising effect becomes stronger as the domain size decreases, and therefore the signal from the play-back head decreases as the information storage density goes up. This limits the information storage densities which are possible using longitudinal magnetic recording (Iwasaki and Takemura 1975).

Perpendicular recording:

Iwasaki and Nakamura (1977) proposed a perpendicular mode of magnetic recording as a means of overcoming the effects of demagnetising fields at high recording densities. The domain structure in this type of recording consists of individual domains magnetised along the film normal, this is shown in figure 1.3 b). The magnetic fields from the surface free poles of oppositely magnetised domains in this type of structure act to reinforce the magnetisation on either side of the transition rather than reduce it as shown in figure 1.3 d). Once again the ideal curve corresponds to the magnetisation produced by the

write head, and the second curve corresponds to the remanent magnetisation within the medium once the head has moved on. Although the magnetisation within the domains is slightly reduced, due to individual columns having their magnetisation switched by the stray field (Ouchi and Iwasaki 1984), the transition is very sharp and is reinforced by the stray field rather than being degraded. The signal from the play-back head is, therefore, still appreciable at very high recording densities.

The materials used for perpendicular recording must have a very strong perpendicular anisotropy, so that the normal state of the film is for it to consist of domains magnetised along $\pm n$, the film normal. One material which has been found to have a strong perpendicular anisotropy is sputtered CoCr, which was the material originally proposed by Iwasaki and Nakamura in their 1977 paper. The anisotropy in this film is thought to be primarily due to magnetocrystalline anisotropy. Another contributory factor, to some extent, is the columnar microstructure of these films. The columns in this microstructure may act as isolated magnetic needles oriented along the film normal and this will be discussed in more detail in chapters 5 and 6.

An added advantage of perpendicular over longitudinal recording is the width of the transition region between oppositely magnetised domains. In longitudinal recording media the width of the transition region is determined by the ratio of the remanent magnetisation of the film to its coercivity (Suzuki 1984). In thin film longitudinal media, which generally have shorter transition widths than particulate media, the transition width is approximately 1/3 to 1/2 of the thickness of the film. Although the transition widths in longitudinal recording media are generally of the order of 1000nm, transition lengths as small as 200nm have been reported in modern, high density, longitudinal media (Yoshida *et al*/1983). This transition width is not the width of the domain wall in these thin films, it is the width of the zig-zag pattern that the wall follows, as shown in figure 1.5 a). The zig-zag domain wall develops to

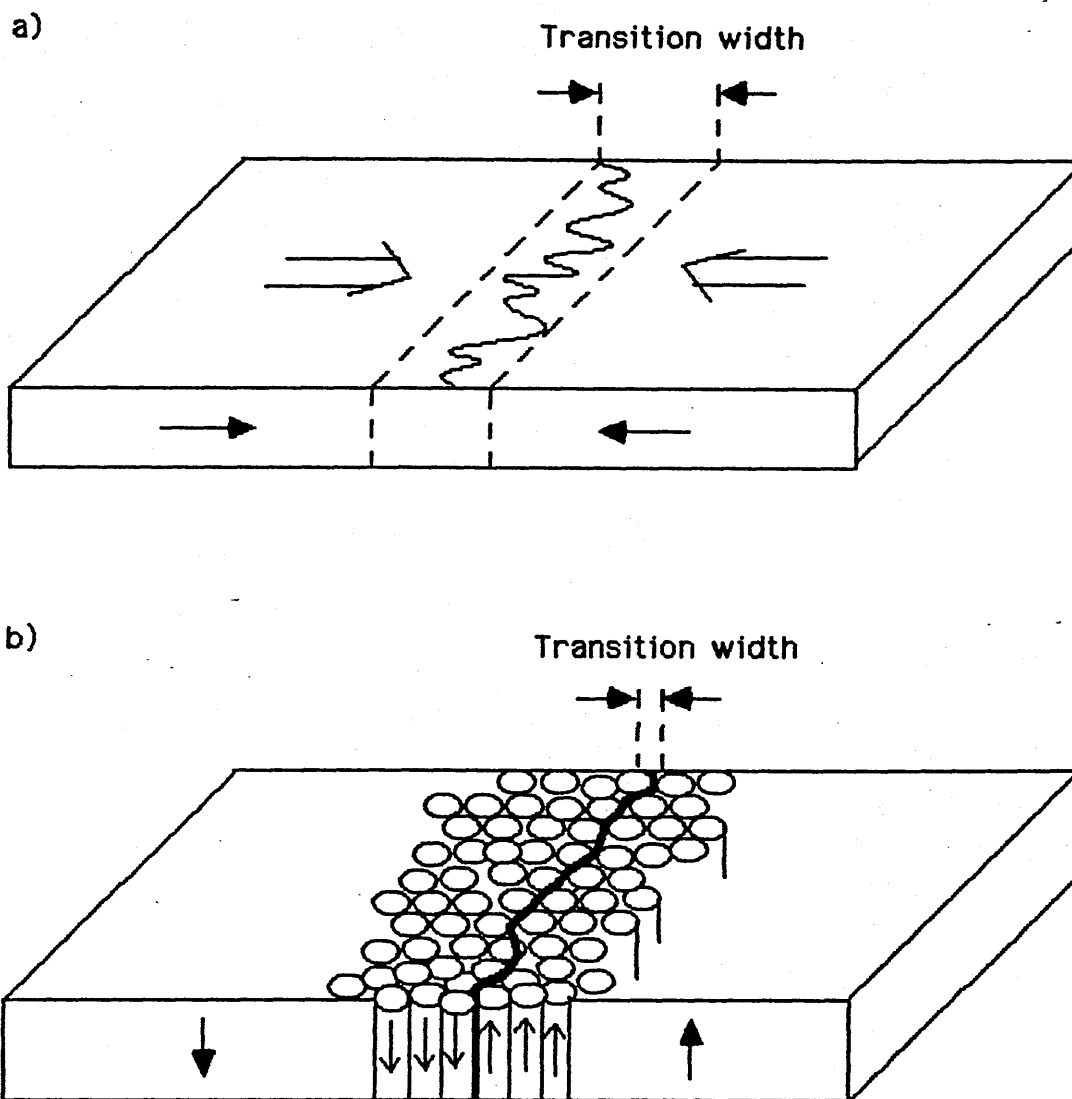


Figure 1.5: Transition widths in a) thin film longitudinal and b) perpendicular recording media.

reduce the magnetostatic energy associated with the head-on domain structure by reducing the angle between the magnetisation vectors on either side of the domain wall. As the domain sizes decrease the zig-zags add to the noise in the play-back signal and further reduce the attainable recording densities in longitudinal media.

In perpendicular media such as CoCr the transitions are thought to be much shaper than in longitudinal media, with the transition width being approximately the same as the diameter of the columns which can be between 40 and 100nm. This is shown in figure 1.5 b). So far the highest density recorded and reproduced using perpendicular recording is 200k flux reversals per inch (FRPI) (Ouchi and Iwasaki 1984), in which case the domain size is 125nm. The highest recording density obtained with longitudinal recording is approximately 170kFRPI which gives rise to a domain sizes of the order of 150nm. This was reported by Yoshida *et al* (1983) who used electron holography to investigate the Co film on which the high density recording had been made. However, they did not observe magnetic structure within the film, only the stray field beyond its surface. This stray field corresponded to an individual bit size which was 50 nm smaller than the smallest transition widths they observed in other films of this type, it is not certain, therefore, if the domains were continuous within this film.

It appears, from the recording densities so far reported in the literature that, even although it is in the early stages of development, perpendicular magnetic recording has potential for much higher information storage densities than longitudinal recording. Since perpendicular recording is relatively new, there is a lot of interest in the microstructure and micromagnetics of perpendicular recording media and these media will be investigated in chapters 5 to 7.

Effect of soft magnetic underlayers:

Some of the perpendicular recording media studied in this work had soft magnetic underlayers beneath the CoCr. The reason for putting a soft magnetic layer, such as NiFe, beneath a perpendicular recording

medium is two fold: 1) it reduces the current in the write head needed to saturate the recording medium and 2) it increases the play-back signal from the medium.

These two properties of the soft magnetic layer can be understood by reference to figure 1.6. From this figure it can be seen that the soft magnetic layer acts as a magnetic keeper. During the write process, this layer provides a low reluctance path for the flux from the write head, therefore reducing the overall reluctance of the head. This, in turn, reduces the current required in the head to provide a magnetic field strong enough to saturate the recording medium. After the information has been written onto the perpendicular medium, the soft magnetic layer reduces the demagnetising field from the perpendicularly magnetised domains by providing a low reluctance path for the field from one domain to reinforce the magnetisation in the oppositely magnetised domains next to it. Therefore the effect of demagnetisation is reduced with the result that the readback signal is stronger.

One drawback of a soft magnetic underlayer, which has emerged as a result of magnetic recording studies, is that films which have this layer are subject to random noise in the readback signal which is not present in films which do not have this layer (Luitjens *et al*/1985). The noise appears as sharp spikes in the readback signal and is thought to be due to the rapid motion of domain walls within the soft magnetic layer. The reason for these Barkhausen-like jumps is not known although Luitjens *et al* suggest a number of possibilities including the change of boundary conditions due to the presence of the readback head. A knowledge of the magnetic structure within the soft magnetic underlayer may help in understanding what causes these jumps and how they can be prevented. In chapter 7 the magnetic structure within the soft magnetic underlayer of a number of perpendicular recording media are investigated.

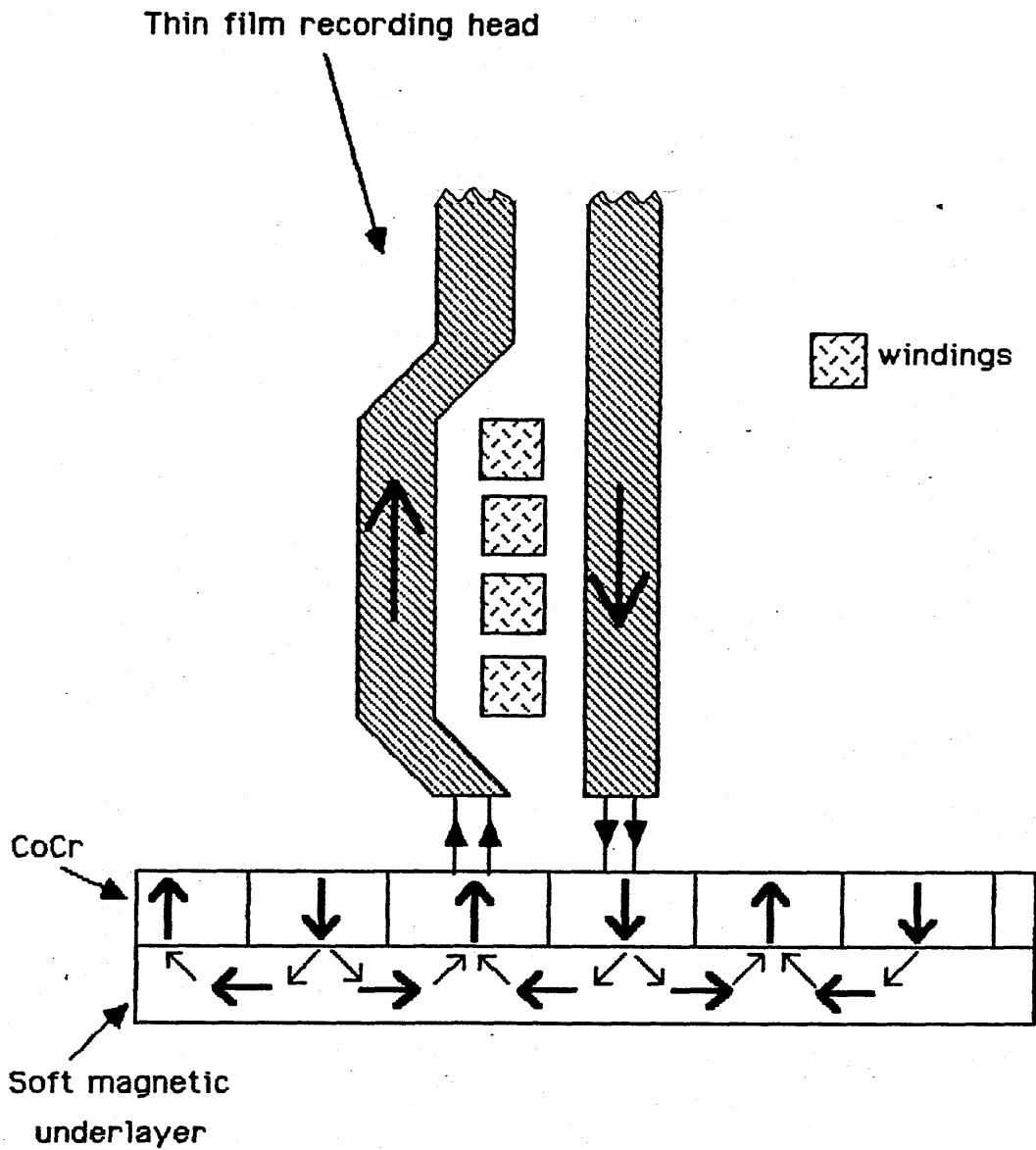


Figure 1.6: Effect of soft magnetic underlayer on write process in perpendicular recording media.

1.5 Organisation Of Thesis

In this chapter the factors which determine the magnetic domain structures in ferromagnetic materials have been discussed. In particular the special case of thin films in which the magnetostatic energy dominates has been discussed. The requirements for both longitudinal and perpendicular magnetic recording have been discussed in terms of the properties of the recording medium. From this it was seen that perpendicular recording promises the possibility of higher recording densities than longitudinal recording. The remainder of this work deals with the use of a dedicated scanning transmission electron microscope (STEM) to characterise the properties of magnetic thin films in general and CoCr perpendicular magnetic recording media in particular.

The STEM instrument and the operating conditions used are described in chapter 2. The theory of image formation in the scanning transmission electron microscope is also dealt with in this chapter. Chapter 3 demonstrates the use of the STEM in characterising the physical microstructure and relatively simple magnetic structure of a thin cobalt film. In chapter 4 the stray fields from the cobalt foil are investigated using differential phase contrast imaging, and this technique is also applied to the stray fields from a longitudinal magnetic recording medium. The techniques used in chapters 3 and 4 to investigate the magnetic structure of the cobalt film are used in chapters 5 and 7 to investigate the more complicated magnetic structure of CoCr magnetic recording materials. In chapter 6 local elemental segregation within cross-sections of CoCr magnetic recording material is demonstrated using high spatial resolution x-ray microanalysis. The final chapter, chapter 8, contains general conclusions and suggestions for future work.

CHAPTER 2

INSTRUMENTATION

2.1 Observation Of Magnetic Domains

The first direct observations of magnetic domains were made by Bitter (1931) using a colloidal suspension of very fine ferromagnetic particles. When applied to a polished ferromagnetic surface, these particles accumulate at regions of high magnetic field gradient, so delineating regions where magnetic domain walls intersect the surface of the sample. Although useful for determining domain size and shape in many materials, the Bitter technique gives no information on the direction of magnetisation within the domains and does not have a high resolution. Furthermore, the Bitter technique and other forms of surface decoration only probe the surface layer of a sample and are very dependent on specimen preparation (Kaya 1934).

Optical techniques, such as the magnetic Kerr effect and the Faraday effect can also be used to study magnetic domain structures. These techniques have two main advantages over decoration techniques:

- 1) They can be used for dynamical studies of magnetic structures.
- 2) The specimen surface remains clean and unchanged by the observation.

The Kerr effect is the rotation of the plane of polarisation of light upon reflection from a magnetised surface. With the advent of lasers and computer image processing the Kerr effect has proved useful in imaging, for example, domain wall motion in thin film recording heads (Argyle and Suits 1985) without the need to remove dielectric coatings from the heads. For transparent materials the Faraday effect is more useful. This involves the rotation of the plane of polarisation of light as it is transmitted through a magnetised material. Although of limited use in studying metals, it has been used to study domain structures in transparent magnetic garnets (Dillon 1958).

Optical techniques are, however, limited to either transparent

materials, in the case of the Faraday effect, or surface magnetic structure in the case of the Kerr effect. As such they are of little use in the study of the magnetic structures within magnetic recording materials.

Neutrons have a magnetic moment and therefore can interact with magnetic materials. This fact has been used in neutron depolarisation studies of magnetic recording materials (Hemmes *et al* 1984). In this case Larmor precession of the magnetic moment of the neutron about the spontaneous magnetisation within the sample gives information on the average domain size. Neutron diffraction gives information on the spatial distribution, direction and order of magnetic moments within a sample, and has led to advances in the understanding of the spin configurations in the rare earths (Kjims *et al* 1979; Hastings and Carliss 1962). Both neutron techniques, however, give general information about a sample as a whole, and cannot provide high resolution information on actual domain configurations. In addition, there are only a limited number of intense neutron sources available, for example, the new Spallation Neutron Source at the Rutherford Appleton Laboratory (Physics Bulletin 1985). Even here acquisition times are measured in hours rather than minutes or seconds.

Scanning electron microscopy can provide information on stray fields and surface domain structures in large samples using type I and type II magnetic contrast respectively. Ferrier *et al* (1985) demonstrated the use of type I and type II contrast to study domain wall motion in thin film recording heads and to image high density recorded tracks. With the recent addition of electron spin analysis to the SEM, Unguris and his colleagues have developed a powerful means of obtaining quantitative magnetic information about surface domain structures (Unguris *et al* 1986). However SEM can only probe the surface layers of magnetic materials. To obtain high resolution information about the magnetic domain structures within thin magnetic films, Lorentz transmission electron microscopy has to be used. The Fresnel, or defocus, mode of Lorentz microscopy delineates magnetic

domain walls as narrow dark or light bands, and also allows stray fields to be identified. However, the relationship between image contrast and magnetic structure is highly non-linear. To obtain quantitative information on magnetic structures using this technique it is necessary to carry out detailed analysis of a number of images at different values of defocus. Linear extrapolation of divergent wall images to zero defocus has been used to obtain domain wall widths (Wade 1965). Inversion techniques have also been used to obtain domain wall profiles from divergent wall images (Cohen and Harte 1969). These techniques are, however, complicated and not universally applicable. For qualitative information the technique is very useful, for example in the identification of domain wall pinning sites in $\text{Fe}_{77}\text{Nd}_{15}\text{B}_8$ permanent magnets (Suzuki and Hiraga 1986).

The displaced aperture, or Foucault mode of Lorentz microscopy gives strong contrast between oppositely magnetised domains, but gives limited information about magnetic domain walls (Tsukahara 1984), the wall intensity being very dependent on aperture position. In addition diffraction effects due to the aperture can strongly affect the image, as can electrostatic charging of dirt on the aperture blade. Instead of imaging with part of an electron deflection pattern, as in the Foucault mode, the entire deflection pattern can be projected onto the viewing screen. From the splitting of the straight through beam some information on the type of domain walls in the field of view can be ascertained (Tsukahara 1984). As with the Fresnel mode of Lorentz microscopy, the relationship between the intensity in the final image and the magnetic structure in the sample in the above two techniques is a non-linear one.

Two modes of Lorentz microscopy do give direct, quantitative information about the distribution of magnetisation within magnetic thin films. These are electron holography and differential phase contrast microscopy (DPC). Electron holography was first proposed by Gabor (1948) as a means of improving the resolution of images obtained in the electron microscope. It is only recently that the technique has

been put into practice to study magnetic domain structures (Tonomura *et al* 1980). The main drawback of electron holography is that the hologram has to be optically reconstructed before information on the magnetic structure can be extracted.

Differential phase contrast electron microscopy involves the use of a scanning transmission electron microscope (STEM) fitted with a split or quadrant detector (Dekkers and de Lang 1974). By taking difference signals from opposite quadrants of a quadrant detector fitted to their extended V.G. Microscopes HB5 STEM, Chapman and Morrison (1983) obtained high resolution images of the spatial variation of magnetisation within magnetic thin incalloy films. The DPC mode of Lorentz microscopy gives direct images of the induction within a sample without the need for optical reconstruction techniques. In addition, as the images are acquired sequentially in a STEM, on-line computer image acquisition and analysis are readily available. DPC imaging has been used throughout this work and in this chapter the STEM instrument and experimental conditions used, as well as the theory of DPC imaging, will be described.

2.2 The Scanning Transmission Electron Microscope

The scanning transmission electron microscope used in this work was an extended V.G. Microscopes HB5 STEM, a schematic of which is shown in figure 2.1.

Cowley (1981) has shown, using the idea of reciprocity, that images which can be obtained in a conventional transmission electron microscope (CTEM) can also be obtained in a STEM, provided that certain constraints are adhered to. In particular, the detector in the STEM must subtend the same angle at the specimen as the source in the CTEM subtends at the specimen. For bright field imaging this means that the detector in the STEM collects only a small fraction of the signal transmitted through the specimen (Thomson 1973). To be able to acquire an image with a good signal to noise ratio, it is therefore necessary to either acquire for a long period of time or to use a high

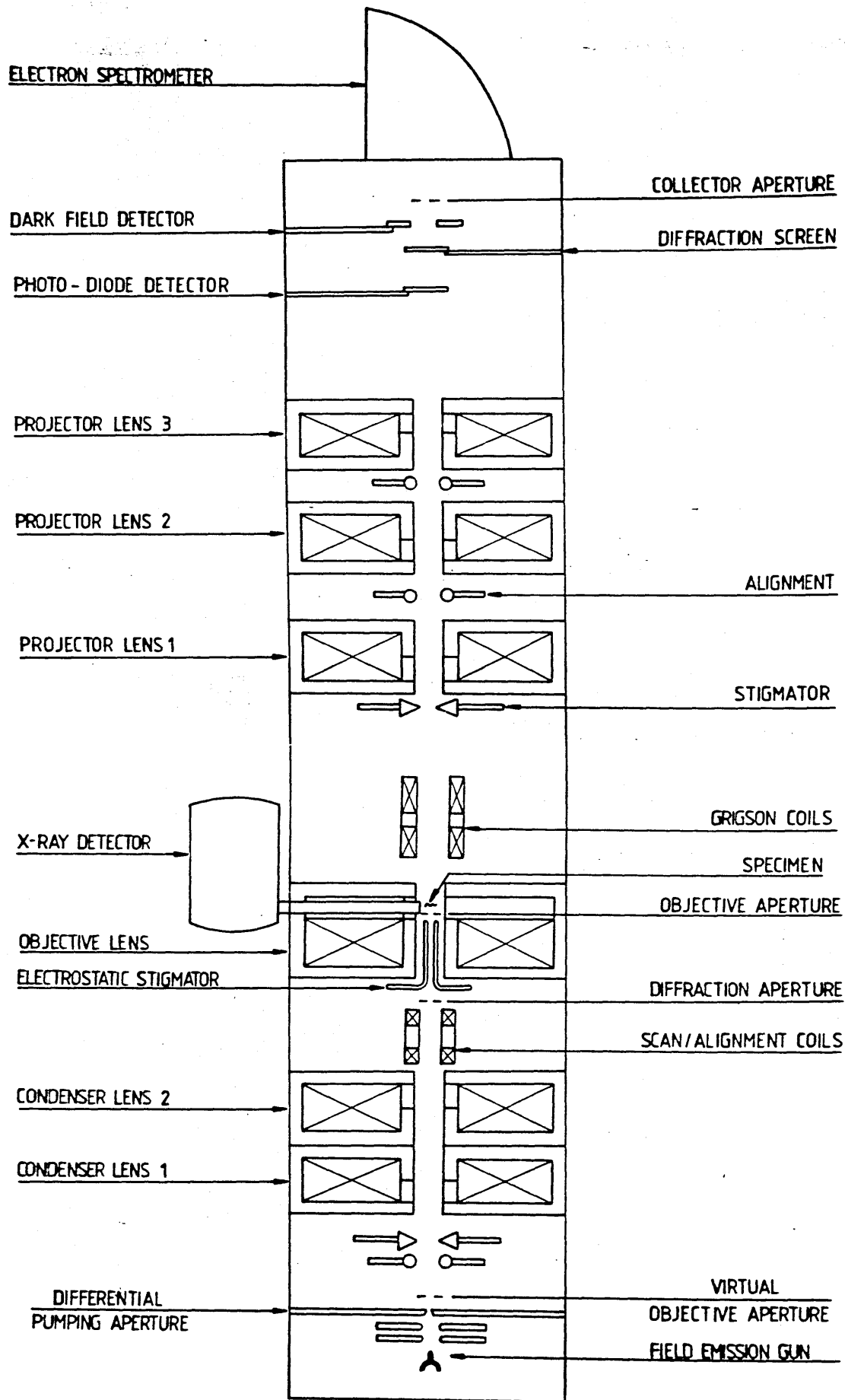


Figure 2. 1: Schematic of Y.G. Microscopes HB5 STEM

brightness electron source. In a dedicated STEM, such as the HB5, a high brightness field emission gun is used and this allows images to be viewed at TV rates. When images are recorded, either on film or digitally, line acquisition times of around 20ms are used in order to minimise mains frequency noise. This gives total acquisition times of 20 seconds for film and just over 5 seconds for digital images.

The field emission gun

The gun in the HB5 has a single crystal tungsten cathode, an extraction electrode held at a few kV with respect to the cathode, and a third electrode which accelerates the electrons to 100kV. The emitting surface of the cathode is a (310) crystal face which has a low electron work function Φ_e . The tip of the cathode has a radius R of about 100nm and with a voltage, V_1 , of 3.5-4kV between the cathode and the extraction electrode a tunnel emission current can be produced. The current density from the gun is given by the Fowler-Nordheim Law:

$$J_s = AF^2 \exp\left[\frac{-B\Phi_e^{3/2}}{F}\right] \quad (2.1)$$

and is typically 10^4 - 10^7 Acm^{-2} . A and B are constants, and F is the electric field strength at the emitting surface, which is of the order of $(3.5-4) \times 10^{10} \text{Vm}^{-1}$. These current densities are many orders of magnitude greater than those available from thermionic emission guns; even those fitted with LaB₆ filaments have current densities $\leq 200 \text{Acm}^{-2}$. Furthermore, the very much smaller emitting area of a field emission gun gives it a much higher brightness.

The radius of the real cross-over at the cathode tip is given by:

$$r_{\text{tip}} = R\sqrt{V_T / V_1} \quad (2.2)$$

where V_T is the mean transverse energy of the electrons, which is $\sim 0.23\text{eV}$. This gives the radius of the emitting area on the cathode as $\sim 1\text{nm}$. However, the gun itself acts as an electrostatic lens producing a virtual cross-over behind the actual cathode tip. Following Morrison

(1981), the diameter of the virtual cross-over is 6.5nm and is situated ~170mm from the first condenser lens, this assumes that the gun is operated at an extraction voltage to accelerating voltage ratio of 3/100. In practice this ratio is closer to 4/100; however these figures can be regarded as good approximations to the actual values. Morrison gives a more detailed discussion of the assumptions made in calculating these figures.

As any ions produced in the vicinity of the gun cathode by electron bombardment would be accelerated towards the tip by the very strong electrostatic field, and so damage the emitting surface, it is essential that the gun chamber is maintained at a very high vacuum. In the HB5 the gun chamber is always kept at a vacuum of better than 10^{-10} torr when the gun is operating.

Probe forming optics:

The probe forming optics consist of three lenses: two condenser lenses C1 and C2, and the objective lens. In normal imaging mode the two condenser lenses are used to transfer an image of the virtual cross-over, produced by the gun, to the plane of the selected area diffraction aperture (SAD). The objective lens is kept at an almost constant excitation and is used to produce a demagnified image of the cross-over in the SAD plane, on the specimen plane. With the objective lens on, the objective aperture defines the probe half-angle α_0 . The total magnification of these three lenses can be as small as 1/100. However the probe size is given by the superposition of the demagnified Gaussian image of the source and the aberration disk of the probe forming optics. The objective lens is operated at a high excitation in order to reduce the spherical aberration coefficient rather than to produce such a demagnified image of the Gaussian source. To obtain very small probe diameters the specimen must be situated within the magnetic field of the objective lens, which at the normal specimen position is $\approx 0.85T$. This is obviously an undesirable condition for studying magnetic domains, as any domain structure within a specimen

would be destroyed by the magnetic field of the objective lens. There are two ways in which this problem can be overcome.

1) The specimen can be raised out of the objective lens using a special specimen cartridge, and the objective lens operated at a much reduced excitation.

2) The objective lens can be switched off and the condenser lenses used to form the image of the gun cross-over on the specimen situated at the normal specimen height.

In practice the resolution available with the objective lens off, and using only one of the condenser lenses is sufficient for studying most magnetic structures (Morrison 1981). In this case the full range of specimen cartridges is available, allowing the specimen to be tilted while in the microscope. With the objective lens off the probe defining aperture is the SAD aperture.

The post-specimen lenses:

The three post-specimen lenses situated above the specimen are used to match the angular distribution of the electrons scattered by the specimen to the physical dimensions of the detectors attached to the microscope. These lenses can be controlled manually or by a microprocessor controller which has specific camera lengths stored in an EPROM.

The detectors:

A range of detectors are situated after the post-specimen lenses. The bright field detector is a small on-axis scintillator coupled to a photomultiplier. This subtends a small angle at the specimen, and under normal imaging conditions gives images analogous to bright field images in the CTEM.

The dark field detector is a large annular detector, once again consisting of a scintillator-photomultiplier assembly. It subtends a relatively large angle at the specimen, and is generally used to collect electrons which have been elastically scattered out of the primary

beam. In addition there is an electron spectrometer in front of the bright field detector, thus allowing energy filtered images to be obtained. By using the collector aperture in front of the spectrometer it is possible to obtain images using the bright field detector which are the equivalent of coherent bright field images in the CTEM (reciprocity implies that a small axial detector in the STEM is equivalent to a small axial source in the CTEM). The bright field and dark field detectors are designed so that both can be used at the same time, the quadrant detector and the diffraction screen, on the other hand, are incompatible with the other electron detectors.

The diffraction screen is used to view convergent beam electron diffraction patterns, and once in the beam it can be photographed using a 35mm camera, or viewed using a videcon camera.

The quadrant detector is a commercial position sensing photodiode, split into four quadrants. The signals from the four quadrants can be added to give an incoherent bright field image. It is also possible for the difference of the signals from any two opposite quadrants or semicircles to be obtained. These signals are, for small shifts, directly proportional to angular shifts of the electron beam across the detector. As this means that the detector has a response function which is dependent upon the position of the electron beam, and which is antisymmetric, it has no direct equivalent in the CTEM. It is, in theory, possible to produce a similar image in the CTEM but this requires two exposures with alternative half plane apertures, followed by the subtraction of the resulting image intensities. In practice problems of alignment of the specimen and of the resultant images makes this method impractical.

In addition to obtaining images, the HB5 STEM can be used to obtain electron energy loss spectra (EELS) and x-ray spectra. The electron spectrometer in the detector chamber is used for EELS and the post-specimen lenses are used to provide angular compression of the electron beam into the spectrometer. The x-ray detector is situated very close to the specimen in order to collect as many of the x-rays,

produced in the specimen by the electron beam, as possible. Both the EELS and the x-ray spectra provide information on the composition of the volume of specimen being irradiated by the electron beam.

All the signals from the detectors on the HB5, with the exception of the diffraction screen image, can be acquired digitally using a minicomputer. This allows immediate on-line data processing without the need to digitise micrographs, or type spectrum values into a computer.

In the following sections of this chapter, image formation in the STEM will be discussed with particular reference to the quadrant detector. The imaging conditions used will be described, together with modifications to the apparatus. The EELS and x-ray acquisition systems will also be described, as will the general principles of EELS and x-ray spectroscopy of thin metallic films.

2.3 Image Formation In The STEM

Object transmittance:

For a sufficiently thin specimen, it can be shown that the effect of a specimen upon an incident electron wave can be represented by a multiplicative transmission function. In this case the electron wave at the specimen exit plane is given by:

$$\Psi_o(x,y) = \Psi_i(x,y) \cdot q(x,y) \quad (2.3)$$

where $\Psi_i(x,y)$ is the incident electron wave function and $q(x,y)$ is the specimen transmittance. It will be shown that a magnetic specimen can be approximated to a pure phase object. For a pure phase object

$$q(x,y) = \exp \{-i\phi(x,y)\} \quad (2.4)$$

where $\phi(x,y)$ is the phase change of the electron wave caused by the specimen. For a non-magnetic specimen this is given by:

$$\phi(x,y) = \frac{\pi}{E\lambda} \int V(\underline{r}) dz$$

where $V(\underline{r})$ is the electrostatic potential of the specimen, referenced to the free space potential, E is the accelerating voltage and λ is the electron wavelength. For a magnetic specimen, however, $\phi(x,y)$ is given, as will be shown in section 2.4, by

$$\phi(x,y) = -\frac{2\pi e}{h} t \int_0^x B_y(x_1) dx_1$$

where t is the specimen thickness and $B_y(x_1)$ is the average in-plane component of magnetisation. In the expression for the phase due to an electrostatic potential, $V(\underline{r})$ was referenced to the free space potential, and in the case of the magnetic specimen, the magnetisation is integrated from some arbitrary origin to the point x . In the interference effects governed by the phase of the electron wave it is the relative phase, rather than the absolute phase, which is important and therefore the choice of reference points in the above equations is for convenience only. A more detailed discussion of the effect of a magnetic specimen on the electron wave is given in section 2.4.

To include absorption in the expression for the specimen transmittance we include a factor $\mu(\underline{r})$ in the exponential so that equation (2.4) becomes:

$$q(\underline{r}) = \exp \{-i\phi(\underline{r}) - \mu(\underline{r})\} \quad (2.5)$$

Now \underline{r} replaces (x,y) .

Intensity on the detector plane due to coherent point source:

In general the electron source will have a finite size and therefore the incident electron wave will be only partially coherent. However,

Burge and Dainty (1976) have shown that the effect of a partially coherent electron source can be accounted for by a convolution of the image due to a point source with a function representing the source intensity distribution.

For a point source on the optical axis, the incident electron wave is given by

$$\Psi_i(\underline{r}) = \mathcal{F}[A(\underline{u}) \exp\{i\chi(\underline{u})\}] \quad (2.6)$$

where $\mathcal{F}[\]$ implies a Fourier transform, $A(\underline{u})$ is an aperture function such that

$$A(\underline{u}) = 1 \text{ if } |\underline{u}| < u_0$$

$$= 0 \text{ if } |\underline{u}| > u_0$$

\underline{u} is the two dimensional reciprocal space vector, and $\chi(\underline{u})$ is the phase change due to defocus and aberrations of the probe forming lens. In most cases the major lens aberration that contributes to $\chi(\underline{u})$ can be represented by the third order spherical aberration coefficient C_s . Astigmatism is generally correctable, and chromatic aberration can be neglected in comparison to spherical aberration due to the high stability of the voltage and current supplies in modern microscopes. Therefore, following Hawkes (1978)

$$\chi(\underline{u}) = -\frac{1}{4} (C_s \lambda^3 \underline{u}^4) + \frac{1}{2} (z \lambda \underline{u}^2)$$

where C_s is the third order spherical aberration coefficient and z is the defocus, which is positive if the lens excitation is reduced from its in-focus value.

The detectors in the STEM are situated a long distance from the specimen; therefore the wave amplitude in the detector plane is the Fourier transform of the amplitude at the specimen exit plane:

$$\begin{aligned}\Psi(\underline{u}) &= \mathcal{F}[\Psi_i(\underline{r}) \cdot q(\underline{r})] \\ &= Q(\underline{u}) * A(\underline{u}) \cdot \exp\{i\chi(\underline{u})\}\end{aligned}\quad (2.7)$$

where * denotes a convolution integral. The convolution is taken to be applied after the multiplication. $Q(\underline{u})$ is the Fourier transform of $q(\underline{r})$ and $A(\underline{u}) \cdot \exp\{i\chi(\underline{u})\}$ is the Fourier transform of $\Psi_i(\underline{r})$.

The intensity in the detector plane is

$$I(\underline{u}) = |Q(\underline{u}) * A(\underline{u}) \cdot \exp\{i\chi(\underline{u})\}|^2 \quad (2.8)$$

\underline{u} is the same variable in both the objective aperture and the detector plane; for the real space planes a scaling factor is necessary.

$Q(\underline{u})$ may be written as:

$$Q(\underline{u}) = \delta(\underline{u}) - \mathcal{C}(\underline{u}) - i\mathcal{S}(\underline{u}) \quad (2.9)$$

Written like this, the delta function represents the forward scattered, undeflected wave, and

$$\mathcal{C}(\underline{u}) \equiv \mathcal{F}[1 - \exp\{-\mu(\underline{r})\} \cdot \cos(\phi(\underline{r}))]$$

$$\mathcal{S}(\underline{u}) \equiv \mathcal{F}[\exp\{-\mu(\underline{r})\} \cdot \sin(\phi(\underline{r}))]$$

In general, both $\mathcal{C}(\underline{u})$ and $\mathcal{S}(\underline{u})$ are complex with real and imaginary parts $\mathcal{C}_R(\underline{u})$, $\mathcal{C}_I(\underline{u})$, $\mathcal{S}_R(\underline{u})$ and $\mathcal{S}_I(\underline{u})$. $\mathcal{S}(\underline{u})$ contains the first and higher order odd terms in $\Phi(\underline{u}) \equiv \mathcal{F}[\phi(\underline{r})]$, and $\mathcal{C}(\underline{u})$ contains the second and higher order even terms.

The intensity in the detector plane is then given by:

$$\begin{aligned}
 I(\underline{u}) = & A^2 + 2A \cos \chi [(S_R + C_I) * A \sin \chi - (C_R - S_I) * A \cos \chi] \\
 & + 2A \sin \chi [(S_R + C_I) * A \cos \chi + (C_R - S_I) * A \sin \chi] \\
 & + |(S * A \sin \chi) - (C * A \cos \chi)|^2 \\
 & + |(C * A \sin \chi) + (S * A \cos \chi)|^2 \\
 & + 2 \operatorname{Im}[(S * A \sin \chi - C * A \cos \chi)(C^* * A \sin \chi + S^* * A \cos \chi)]
 \end{aligned}
 \tag{2.10}$$

The argument \underline{u} has been omitted for clarity. The first term is simply an image of the aperture on the detector plane. The second and third terms are multiplied by $A(\underline{u})$ and therefore represent modulations of intensity in the direct spot. The fourth, fifth and sixth terms are not limited by the aperture and therefore contribute to intensity both inside and outside the direct beam.

Effect of detector response:

The signal from a STEM detector is given by:

$$J = \int I(\underline{u}) \cdot D(\underline{u}) \, d\underline{u}$$

where $D(\underline{u})$ is the detector response function. It is the ability to vary this detector response function which is the main advantage of STEM over CTEM. The detector in STEM plays the role of the source in CTEM; however, whereas the intensity distribution of the source in CTEM is very difficult to alter, the detector geometry and response in STEM can easily be altered.

The image in STEM is obtained by recording the signal J as a function of \underline{R} , the translation of the incident beam across the specimen.

Alternatively, the specimen can be considered to move relative to a fixed beam. If this is the case we can rewrite equation (2.3) as

$$\Psi_o(\underline{r}, R) = \Psi_i(\underline{r}) \cdot q(\underline{r} - R) \quad (2.11)$$

and $\mathcal{C}(\underline{u})$ and $\mathcal{S}(\underline{u})$ in equation (2.10) become

$$\begin{aligned} \mathcal{C}'(\underline{u}) &= \mathcal{C}(\underline{u}) \cdot \exp\{2\pi i \underline{u} \cdot R\} \\ \mathcal{S}'(\underline{u}) &= \mathcal{S}(\underline{u}) \cdot \exp\{2\pi i \underline{u} \cdot R\} \end{aligned} \quad (2.12)$$

The intensity in the detector plane is then given by $I(\underline{u}, R)$ and the image intensity is

$$J(R) = \int I(\underline{u}, R) \cdot D(\underline{u}) d\underline{u} \quad (2.13)$$

Weakly scattering object:

For a weakly scattering object the exponent in equation (2.5) can be replaced by a power series expansion:

$$q(\underline{r}) = 1 - i\phi(\underline{r}) - \mu(\underline{r}) - \frac{1}{2} \phi^2(\underline{r}) + i\phi(\underline{r}) \cdot \mu(\underline{r}) - \dots$$

In which case

$$\begin{aligned} \mathcal{S}(\underline{u}) &= \Phi(\underline{u}) - \Phi(\underline{u}) * M(\underline{u}) - \frac{1}{6} \{\Phi(\underline{u}) * \Phi(\underline{u}) * \Phi(\underline{u})\} \dots\dots\dots \\ \mathcal{C}(\underline{u}) &= \frac{1}{2} \{\Phi(\underline{u}) * \Phi(\underline{u})\} + M(\underline{u}) - \frac{1}{2} \{\Phi(\underline{u}) * \Phi(\underline{u}) * M(\underline{u})\} \\ &\quad - \frac{1}{24} \{\Phi(\underline{u}) * \Phi(\underline{u}) * \Phi(\underline{u}) * \Phi(\underline{u})\} + \dots\dots\dots \end{aligned} \quad (2.14)$$

$M(\underline{u})$ is the Fourier transform of $\mu(\underline{r})$ and for most electron microscope specimens is usually at least an order of magnitude smaller than $\Phi(\underline{u})$, therefore only low order terms in $M(\underline{u})$ need to be retained. Taking only

the most significant terms in (2.14) gives, to a first approximation:

$$\mathcal{S}(\underline{u}) \approx \Phi(\underline{u}) \quad (2.15)$$

$$\mathcal{C}(\underline{u}) \approx \frac{1}{2} \{\Phi(\underline{u}) * \Phi(\underline{u})\} + M(\underline{u})$$

Keeping only terms of order 2 or less in $\Phi(\underline{u})$ or of order 1 in $M(\underline{u})$, equation (2.10) becomes:

$$\begin{aligned} I(\underline{u}) = & A^2 + 2A \cos \chi [(\mathcal{S}_R + \mathcal{C}_I) * A \sin \chi - (\mathcal{C}_R - \mathcal{S}_I) * A \cos \chi] \\ & - 2A \sin \chi [(\mathcal{S}_R + \mathcal{C}_I) * A \cos \chi + (\mathcal{C}_R - \mathcal{S}_I) * A \sin \chi] \\ & + |\mathcal{S} * A \sin \chi|^2 + |\mathcal{S} * A \cos \chi|^2 \end{aligned} \quad (2.16)$$

Bright field imaging:

Provided the assumption $\phi(\underline{r}) \ll 1$ holds, then only the zeroth and first order terms in \mathcal{C} and \mathcal{S} need to be considered. The STEM bright field image is then given by the first three terms in equation (2.16) integrated over a detector response function $D(\underline{u})$ of smaller area than $A(\underline{u})$ i.e.

$$J_1 = \int D(\underline{u}) \cdot I_1(\underline{u}) \, d\underline{u} \quad (2.17)$$

where $I_1(\underline{u})$ is obtained by setting \mathcal{S}_R and \mathcal{S}_I equal to Φ_R and Φ_I respectively, and \mathcal{C}_R and \mathcal{C}_I equal to zero in the second and third terms of equation (2.16). In addition $D(\underline{u})$ is assumed to have a centre of symmetry at $\underline{u} = 0$, which is generally the case for axial bright field or annular detectors. Therefore terms involving the antisymmetric function $\mathcal{S}_I(\underline{u})$ vanish, giving

$$\begin{aligned} I_1(\underline{u}) = & 2A(\underline{u}) \cos \chi(\underline{u}) [\Phi_R(\underline{u}) * A(\underline{u}) \sin \chi(\underline{u})] \\ & - 2A(\underline{u}) \sin \chi(\underline{u}) [\Phi_R(\underline{u}) * A(\underline{u}) \cos \chi(\underline{u})] \end{aligned} \quad (2.18)$$

Here the zero order term $A^2(\underline{u})$ has been dropped as it contains no information about the specimen, but merely provides a uniform background intensity.

For a very small central detector of radius u_0 $\cos\chi=1$ and $\sin\chi\approx 0$ which gives

$$\begin{aligned} J_1 &= 2 \int D(\underline{u}) \cdot \int \Phi_R(\underline{u}) \cdot A(\underline{u} - \underline{U}) \sin\chi(\underline{u} - \underline{U}) d\underline{U} d\underline{u} \\ &\approx 2\pi u_0^2 \int \Phi_R(\underline{U}) \cdot A(\underline{U}) \sin\chi(\underline{U}) d\underline{U} \\ &\approx 2\pi u_0^2 \int \phi_e(\underline{r}) \cdot s(\underline{r}) d\underline{r} \end{aligned} \quad (2.19)$$

where $s(\underline{r})$ is the Fourier transform of $A(\underline{u})\sin\chi(\underline{u})$ and $\phi_e(\underline{r}) = \{\phi(\underline{r}) + \phi(-\underline{r})\}/2$ is the Fourier transform of $\Phi_R(\underline{u})$.

If we introduce a relative translation of $\phi(\underline{r})$ and $\Psi_i(\underline{r})$ as we did in equation (2.11) then, including the zero order term:

$$J_1(\underline{R}) = \pi u_0^2 [1 + \phi_e(\underline{R}) * s(\underline{R})] \quad (2.20)$$

Therefore, as in coherent bright field phase contrast CTEM, the image is a linear representation of the projected potential of the specimen convolved with a spread function given by the microscope aberrations.

The inefficiency of using STEM to produce images which can be obtained in the CTEM is demonstrated by the multiplicative term u_0^2 in equation (2.20). This implies that the signal is very weak for a small aperture, as would be expected since only a small proportion of the beam is being intercepted.

To obtain a stronger signal, a larger detector has to be used, in which case the full expression in equation (2.18) has to be used. This gives

$$\begin{aligned} J_1 &= 2 \int D(\underline{u}) [A(\underline{u})\cos\chi(\underline{u})\{\Phi_R(\underline{u}) * A(\underline{u})\sin\chi(\underline{u})\} \\ &\quad - A(\underline{u})\sin\chi(\underline{u})\{\Phi_R(\underline{u}) * A(\underline{u})\cos\chi(\underline{u})\}] d\underline{u} \end{aligned} \quad (2.21)$$

which can be written as:

$$J_1(R) = \int d(\underline{r}) \cdot a(\underline{r}) \, dr + 2\phi_e(R) * [s(R)\{d(R) * c(R)\} - c(R)\{d(R) * s(R)\}] \quad (2.22)$$

where $a(R)$, $c(R)$ and $d(R)$ are the Fourier transforms of $A(\underline{u})$, $A(\underline{u})\cos\chi(\underline{u})$ and $D(\underline{u})$ respectively. Once again it can be seen that the image contrast is a linear representation of the specimen potential, however, with a much more complicated spread function than that for the very small axial detector.

In general, for high resolution STEM imaging the defocus and the detector response function are chosen so as to make the spread function in the square brackets as narrow as possible. Novel detector response functions have been discussed by Cowley and Au (1978), and by Rose (1974) who suggested a series of concentric annular rings, with the signals from individual rings being added with the appropriate sign to maximise the desired contrast.

Asymmetric detectors:

Equation (2.18) is only true for detectors which have a symmetrical response about the optic axis $\underline{u} = 0$. For a general detector response the full expression in equation (2.16) is required. However any detector response function $D(\underline{u})$ can be replaced by the sum of a symmetric response function and an antisymmetric response function $D_o(\underline{u}) = -D(-\underline{u})$. For an antisymmetric response function, equation (2.18) becomes

$$I_1(\underline{u}) = -2A(\underline{u})\cos\chi(\underline{u}) \{\Phi_I(\underline{u}) * A(\underline{u})\cos\chi(\underline{u})\} + 2A(\underline{u})\sin\chi(\underline{u}) \{\Phi_I(\underline{u}) * A(\underline{u})\sin\chi(\underline{u})\} \quad (2.23)$$

The Fourier transforms of $D_o(\underline{u})$ and $\Phi_I(\underline{u})$ are the imaginary antisymmetric functions $id_o(\underline{r})$ and $i\phi_o(\underline{r}) \equiv i\{\phi(\underline{r}) - \phi(-\underline{r})\}$. Both $D_o(\underline{u})$

and $\Phi_I(\underline{u}) = 0$ for $\underline{u} = 0$. Therefore for a small detector the resultant contrast is zero; this is the equivalent of the result using equation (2.19) where $J_1 = 0$ for $u_0 \rightarrow 0$. For large detectors, strong contrast is possible with antisymmetric detector response functions. In the equivalent of equation (2.22) the term $\int d_o(\underline{r}) \cdot a(\underline{r}) d\underline{r}$ is zero as $a(\underline{r})$ is symmetric and $d_o(\underline{r})$ is antisymmetric, therefore

$$J_{1,0}(\underline{R}) = -2\phi_o(\underline{R}) * [c(\underline{R})\{d_o(\underline{R}) * c(\underline{R})\} + s(\underline{R})\{d_o(\underline{R}) * s(\underline{R})\}] \quad (2.24)$$

The split detector proposed by Dekkers and de Lang (1974) can be represented by the detector response function

$$D_o(\underline{u}) = D_e(\underline{u}) \cdot H(\underline{u}) \quad (2.25)$$

where $H(\underline{u}) = +1$ if $u > 0$

-1 if $u < 0$

$D_e(\underline{u})$ is the conventional detector response function, and u is the coordinate of \underline{u} parallel to the real space x -axis.

The Fourier transform of this equation gives:

$$id_o(\underline{r}) = d_e(\underline{r}) * (\pi i x)^{-1} \quad (2.26)$$

It can be shown that convolution with $1/x$ is approximately equal to differentiation with respect to x . Therefore, to a first approximation, equation (2.24) becomes

$$J_{1,0}(\underline{R}) \propto \frac{d}{dx} \phi_o(\underline{R}) * [c^2(\underline{R}) + s^2(\underline{R})] \quad (2.27)$$

The term in square brackets $c^2(\underline{R}) + s^2(\underline{R})$ is the intensity distribution of the incident beam on the specimen.

The effect of partial coherence:

The actual source in the microscope must have a finite size and therefore the illuminating wave will be only partially coherent. We can replace the ideal on-axis point source, assumed so far, by an ideally incoherent source with intensity distribution $I_s(r)$, where the dimensions of the source are referenced to the source image on the specimen plane. For a source point $\underline{r} = \underline{I}$, the exit wave from the specimen is

$$\Psi_o(\underline{r}) = |\Psi_i(\underline{r}) * \delta(\underline{r} - \underline{I})|. q(\underline{r}) \quad (2.28)$$

(As the source is considered to be incoherent, it is the modulus of the incident wave which should be considered rather than the complex amplitude.) The intensity in the detector plane is then calculated for each source point and is given a weighting $I_s(\underline{I})$. The total intensity is then found by integrating over \underline{I} . Therefore equation (2.13) becomes

$$J(\underline{R}) = \iint I(\underline{u}, \underline{R}, \underline{I}) \cdot D(\underline{u}) \, d\underline{u} \, d\underline{I} \quad (2.29)$$

As with the translation \underline{R} of the beam, we can consider \underline{I} as a displacement of the specimen rather than the beam, in which case:

$$\begin{aligned} \mathcal{C}''(\underline{u}) &= \mathcal{C}(\underline{u}) \exp\{2\pi i \underline{u} \cdot (\underline{R} + \underline{I})\} \\ \mathcal{S}''(\underline{u}) &= \mathcal{S}(\underline{u}) \exp\{2\pi i \underline{u} \cdot (\underline{R} + \underline{I})\} \end{aligned} \quad (2.30)$$

and $q(\underline{r} - \underline{R})$ is replaced by $q(\underline{r} - \underline{R} - \underline{I})$.

Using (2.29) the image intensity for a small axial bright field detector is given by

$$J_1(\underline{R}) = \pi u_0^2 [1 + \phi_e(\underline{R}) * s(\underline{R}) * I_s(\underline{R})] \quad (2.31)$$

where the total source intensity is normalised so that $\int I_s(\underline{r}) \, d\underline{r} = 1$.

Similarly the expression for a large bright field detector becomes

$$J_1(\underline{R}) = \int d(\underline{r}) \cdot a(\underline{r}) d\underline{r} \\ + 2\phi_e(\underline{R}) * [s(\underline{R})\{d(\underline{R}) * c(\underline{R})\} - c(\underline{R})\{d(\underline{R}) * s(\underline{R})\}] * I_s(\underline{R}) \quad (2.32)$$

Therefore it can be seen that partial coherence can be taken account of by convolving the image intensity due to a perfectly coherent point source with a function representing the source intensity distribution.

The effect of a finite source size is to broaden and smooth out the oscillations of the spread function for bright field imaging. It will have a similar effect on the image from an antisymmetric detector. In both cases the resolution will be degraded.

2.4 The Aharonov And Bohm Effect

In classical electrodynamics, electrons in a magnetic field experience a force:

$$F_L = e \underline{V} \times \underline{B}$$

called the Lorentz force. As this force acts perpendicular to both the electron velocity and the magnetic field, it does not lead to any change in the electron energy, merely to a change in the direction of travel. In quantum mechanics this change in direction corresponds, as stated in section 2.3, to a change in phase of the electron wave. Aharonov and Bohm (1959) have shown that a phase difference can be introduced between two electrons even if they do not actually experience a force.

Consider two electrons travelling, by different paths ℓ_1 and ℓ_2 , from point P_1 to point P_2 such that they pass either side of a region of magnetic flux, as shown in figure 2.2. If the two electrons were in phase at the point P_1 , then at point P_2 , the phase difference between them is:

$$\Delta\phi = 2\pi \left[\frac{\ell_2 - \ell_1}{\lambda} - \frac{e\Phi_m}{h} \right] \quad (2.33)$$

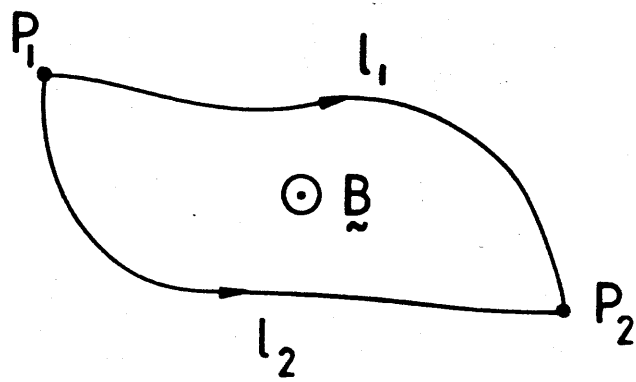


Figure 2.2 Experimental set-up to illustrate Aharonov-Bohm effect

where Φ_m is the total magnetic flux enclosed by the electron paths. If the electron paths are the same length then the phase difference is

$$\Delta\phi = - \frac{2\pi e}{h} \Phi_m \quad (2.34)$$

For the arrangement in figure 2.3 the phase difference between the electron waves travelling via x_1 and those travelling via x_2 is given by

$$\Delta\phi = - \frac{2\pi e}{h} t \int_{x_1}^{x_2} B_y(x) dx \quad (2.35)$$

$B_y(x)$ is the average value of $B_y(x,z)$ found by taking the integral

$$B_y(x) = \frac{1}{t} \int_{-\infty}^{\infty} B_y(x,z) dz \quad (2.36)$$

The limits of integration are chosen so that stray fields above and below the magnetic specimen can be taken into account.

It can be seen therefore that if only the magnetic interaction is considered, then a magnetic specimen can be considered a pure phase object.

2.5 Differential Phase Contrast Imaging

Dekkers and de Lang (1974) proposed a large axial STEM detector split into two semicircles. From equation (2.27) the response function for the split detector gives a signal $J_{1,0}(R)$ which can be described by

$$J_{1,0}(R) \propto \frac{d}{dx} \phi_0(R) * \{ c^2(R) + s^2(R) \} \quad (2.37)$$

In other words, the signal from a split detector, where the individual signals from each half are added with opposing signs, is proportional to the derivative of the phase of the electron wave with respect to x , convolved with the intensity distribution of the incident

beam on the specimen.

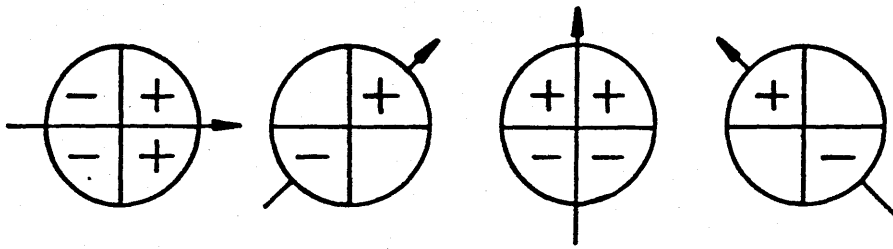
The major drawback of a split detector is the fact that only the phase gradient in the x-direction can be obtained. A logical extension to the split detector is a detector split into four quadrants (Rose 1977). In this case the phase derivative can be obtained with respect to any one of four directions as shown in figure 2.3, where the arrows give the direction of differentiation. (A more detailed discussion of the contrast transfer functions of the split and quadrant detectors in STEM is given by Morrison (1981).)

It was shown in section 2.4 that, for a magnetic specimen, the phase of the electron wave is proportional to the integral of $B_Y(x) dx$. Therefore, the differential phase contrast signal is proportional to $B_Y(x)$, the in-plane component of magnetisation.

A classical interpretation of this mode of image formation can be made by considering figure 2.4. The signal on the left hand side of the detector is proportional to $\pi\alpha^2/2 - 2\beta_L\alpha$ while that on the right hand side is proportional to $\pi\alpha^2/2 + 2\beta_L\alpha$, therefore the difference signal is proportional to $4\beta_L\alpha$. Moreover β_L is given by

$$\begin{aligned}\beta_L &= \frac{e\lambda}{h} \int_{-\infty}^{\infty} B_Y(x,z) dz \\ &= \frac{e\lambda}{h} B_Y(x)t\end{aligned}\tag{2.38}$$

for a specimen of thickness t . Hence the difference signal from the split detector is proportional to the average in-plane component of magnetisation multiplied by the specimen thickness.



$$\begin{array}{|c|c|} \hline & + \\ \hline - & \\ \hline \end{array} \equiv \frac{1}{2} \left[\begin{array}{|c|} \hline + \\ \hline - \\ \hline \end{array} + \begin{array}{|c|c|} \hline - & + \\ \hline \end{array} \right]$$

$$\begin{array}{|c|c|} \hline + & \\ \hline & - \\ \hline \end{array} \equiv \frac{1}{2} \left[\begin{array}{|c|} \hline + \\ \hline - \\ \hline \end{array} - \begin{array}{|c|c|} \hline - & + \\ \hline \end{array} \right]$$

Figure 2.3 Relationship between quadrant and split detector

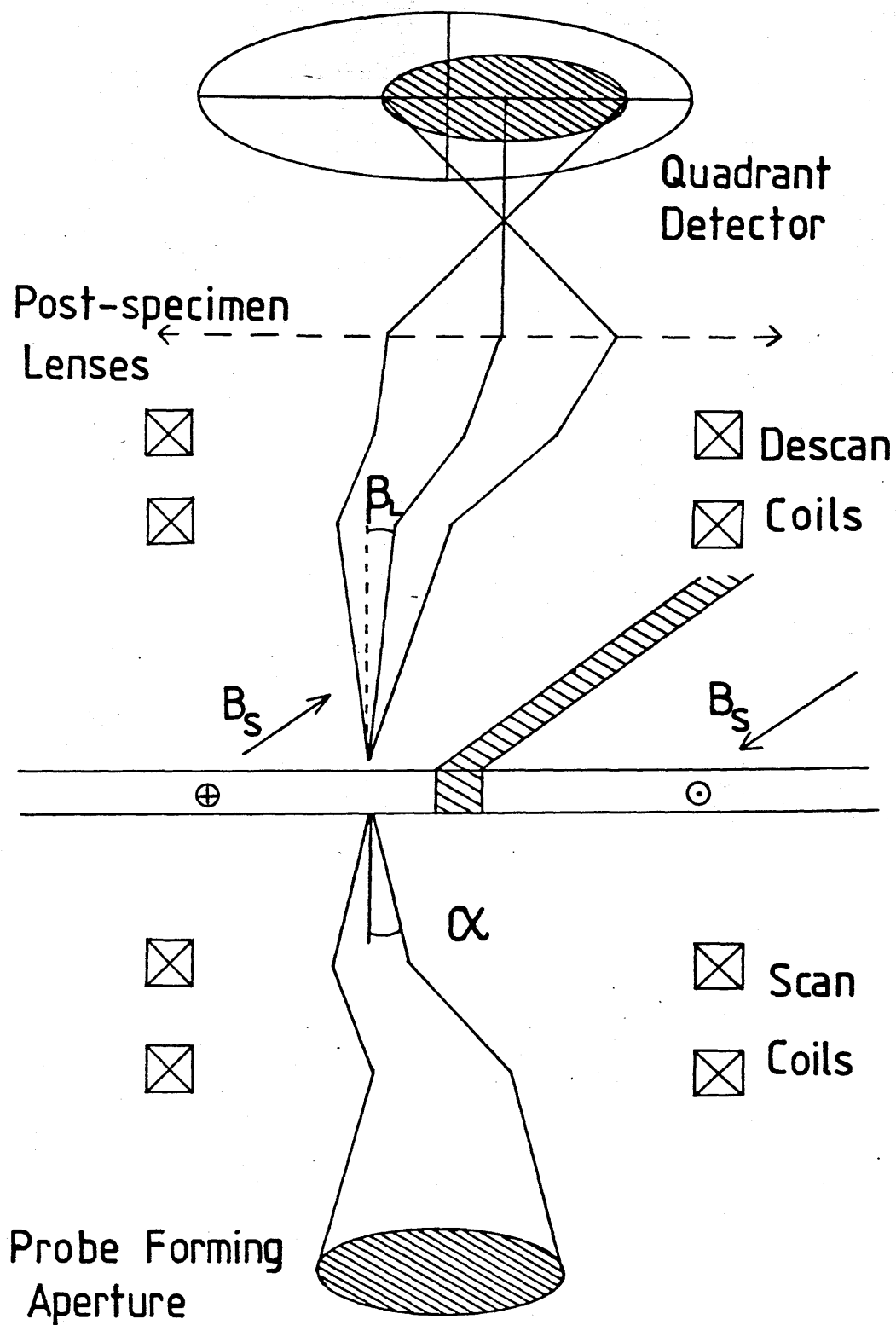


Figure 2.4 Schematic of DPC imaging in the HB5

2.6 Microscope Operating Conditions For DPC

A systematic study of the effects of spherical aberration and defocus on the phase and amplitude contrast transfer functions (PCTF and ACTF respectively) for a split detector and a quadrant detector was carried out by Morrison (1981). In this section a brief summary of the results of this study will be given to justify the operating conditions used in this work.

Firstly the notation used will be defined: C_s is the third order spherical aberration coefficient of the probe forming lens. For a given spherical aberration the optimum probe forming aperture is given by

$$\alpha_0 = (4\lambda/C_s)^{1/4}$$

This leads to the definition of a dimensionless spherical aberration coefficient

$$C = \frac{C_s \alpha_0^4}{4\lambda}$$

$C = 1$ corresponds to one wavelength of spherical aberration at the aperture edge. The dimensionless defocus is given by

$$D = \frac{z \alpha_0^2}{2\lambda}$$

where z is the actual defocus, and is taken to be positive if the lens excitation is reduced with respect to the in focus condition.

The reduced spatial frequency vector is \underline{u}_r and $|\underline{u}_r| = 1$ corresponds to the spatial frequency cut-off of the probe forming aperture, α_0/λ .

Using this notation the lens aberration function can be written as

$$\chi(\underline{u}) = -C\underline{u}_r^4 + D\underline{u}_r^2 = \chi(\underline{u}_r)$$

In general the PCTF and the ACTF will oscillate about zero as shown in figure 2.5. The n^{th} transfer interval can be made broad and flat by

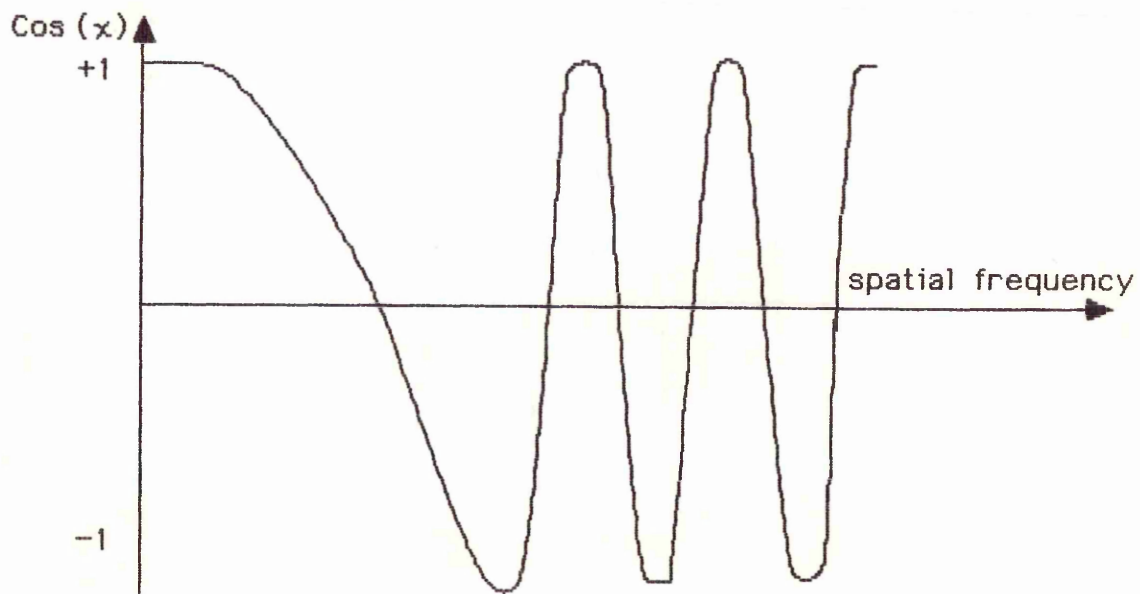
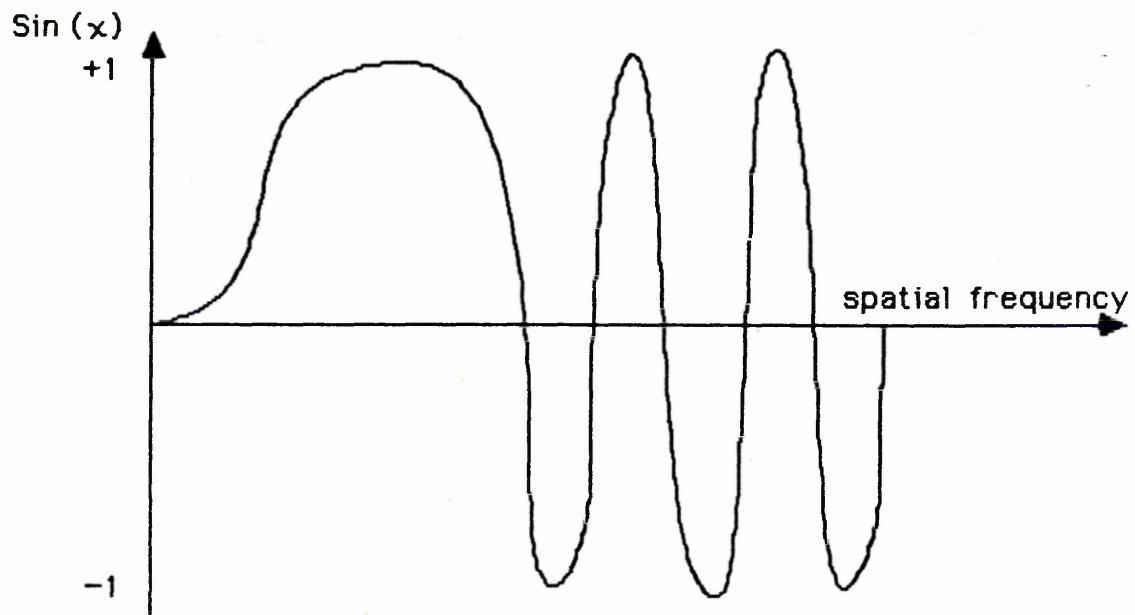


Figure 2.5 Typical Phase and Amplitude contrast transfer functions for an electron microscope

setting $D = \sqrt{[(2n-1)C]}$. The first transfer interval can be made as broad as possible by setting $D = C = 1$. This is the Scherzer defocus condition.

Morrison has shown that with $C = 0$, the PCTF is the same on both sides of focus and that at $D = 0$, the ACTF is zero. Moreover there are no zeros or contrast reversals in the PCTF in the range $0 < u_r < 2$. Therefore, in the absence of aberrations, DPC imaging provides pure phase information, if the specimen is a pure phase object. This is in contrast to the other forms of phase contrast imaging which require some form of aberration in the microscope to produce phase contrast.

In practice $C = 0$ cannot be achieved in the electron microscope. When the form of the contrast transfer function is considered for $C = 1$ and 2 and for various values of D satisfying $D = \sqrt{[(2n-1)C]}$ it can be seen that

- 1) If C and D act together then the PCTF is small and limited to a region close to $u_r = 0$. Furthermore the ACTF is sharply peaked around $u_r = 0$.
- 2) If C and D act against each other then the PCTF can be broad and non-zero out to $u_r = 2$, and the ACTF can be small.

The most favourable conditions are $C = D = 1$ (Scherzer focus) where PCTF is very similar to the $C = D = 0$ case and the ACTF is a minimum. Therefore it is possible to find conditions where, using DPC imaging, the PCTF extends out to $u_r = 2$ without zeros or contrast reversals. In addition the detector, unlike the coherent bright field detector, covers a larger area in frequency space than the probe defining aperture, and therefore collects the entire zero order beam.

Scherzer focus in the HB5:

For the single condenser lens mode of operation in the HB5 used in this work, the third order spherical aberration coefficients of condensers 1 and 2 are 1960m and 195m respectively, with the condensers focused on the normal specimen position. This implies optimum probe forming aperture half angles, α , of 0.3 and 0.5 mrad respectively. With the specimen at the normal height the 100 μ m

selected area aperture gives $\alpha_0 = 0.53$ mrad and the $50\mu\text{m}$ aperture gives $\alpha_0 = 0.26$ rad. Hence for most of this work condenser C2 and the $100\mu\text{m}$ SAD aperture have been used. This gives a greater resolution than condenser C1 because C2 forms a demagnified image of the source on the specimen plane. The choice of the $100\mu\text{m}$ aperture was taken to obtain the best PCTF with C2. For specimens which were near the thickness limit for imaging with 100keV electrons (about 150nm for polycrystalline specimens) C1 and either the $50\mu\text{m}$ or $100\mu\text{m}$ aperture was used. This maximised the probe current and improved the signal to noise ratio at the expense of resolution, and to some extent the PCTF.

Post specimen lens settings:

Once α_0 has been chosen it is necessary to select a camera length, using the post specimen lenses, that matches the bright field cone to the size of the quadrant detector. The quadrant detector is 11mm in diameter, and in general the bright field cone should be approximately half of this size. This gives a camera length of $\sim 5\text{m}$ for the $100\mu\text{m}$ aperture. In fact, a camera length of 5.4m was used. This was obtained by using a series of lens settings stored in a ROM of a microprocessor used to control the PSL's.

In theory there is no need to match the size of the bright field cone to the size of the detector, so long as the cone is small enough that it never moves off the detector due to a deflection from the specimen. However, in practice, it is better to have a low level of illumination over a large fraction of the detector surface, rather than a high level of illumination on a small fraction of the surface. This is because there are "dead" regions between the quadrants, $\sim 200\mu\text{m}$ wide. For small camera lengths, and therefore a small bright field spot on the detector, these "dead" regions intercept a not negligible proportion of the current. Furthermore it is the electron beam, rather than the specimen, which is scanned. Hence it is necessary to descan and position the beam so that for no deflection due to the specimen, the bright field cone is stationary and centred on the detector. This is

much easier to achieve if the bright field cone covers a large fraction of the active detector surface, as the detected signal is then more sensitive to small shifts of the beam.

2.7 Image Acquisition On The HB5

The quadrant detector used in the HB5 is a commercially available Centronic QD-100 windowless detector. This consists of four quadrant shaped P-N junction photodiodes separated by inactive SiO₂ strips as shown in figure 2.6. The diodes are operated, without bias, in the photoamperic mode, by connecting them to four matched preamplifiers. A schematic of the quadrant-preamplifier circuit is shown in figure 2.7. The output voltage from the preamplifiers is given by

$$V_0 = i_s R_f$$

where R_f is the feedback resistance of the operational amplifier, and i_s is the signal current from the photodiode. i_s is given approximately by

$$i_s = i_0 \times 10^5 / 3.6$$

where i_0 is the electron current falling onto the detector, 10^5 eV is the energy of the incident electrons and the energy required to produce one electron-hole pair in silicon is 3.6eV. Therefore the output voltage is directly proportional to the electron current falling on the detector.

Operating in the photoamperic mode was found to be the best compromise between junction leakage current and frequency response. In practice the detector can be operated at frequencies up to 25kHz, which is fast enough for general observation and focussing. A more detailed discussion of the detector and the amplification circuitry is given by Morrison (1981).

From the preamplifiers the four signals, A, B, C and D, are fed to mixing circuitry, which can produce any of the following five

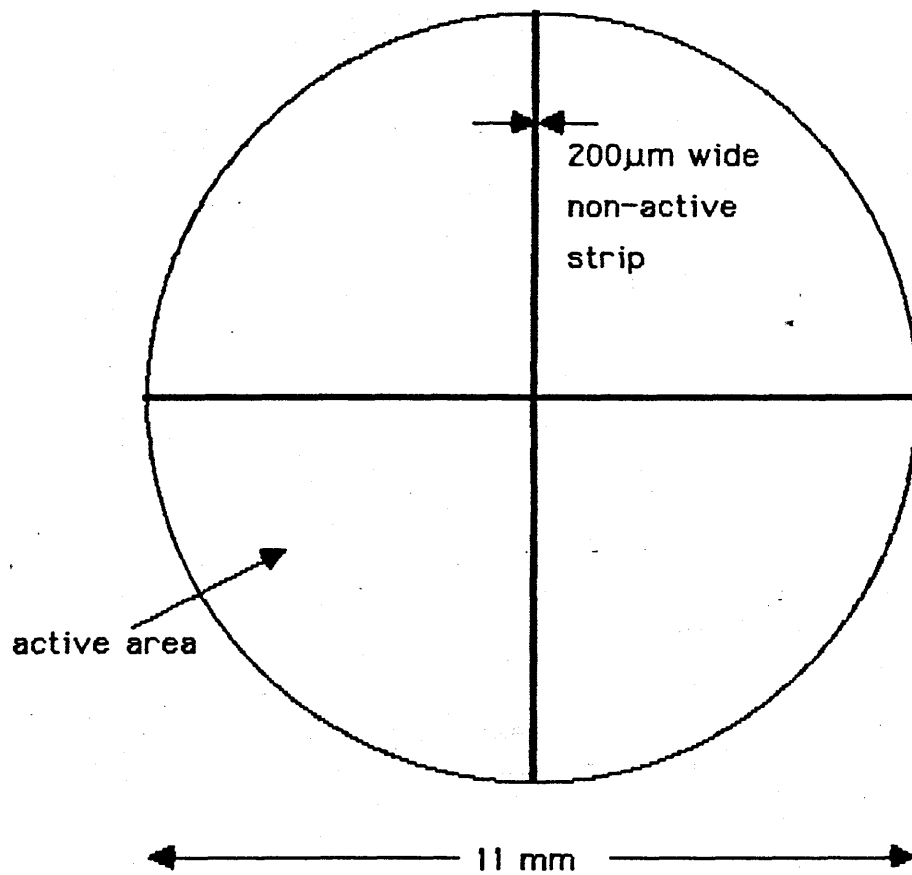


Figure 2.6: Schematic of the quadrant detector

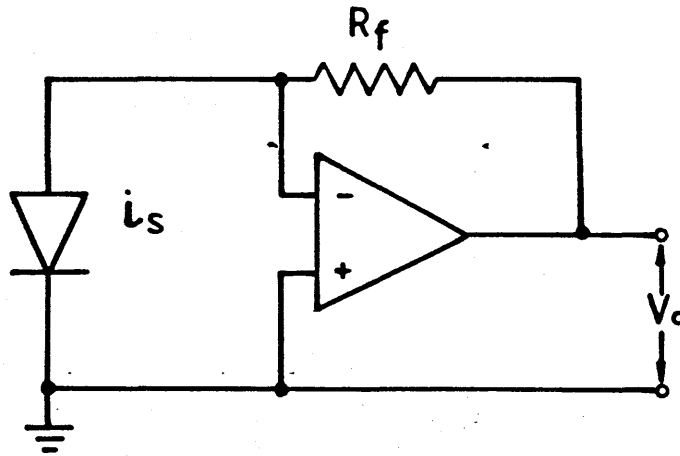


Figure 2.7 Quadrant-preamplifier circuit illustrating photoamperic mode of operation

combinations: $(A + B + C + D)$; $(A - C)$; $(B - D)$; $(A + B) - (C + D)$ and $(A + D) - (B + C)$. The sum signal, $(A + B + C + D)$, is a pseudo bright field image and is displayed on one of the two T.V. monitors on the HB5. It is used in focussing and stigmating the electron probe. Any one of the four remaining DPC signals can be displayed on the other T.V. monitor on the HB5 console.

A permanent record of the images on these T.V. monitors can be obtained by displaying the image on a third T.V. monitor which can be photographed using a 35mm camera.

In addition to analogue photography, the images produced by the quadrant detector (and indeed the normal bright field and dark field images), can be recorded digitally and stored in a computer frame store. This is done using a Toltec computer system, interfaced to the microscope as shown in figure 2.8.

Computer controlled image acquisition:

When images are being acquired digitally, the area scan on the HB5 STEM is controlled by the CA 4/30 computer rather than the HB5 time base. This is done via a Data Translation (D.T.) interface card which produces digital ramps for the line (x) and the frame (y) components of the scan. In general the image is scanned using a 256x256 square raster, with the frame component being incremented by one for every 256 steps of the line component. The form of the x and y scan ramps is shown in figure 2.9. Each line scan is stored in a temporary buffer as it is acquired, and at the end of the line scan it is transferred to a GEMS frame store. The processing at the end of each line takes ~32ms. The pixel dwell time can be varied from $20\mu\text{s}$ to $255 \times 20\mu\text{s} = 5.12 \text{ ms}$. For most specimens a short dwell time is sufficient to produce a good signal to noise ratio, and a sample and hold amplifier on the D.T. card samples the output from a differential line receiver for each pixel. For thicker specimens however it is desirable to use a longer dwell time per pixel, and to integrate the detected signal over this dwell time. To this end an integrating line receiver was constructed. This is shown in

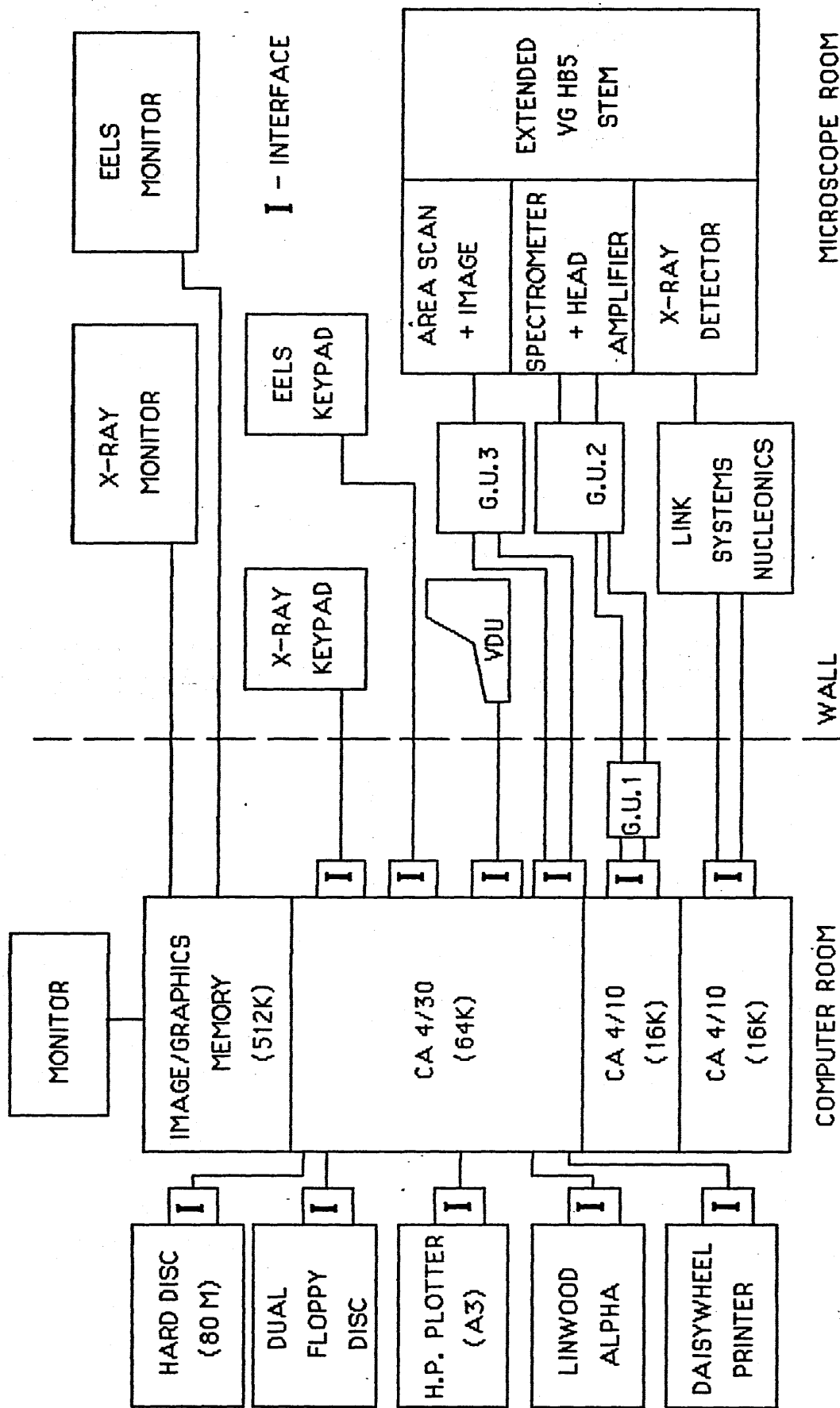
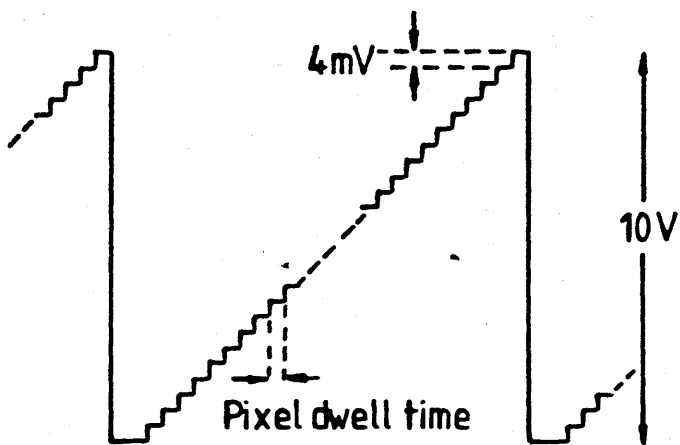


Figure 2.8: schematic of the computer interface to the HB5 STEM

Line (x) scan



Pixel dwell time + time to transfer
256 values to GEMS frame store

Frame (y) scan

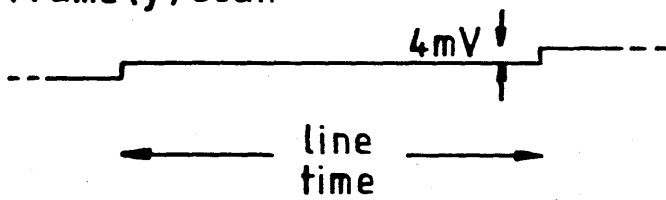


Figure 2.9 Line and Frame scan outputs from the Data Translation board

figure 2.10. The first operational amplifier acts as a buffer between the HB5 line drivers and the integrator and has a gain of 10x. The output voltage from the integrator is given by

$$V_{out} = \frac{1}{R_1 C} \int_0^{T_d} V_{int} dt$$

The maximum video level produced by the HB5 is 1V, and the D.T. card is set up to use 0-10V input; therefore the total gain of the line receiver should be 10x. The gain of the integrator is

$$\frac{V_{out}}{V_{int}} = \frac{T_d}{R_1 C} = \alpha$$

For $\alpha \approx 1$ and $C = 0.047\mu\text{F}$, this implies that for a 2ms dwell time $R_1 = 42\text{k}\Omega$. In the actual circuit, R_1 consists of a $30\text{k}\Omega$ fixed resistor and a $20\text{k}\Omega$ variable resistor, the variable resistor was adjusted so that, for a 2ms dwell time, 1 volt in gave 10 volts out. For dwell times different from 2ms the video level was adjusted at the HB5 to utilize the full pixel range of the computer.

An additional operational amplifier was used after the integrator to ensure that for $V_{in} = 0$ volts, the input to the D.T. card was 10 volts, and for $V_{in} = 1$ volt the input to the D.T. card was 0 volts. This was necessary because a bright signal corresponds to a high voltage level in the HB5 STEM, whereas a high pixel intensity in the frame store corresponds to a low voltage level input to the D.T. card.

Zeroing the integrator:

Ideally the integrator should be zeroed while the analogue to digital converters on the D.T. card are converting the sampled voltage level to a pixel intensity. However, the difficulty involved in obtaining a logic pulse from the D.T. card, to initiate the zeroing, rules this out. Instead the steps in the x-scan ramp are used to trigger a monostable multivibrator IC. This is done using the circuitry in figure 2.11. The

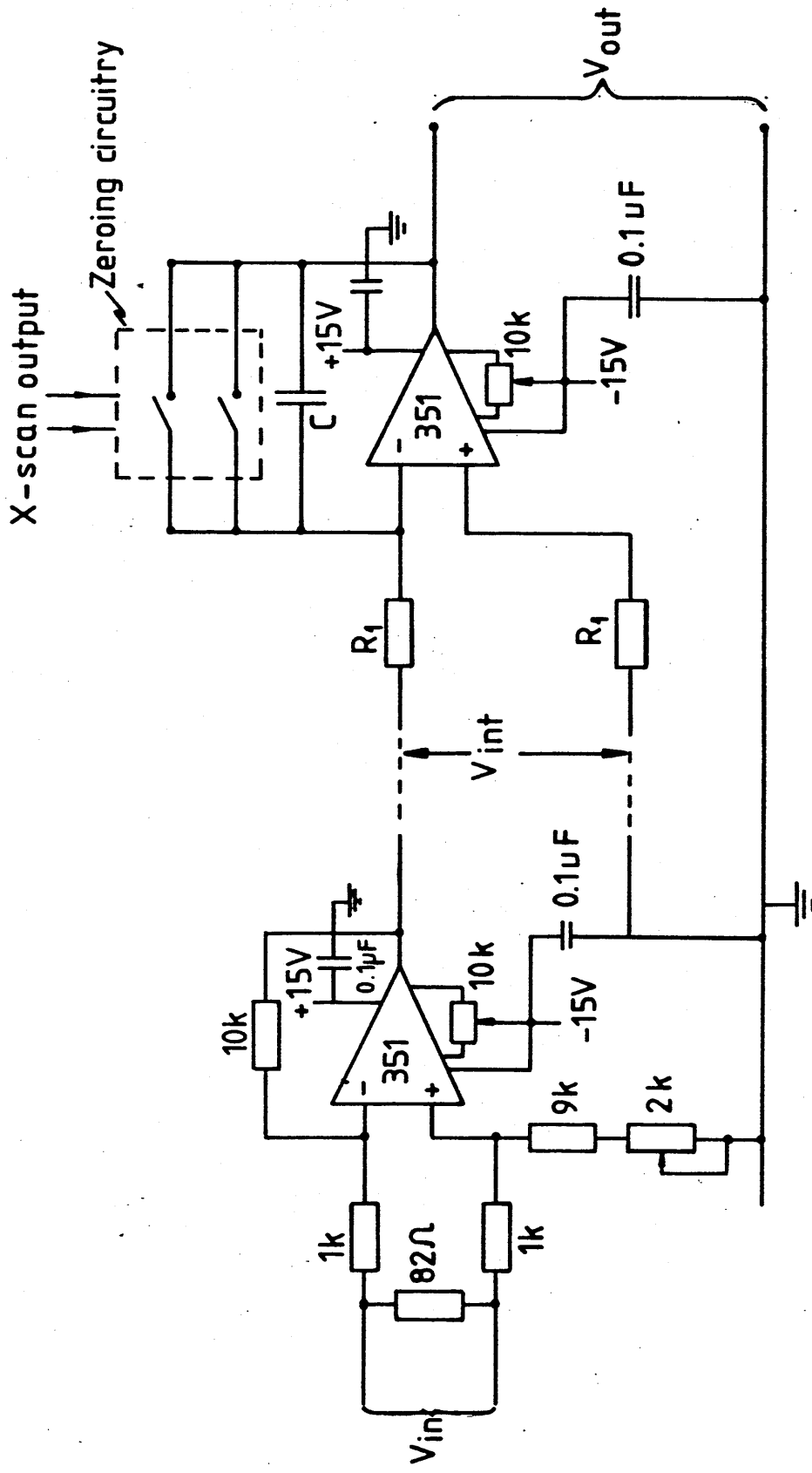


Figure 2.10 Integrating line receiver

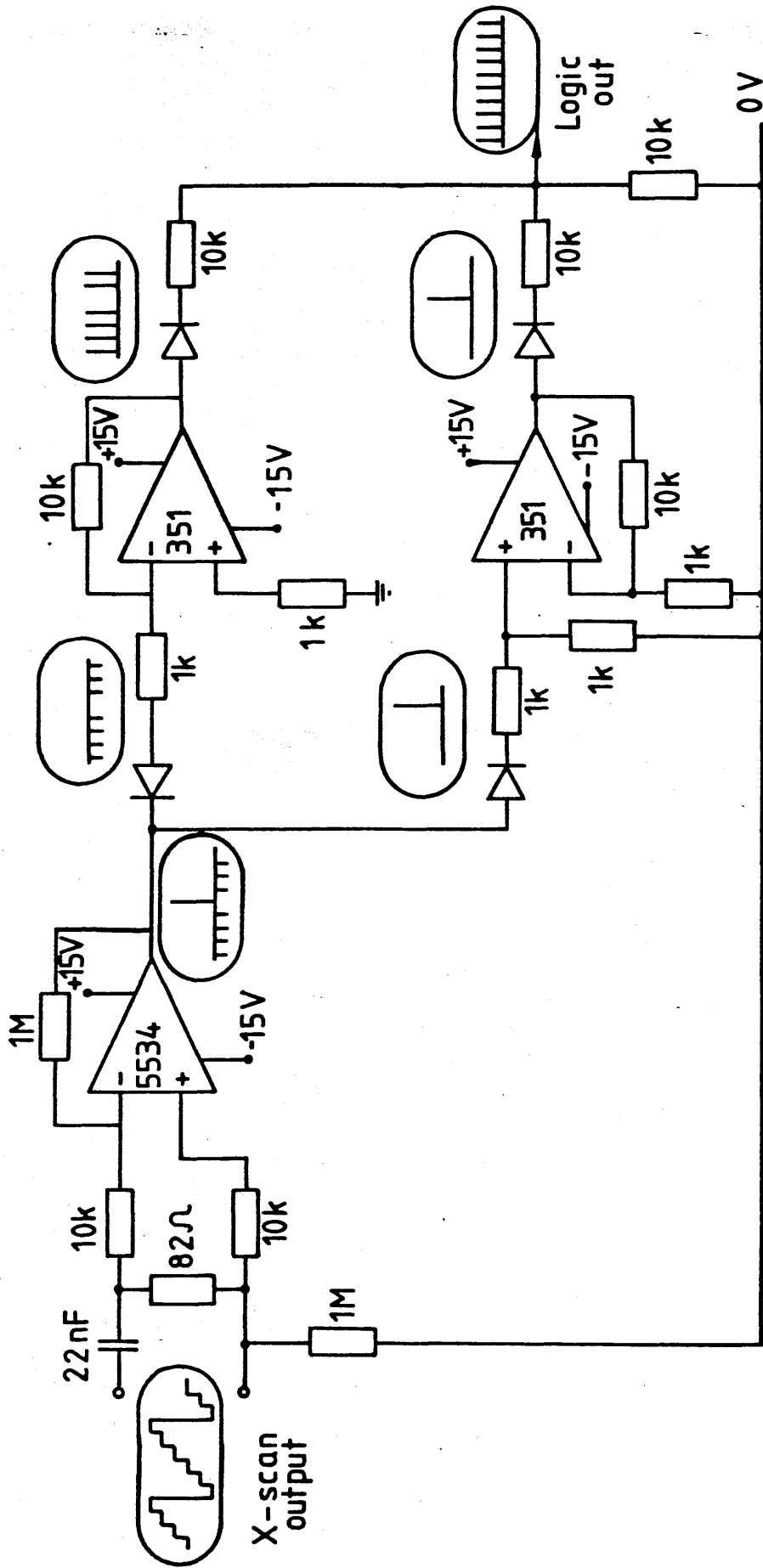


Figure 2.11 Ramp to pulse converter for integrating line receiver

x-scan ramp is differentiated by the first operational amplifier assembly to produce a series of 255 small unipolar pulses followed by one large unipolar pulse of the opposite polarity (as shown). The second stage then amplifies these and inverts the small pulses. The diode-resistor chain at the output acts as an OR gate and produces a stream of positive pulses, one each time the x-scan increments.

Once triggered, the monostable sends a square pulse of length T_0 to two switches S1 and S2 in a digital switch IC, as shown in figure 2.12. When the switches close they provide a low resistance path through which the capacitor C can discharge.

The zeroing time, T_0 , should be a small fraction of the dwell time per pixel, T_d , typically $\sim 1\%$. For $T_d = 2\text{ms}$ this implies that T_0 should be $\sim 20\mu\text{s}$. T_0 is set by the values of R_t and C_t such that

$$T_0 = R_t C_t$$

With $R_t = 50\text{k}\Omega$ and $C_t = 220\text{pF}$ this gives $T_0 = 11\mu\text{s}$, which is sufficient to allow the capacitor, C, to discharge to less than 0.05% of its initial value if two of the switches in the digital IC are used (typical resistance 30Ω).

Two tests were carried out on the integrating line receiver. Firstly the resultant pixel intensity for a constant input voltage was measured as a function of pixel dwell time. This is shown in figure 2.13. The input voltage was set accurately at 0.5V using a Time Electronics 2004 standard voltage supply. As can be seen from the figure, the pixel intensity varies linearly with dwell time. From the intercept with the x-axis, the effective zeroing time can be seen to be $80\mu\text{s}$. This is longer than the expected zeroing time, as it includes the effect of amplifier offsets in addition to the time for which the switches S1 and S2 are closed. As the integrator need only be used for pixel dwell times $\geq 0.5\text{ms}$ this effective zeroing time can be considered as having the effect of an additive blacklevel.

The second test of the integrating line receiver was a

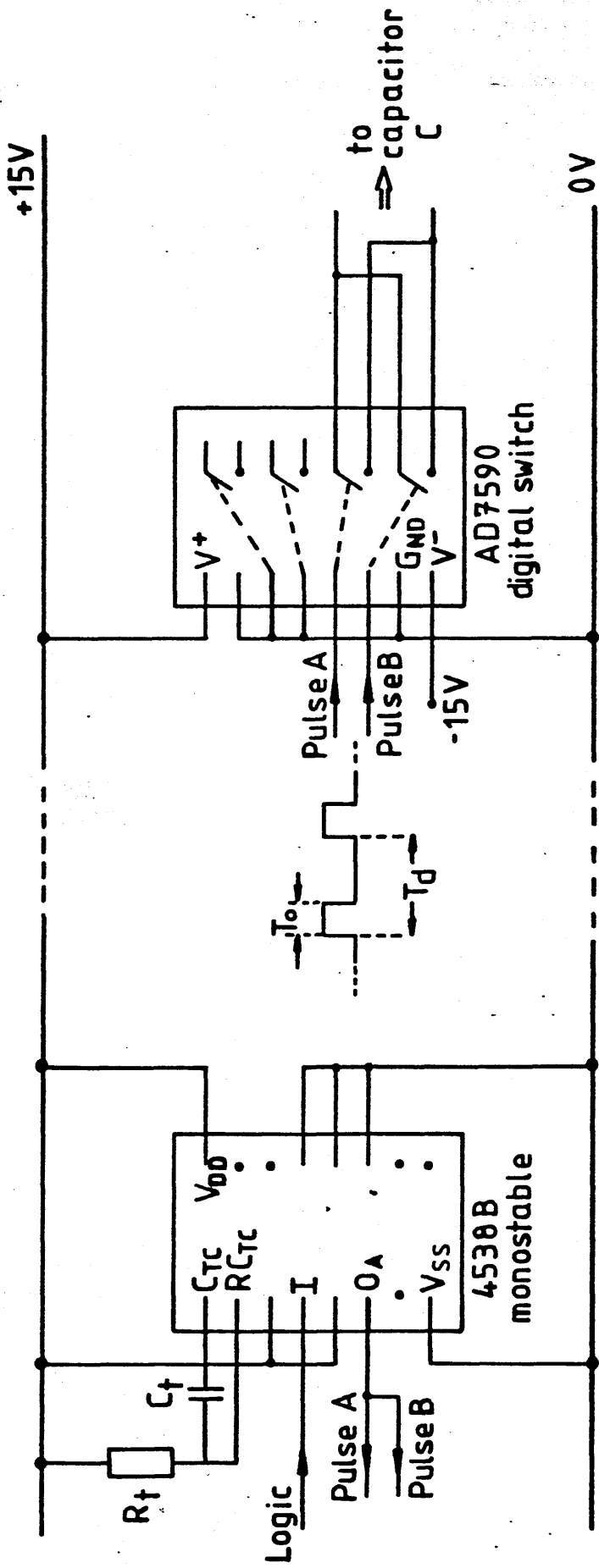


Figure 2.12 Monostable pulse generator and digital switch for zeroing integrator

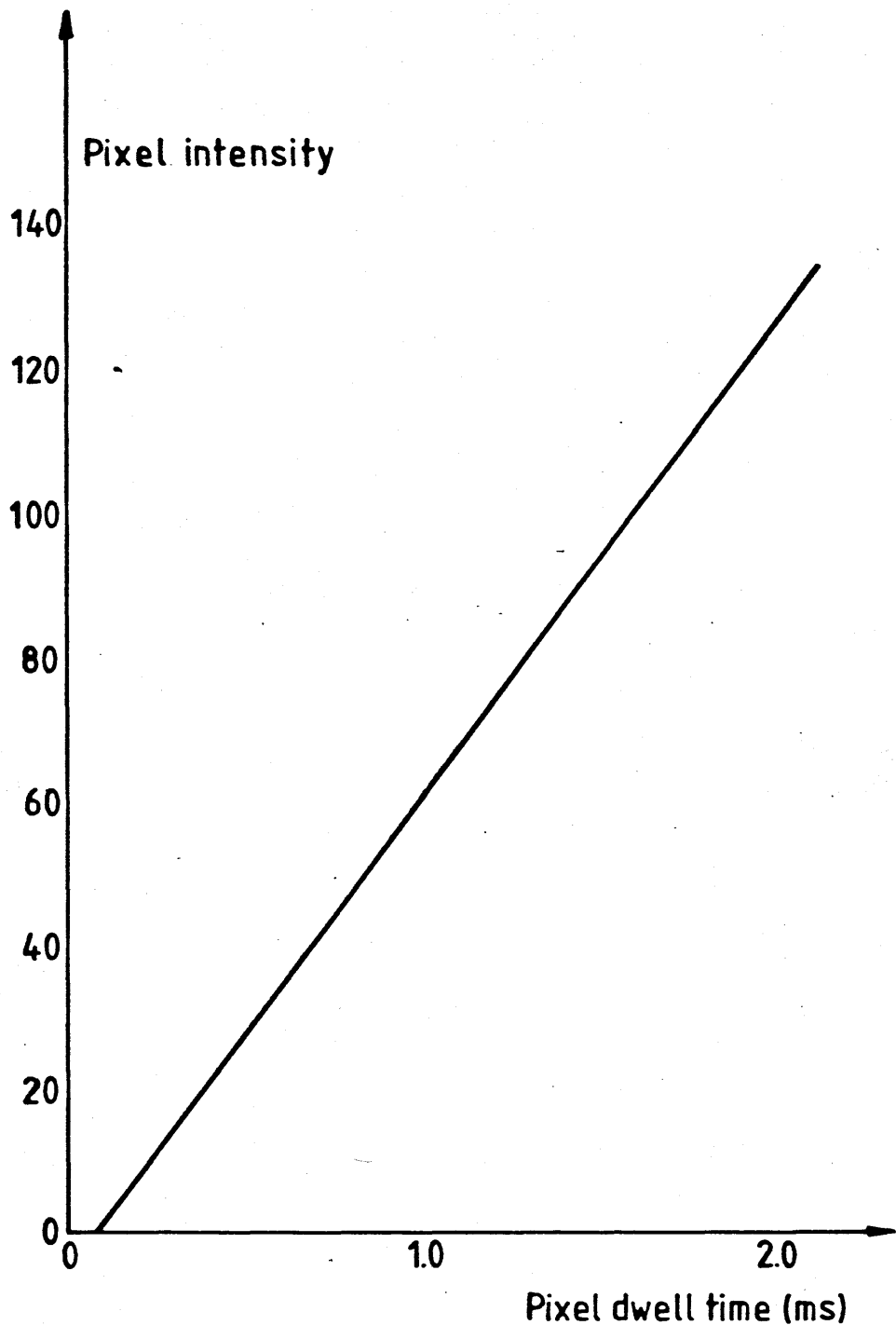


Figure 2.13 Pixel intensity versus pixel dwell time for 0.5V input to integrating line receiver

measurement of the resultant pixel intensity, for a given pixel dwell time, as a function of input voltage. This is shown in figure 2.14. In this case the input voltage was provided by the HB5 video level module. This is the reason for the large error bars in the voltage direction as the meters on the video level module are not very accurate. The pixel dwell time was 2ms. It can be seen from this graph that the pixel intensity varies linearly with input voltage.

As well as being used to observe thick specimens, the integrator has been used to acquire the images of stray magnetic fields, beyond the surfaces of samples, which are discussed in chapter 4. Towards the edges of these fields the DPC signals are very small and integrating the signals reduces the influence of noise, both from the detector and from the field emission tip.

2.8 Electron Energy Loss And X-ray Spectra

When a 100keV electron strikes a thin microscope specimen, it can interact with it in a variety of ways:

- 1) The electron can pass through the specimen unscattered, that is to say, with no change in either energy or direction.
- 2) The electron may be elastically scattered, undergoing a change in direction, but not in energy.
- 3) The electron may be inelastically scattered, giving up some energy to the specimen. This energy transfer may be localised and take the form of the excitation of an atomic electron to an unfilled energy level above the ground state, or indeed in the continuum. Alternatively the energy transfer may be a non-localised process giving rise to a collective lattice vibration, or phonon; or a collective oscillation of the conduction electrons, a plasmon.
- 4) The electron may undergo a number of scattering events, which may be both elastic and inelastic.

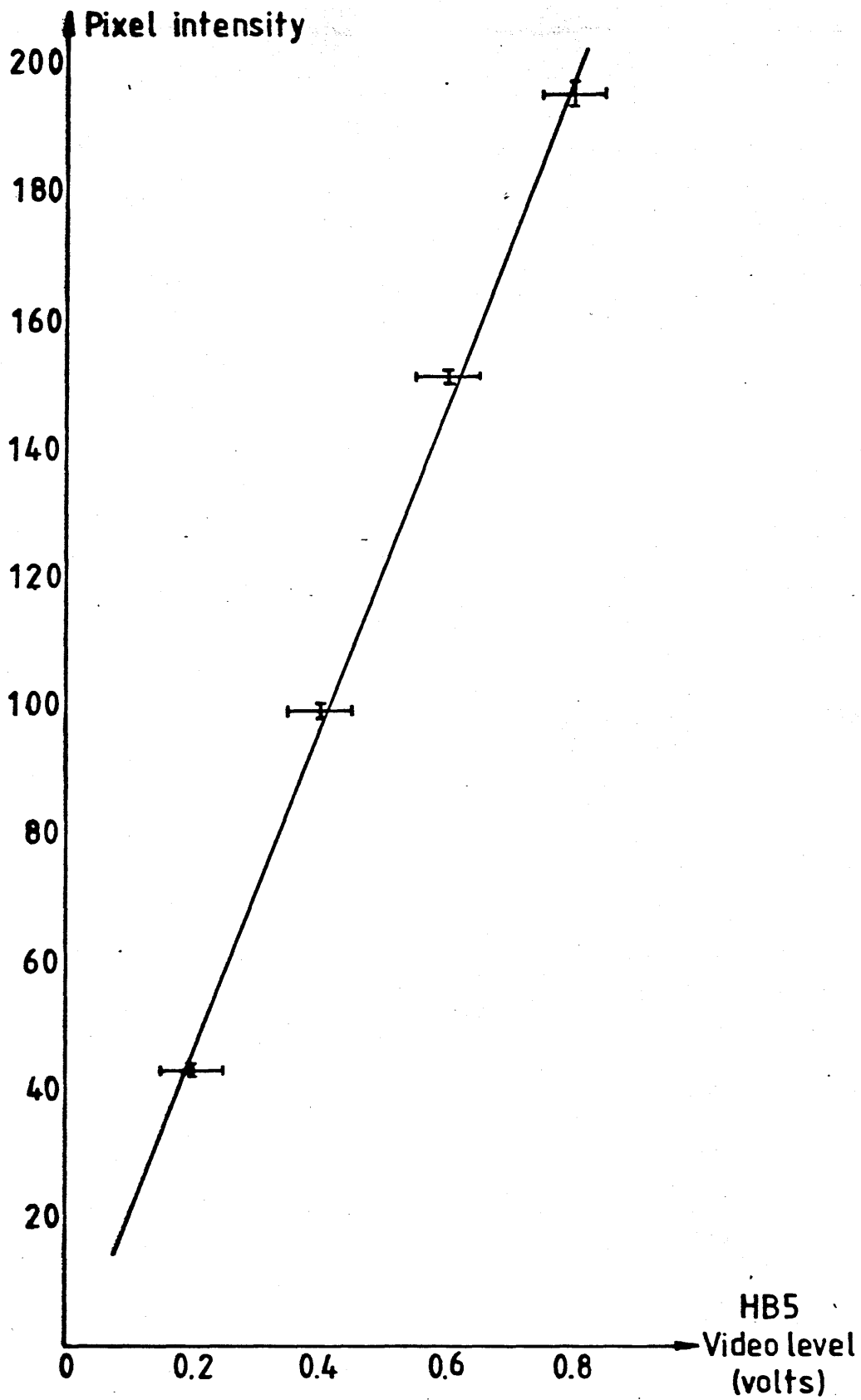


Figure 2.14 Pixel intensity versus HB5 video level for integrating line receiver with 2ms pixel dwell time

Electron energy loss spectroscopy:

Due to these scattering events, the electrons leaving the specimen have a spread in both energy and direction. By analysing the energy spread of the electrons leaving the specimen, it is possible to obtain information about the chemical composition, structure and thickness of the specimen. An example of an electron energy loss spectrum is shown in figure 2.15

The first peak, centred on zero energy loss, corresponds to the unscattered electrons, and to elastically scattered electrons. The atomic scattering factor for 100keV electrons is a strong function of scattering angle, and is strongly forward pointing, dropping to $\sim 0.2x$ the forward scattering value by the time the deflection angle reaches 20mrad. A further constraint on the direction of scattering is the fact that, in crystalline materials, only certain scattering angles are permitted. These correspond to the Bragg angles given by $\theta_m \approx m\lambda/2d$ where λ is the electron wavelength and d is the crystal lattice spacing. Given a typical lattice spacing of $\sim 2.5\text{\AA}$ this gives $\theta_m \approx 10\text{mrad}$. For this reason, a spectrometer collection half angle of $>20\text{mrad}$ will be sufficient to include some of the elastically scattered electrons in the energy loss spectrum.

Also included in the zero loss peak are inelastically scattered electrons which have given rise to phonons within the specimen. These electrons have lost typically a few meV, and as the resolution of electron spectrometers is $\sim 1\text{eV}$, they cannot be resolved from the unscattered electrons.

The second, broader peak, corresponds to inelastically scattered electrons which have given rise to plasmons or valence band excitations in the specimen. The plasmon peak is typically centred around 25-30eV. There may also be peaks in the spectrum corresponding to 2 or more plasmon excitations and, although these are generally small they can, in for example thick single crystal aluminium, be quite large (Egerton 1983). The valence band losses, together with any tail from the plasmon peaks, extend out to the high

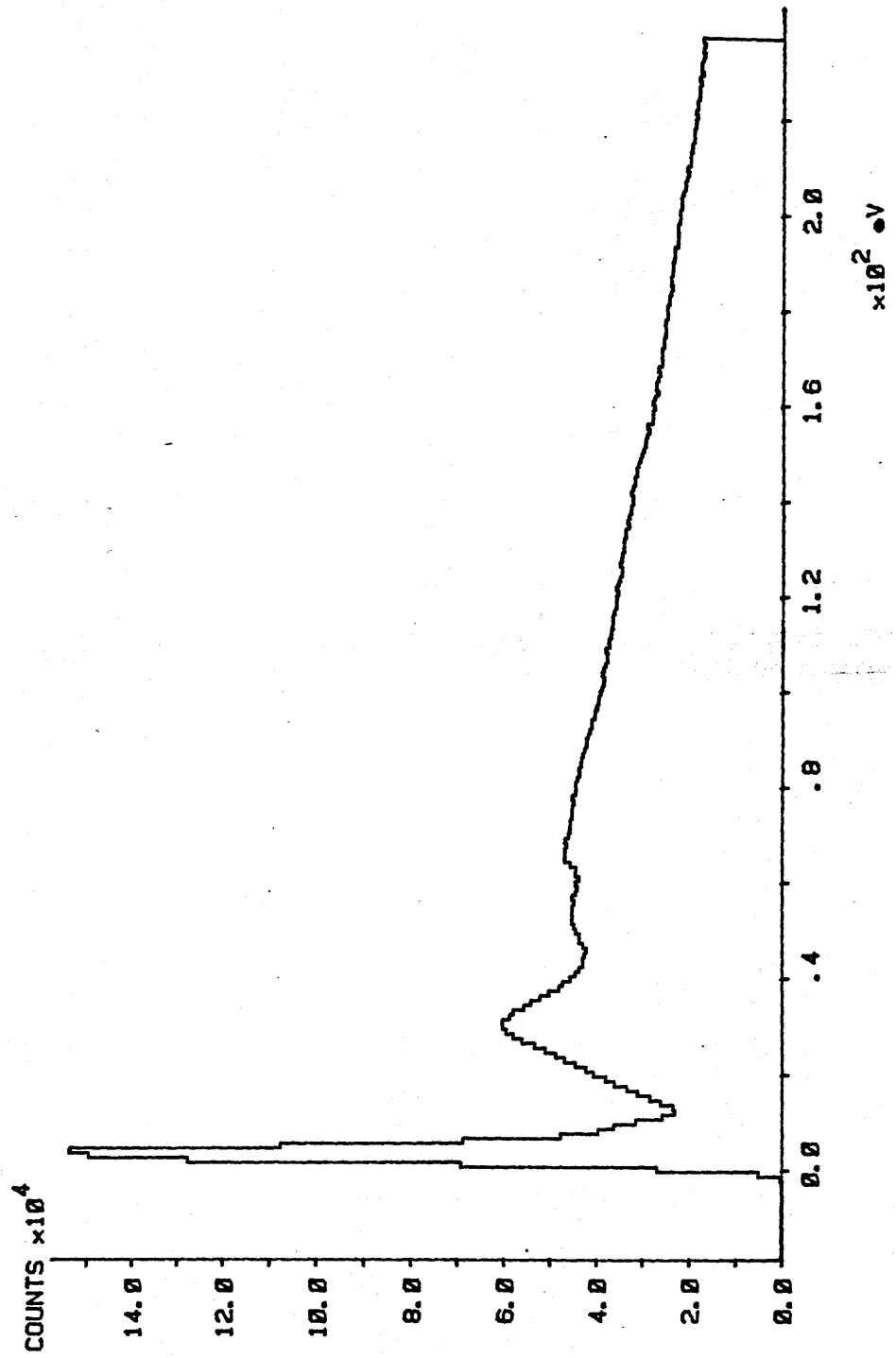


Figure 2.15: Typical EELS spectrum from a 130nm thick CoCr alloy film

energy loss region of the spectrum. This acts as a background on top of which signals due to inelastic interactions with atomic electrons are superimposed.

These signals are characteristic of the atoms within the sample. The onset of each of these signals is at an energy corresponding to the ionisation energy of an inner shell electron of one of the atomic species in the specimen. These signals, known as ionisation edges, often have an abrupt rise, although a number have a delayed maximum, and drop off gradually on the high energy side. From the number of electrons in these edges it is possible to ascertain the atomic composition of the specimen. Fine structure associated with the ionisation edges gives information on conduction and valence band structure and atomic ordering within the specimen.

Measurement of specimen thickness:

For thick specimens it is difficult to use electron energy loss spectroscopy (EELS) to ascertain atomic composition. However, from the ratio of the counts in the zero loss peak to those in the remainder of the spectrum, it is possible to estimate the thickness of the specimen: From the Poisson Law of statistics, the probability of n rare events occurring in one target is

$$P(n) = \frac{m^n}{n!} \exp(-m)$$

where m is the average number of events. For an electron travelling through a specimen of thickness t , the average number of scattering events is given by $m=t/\Lambda$, where Λ is the mean free path between scattering events. This implies that the intensity in the unscattered beam is

$$I_{un} = I_0 \exp(-t/\Lambda_e) \exp(-t/\Lambda_i)$$

and the intensities in the elastic, inelastic and mixed elastic-inelastic

beams are given by

$$I_{e1} = I_0 \exp(-t/\Lambda_i) [1 - \exp(-t/\Lambda_e)]$$

$$I_{in} = I_0 \exp(-t/\Lambda_e) [1 - \exp(-t/\Lambda_i)]$$

$$I_{i,e} = I_0 [1 - \exp(-t/\Lambda_e)] [1 - \exp(-t/\Lambda_i)]$$

where the subscripts i and e refer to inelastic and elastic scattering respectively. For a large spectrometer collection angle the intensity in the zero loss peak is given by:

$$I_1 = I_{un} + I_{e1} = I_0 \exp(-t/\Lambda_i)$$

and the intensity in the remainder of the spectrum is given by

$$I_2 = I_{in} + I_{i,e} = I_0 [1 - \exp(-t/\Lambda_i)]$$

Hence the thickness is given by

$$t = -\Lambda_i \ln \left[\frac{I_1}{I_2 + I_1} \right] \quad (2.39)$$

This equation also holds for small spectrometer collection angles where both I_{e1} and $I_{i,e}$ are excluded from the spectrum. The mean free path for inelastic scattering is given by $\Lambda_i = 1/N\sigma_{in}$ where N is the number of scattering atoms per unit volume and σ_{in} is the atomic cross-section for inelastic scattering. From Colliex and Mory (1984)

$$\sigma_{in}(\text{\AA}^2) \approx \frac{1.5 \times 10^{-4}}{\beta} Z^k \ln \left[\frac{2}{\langle \theta_E \rangle} \right] \quad (2.40)$$

where $\langle \theta_E \rangle = \langle \Delta E \rangle / 2E_0$ is the scattering angle corresponding to the average inelastic loss $\langle \Delta E \rangle$, $\beta = v/c = 0.3005$ for 100keV electrons

and Z is the atomic number of the atoms in the specimen. This equation for σ_{in} is dependent on the scattering potential assumed. Eusemann *et al* (1982) have proposed refinements which take into account the shell nature of the scattering potential. However, equation (2.40) provides a useful order of magnitude value for σ_{in} . In this work EELS has been used only to estimate the thickness of specimens. In order to ascertain the atomic composition of the specimens, x-ray microanalysis has been used.

X-ray spectra from thin specimens:

When electrons are inelastically scattered from the inner-shell electrons of atoms, these inner-shell electrons are promoted out of their ground level states. When these states are reoccupied an x-ray, characteristic of the excited atom, can be produced. Using an energy dispersive x-ray (EDX) system, it is possible to measure the atomic composition of electron microscope specimens. All elements with $Z > 11$ can be detected by EDX systems, x-rays from elements with $Z < 11$ being absorbed by the beryllium window on the EDX spectrometer (windowless detectors are now becoming available but are not, at the moment, common).

In principle, the number of atoms of a given element which are being irradiated by the electron probe in the microscope, can be calculated if the absolute x-ray intensity, specimen thickness, beam current, absorption coefficient of the specimen and the detector characteristics are known. In practice many of these parameters are unknown. However, by taking the ratio of two observed x-ray intensities, I_A and I_B , it is possible to calculate the ratio of the number of atoms of A to the number of atoms of B. i.e. for the K_{α} x-rays the ratio of the number of atoms is given by

$$\frac{n_A}{n_B} = \frac{N_A}{N_B} \left[\frac{\sigma_B}{\sigma_A} \right] \quad (2.41)$$

where N is the number of counts in the K_{α} peak after subtraction of background counts (mostly due to Bremsstrahlung), and σ is the cross-section for production of K_{α} x-rays. This formula assumes that the specimen is thin enough that no absorption, or secondary x-ray fluorescence need be taken into account. The ratio of x-ray production cross-sections can be calculated using (Gray *et al* 1983):

$$\frac{\sigma_A}{\sigma_B} = \frac{P_A \omega_A \ln(0.89 E_0/E_{i,A})}{E_{i,A}} \cdot \frac{E_{i,B}}{P_B \omega_B \ln(0.89 E_0/E_{i,B})} \quad (2.42)$$

where P is the ratio of K_{α} to $(K_{\alpha} + K_{\beta})$ x-ray production, ω is the fluorescence yield and E_i is the ionisation energy, the subscripts denote whether the quantity refers to A or B. E_0 is the incident electron beam energy.

For all but the thinnest of specimens, x-ray absorption has to be considered. X-ray absorption can be described by Beer's Law

$$I_A = I_{0A} \exp \{-(\mu/\rho)^A_{\text{spec}} \rho \ell\} \quad (2.43)$$

where I_A is the transmitted x-ray intensity, I_{0A} is the initial x-ray intensity, ℓ is the path length that the x-rays travel through the specimen and $(\mu/\rho)^A_{\text{spec}}$ is the absorption coefficient for x-rays from A in a specimen of density ρ . This leads to a correction factor for equation (2.41) of

$$\frac{(\mu/\rho)^A_{\text{spec}} [1 - \exp \{-(\mu/\rho)^B_{\text{spec}} \rho \ell\}]}{(\mu/\rho)^B_{\text{spec}} [1 - \exp \{-(\mu/\rho)^A_{\text{spec}} \rho \ell\}]} \quad (2.44)$$

If the absorption coefficients of A and B are very similar then this correction factor is close to unity and can be neglected.

In general, secondary x-ray fluorescence effects are very much less in thin films than in bulk, and need only be considered if strong x-ray fluorescence occurs in equivalent bulk specimens. It will not be considered in this work.

Estimation of volume analysed:

In the HB5 STEM, EELS and x-ray spectra are obtained from very small volumes of the specimen by positioning a stationary, focussed electron probe on the specimen. The radius of the electron probe is determined by spherical aberration in the probe forming lenses and by diffraction at the probe defining aperture. Adding these contributions in quadrature gives:

$$r_{\text{total}}^2 = r_s^2 + r_d^2 = \left[\frac{C_s \alpha_0^3}{4} \right]^2 + \left[\frac{0.61 \lambda}{\alpha_0} \right]^2$$

where α_0 is the probe half angle, λ the electron wavelength ($3.7 \times 10^{-12} \text{m}$ for 100keV electrons) and C_s is the third order spherical aberration coefficient of the probe forming lenses. Under normal microanalysis conditions in the HB5 (given in table 2.1), C_s is 3.5mm and α_0 is 11mrad, this then gives r_{total} as 1.2nm. In fact the volume of specimen irradiated by the electron probe is very much greater than a cylinder of radius r_{total} and length t , the specimen thickness. This is due to beam broadening within the specimen, and it is this beam broadening which imposes the fundamental limit on how small a volume can be analysed. The extent to which the beam is broadened has been calculated by Reed (Goldstein *et al* 1977). For a sample of thickness t , he gives the diameter of the circle on the exit surface which contains 90% of the electron trajectories to be

$$b = 6.25 \times 10^5 \frac{Z}{E_0} \left[\frac{\rho}{A} \right]^{1/2} t^{3/2} \text{ cm} \quad (2.45)$$

where ρ is the density in gcm^{-3} , E_0 is the primary beam energy in eV and t is in cm.

Figure 2.16 a) gives this beam diameter for 100keV electrons in $\text{Co}_{78.5}\text{Cr}_{21.5}$ up to a thickness of 130nm. Figure 2.16 b) shows the result of a Monte Carlo calculation of electron trajectories in the same material. The excellent agreement between the two beam profiles indicates that, to calculate the volume irradiated by the probe in the HB5, the Reed model can be used.

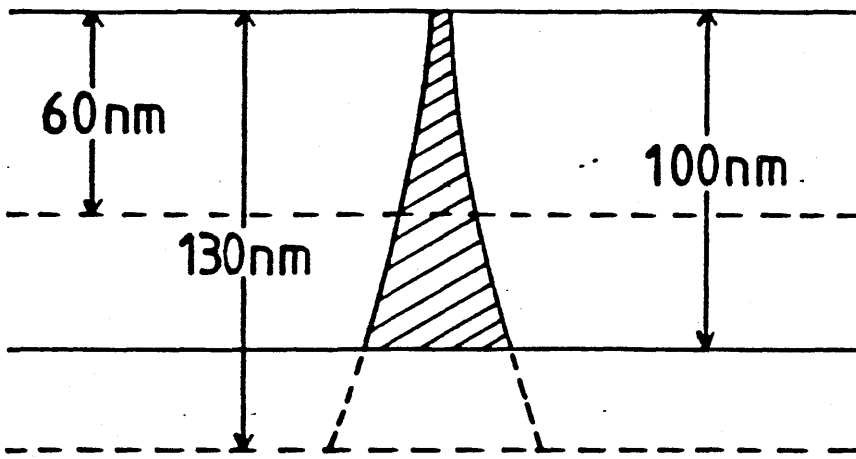
Operating conditions for spectrum acquisition:

The conditions for acquiring EELS spectra on the HB5 are the same as those for acquiring x-ray spectra; i.e. the focussed probe is produced using condenser C1 and the objective lens. This maximises the current in the electron probe. The objective lens is kept at an almost constant excitation, and the specimen is brought into focus by moving it in the z direction. This leads to greater thermal and magnetic stability of the objective lens and therefore to less specimen drift. Moreover, by using a standard objective focus, it is possible to use standard post-specimen lens settings to match the electron angular spread leaving the specimen, to the electron spectrometer entrance pupil. The lens and aperture settings used throughout this work are given in table 2.1.

A virtual objective aperture is used instead of a real objective aperture, as x-rays from electrons striking a real objective aperture would lead to unwanted instrumental peaks in the x-ray spectra. Similarly the smallest selected area aperture is used as a spray aperture to stop stray electrons from proceeding further up the column. These stray electrons, if allowed to pass up the column would produce unwanted instrumental contributions from, for example, the specimen grid and the objective lens pole pieces.

To minimise absorption of x-rays from the specimen in the specimen holder and grid, the specimen is tilted towards the x-ray detector through an angle of 20° . In an attempt to reduce instrumental

a)



b)

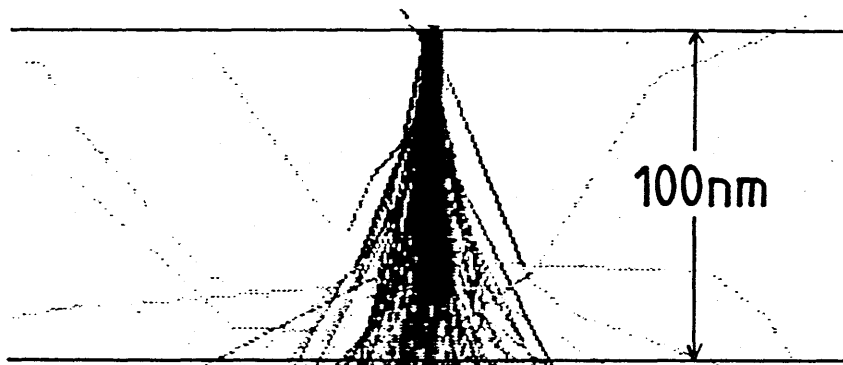


Figure 2.16: a) Beam spreading for 100keV electrons in CoCr alloy calculated using a formula due to Reed.
b) Monté Carlo calculation of 100keV electron trajectories in CoCr alloy

Table 2.1 Operating conditions for spectrum acquisition

Probe forming optics:	Condenser C1 focussed on SAD plane
	Objective lens at setting: coarse 18
	medium 11
Probe defining aperture:	100 μ m Virtual objective aperture
Spray aperture:	25 μ m SAD aperture
Post-specimen lens settings:	P1 at setting: coarse -6
	medium 4.82
	or P3 at setting: coarse -2
	medium 8.75
EELS spectrometer aperture:	500 μ m collector aperture
Specimen position:	z = -0.2mm; x tilt = -20 ⁰
	y tilt = +20 ⁰
All other lenses :	OFF

contributions still further, two special specimen holders were used during this work: One of the holders was a standard V.G. Microscopes beryllium x-ray cartridge - any characteristic x-rays produced in this are absorbed by the beryllium window of the EDX detector. The other was a cartridge designed at Glasgow by Adam (1986). This has very little material near the specimen, thus greatly reducing the volume of unwanted material which can produce x-rays.

The x-ray detector used was a Link Systems Si(Li) detector, controlled by either the Toltec computer or a Link Systems 860 series I energy dispersive system. The detector itself had a Ta collimator, and the Si(Li) crystal was isolated from the microscope by an 8 μ m beryllium window. The take off angle to the spectrometer was 100.5 $^{\circ}$ to the primary beam direction. The energy resolution of the detector was \sim 160eV FWHM for Mn K $_{\alpha}$ and 20 μ s integration time.

The entrance pupil of the electron spectrometer was a 500 μ m collector aperture, this gives a collection half angle of 27mrad with P1 alone, or approximately 3mrad with P3 alone. The spectrometer itself consists of an electromagnet producing a magnetic field at 90 $^{\circ}$ to the electron beam. This bends the electron beam through approximately 90 $^{\circ}$ and produces a dispersion of the beam according to its component energies. A set of scan coils after the spectrometer magnet are used to scan the energy loss spectrum across a slit in front of a scintillator-photomultiplier assembly (in fact the bright field detector). Due to the large dynamic range of EELS spectra (10^6 - 10^8 between the zero loss and high energy loss ends), the bright field electronics have to operate in both a pulse counting mode, for very small signals, and a current mode, for very large signals. A detailed description of this system is given by Craven and Buggy (1984).

Spectrum acquisition:

For simultaneous EELS and x-ray acquisition, the Toltec computer was used. These spectra were processed using methods described by Crozier (1986). Some x-ray spectra were acquired using a Link 860

series I computer, and these were analysed on a Data General Nova 2 minicomputer fitted with a Link 290 extension supplied by Link Systems.

CHAPTER 3

LARGE GRAIN POLYCRYSTALLINE COBALT

3.1 Introduction

In this chapter it will be shown that a single machine, a dedicated STEM fitted with a quadrant detector such as the HB5 at Glasgow, is capable of providing a complete description of both the physical and the magnetic microstructure of a thin electron microscope specimen. The film used to illustrate this was a polycrystalline cobalt film with an hcp structure. The variation of domain size with crystal orientation and film thickness for this type of film has been described in the past (see for example Jakubovics 1966) and this will be used to check the validity of the results obtained in this work. In addition it will be shown that the dedicated STEM allows the local specimen thickness, the domain wall width, and the angle of the magnetisation vector to the film normal to be measured accurately.

In general, the magnetic domain structure within a magnetic material is dependent upon many factors: temperature during manufacture, and therefore crystal defects within the film; past magnetic history; etc. However in thin magnetic films, such as the above mentioned cobalt, in which the grain size is very much larger than the domain size, and in which there is a strong magnetocrystalline anisotropy, this is not the case. In these films the equilibrium domain structure is determined primarily by the physical microstructure of the film, i.e. film thickness, crystal axes orientation etc.

The magnetic structure of the cobalt film was studied using DPC imaging, and the crystal orientation was determined using electron diffraction. Although it is possible to carry out electron diffraction studies in the HB5 STEM, it was found to be more convenient to carry out these studies on a JEOL JEM1200EX conventional transmission electron microscope. This was due both to pressure for time on the HB5 and to the availability of a eucentric tilt-rotate holder for the JEOL

machine. This tilt-rotate holder allows the specimen orientation to be easily changed within the microscope, so that it can be tilted about an axis perpendicular to the plane of the domain walls. The c-axis for this film lies in the plane of the domain walls; therefore tilting about an axis perpendicular to the domain walls allows the c-axis orientation to be ascertained. The local film thickness was measured using the split spot technique (Chapman and Morrison 1983) which will be discussed in more detail in section 3.4 on experimental results.

The film preparation techniques and the nomenclature used to describe the magnetic structure of the films is given in section 3.2, and the theoretically predicted relationship between the magnetic and physical structure of a thin, uniaxial single crystal is described in section 3.3.

3.2 Polycrystalline Cobalt

As stated in section 3.1, the sample under investigation was a polycrystalline cobalt film with an hcp structure. Electron microscope samples were prepared by electropolishing a cold rolled polycrystalline cobalt foil using the window technique (for a description of this technique see Hirsch *et al* Ch.2 1965). This technique perforates the foil and leaves areas of foil around the perforations which are thin enough to be studied with a 100keV transmission electron microscope. These areas are however limited in size and the foil thickness increases rapidly as you move away from the perforations. The areas under study are therefore wedge shaped in cross-section. Once thinned, the foil was cut into squares approximately 2mm x 2mm and mounted on folding Cu electron microscope specimen grids. An example of the sort of sample produced by this method is shown in figure 3.1. The average grain size in the sample was $\approx 30\mu\text{m}$ and the c-axis direction varied randomly from grain to grain.

hcp cobalt has a strong magnetocrystalline anisotropy ($K_1 \approx 4.1 \times 10^5 \text{ Jm}^{-3}$ at room temperature) along the c-axis direction. In



Figure 3.1 Low magnification Fresnel image of a typical area from a window thinned cobalt film.

thin single crystal cobalt this crystalline anisotropy confines the in-plane component of the saturation magnetisation, \underline{M}_s , to the projection of the c-axis in the plane. Following Jakubovics (1966), it will be taken that the c-axis and \underline{M}_s lie in the same vertical plane; that the c-axis makes an angle θ with the film normal; and that the magnetisation within the domains makes an angle Φ_0 with the film normal. This is shown in figure 3.2. Also illustrated in figure 3.2 is a tilt, η , of the specimen with respect to the z-axis (the optic axis of the microscope). The z-axis and the film normal both lie in the same plane as the c-axis and \underline{M}_s . The film thickness is denoted by t .

The magnetic structure is assumed to consist of a regular array of domains, of width D , within which the magnetisation is constant, separated by 180° domain walls. The wall model used by Jakubovics in his 1966 paper describing the theoretical relationship between the magnetic and physical structures of a thin uniaxial single crystal, was a one dimensional tanh model, which can be characterised by a domain wall half width b . Using this model, the angle, Φ , between the magnetisation and the film normal is given by the equations

$$\cos(\Phi - \Phi_0) = \tanh \{(x - 2nD)/b\} \text{ for } (2n - 1/2)D < x < (2n + 1/2)D \quad (3.1)$$

$$\cos(\Phi - \Phi_0) = \tanh \{[x - (2n + 1)D]/b\} \text{ for } (2n + 1/2)D < x < (2n + 3/2)D$$

where $n = 0, \pm 1, \pm 2, \dots$

This model leads to discontinuities in Φ at $x = \pm D/2$; however if $D \gg b$ these are negligible. Landau and Lifshitz (1935) proposed a similar model for magnetic domain walls in bulk crystals where $b = (A/K)^{1/2}$, A being the exchange constant and K the anisotropy constant. However, although this type of model provides a good description of the domain walls within bulk materials, it may not be appropriate for thin films as it takes no account of magnetostatic effects at the film surfaces. In this case a two dimensional wall model may be more appropriate (Jakubovics 1978).

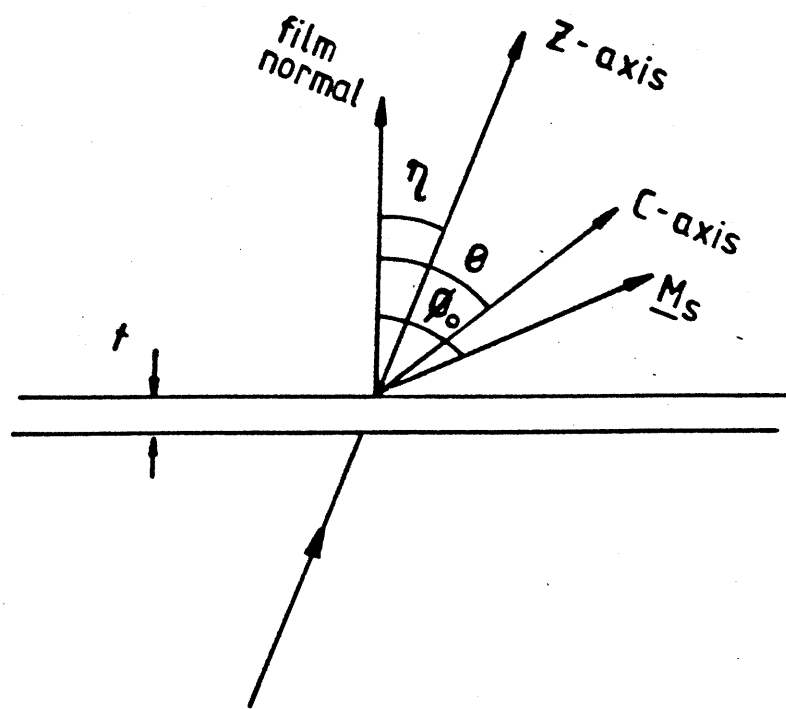


Figure 3.2 Coordinate system used in analysis of cobalt film microstructure.

3.3 Theoretical Relationship Between Physical And Magnetic Structure

As discussed in chapter 1, the equilibrium magnetic domain structure of a thin film represents a potential energy minimum in which the exchange, magnetostatic, anisotropy and wall energies all have to be considered. Jakubovics (1966) has calculated equilibrium magnetic domain structures for single crystal cobalt films of uniform thickness by minimising this total potential energy. As stated in section 3.2, the samples used here were polycrystalline and wedge shaped in cross-section, However as the grains are large compared to the average domain size and the angle of the wedge is small, small areas of individual grains may be approximated to single crystals of uniform thickness. Although the domain wall model used by Jakubovics may be too simple to adequately describe the domain walls within cobalt thin films, the calculations of domain width, D , and the direction of magnetisation, Φ_0 , have been shown to be reliable (experimental section of Jakubovics 1966). In this section the results obtained from these calculations, as they apply to the sample under investigation, will be presented.

Figures 3.3 and 3.4 (taken from Jakubovics 1966) show, in detail, how the calculated values of $(\Phi_0 - \theta)$ and D^{-1} vary with θ over a range of film thicknesses from 50-700 nm. The experimental measurements presented here will be shown to be in good agreement with them.

In a uniaxial crystal such as cobalt, there is a strong tendency for the saturation magnetisation, \underline{M}_S , to lie along one direction, in this case the c -axis. However, for films of interest in the electron microscope, i.e. of thickness ≤ 150 nm, the effect of free magnetic poles on the film surface acts to keep \underline{M}_S within the plane of the film. In cobalt these two effects determine the direction of \underline{M}_S and the domain width, D .

If the c -axis lies within the plane of the film, $\theta = 90^\circ$ in figure 3.2, then \underline{M}_S lies along the c -axis and both the anisotropy and magnetostatic energy contributions are minimised. The domain width, D , is large as

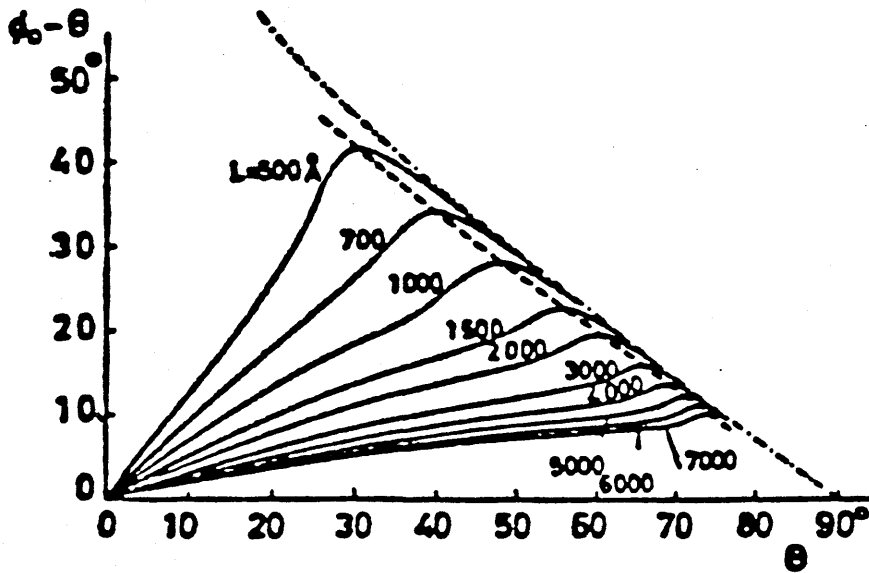


Figure 3.3 Variation of $(\phi_0 - \theta)$ with c-axis orientation, θ for a single crystal cobalt film (from Jakubovics 1966, figure 4)

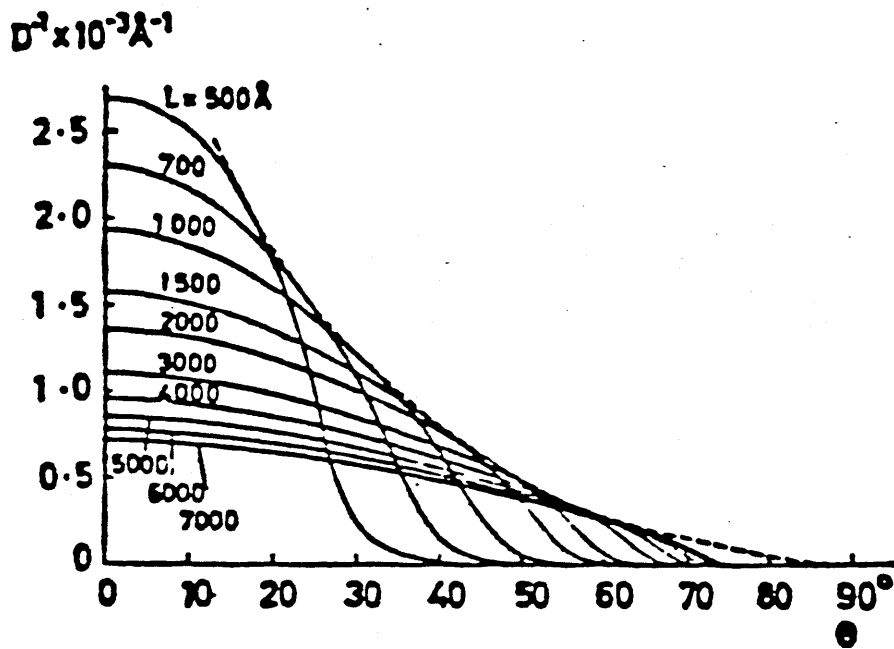


Figure 3.4 Variation of domain width, D , with c-axis orientation, θ for a single crystal cobalt film (from Jakubovics 1966, figure 7)

there are no magnetostatic energy contributions from the film surfaces, only from the film edges. The domain walls run parallel to the c -axis as this reduces the magnetostatic contribution to the domain wall energy.

In the other extreme, with the c -axis parallel to the film normal, $\theta = 0^\circ$, there is no preferred direction for \underline{M}_S in the film plane. In this case \underline{M}_S also points along the film normal, which reduces the anisotropy energy at the expense of a high magnetostatic energy. The magnetostatic energy is reduced by having the domain width, D , very small (Jakubovics 1981). As there is no preferred direction for the magnetisation in the film plane, the domain walls do not lie along any preferred direction, and therefore the domains form a maze like structure (see for example Grundy and Ali 1983).

For films in which the c -axis lies at some angle θ such that $0^\circ < \theta < 90^\circ$, the magnetisation, \underline{M}_S , will lie at an angle Φ_0 such that $90^\circ > \Phi_0 > \theta$. Furthermore, the in-plane component of \underline{M}_S will lie along the projection of the c -axis in the plane of the film. As the angle Φ_0 between \underline{M}_S and the film normal decreases, the domain width, D , will also decrease to reduce the magnetostatic energy. For a given value of θ , the value of Φ_0 and D will depend on t , the film thickness. In general, Φ_0 will be larger for thinner films, as these films have a larger magnetostatic energy for a given value of Φ_0 .

The theoretical domain wall half width, b , was also calculated by Jakubovics as a function of θ and t ; this is shown in figure 3.5, also taken from Jakubovics 1966. Direct measurement of the domain wall profile in a film in which θ and t are known should allow the calculated wall half width to be compared with an experimentally measured wall half width. Conventional techniques of Lorentz microscopy do not allow domain wall profiles to be measured directly; however, as shown in chapter 2, DPC imaging provides a direct map of the in-plane component of induction, convolved with a source intensity distribution. In the next 2 sections experimental measurements of D , t , Φ_0 and θ will be presented and a domain wall profile calculated from the value of b due

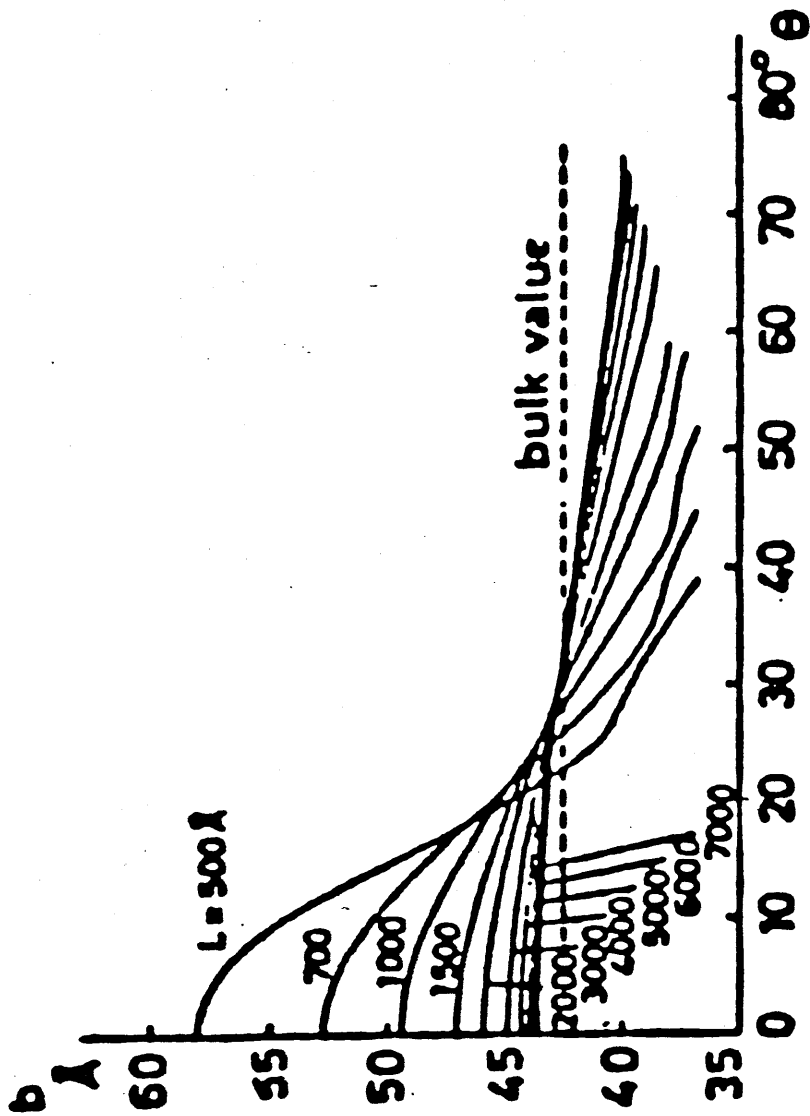


Figure 3.5 Variation of domain wall half width, b , with c -axis orientation, θ (from Jakubovics 1966, figure 10)

to Jakubovics will be compared with an experimentally measured domain wall profile.

3.4 Experimental Measurements

General observations:

An example of the range of domain widths found in the cobalt samples is given in figure 3.6. Micrographs a) and b) are DPC images, taken using the quadrant detector, which show two orthogonal components of in-plane magnetisation. The direction of the component mapped in each micrograph is given by the arrow below that micrograph. As can be seen, the domain size ranges from a few hundred nanometres to $>5\mu\text{m}$. The stray field distributions beyond the film can also be seen, and these, together with the stray fields from written tracks on magnetic recording material, will be discussed in chapter 4.

Figure 3.6 d) is a schematic showing the direction of magnetisation within each of the domains; it also identifies three areas A, B and C in which the domain sizes are different. Areas A and B are both in the same grain and therefore the angle, θ , between the c-axis and the film normal is the same in both of these regions. The increase in the domain width between area A and area B must therefore be due to a change in the film thickness. It can be seen from figure 3.6 c), which is a bright field image of the same area as figure 3.6 a) and b), that, in fact, area B is very much thinner than area A.

The film thickness in area A was measured using the split spot technique. This involves measuring the shift in position, on the diffraction screen, of the bright field cone as the electron probe is moved between two oppositely magnetised domains. The shift, $2\beta_L$, is twice the Lorentz deflection angle which is given by

$$\beta_L = (e\lambda/h) B_S t \sin\Phi_0 \quad (3.2)$$

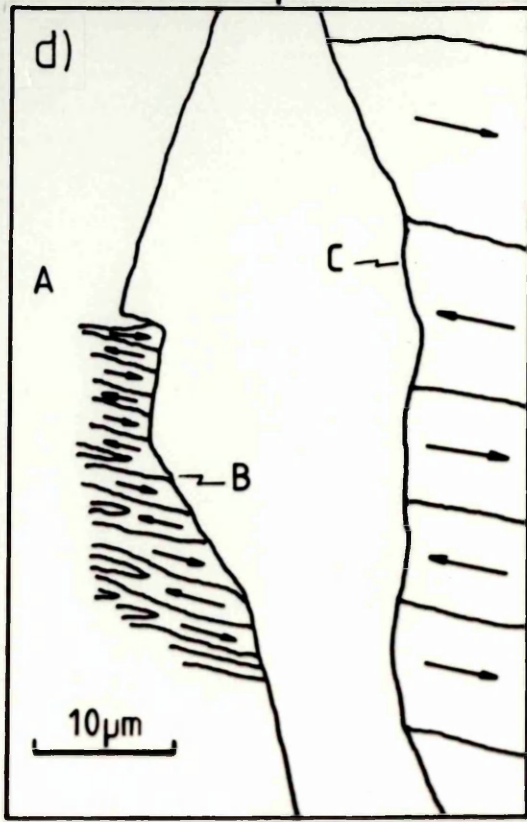
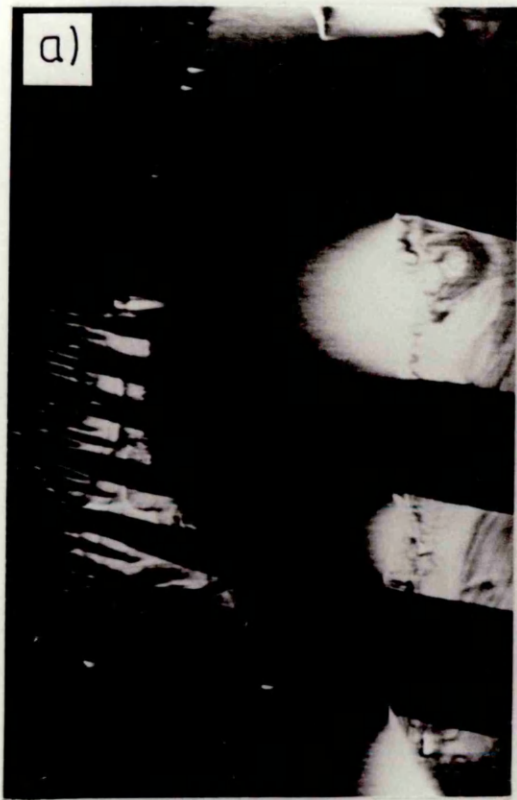


Figure 3.6 Domain structures in a cobalt film. a) and b) are two DPC images, the arrows give the direction of in-plane induction to which each is sensitive, c) is a bright field image of the same area, and d) is a schematic of the magnetic structure.

Therefore if the saturation magnetisation B_s is known, the value of $t \sin \Phi_0$ can be obtained. In practice, $2\beta_L$ is measured as a fraction of the probe half angle as shown in figure 3.7. It was found that $t \sin \Phi_0 = (95 \pm 5) \text{ nm}$ for area A, i.e. $t \geq 100 \text{ nm}$.

Using figure 3.4 and the measured domain width of 230nm, this implies that $\theta \geq 45^\circ$, in which case for this area, $\Phi_0 \geq 65^\circ$ (from figure 3.3). In addition, figure 3.4 predicts that for $\theta \geq 30^\circ$, a decrease in the film thickness t from 100nm will result in an increase in D , the domain width, as is observed in the sample. It can be seen from figure 3.6 a) that although t decreases rapidly, the domain contrast remains strong; this is due to the increase in the current transmitted by the thinner region of the film.

In area C the domains are large, even where the film is thick, by comparison with figures 3.3 and 3.4 this implies that both the c -axis and the saturation magnetisation are close to the film plane, with $\theta \geq 60^\circ$ and $\Phi_0 \geq 80^\circ$.

Edge effects:

Figure 3.4 predicts that for very thin films, as found at the edges of the grains described above, the domain size should be many tens of μm , regardless of the angle θ . This is not seen to occur in areas B and C.

There are extensive stray field distributions associated with the large domains of area C. These stray fields contribute to the overall energy of the domain structure of area C, and an increase in the size of the domains, although leading to a slight decrease in exchange energy, would greatly increase the magnetostatic energy of the domain structure. Moreover, in order to increase the domain size it would be necessary to terminate some domain walls within the film, as happens in area B. This would result in an increase in the total energy associated with the domain walls. Therefore the domain width does not increase in area C, as the film thickness decreases, to that which would be expected in a uniformly thin film.

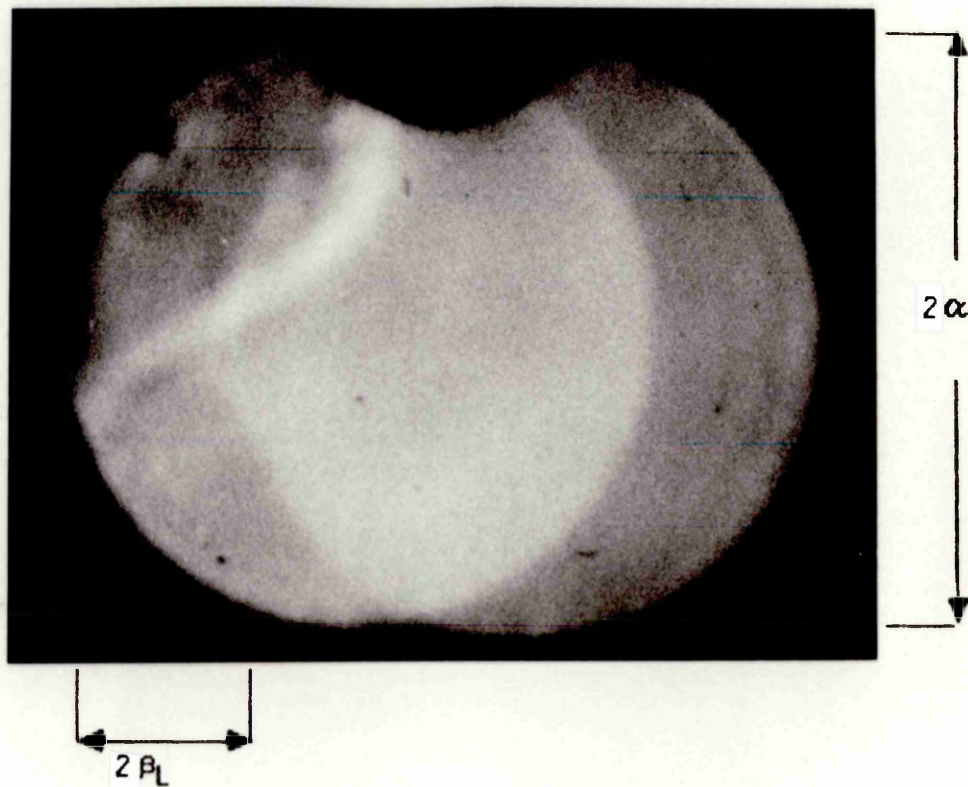


Figure 3.7: Double exposure showing the shift of the bright field cone on the diffraction screen due to the in-plane component of magnetisation within the sample. α is the probe half angle and β_L is the Lorentz deflection angle.

A higher magnification image of area B is shown in figure 3.8. Micrograph 3.8 a) is a bright field image of this area, and it can be seen from the variation in intensity from top to bottom, and the lower resolution in the lower half of the micrograph due to inelastic scattering, that the film is thinner at the top of this micrograph than at the bottom. Figure 3.8 b) is a DPC image of the same area as figure a), showing the major in-plane component of magnetisation. The magnetic structure is also depicted in figure 3.8 c) which is a Fresnel image (obtained in the STEM); however the domain wall contrast is low in the thicker regions of the film, compared to the DPC image. This is a result, both of the poor efficiency of Fresnel imaging in the STEM, and of inelastic scattering within the specimen which for thicker films can have a characteristic angle comparable to or greater than the Lorentz deflection angle β_L .

From figure 3.8 it can be seen that the domain size increases, between areas A and B, by the termination of some domains and the merging of others which have the same direction of magnetisation. The energy involved in this mechanism prevents large numbers of terminations occurring within a small area of the film. Therefore for large domains to form, a large, thin area of film is necessary. Hence it is the linear extent of area B which determines the maximum size of the domains that can form in this part of the film.

Approximation to ideal single crystal:

In the above examples, the crystal axes orientation and the direction of the magnetisation vector have been deduced from the graphs in figures 3.3 and 3.4, rather than measured directly. This is a valid procedure as these graphs have, as has been stated, been verified by experiment previously, although the domain structure has been influenced, to some extent, by edge effects. In this section an area of film, far from an edge of the foil, will be discussed. For this area, shown in figure 3.9, all the available parameters (Φ_0 , θ , t , D , and b) were measured and these will be compared with the predictions of

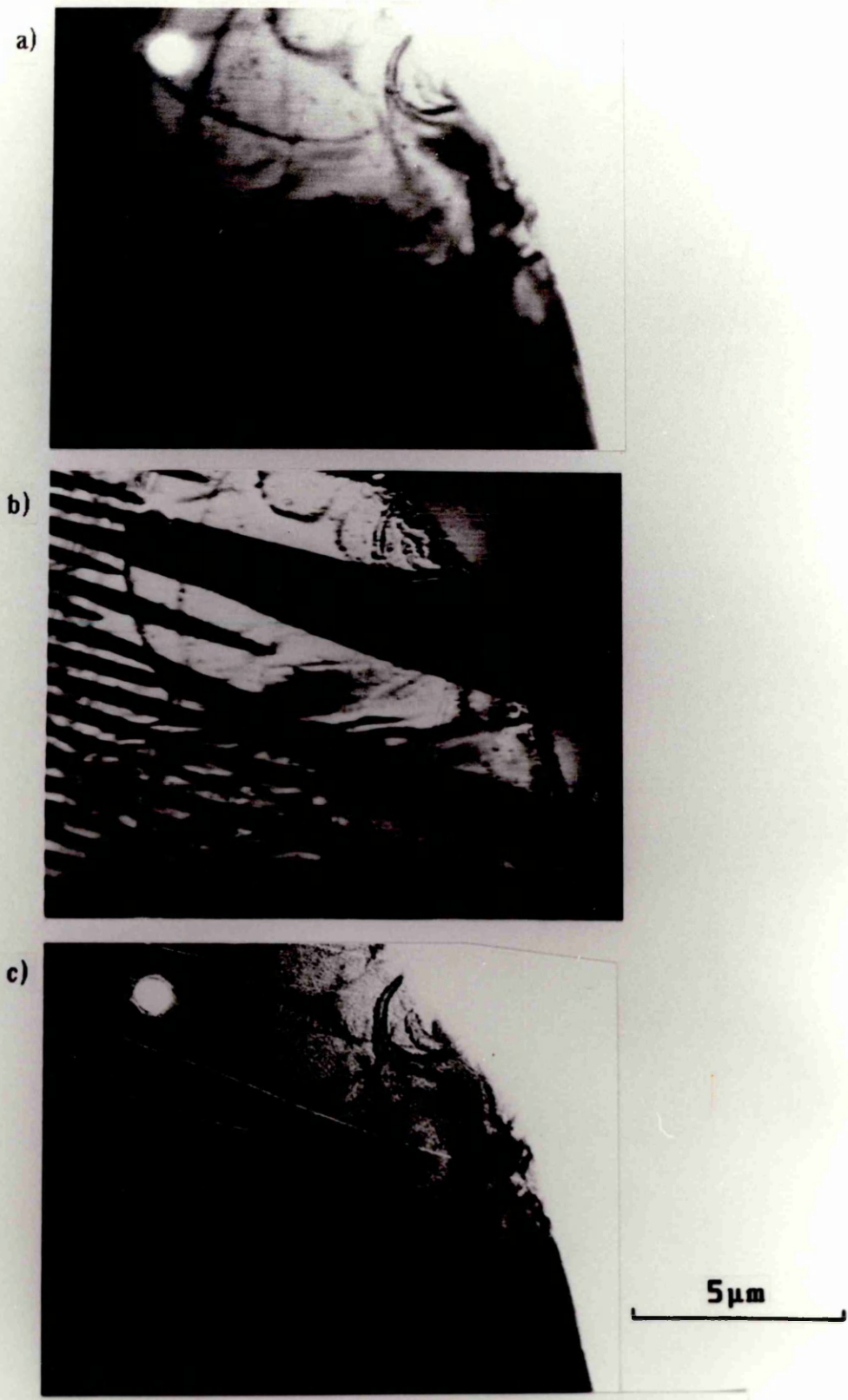


Figure 3.8 a) Incoherent bright field image of area B, b) DPC image of area B, showing main in-plane component of magnetisation, and c) Fresnel image of area B, depicting the domain walls.

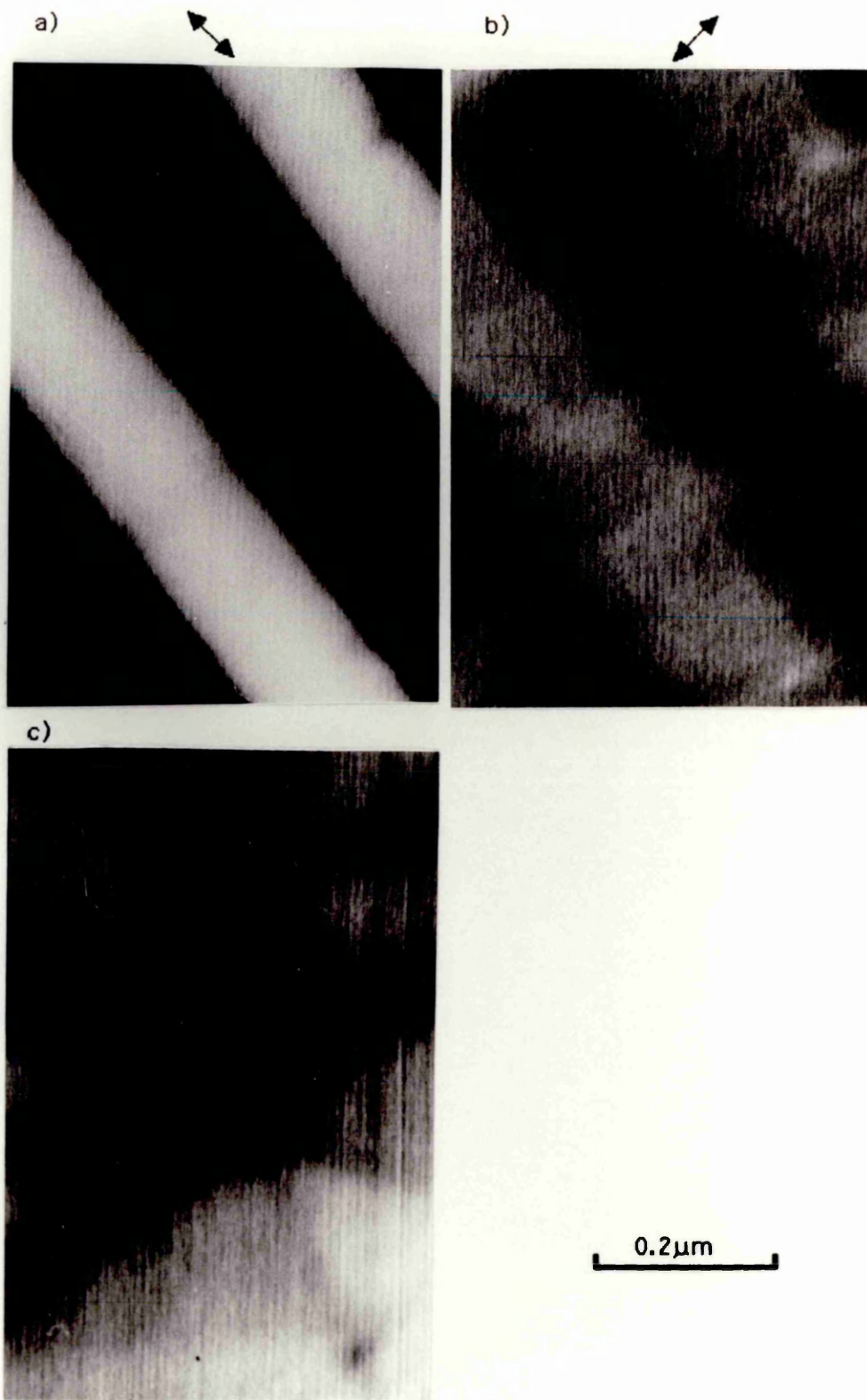


Figure 3.9 a) and b) two DPC images showing two orthogonal components of in-plane magnetisation in a cobalt film, c) incoherent bright field image of the same area.

figures 3.3 and 3.4.

Figure 3.9 shows two DPC images and a bright field image of the area mentioned, once again the arrows indicate which component of induction is mapped in each DPC micrograph. It can be seen from these micrographs that the domain walls are 180° walls and that they run parallel to the direction of magnetisation within the domains. Using the split spot technique it was found that $t \sin \Phi_0$ varied from $(85 \pm 10) \text{ nm}$ to $(115 \pm 12) \text{ nm}$ over the crystal grain in figure 3.9.

Measurement of θ and Φ_0 :

As stated in section 3.1, θ was measured by tilting the film about an axis perpendicular to the plane of the magnetic domain walls and observing the selected area electron diffraction pattern from the film. Figure 3.10 shows two such diffraction patterns, a) with the film untilted and, b) with the film tilted through an angle of $(40 \pm 2)^\circ$. Both diffraction patterns correspond to the same grain as that in figure 3.9. The diffraction pattern in figure 3.10 a) does not correspond to a prominent crystal axis, whereas that in figure 3.10 b) corresponds to the electron beam being parallel to the c-axis. This indicates that $\theta = (40 \pm 2)^\circ$ and that, as the tilt axis was perpendicular to the domain walls (and therefore the magnetisation direction within the domains), the in-plane component of magnetisation lies along the projection of the c-axis in the film plane.

From figure 3.2, it can be seen that the component of magnetisation which is perpendicular to the z-axis, and therefore the electron beam, in the microscope is $B_s \sin(\Phi_0 - \eta)$ and that the deflection of the electron beam is proportional to this multiplied by $\sec(\eta)$. Hence

$$\begin{aligned} \beta_L &\propto B_s t \sin(\Phi_0 - \eta) \sec(\eta) \\ &\propto k [1 - \cot(\Phi_0) \tan(\eta)] \end{aligned}$$

where k is a constant. If the thickness of the specimen is known, then

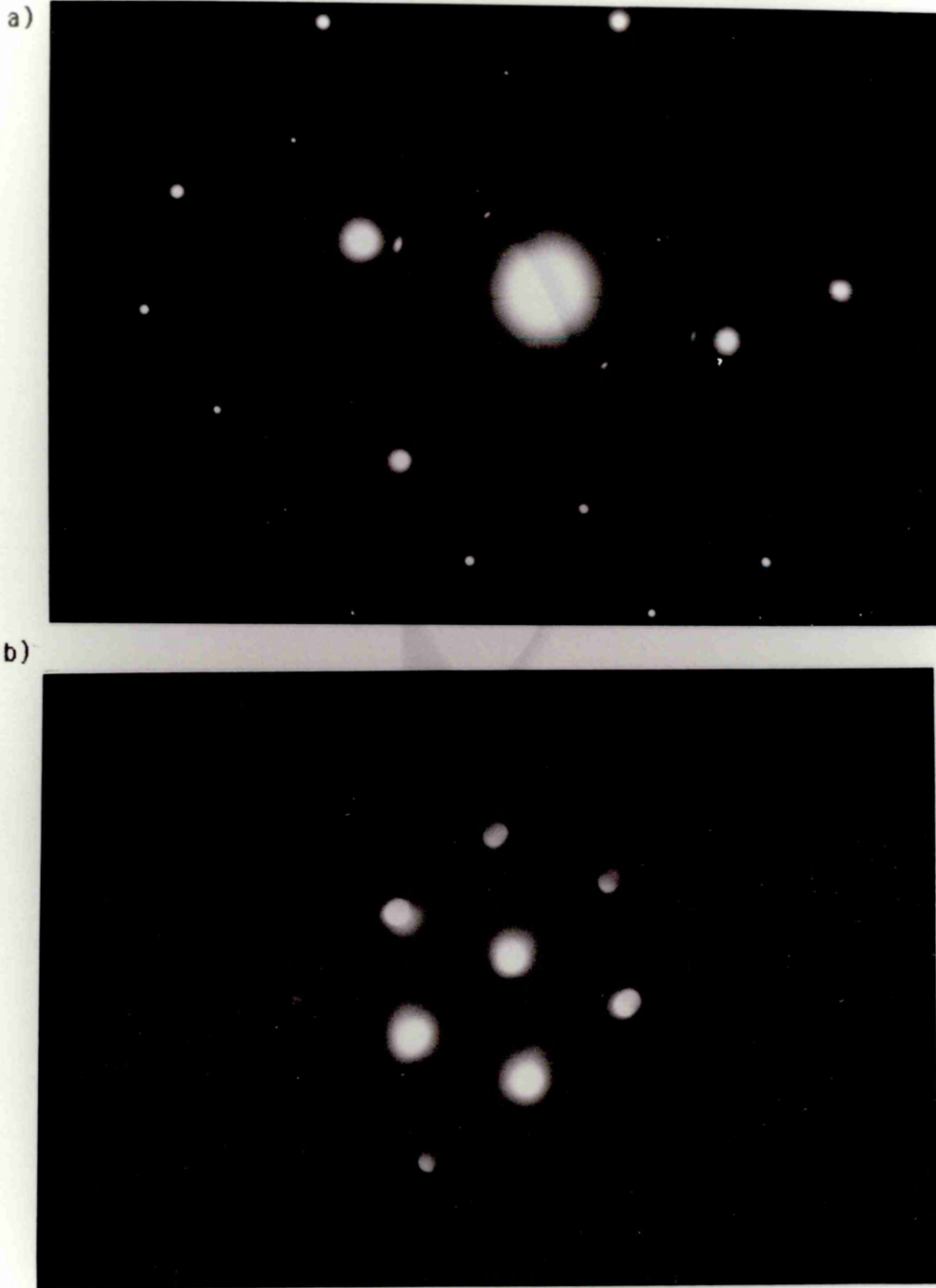


Figure 3.10 Selected area diffraction patterns from cobalt foil, a) specimen untilted, b) specimen tilted by 40° about an axis perpendicular to the domain walls.

using the measured deflection, β_L , for two tilts η_1 and η_2 , allows the value of Φ_0 to be obtained. As a check the deflections for three tilts can be taken: $\eta = 0^\circ$, in which case $\beta_L = k$, and $\eta = \pm\eta'$, in which case $\beta_L = k [1 \pm \cot(\Phi_0) \tan(\eta')]$. It can be seen therefore that:

$$\Phi_0 = \cot^{-1} \left\{ \left[\frac{\beta_L(-\eta')}{\beta_L(0)} - 1 \right] \frac{1}{\tan(\eta')} \right\}$$

By measuring the deflection angle, using the split spot technique, for $\eta' = \pm 20^\circ$, Φ_0 was found using this equation to be $(75 \pm 5)^\circ$ for the area in figure 3.9.

Comparison with figures 3.3 and 3.4:

For $\Phi_0 = 75^\circ$, $\sin \Phi_0 = 0.97$ therefore the crystal grain in figure 3.9 has a thickness varying between $(90 \pm 10)\text{nm}$ and $(120 \pm 15)\text{nm}$. For a crystal of this thickness and for which $\theta = 40^\circ$, the predicted value of Φ_0 from figure 3.3 is just over 70° which is in good agreement with the measured value of $(75 \pm 5)^\circ$. The predicted value of D from figure 3.4 is $(160 \pm 40)\text{nm}$ (for $\theta = (40 \pm 2)^\circ$ and $t = 100\text{nm}$) which agrees well with the measured value of $(180 \pm 10)\text{nm}$. The large error bar for the predicted domain width is due to the fact that the graph of D^{-1} vs θ in figure 3.4 is changing rapidly in the region of $\theta = 40^\circ$ for a 100nm thick film.

It can be seen therefore that the calculations of Φ_0 and D as a function of t and θ , due to Jakubovics, are in good agreement with the measured values. At least for specimens that approximate to a uniform single crystal, in which edge effects are negligible, and in which the thickness, t , is suitable for investigation by 100keV electron microscopy.

For a crystal which is not of a uniform thickness, or in which edge effects cannot be neglected, these calculations indicate the general trend that the domain structure will follow. However, in predicting the detailed domain structure, edge effects and the energy involved in terminating domain walls within the film have to be taken into account.

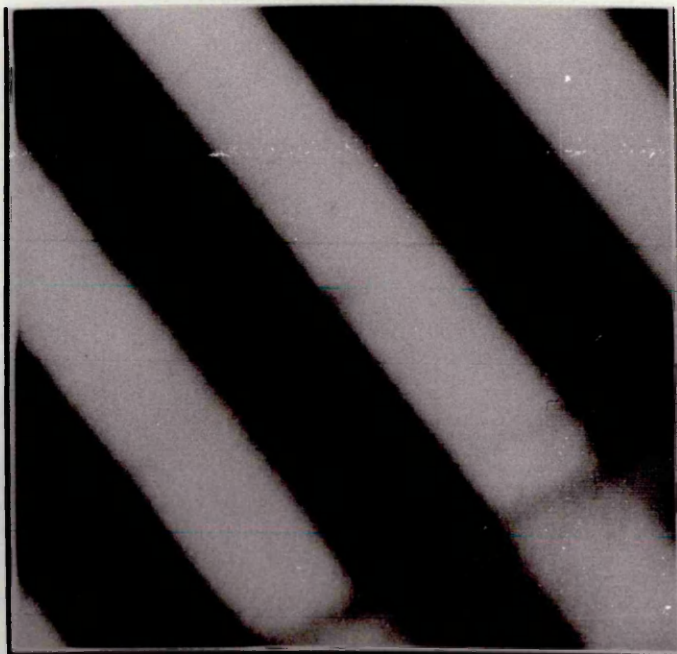
3.5 Domain Wall Profiles In Thin Crystal Cobalt

As stated in chapter 2, images are acquired sequentially in a STEM instrument, and can therefore be stored in a computer frame store. This allows the image signal variation across a magnetic domain wall to be obtained easily. In chapter 2 it was also shown that the signal level in a DPC image is a map of the in-plane component of induction convolved with a source intensity distribution. Thus the variation in the image signal level along a line at 90° to a domain wall in figure 3.9 a) can be regarded as an experimental measurement of the magnetic domain wall profile of the sample. If the diameter of the electron probe is much smaller than the distance over which the in-plane component of magnetisation varies, the effect of convolution with the source intensity distribution can be neglected. In a material such as cobalt in which there is a strong anisotropy, the domain walls can be very narrow, and therefore this effect has to be taken into account.

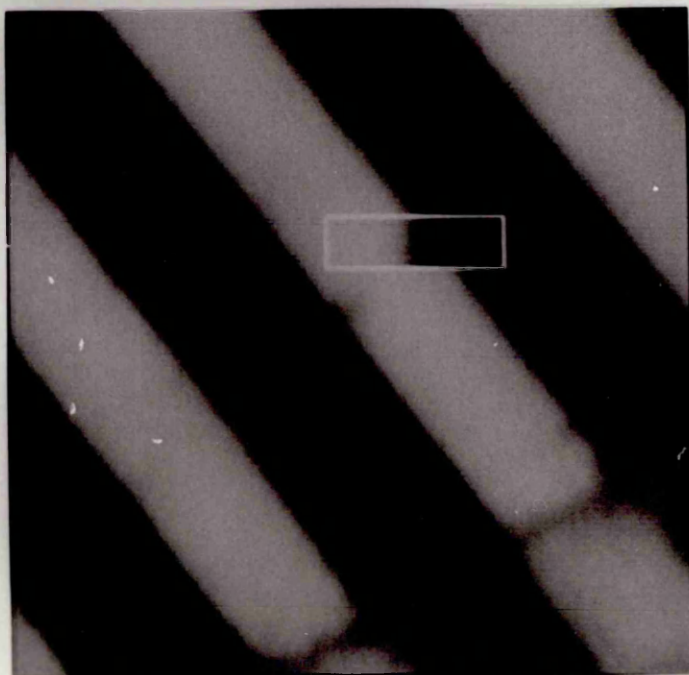
To remove any artifacts due to non-magnetic contrast an average of the domain wall profile along the length of the wall is taken. This is done using a computer to bring successive rows of a high magnification image of a domain wall into vertical registration as shown in figure 3.11. Figure 3.11 a) shows the original image, and figure 3.11 b) shows the image with a section of domain wall which has been aligned. The algorithms used to align the domain walls, and the problems involved in using this technique are discussed in appendix B. Once the wall has been aligned, a column sum of the aligned area is done to produce an average wall profile for this section of wall. Figure 3.12 a) shows a wall profile produced in this way from an image of a wall from the area shown in figure 3.9.

For $\theta = 40^\circ$ and $t = 100\text{nm}$, figure 3.5 gives $b \approx 4.3\text{nm}$, the bulk value of b . Using this and $\Phi_0 = 75^\circ$, equation (3.1) was used to calculate the in-plane component of magnetisation, and this is shown in figure 3.12 b). This calculated domain wall profile is very narrow and therefore the effect of the finite probe size and aberrations in the

a)



b)



200 nm

Figure 3.11 : a) Digitally acquired image of domains in a cobalt film. b) As a) with a section of domain wall aligned.

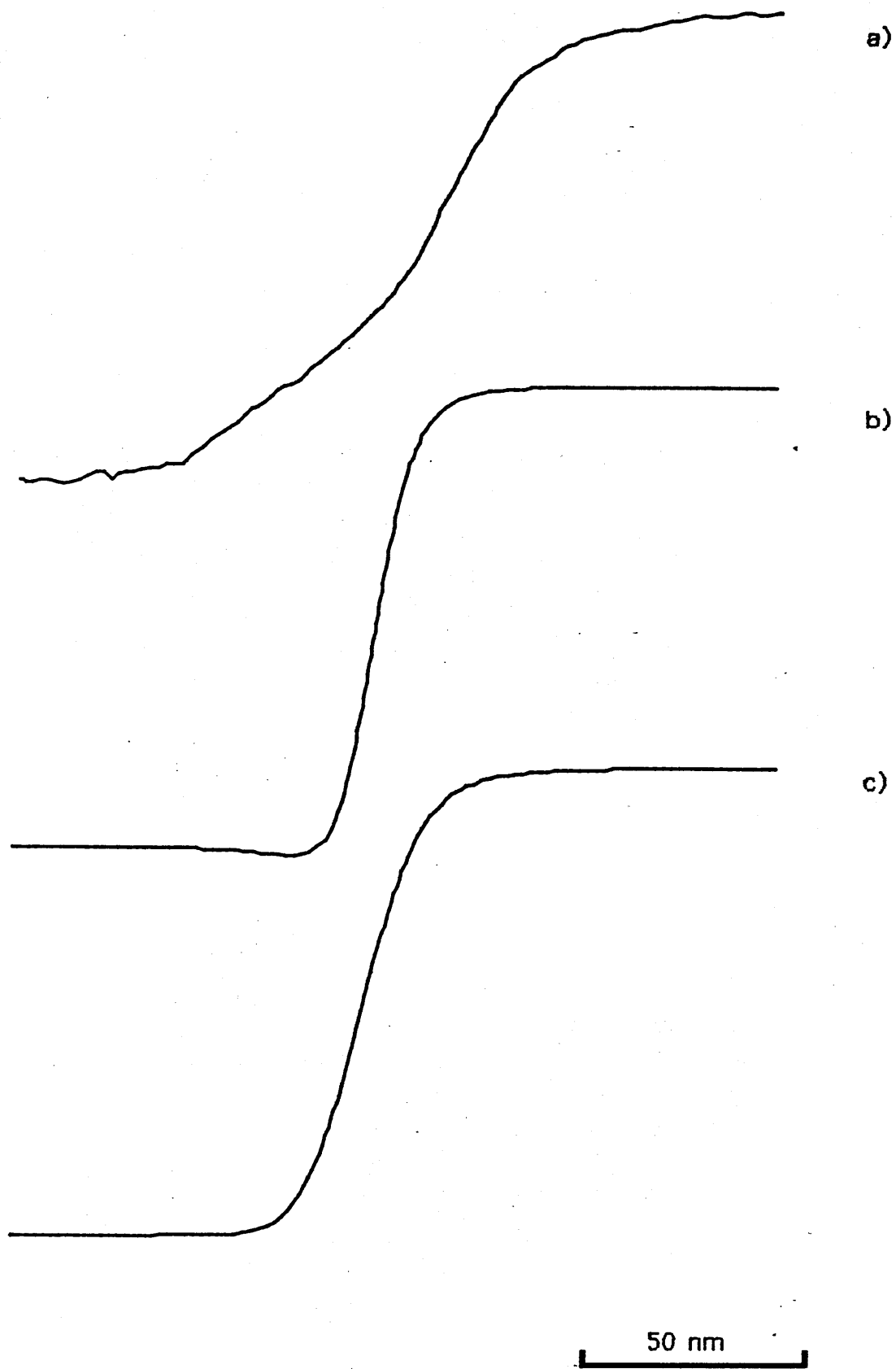


Figure 3.12: a) Experimental DPC domain wall profile from of a cobalt film; b) Theoretical variation of in-plane component of magnetisation (following Jakubovics 1966); c) Theoretical DPC image of b) using standard HB5 DPC imaging conditions.

microscope have to be taken into consideration if this is to be compared with the experimentally measured profile. This was done using a 2D image calculation program and the result is shown in figure 3.12 c). The wall profile in figure 3.12 a) was obtained using condenser 2 as the probe forming lens and the 100 μ m SAD aperture as the probe forming aperture, hence the spherical aberration coefficient was 195m, and the probe half angle was 5.3×10^{-4} rad. In the image calculation program the array size together with the range of spatial frequencies used and the real dimensions of the object being considered, are related to the probe half angle through the following equation:

$$\lambda/\alpha_0 = (\text{XSIZE}/\text{ISIZE}) \times 2 \times \text{FLIM}$$

where λ is the electron wavelength (3.7pm for 100keV), XSIZE is the size of the object in real space, ISIZE is the size of the array used, and FLIM is the range of reduced spatial frequencies to be considered (usually FLIM = 2, i.e. frequencies between $\pm 2\alpha_0/\lambda$ are considered).

The maximum size of array that could be used was 128x128, a larger array size would have required much longer computing times due to the Fourier transforms involved. Therefore, to set α_0 to 5.3×10^{-4} rad, XSIZE was chosen to be 223nm. The dimensionless spherical aberration, C, was set to 1.04 (i.e. $C_s = 4C\lambda/\alpha_0^4 = 195\text{m}$), and the defocus was set to the Scherzer defocus condition, i.e. $D = \sqrt{C} = 1.02$ (once again, D is dimensionless, the actual defocus $z = 2\lambda D/\alpha_0^2 = 26.9\mu\text{m}$) to match the conditions used in the microscope.

It can be seen from figure 3.12 that the value of b calculated by Jakubovics is much smaller than the experimentally measured value. This suggests that the model used by Jakubovics, which has only one variable parameter, is too simplistic to be able to describe domain walls in a material with as strong an anisotropy as cobalt. Sekiguchi *et al* (1985) have also measured domain wall profiles in cobalt using DPC imaging, in this case in a 260nm thick film, and have found that the

measured domain wall width is larger than that predicted by theory (34nm as opposed to a predicted 16nm). They suggest that a 2D wall model, such as those proposed by La Bonte (1969) with some degree of flux closure may be more appropriate in this type of film rather than the 1D Bloch type wall assumed in these calculations.

3.6 Summary

In this chapter it has been shown that the dedicated HB5 STEM can provide a complete description of both the physical and the magnetic structure of a thin electron microscope specimen. A cobalt film was chosen to demonstrate the techniques available in the HB5 as this has a relatively simple and well understood magnetic structure. Furthermore it was shown that DPC imaging can provide high resolution information on the variation of magnetisation within a magnetic film which is not available via more conventional electron microscope techniques.

In addition to the crystallographic orientation and the magnetic structure of a thin film, the HB5 can also be used to measure local elemental segregation within a thin film using x-ray microanalysis (Chapman *et al*/1986).

In the following chapters the above mentioned techniques, including x-ray microanalysis, will be used to study the magnetic and physical structures of both Co-Cr artificial superstructures and CoCr alloys. The interest in these materials is due to their promise as high density perpendicular magnetic recording media. An understanding of the mechanism behind the perpendicular anisotropy in these materials will aid in the optimisation of the properties of materials for perpendicular magnetic recording.

CHAPTER 4

MAGNETIC STRAY FIELD MAPPING

4.1 Introduction:

Magnetic stray fields were investigated in this work for the following two reasons:

1) In magnetic recording systems, the play back signal originates from a current induced in the play back head by the magnetic stray fields above the surface of the magnetic recording media. It is therefore, the stray field distribution, rather than the actual magnetic structure within the magnetic recording media, which is of most importance.

2) In some materials, in which the magnetic domains are very small, and are of approximately the same size as the major topographic features (e.g. crystallites), it can be very difficult to image the domains, even using high resolution Lorentz microscopy. If the stray fields due to the magnetic structure within such a film can be measured then an estimate of the domain structure can be obtained. Cross-sections of CoCr alloys present this problem and these are dealt with in chapter 7.

In this chapter the method by which the stray fields are measured will be described with reference to a cobalt film, and the magnetic stray fields from written tracks on magnetic recording material will be discussed.

As stated in chapter 2, the DPC signals produced in the HB5 are proportional to the in-plane components of magnetic induction, integrated along an electron trajectory. Therefore, using two DPC images corresponding to two orthogonal components of in-plane induction, it is possible to measure the in-plane component of stray field distributions emanating from the surfaces of specimens in the electron microscope. Other techniques of Lorentz microscopy can be used to study stray field distributions, for example, type I contrast in

the SEM (Jakubovics 1975); or the use of an SEM equipped with a 2D charge coupled device situated after the specimen, as proposed by Elsbrock and Balk (1984). However neither of these techniques are capable of the spatial resolution of $\sim 10\text{nm}$ which DPC imaging in the HB5 can achieve. Electron holography has also been used to study stray fields, with high spatial resolution (Yoshida *et al* 1983). In this technique, however, images have to be recorded photographically, Computer analysis is therefore a lengthy procedure involving the digitisation of micrographs. DPC images on the other hand can be recorded directly into a computer frame store, thereby allowing immediate computer analysis.

4.2 Stray Fields From A Cobalt Foil

In chapter 3 it was shown that the domain structure of a polycrystalline cobalt foil, in which the crystallite size is much greater than the domain size, is quite simple. For crystallites in which the c-axis lies close to the plane of the film the domains are large with the domain walls parallel to the magnetisation vector and the c-axis. At the edges of the film where the magnetisation vector is not parallel to the film edge large stray fields are present. Figure 4.1 shows such a case in which the magnetisation vector within the sample is at approximately 90° to the film edge; the arrows show which component of induction is mapped in each DPC image. The stray fields are very obvious in this figure and it can be seen that the magnitude of the stray field decreases with distance from the film edge, and that there is a continuous variation of the stray field along the film edge.

Since these two DPC images are maps of two orthogonal components of in-plane magnetic induction, it should be possible to use them to obtain the magnitude and direction of the stray field at each point in the image. A vector map of the stray field distribution in figure 4.1 is shown in figure 4.2(a). In this case the lengths of the arrows are proportional to the logarithm of the in-plane magnetic induction. This map was produced from the images in figure 4.1 using Fortran

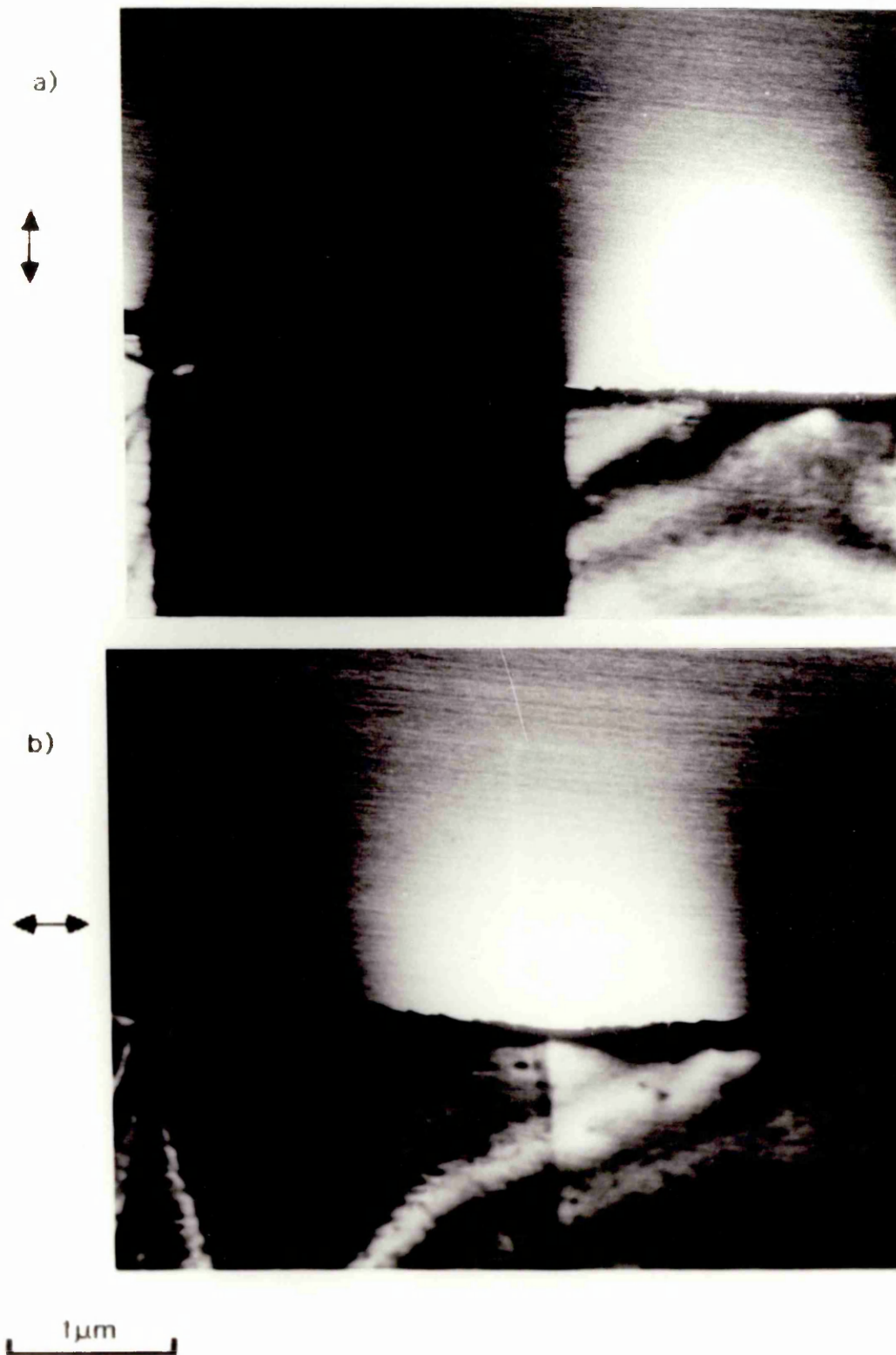


Figure 4.1 DPC images showing the domain structure within, and the stray fields outside a cobalt film. The component of magnetisation to which each image is sensitive is given by the arrow next to that image.

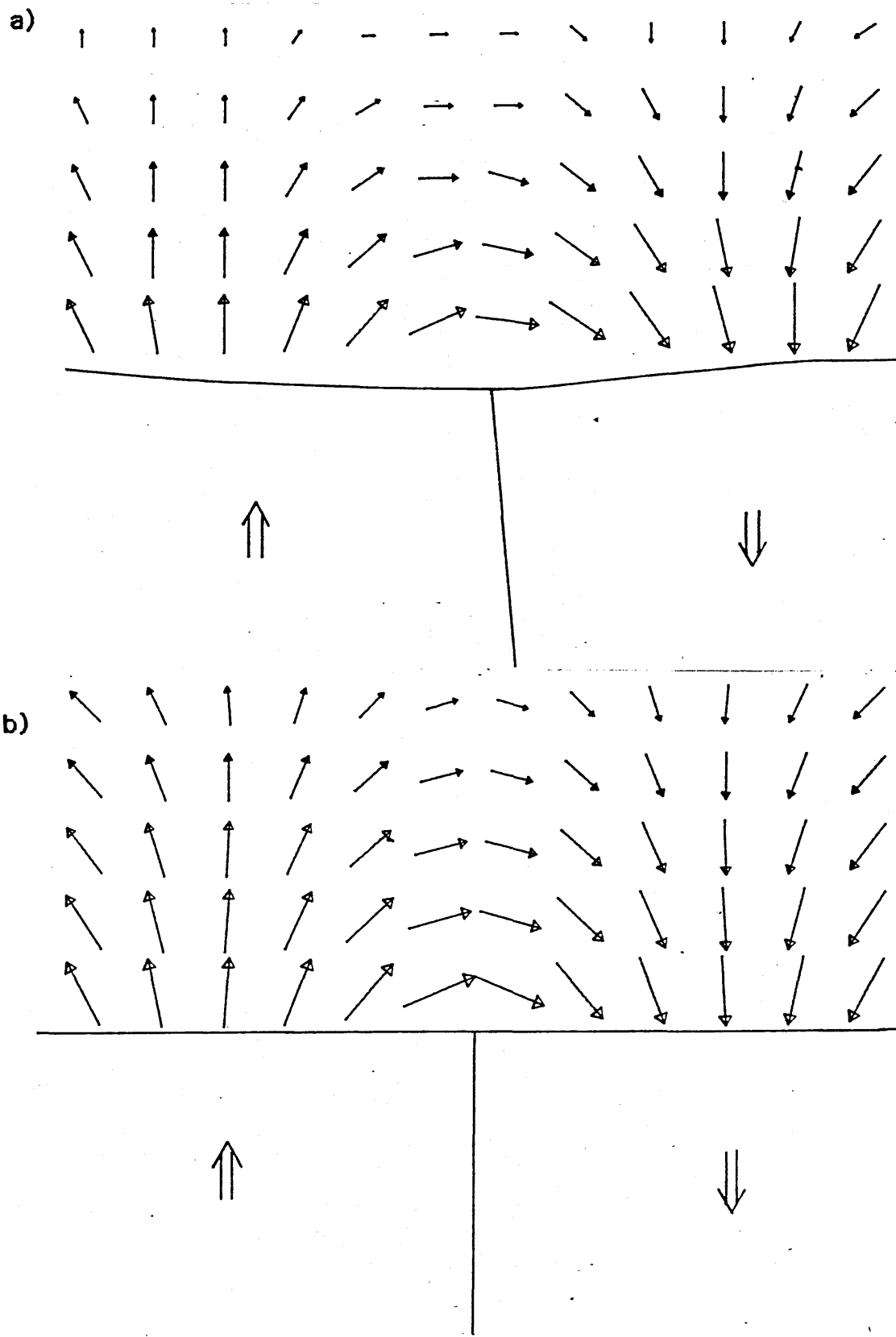


Figure 4.2 a) Vector map of the stray field beyond the edge of a cobalt film, b) vector map of the theoretically calculated stray field from the domain structure in figure 4.4. In both cases the length of the arrows is proportional to the logarithm of the in-plane component of induction

programs on the Toltec computer system as described below.

Production of vector maps from digitally acquired images:

To produce a vector map of the stray field distribution two images, corresponding to x- and y-components of in-plane magnetic induction have to be obtained using the Toltec computer system. In order to reduce the noise in the image due to fluctuations of the current from the field emission tip in the electron microscope, a long pixel dwell time is used. Under computer acquisition, pixel dwell times of between $1 \times 5 \mu\text{s}$ and $255 \times 5 \mu\text{s}$ are available. In this work a dwell time of $149 \times 5 \mu\text{s}$ was used, which together with a processing time per line of 30ms gave a total acquisition time of 220ms per line. A line acquisition time which is a multiple of 20ms is desirable as this reduces as far as possible the effect of mains frequency pick up. It is in theory possible to remove the noise due to the field emission tip by dividing the DPC images by the bright field image formed by summing the four quadrant signals. However this bright field image has to be acquired simultaneously with the DPC image that is being divided by it, and unfortunately the Toltec computer system does not allow this to be done.

Once the two DPC images corresponding to the x- and y-components of in-plane induction have been stored in the computer frame store they can be easily accessed using a Fortran computer program called VMAP. This program calculates, from the pixel intensity in the images, the magnitude and sign of both components of induction at regularly spaced intervals across the images. This is done, for each component, by comparing the pixel intensity, averaged over an $N \times N$ square (N being a power of 2 entered by the user), with a pixel intensity corresponding to zero in-plane induction for that component. This value is then associated with the pixel in the centre of this $N \times N$ square. Figure 4.3 shows the type of grid used, the numbers in each square indicate the order in which the values are obtained. To make maximum use of the pixel grey levels available, the system gain

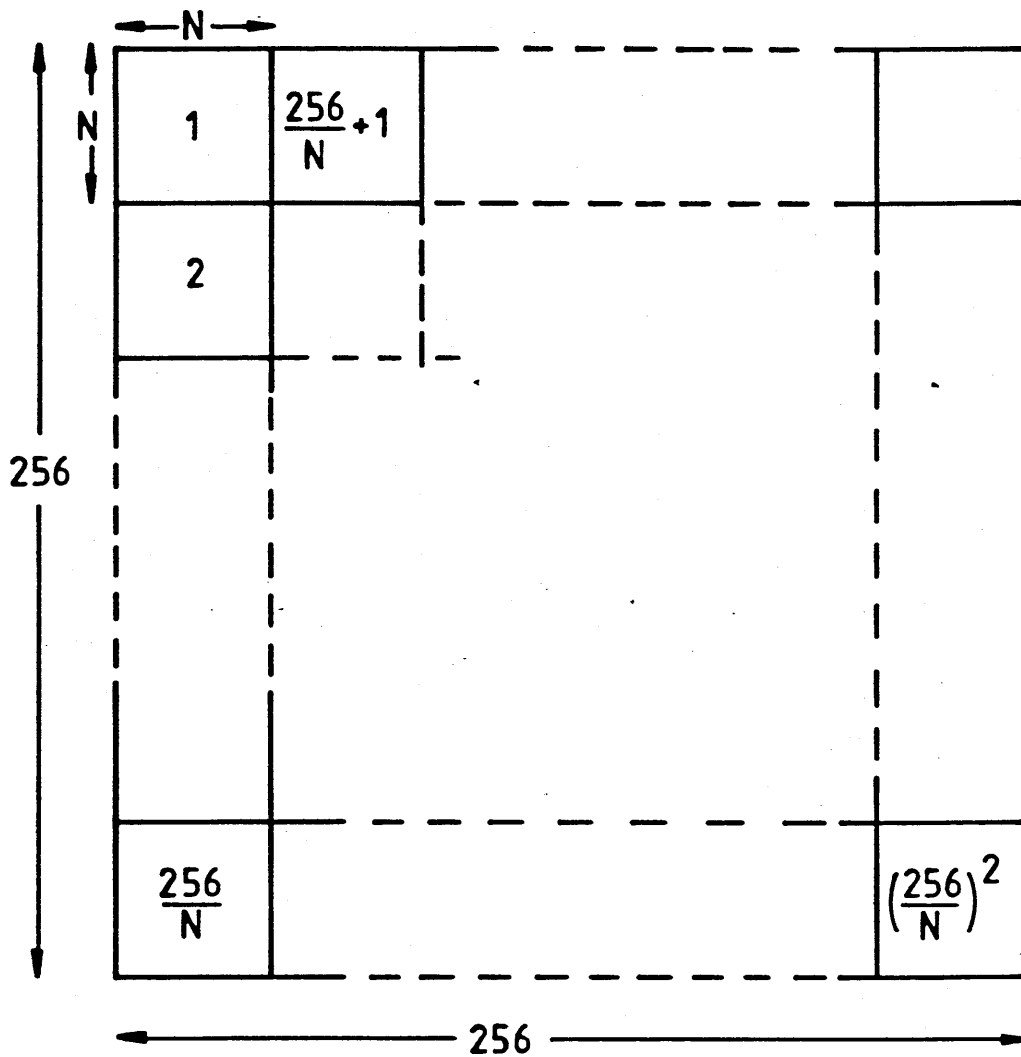


Figure 4.3 Grid of squares in which the average pixel intensities are calculated. The number in each square corresponds to the order in which the averages are stored.

is chosen so that the darkest and brightest areas of stray field correspond to pixel intensities just above 0 and just below 255 respectively. In this case the zero grey level intensity is ~ 128 . The actual value for any specific image can be entered into the program by the operator, or if the image is suitable, it can be obtained automatically by the program (a suitable image is one in which there is an equal amount of light and dark areas as the routine used simply takes the average pixel intensity over the whole image as the zero grey level). Once the x- and y-components of in-plane induction have been obtained, the magnitude and direction of the in-plane magnetic induction vector at the centre of each of the grid squares is calculated, and all this information is then written out to disc. (N.B. the x- and y-axes in this case form a LEFT handed coordinate system).

A hard copy of the information stored to disc by VMAP can be obtained in the form shown in figure 4.2 using a program called DRMP. This reads in the information filed by VMAP and plots out, on either A3 or A4 paper the type of arrow plot shown in figure 4.2 where each arrow corresponds to the average in-plane induction vector at that point in the image. The arrows corresponding to the entire image can be plotted, or a subset which corresponds to a specific area of the image. This is useful if some parts of the image contain intensity variations which are not due to stray fields but to, for instance, amplitude contrast.

To enable a large range of induction values to be displayed, the logarithm of the magnitude of the in-plane induction can be plotted. This is done using a program called LOG1 which reads the data produced by VMAP, takes the logarithm of it and writes it back to disc in the correct format for DRMP to read.

Listings of VMAP, DRMP and LOG1 are contained in appendix A.

Comparison with theory:

Figure 4.2(b) shows a theoretical calculation of the stray fields from the regular domain structure shown in figure 4.4. For this

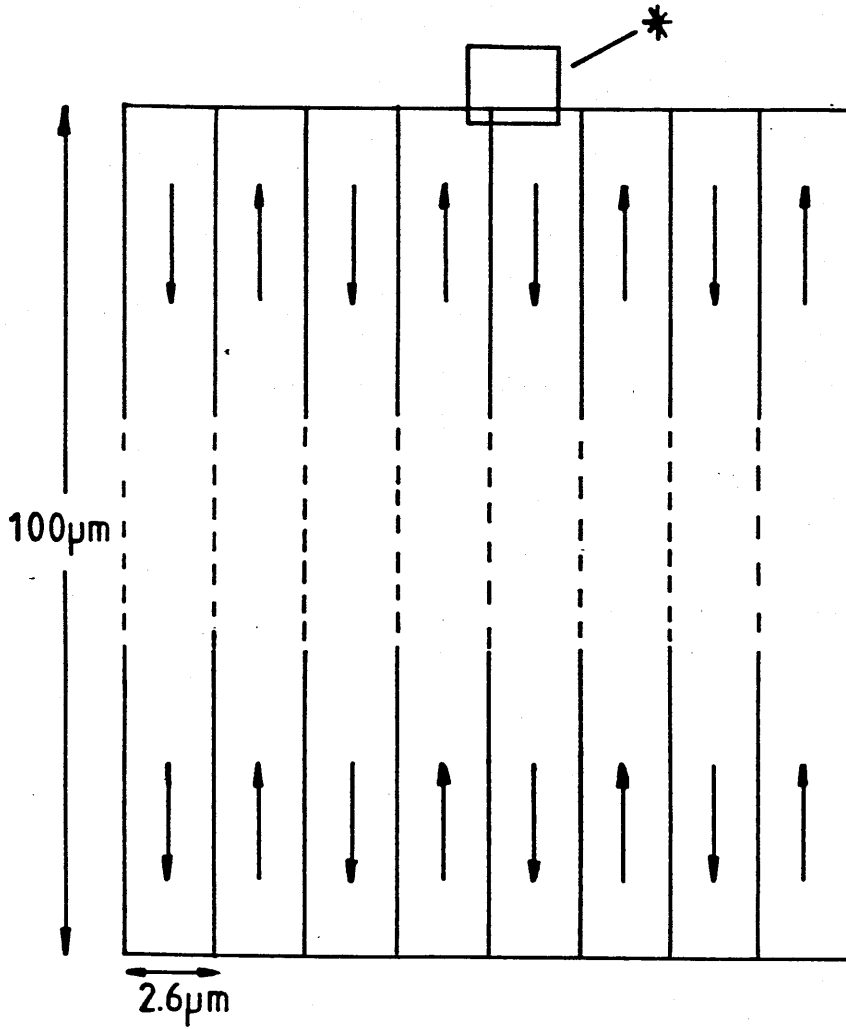


Figure 4.4 Domain structure used in theoretical calculation of stray fields. The small box marked * denotes the area plotted in figure 4.2 b)

calculation the domains were assumed to be uniformly magnetised along the $\pm y$ direction. Although in the actual sample the magnetisation did not lie in the plane of the film, the angle between the magnetisation and the film plane was small enough for the cosine of the angle to be approximately 1, therefore the above assumption is valid. The film thickness was taken to be 35nm throughout, which was the thickness, determined by the split spot technique, at the edge of the sample in figure 4.1. The domain width was taken to be $2.6\mu\text{m}$ which is the same as that of the domains in figure 4.1. Although the actual sample increased in thickness away from the edge, and the edge itself was not straight for a full eight domains, the structure in figure 4.4

is an idealisation of that in figure 4.1. A simple, regular domain structure has to be used in the calculation if the integrals used in calculating the stray field are to be solved (Rhodes and Rowlands 1952-55). The choice of $100 \times 20.8 \mu\text{m}$ for the dimensions of the block was to reduce edge effects due to the finite size of the block; these effects were absent in the actual sample since there was a large area of magnetic material on the three sides of the domains in figure 4.1.

It can be seen from figure 4.2(b) that the stray field distribution measured using DPC imaging is very similar to that calculated using the structure in figure 4.4. This close agreement shows that the technique described does allow the direct measurement of stray field distributions, and that these agree with calculated stray field distributions in the simple cases where these calculations can be carried out.

Sensitivity limit of technique:

The sensitivity of this technique is, in theory, limited by the noise in the semiconductor quadrant detector. However, as stated earlier this is only true if the DPC images can be normalised using a bright field image, which has been acquired simultaneously, to remove the effect of fluctuations in the probe current. As this cannot be done on our machine at present, it is this tip noise which limits the sensitivity

of the technique.

By taking two DPC images of a region of field free space, using the same conditions as those used for acquiring stray field images, the fluctuation in pixel intensity due to the tip noise can be obtained, as can the pixel intensity which corresponds to zero in-plane induction for the two in-plane components. For the conditions used in acquiring the images for the map in figure 4.2(a) the standard deviation of the pixel intensity in field free space was found to be 1.3 pixel intensity levels. Therefore a change in pixel intensity of ≥ 3 grey levels due to stray fields should be detectable above the background noise.

In the images used to calculate the map in figure 4.2(a) the difference in pixel grey level intensities between the darkest and brightest areas of stray field was ~ 200 . This corresponds to twice the Lorentz deflection angle, β_L , which for 100keV electrons and a 35nm thick cobalt film of saturation magnetisation 1.8T (i.e. 63Tnm) is $57\mu\text{rad}$. Therefore the limit of sensitivity imposed by the current fluctuations of the field emission tip corresponds to $< 2.2\text{Tnm}$ which is the equivalent to the integrated flux through a 1.2nm thick Co film (for 100keV electrons this would give a deflection angle of $2\mu\text{rad}$).

4.3 Stray Fields From Written Tracks On Magnetic Recording Material

In longitudinal magnetic recording materials, information is stored as a variation of the in-plane, longitudinal component of magnetisation, as shown in figure 4.5(a). Conventional materials used for this type of recording have a strong magnetic shape anisotropy holding the easy axis in the plane of the magnetic recording disc or tape. Ideally the easy axis should also be constrained to point along the length of the recording track, which for a magnetic recording disc is in the tangential direction. This orientation of the easy axis helps to sustain the head-on domain structure of longitudinal recording. This head-on domain structure produces large stray fields above and below the recording material, as shown schematically in figure 4.5(b), and it is these stray fields which are detected by the play back head.

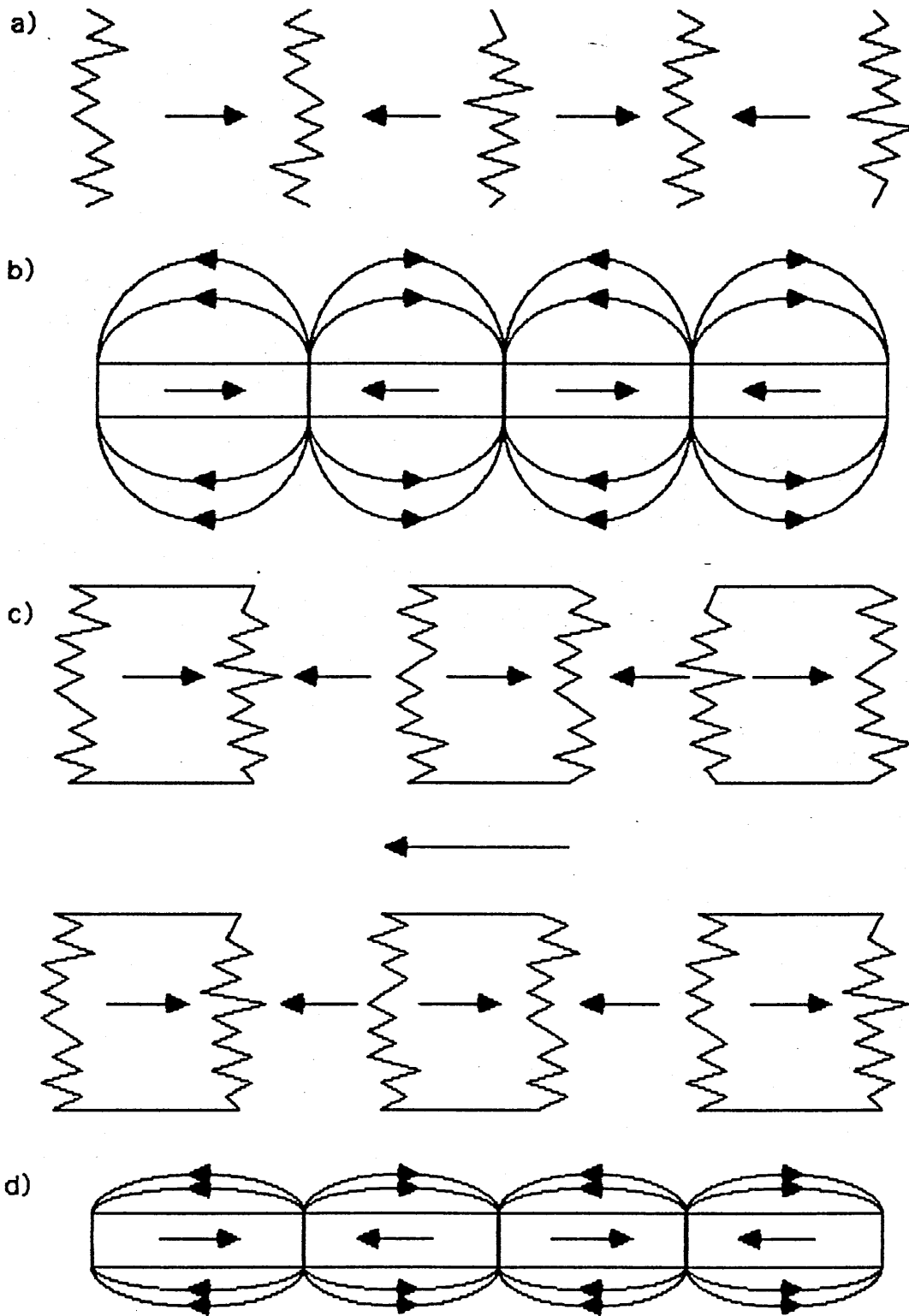


Figure 4.5 a) Domain structure in longitudinal magnetic recording media, b) Expected stray field distribution from domain structure in figure a), c) Reverse magnetisation domains in an otherwise dc magnetised film, d) Possible stray field distribution from high density recording media.

In this section the stray fields from written tracks on a commercial 14 inch diameter hard disc are investigated. Electron microscope specimens were provided by IBM Research Laboratories in San Jose, California, and the methods used to obtain these thin film specimens from the hard disc are described in detail by Ferrier *et al* (1983). The active magnetic layer of the hard disc was a 30nm thick $\text{Fe}_{42.5}\text{Co}_{42.5}\text{Cr}_{15}$ layer, with a saturation magnetisation, M_S , of 1.28T and a coercivity of ~ 500 Oe. The tracks, written on the disc, were 25 μm wide and were written with a thin film inductive head flying at either 160 or 260nm. The disc was first dc erased by using a saturation write current to magnetise the disc in one direction, and bit patterns were then written on it at a range of spatial frequencies up to 1180 flux reversals per mm. This produced a bit pattern consisting of reverse domains on an otherwise uniformly magnetised disc as shown in figure 4.5 c).

Figure 4.6 shows an example of both the written tracks within the magnetic recording material, and the stray fields produced by this type of domain structure. The top two micrographs in this figure are DPC images showing two in-plane components of induction. The third micrograph is a bright field image, and on this striations running parallel to the film edge can be seen. These are produced by the replication in the FeCoCr layer of the tangential polishing marks on the hard disc substrate. This structure, introduced to assist the recording head flying characteristics, helps to some extent to hold the easy axis of magnetisation in the film in the tangential direction. Also shown in figure 4.6 is a vector map plot of the stray fields from this domain structure produced using the vector map programs described above.

The stray fields in these DPC images appear in strong contrast compared to the magnetic domain structure itself; this is due in part to the decrease in the beam current due to scattering in the specimen. An important reason however is the fact that there are stray fields above and below the magnetic domains and in these the magnetic induction points in the opposite direction to that in the domains. This

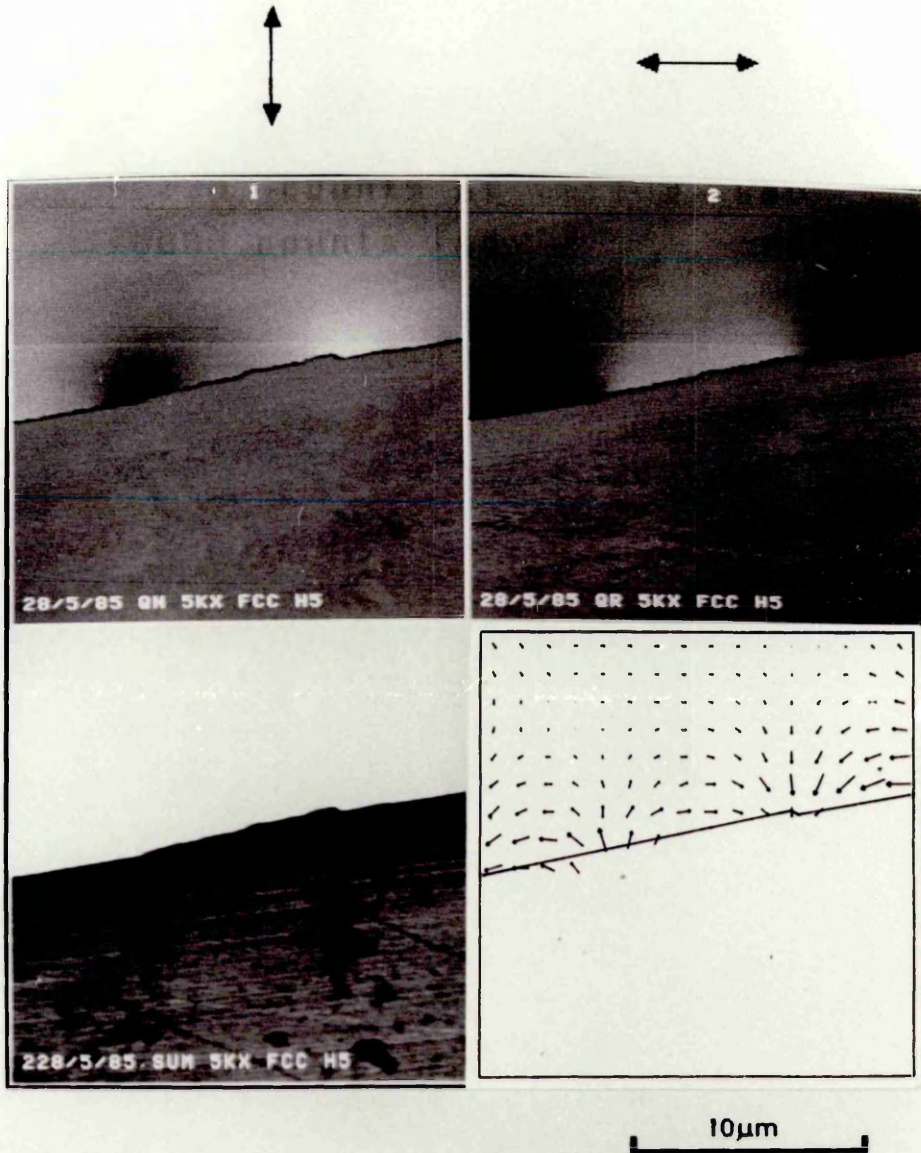


Figure 4.6: Stray fields from the edge of a written FeCoCr longitudinal magnetic recording material. The top two micrographs are DPC images sensitive to two orthogonal components of in-plane induction. The lower micrograph is a bright field image of the same area and the arrow diagram is a vector plot of the magnetic stray fields.

reduces the contrast of the DPC images since the net magnetic induction, integrated along an electron trajectory, is greatly reduced. The uniformity of magnetic contrast across the domains in these images indicates that the magnetic flux, in the stray fields, above the film is almost parallel to the surface as shown in figure 4.5 d) rather than as shown in figure 4.5 b) (Ferrier 1986). In addition, the low level of contrast indicates that most of the flux within the recording material is following a return path outside of the film and will thus contribute to the readback process. The strong contrast at the edge of the film is due to electrostatic and diffraction effects and not to any magnetic structure.

In figure 4.6 the individual bits (domains magnetised in one direction or the other) are separated by zig-zag magnetic domain walls. It has been suggested that the zig-zag nature of these walls leads to random noise in the readback process and that this may ultimately limit the recording density obtainable with longitudinal magnetic recording. However the exact effect of the zig-zags is difficult to judge as the stray fields are, because of the lack of magnetic poles in the stray field region, necessarily smooth functions.

The stray fields imaged in figure 4.6, although of the same periodicity as those above and below the film, are not the actual stray fields detected by a magnetic recording head. A closer approximation to the fields above and below the film can be seen in a region of specimen in which the film is folded back on itself; figure 4.7 shows such a region. It should be noted however that the stray field above a magnetic recording track is determined by the entire domain structure across the width of the recording track, and in a region such as that shown in figure 4.7, the elements contributing to the stray fields are not in the same spatial relationship as they would be in a magnetic recording disc.

Once again the top two micrographs in this figure are DPC images showing two components of in-plane induction, and the third micrograph is a bright field image. The fold in the film can be quite

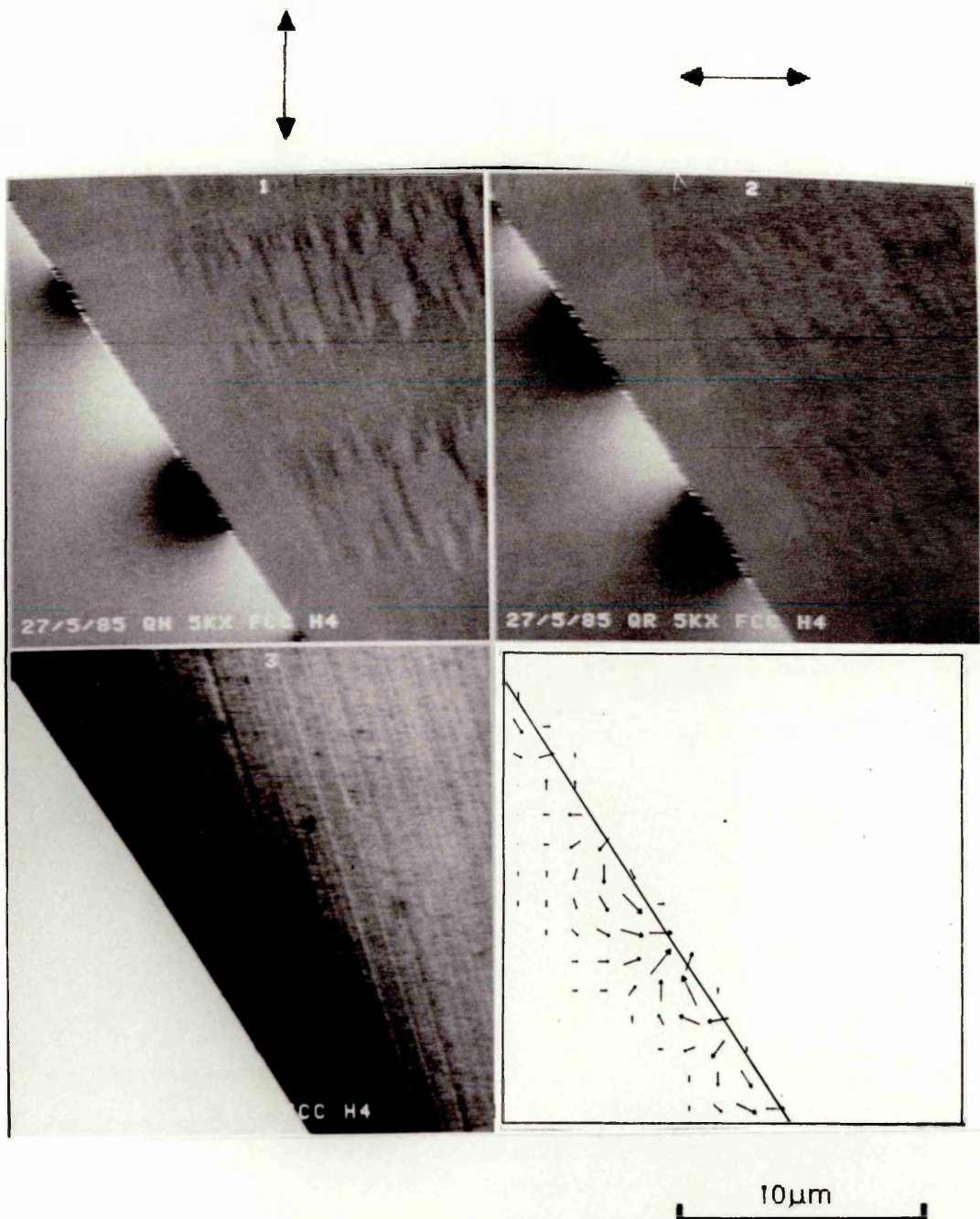


Figure 4.7: Stray fields from a fold in a written FeCoCr longitudinal magnetic recording material. The top two micrographs are DPC images sensitive to two orthogonal components of in-plane induction. The lower micrograph is a bright field image of the same area and the arrow diagram is a vector plot of the magnetic stray fields.

easily seen as the dark area in the bright field micrograph. Small bright "spikes" seen at the film edge in the DPC images are due to extraneous electrical pick up during the imaging process and not to any magnetic effect. The reverse direction magnetic domains in this part of the film do not extend all the way across the written tracks, but consist of a series of isolated island domains across the width of the track. Moreover these domains have smaller dimensions in the track direction than the oppositely magnetised domains. Both of these facts indicate that the write current used was not strong enough to saturate the material in the reverse direction. Tong *et al* (1984) have investigated the effect of the domain structure in these films on the readback signal. They found that this structure lead to an asymmetry between positive and negative readback pulses. It can be seen from the stray field distributions in the DPC micrographs of figure 4.7 that the darker regions, which correspond to the stray fields from the reverse domains, have a smaller linear extent than the stray fields from the saturated domains. This agrees with the results obtained by Tong *et al*, where the asymmetry in the readback signals is caused by the asymmetry in the magnetic field distributions associated with domains magnetised in opposite directions. From the domain contrast in figure 4.7 it can be seen that the stray fields from the reverse domains does not extend along the full width of the track, but has gaps in it between the island domains. This adds to the asymmetry in readback signals from the two domains.

4.4 Conclusions

In the first part of this chapter, it was shown using a cobalt film that it is possible to map magnetic stray field distributions beyond the surfaces of thin films using DPC imaging. The technique has a spatial resolution of $\sim 10\text{nm}$ and it has been shown that it can detect stray fields corresponding to $< 2.2\text{Tnm}$. This value of sensitivity should however be taken as a typical value, as the current fluctuations from a

field emission tip can vary markedly over a tip lifetime. The cobalt film used had a simple magnetic domain structure, and the experimental results obtained from this film agree well with theoretical calculations of the stray fields from such a domain structure.

This technique is a powerful tool for the investigation of the effect of domain structure on the readback properties of longitudinal magnetic recording media. It was seen that, where the write current used was below optimum, the reverse bits consisted of individual island domains rather than one single domain across the full width of the track, and that the stray field distributions associated with the reverse domains were less extensive than those from the saturated regions of the foil.

This technique should allow the stray fields from high density, longitudinal magnetic recording tracks to be investigated with a view to determining how the stray field distribution changes as the bit size decreases. This should be of most interest in materials such as the FeCoCr studied here, where there is a strong magnetic anisotropy holding the magnetisation in the tangential direction even at very small domain widths.

CHAPTER 5

MAGNETIC AND PHYSICAL STRUCTURE OF Co-Cr FILMS FOR MAGNETIC RECORDING

5.1 Introduction

Recently, interest has focussed on the possibility of using perpendicular recording to increase the amount of information that can be stored on a given area of magnetic disk. For a material to be of use in a perpendicular magnetic recording system, it must have an easy axis of magnetisation along the film normal. A number of artificial superstructures made up of thin, alternate layers of non-magnetic and ferromagnetic materials have been shown to possess sufficient perpendicular anisotropy for the easy axis to lie along the film normal.

In addition to artificial superstructures, various thin film alloys have been shown to have sufficient perpendicular magnetic anisotropy for the easy axis to lie along the film normal: FeNdTi (Tsutsumi and Sugahara 1984), TbCo (Yoshino *et al*/1984), HoCo (Suzuki *et al*/1984). However, the material which has shown most promise is sputtered, thin film, CoCr.

Initially proposed by Iwasaki and Nakamura (1977), thin film CoCr alloy is now being used in perpendicular magnetic recording systems. The CoCr alloys of interest are polycrystalline and have a strong columnar microstructure aligned with the film normal. The crystal structure of these films is that of hcp cobalt, and the c-axis of the crystallites is not randomly distributed, but has a large degree of alignment with the film normal. In polycrystalline CoCr there is a strong magnetocrystalline anisotropy along the c-axis. Therefore, this c-axis orientation, together with the columnar structure, may allow a perpendicular magnetic domain structure to be sustained. The columns themselves may be magnetically decoupled from one another by Cr rich column boundaries, and this will be discussed in chapter 6.

Three artificial superstructure films have been investigated in this work, and these will be discussed in section 5.2 of this chapter. In addition to the artificial superstructures, the physical microstructure in sputtered CoCr thin film alloys, produced at different substrate temperatures and varying in thickness from 40nm to 80nm, was investigated. The magnetic domain structures of the films were also investigated and this will be discussed with reference to the physical microstructure, and the conditions used during manufacture.

5.2 CoCr Artificial Superstructure Films

Shinjo *et al* (1986) have reported that thin films composed of alternate ferromagnetic and non-ferromagnetic layers can have the easy axis of magnetisation along the film normal. They found that for very thin Fe layers, i.e. less than 1nm thick, sandwiched between Mg layers the easy axis of magnetisation within the Fe layers lay close to the film normal. Similar results have been presented for other multilayer structures (Shinjo *et al*/1986).

Three artificial superstructure films were investigated in this work, and these were provided by IBM Research Laboratories in San Jose, California. The films had the following compositions:

- 1) 6nm Cr /2nm Co /6nm Cr
- 2) 6nm Cr /2nm Co /1.4nm Cr /2nm Co /6nm Cr
- 3) 6nm Cr /2nm Co /1.4nm Cr /2nm Co /1.4nm Cr /2nm Co /6nm Cr

Where the Co is the ferromagnetic component and the Cr is the non-ferromagnetic component.

Crystal structure:

Figure 5.1 shows a typical diffraction pattern, from one of the these films. It can be seen, from the fact that this is a ring pattern, that the films are polycrystalline. The diffraction patterns from all three films contained rings corresponding to both hcp Co and bcc Cr.

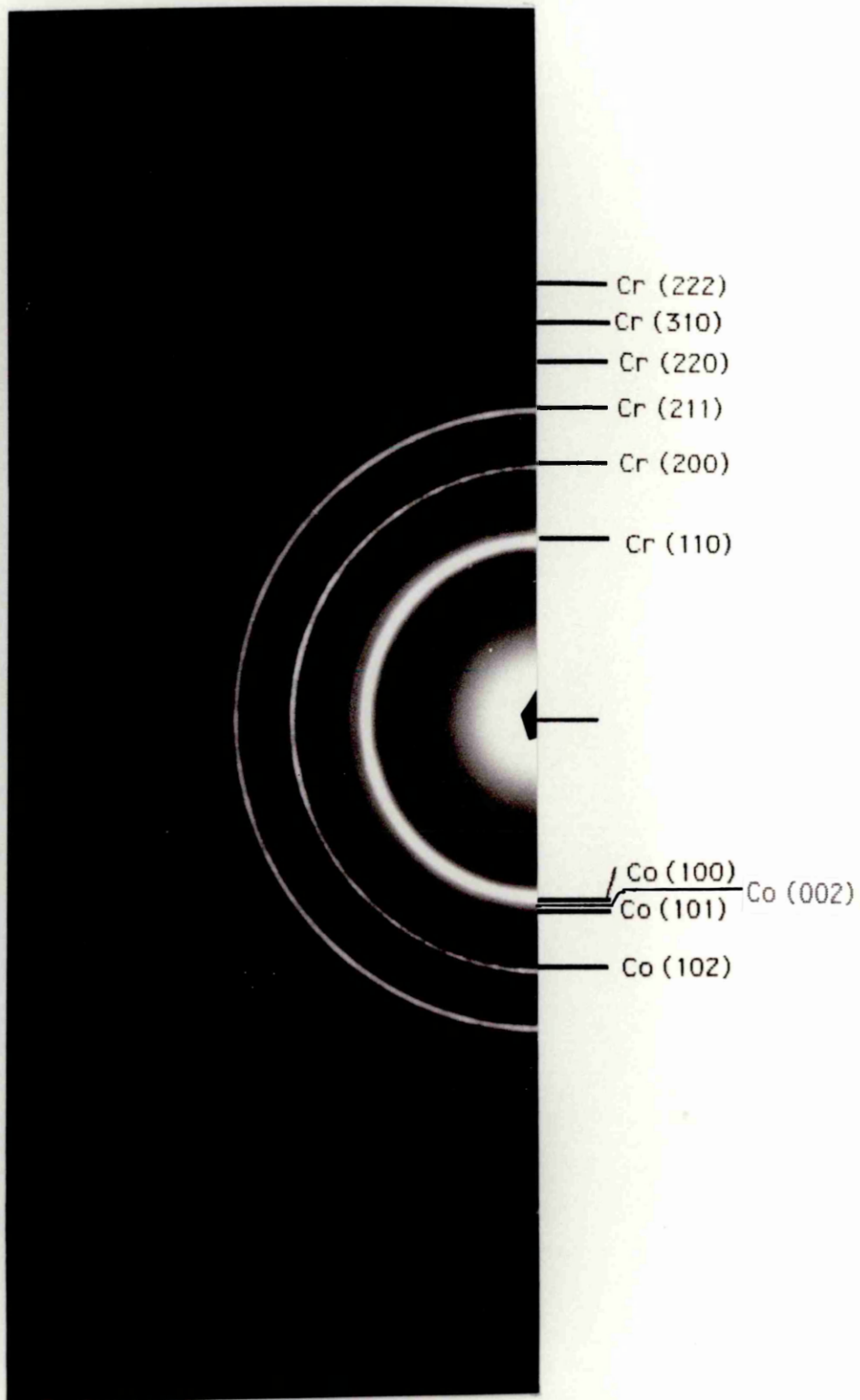


Figure 5.1: Typical selected area electron diffraction pattern from an artificial superstructure film.

This indicates that the Co and Cr layers have remained separate from each other, at least over most of the layer thickness. The first six Cr reflections are present in the diffraction pattern, i.e. there are no preferred directions of crystal growth within the Cr layers. However some of the Co reflections appear to be missing. The Co (101) reflection, which is the strongest Co reflection, is present but the (002) and (004) reflections are missing (or too faint to be seen). This indicates that there is some degree of c-axis orientation within the Co layers. The (100) reflection also appears to be missing, although this is a very weak reflection compared to the other two, and may be present but too faint to be seen.

All of the Co diffraction rings are quite weak; however this is to be expected, as the thickness of Co (6nm or less) is much less than the thickness of Cr in each sample.

Magnetic structure:

No magnetic domains were seen in any of these films; however, magnetisation ripple was seen in films 1 and 3. No magnetic structure at all was seen in film 2.

Figure 5.2 a) is a Fresnel image of film 1, showing magnetisation ripple within the film, figure 5.2 b) is an in focus image of the same area. This type of structure is also typical of that seen in film 3. In both films there was a slight directionality to the ripple structure. This can be seen in figure 5.2 a), where the ripple is running generally from top left to bottom right. The existence of magnetisation ripple but no domain structure within these films indicates that, although these films are ferromagnetic, there is no strong easy axis direction in the film plane. It may be that there are domain walls in these films, but that as the magnetic material is very thin the contrast is consequently very weak. Another possibility is that domains in alternate magnetic layers are oppositely magnetised reducing the net deflection of the electron, integrated along a trajectory. However, the DPC technique has been shown to be very sensitive; therefore it is unlikely that there

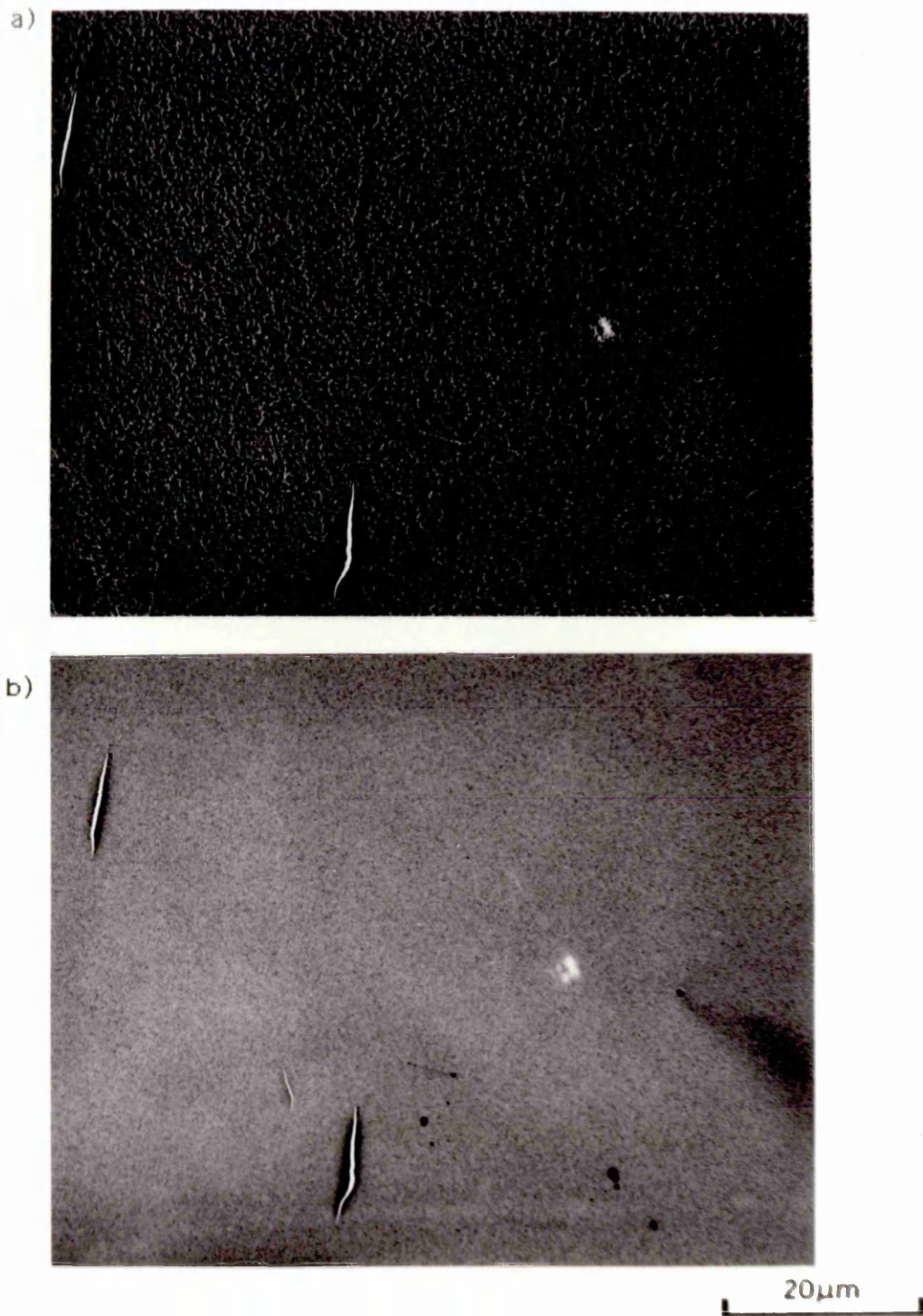


Figure 5.2: a) Low magnification Fresnel image showing magnetisation ripple in film 1, b) infocus image of the same area.

is a significant in plane domain structure within these films.

Figure 5.3 shows two DPC images of film 3 untilted (a and b) and two DPC images of the film tilted by 45° about the axis shown (c and d). The area of film in the two cases is slightly different due to the difficulty in keeping the specimen centred whilst tilting in the HB5. In a and b very little magnetic structure can be seen. However, in c and d the structure is more obvious. This magnetic structure is the magnetisation ripple seen in the Fresnel image of figure 5.2. The component of magnetisation mapped in each micrograph is given by the arrows in the figure.

As was stated in chapter 2, the contrast in a DPC image is proportional to the component of induction perpendicular to the beam, integrated through the specimen thickness. Therefore the low contrast in these four DPC images can be attributed to the fact that the Co is very thin, in this case 6nm. The increase in contrast between the images taken with the film untilted and those taken with the film tilted, indicates that the magnetisation is lying predominantly out of the film plane. The structure in figure 5.3 d) appears narrower than that in 5.3 c), this is due to the fact that tilting about an axis foreshortens features perpendicular to that axis.

Discussion:

In film 2 no magnetic structure was observed, although the diffraction pattern indicated that hcp Co was present in the film. No explanation has been found for this.

In films 1 and 3 magnetisation ripple was observed, and in film 3 the magnetisation was found to lie mostly out of the film plane. The layered structure has, therefore, counteracted the shape anisotropy which acts to keep the magnetisation within the plane of the film. In film 1 this has allowed a magnetisation distribution which is approximately isotropic in three dimensions, to develop, whilst in the case of film 3, there is a weak directionality along the film normal. There is, therefore, no strong easy axis in either of these films and

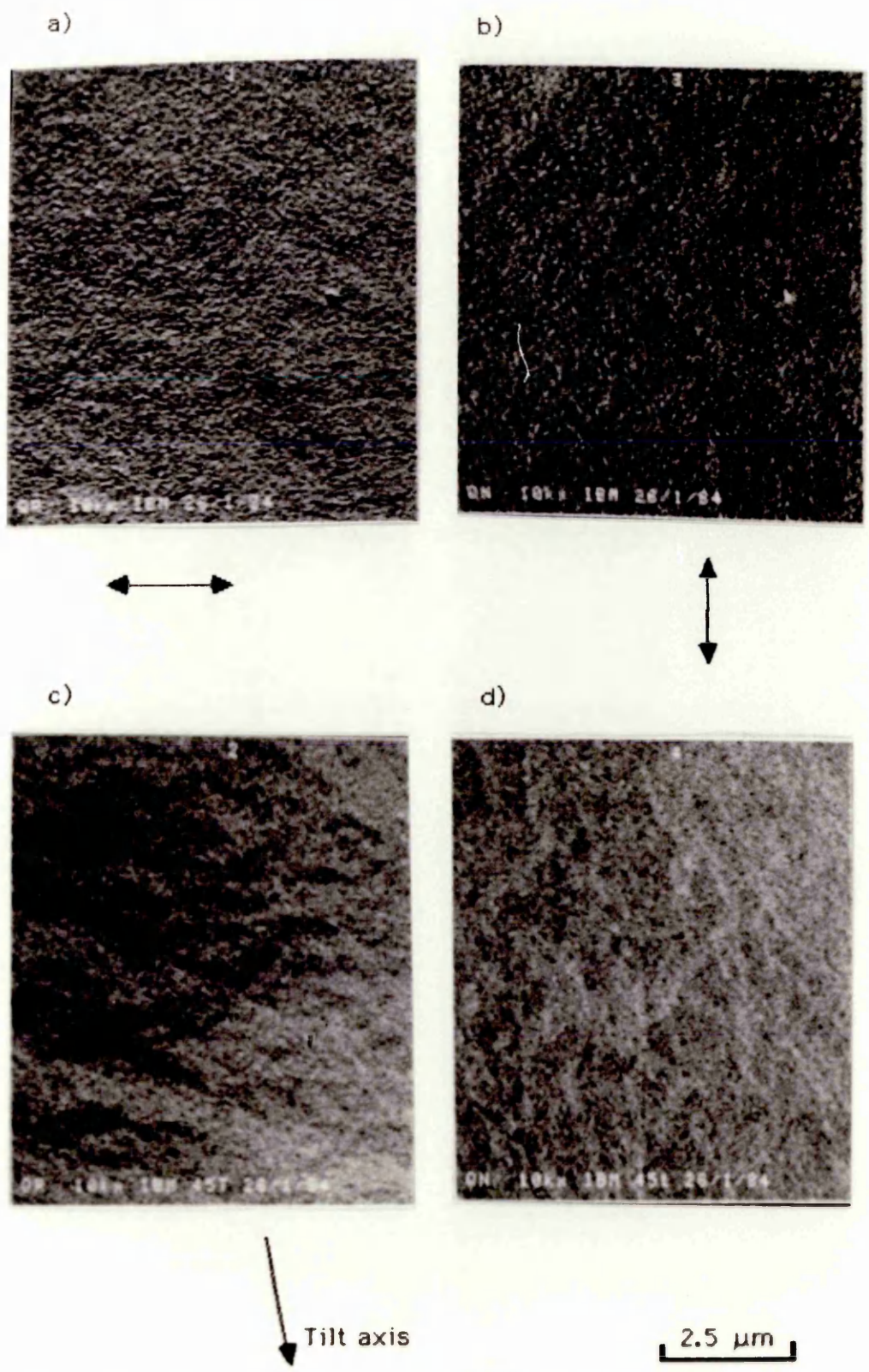


Figure 5.3: a) and b) are two DPC images of film 3 untilted and c) and d) are the corresponding DPC images with the film tilted about the axis shown

the magnetisation direction varies from place to place leading to the magnetisation distribution shown in figures 5.2 and 5.3.

From the above results, it can be seen that as the number of alternate layers is increased the perpendicular anisotropy increases and it becomes easier for the magnetisation to lie out of the plane of the film. The anisotropy developed by the layered structure may be due either to magnetostriction caused by the slight mismatch between the lattice constants of bcc Cr and hcp Co, or to a c-axis texture in the Co layers. Whatever the cause, the Co layers must remain thin if the perpendicular anisotropy is to be maintained, and therefore a large number of layers are required if the film is to have a large magnetic moment.

To progress further in the study of artificial superstructure films it would have been necessary to investigate films with a larger number of alternate layers. As such films were not available, it was decided to concentrate on CoCr thin film alloys. These were provided by Philips Research Laboratories in Eindhoven. The short geographical distance, between Eindhoven and our laboratory in Glasgow, meant that samples could be easily obtained from Philips, and that Philips could respond to requests for different type of samples (e.g. planar films or cross sections of these films). In the next section planar films will be investigated, cross-sections of these films will be discussed in chapters 6 and 7.

5.3 CoCr Thin Film Alloys

The CoCr films investigated here were deposited, onto rock salt substrates, by ion beam sputtering using alloy targets. Two different alloy compositions were used: $\text{Co}_{77}\text{Cr}_{23}$ and $\text{Co}_{75}\text{Cr}_{25}$. The films of composition $\text{Co}_{77}\text{Cr}_{23}$ varied in thickness from 40nm to 160nm, although polycrystalline films of thickness $\geq 150\text{nm}$ are, in general, too thick for investigation by 100keV electron microscopy. Only two films of composition $\text{Co}_{75}\text{Cr}_{25}$ were investigated, and these were both 40nm thick.

Ion beam sputtering, unlike R.F. sputtering, does not generate additional heat in the specimen. Therefore the substrate temperature was easily controlled using resistive heating. One of the 75/25 films was deposited at nominal room temperature and the other at 300°C. The 77/23 films were deposited at a range of substrate temperatures between nominal room temperature and 300°C.

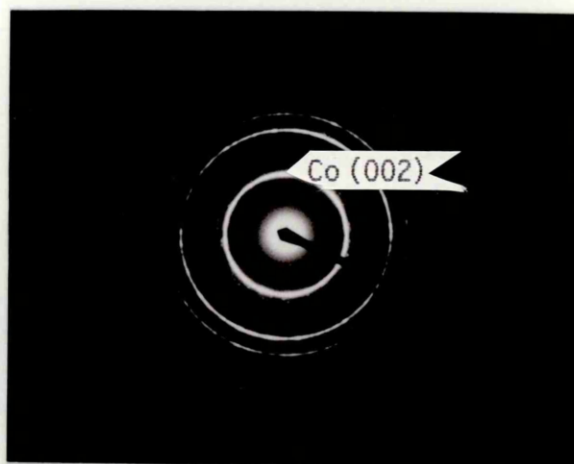
C-axis texture:

Figure 5.4 shows three selected area diffraction patterns from the CoCr films investigated in this work. These are from films deposited at a) room temperature, b) 200°C and c) 300°C. From these it can be seen that the films were polycrystalline, and that the crystal structure was that of hcp Co.

The intensity of the (002) diffraction ring was found to be dependent upon the substrate temperature: The ring was weakest in those films deposited at room temperature and strongest in those deposited at 300°C. The complete absence of the (002) diffraction ring would indicate that there was a strong c-axis texture in the film, with the c-axis lying along the film normal throughout the film. The relative intensities actually observed indicate that there was a greater degree of alignment of the c-axis with the film normal in the room temperature films than in those deposited at higher temperatures.

This is in disagreement with some workers in this field who found, using x-ray diffraction, that the c-axis alignment increased as the substrate temperature was increased (Smits *et al* (1983); Maloney and Lustig (1984)). However, these studies have been on much thicker films than those studied here. In 150nm thick films, Lodder and Wielinga (1984) found that the c-axis texture was better for lower substrate temperatures. Futamoto *et al* (1985) have studied CoCr alloy films ranging in thickness from 5nm to 100nm. They found that only after ~80nm did a columnar microstructure develop. At thicknesses less than this, the grains were equiaxed. It appears, therefore, that in the initial growth layer, lower substrate temperatures, and therefore

a)



b)



c)



Figure 5.4: Selected area diffraction patterns from CoCr alloy film deposited at a substrate temperature of: a) nominal room temperature, b) 200°C, c) 300°C

lower atom mobility, leads to better c-axis texture. There is evidence that once the columnar structure develops, higher substrate temperatures encourage chemical reactions between the Cr atoms and the residual gas in the sputterer and that this favours the c-axis texture (Smits *et al* 1984).

Magnetic structure:

Films deposited at room temperature:

No magnetic structure was observed in the films deposited at room temperature. This may be because the films themselves were non-magnetic or had a very low saturation magnetisation. The saturation magnetisation of bulk CoCr decreases linearly with increasing Cr content, and vanishes for Cr contents above 25 at. % (Smits *et al* 1984). The saturation magnetisation of thin film CoCr has been shown to be greater than that in bulk alloy of the same composition, and Sugita *et al* (1981) suggest that this is due to Cr segregation to the column boundaries. From a study of the variation of Curie temperature and uniaxial anisotropy constant, K_1 , with substrate temperature in ion beam sputtered CoCr films, Smits *et al* (1984) concluded that Cr segregation does take place in CoCr thin films. Furthermore, the segregation was more pronounced in films deposited at higher substrate temperatures.

At low substrate temperatures, the film will have a composition close to that of the alloy target, throughout the entire volume, with only small variations in the local Co to Cr ratio. Films produced at high substrate temperatures, on the other hand, will have Co-rich regions in which the Cr content is substantially less than that of the alloy target and in which the saturation magnetisation is larger than would be expected from the target composition. Therefore, for a target with close to 25 at. % Cr content films produced at a low substrate temperature will have a low saturation magnetisation. In chapter 6 the

question of Cr segregation at column boundaries in sputtered CoCr thin films will be discussed further.

Films deposited at 200 and 250°C:

In films deposited at 200 and 250°C there was a strong, in-plane, domain structure with a ripple structure superimposed upon it. For a given deposition temperature, the domain structure was stronger in the 40nm thick film than in the 80nm thick film. That is to say, there were more domains in a given area of the 40nm film than there were in the same area of the 80nm thick film. However, the domain structure was very dependent on topographic features within the films, as can be seen from figure 5.5. This figure shows a Fresnel image and the corresponding in-focus image from two different areas of a 40nm thick film, deposited at 250°C. It is obvious from this figure that the magnetic structure is greatly influenced by cracks and folds in the film. This was also the case in the film deposited at 300°C.

Figures 5.6 illustrates, more clearly, the magnetic structure of the same film shown in figure 5.5. In this figure, a) and b) are DPC images showing the in-plane components of magnetisation, and c) is a sum image. From figure 5.6 a) it can be seen that the magnetic structure consists of a series of alternately magnetised domains, with relatively straight, 180°, domain walls between them. However, figure 5.6 b), shows that there is also an in-plane component perpendicular to the domain walls which varies most markedly in the vicinity of the walls. This component, although not as prominent in the area between the walls, is still present, and it is this which gives rise to the ripple structure in the Fresnel image of figure 5.5.

Figure 5.7 is a higher magnification image of the structure around a domain wall in figure 5.6. Once again, a) and b) are DPC images showing the two in-plane components of induction, and c) is the sum image of the same area. Figure 5.7 d) is a schematic of the magnetisation distribution in this area.

Ohkoshi and Kusuda (1983) have investigated a 60nm thick $\text{Co}_{80}\text{Cr}_{20}$

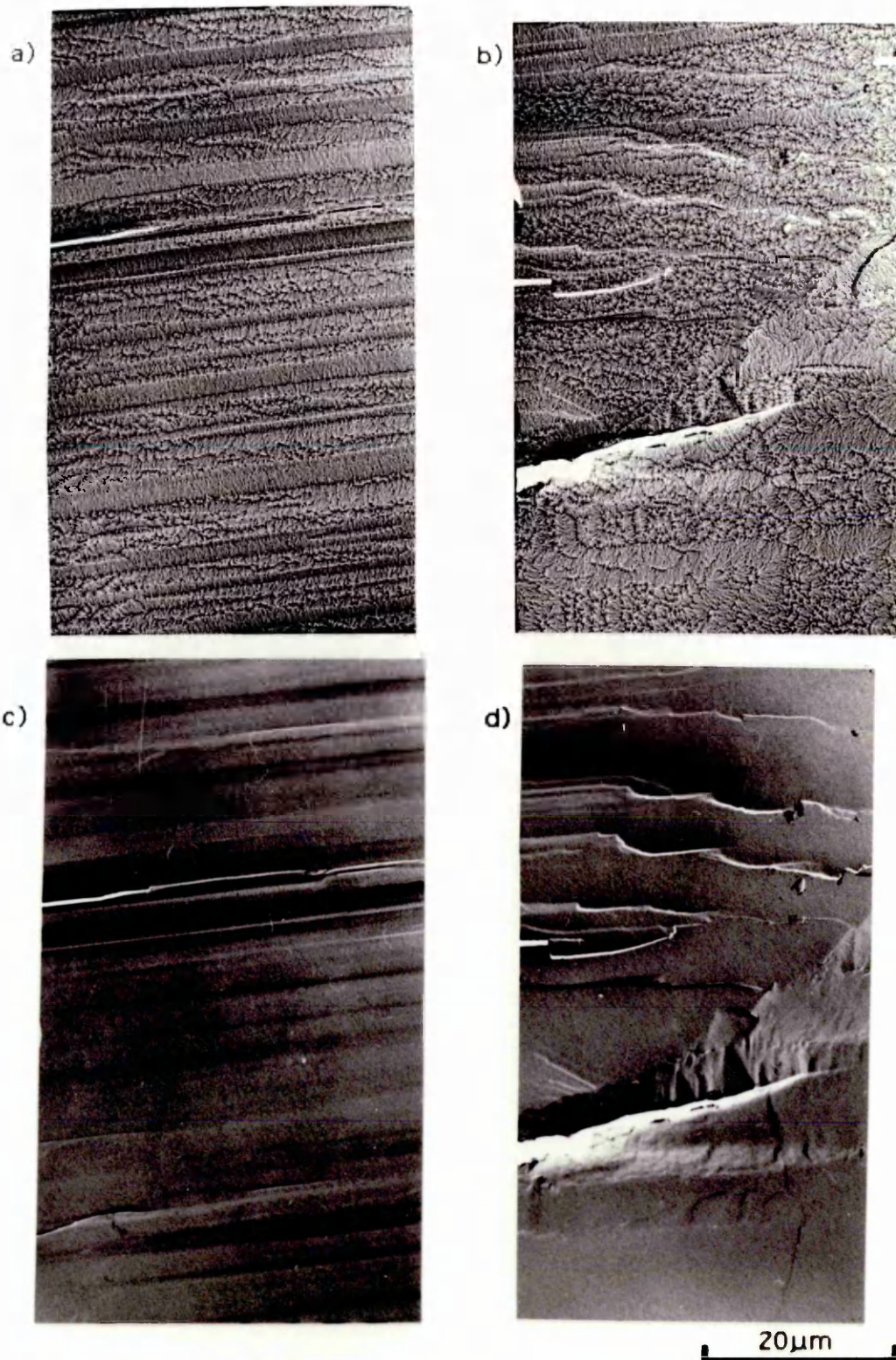
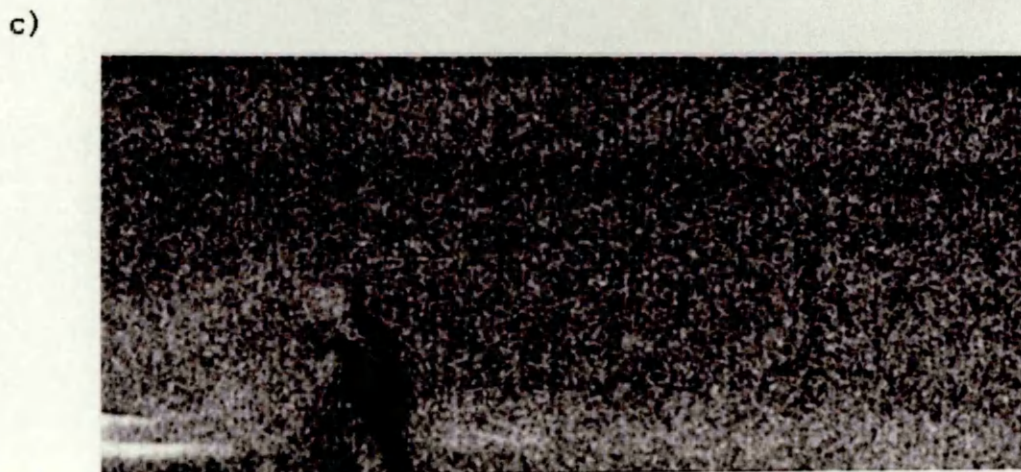


Figure 5.5: a) and b) Fresnel images showing the domain structure and magnetisation ripple in a 40nm thick $\text{Co}_{77}\text{Cr}_{23}$ film deposited at a substrate temperature of 250°C , c) and d) are in focus images of the same areas.



5 μm

Figure 5.6: a) and b) are two DPC images of the 40 nm thick CoCr film deposited at 250^oC. the arrows indicate which component of magnetisation each image is sensitive to c) is an incoherent bright field image of the same area.

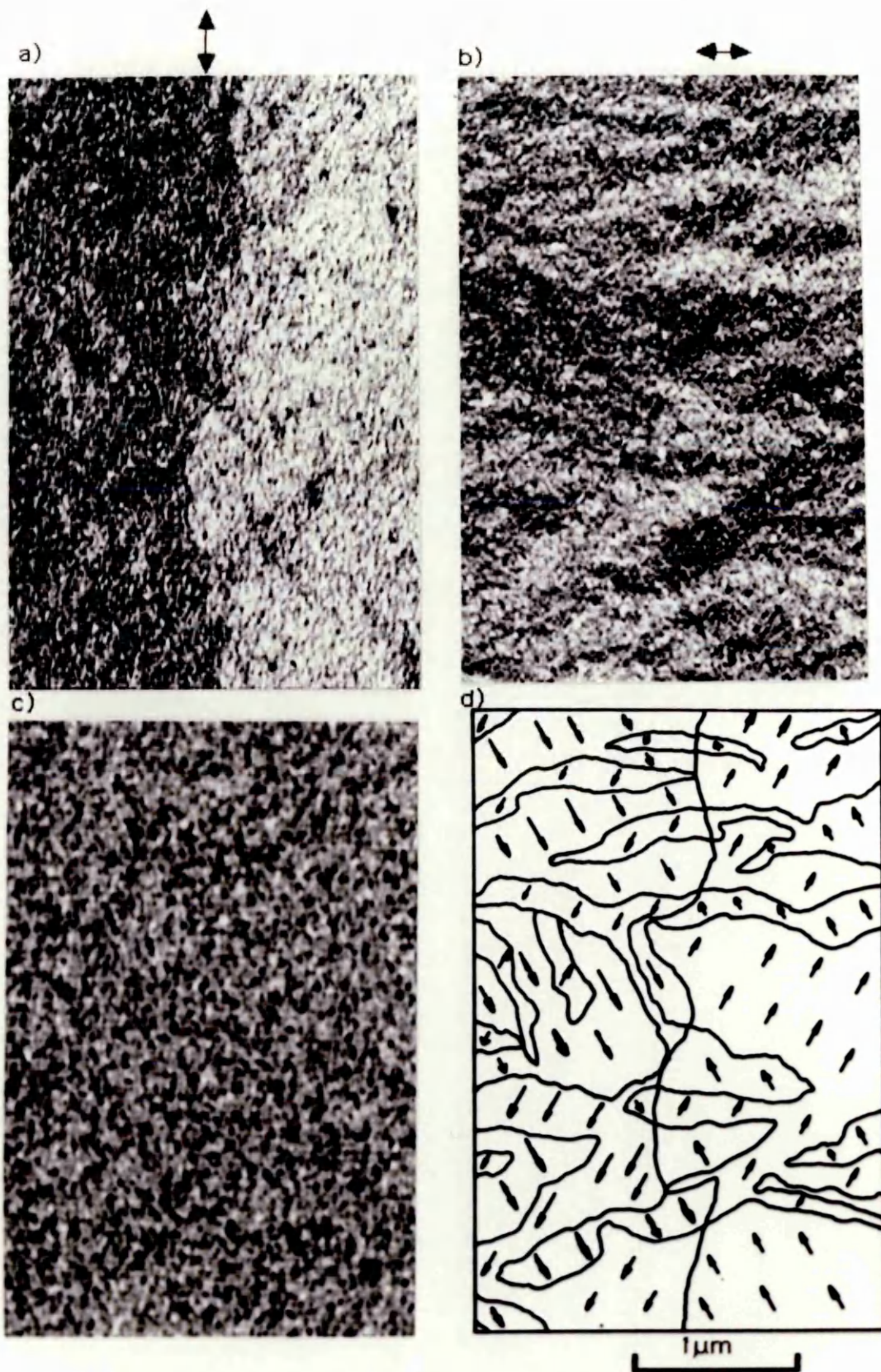


Figure 5.7: a) and b) are two DPC images of the 40 nm thick CoCr film deposited at 250°C. the arrows indicate which component of magnetisation each image is sensitive to c) is an incoherent bright field image of the same area. d) is a vector plot showing the variation of magnetisation.

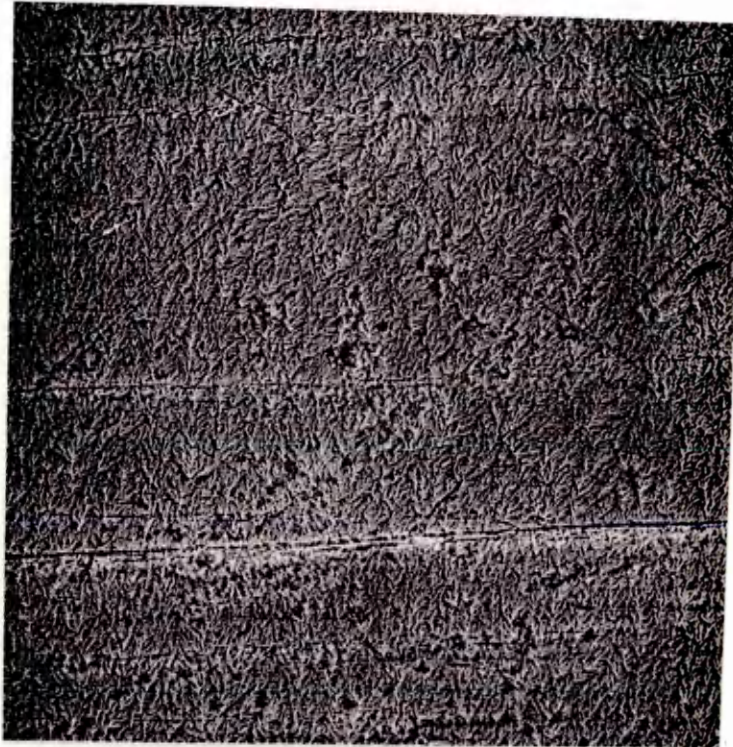
film, using Fresnel Lorentz microscopy, and obtained similar images to that in figure 5.5. From their micrographs they concluded that the domain walls in their sample were a type of cross-tie wall. From the schematic of figure 5.7 it can be seen that the walls in figure 5.7 are more irregular than a simple cross-tie wall. The component of in-plane magnetisation perpendicular to the domain wall, increases on either side of the wall. The angle between the in-plane components of magnetisation on either side of the domain wall is, therefore, less than 180° . Hence the angle through which the magnetic moments in the domain wall have to rotate is reduced and this reduces the exchange energy within the wall. The in-plane component of magnetisation can rotate on either side of the domain wall because there is no strong in-plane anisotropy.

Films deposited at 300°C:

In the films deposited at 300°C magnetisation ripple was observed. Figure 5.8 a) is a Fresnel image of the ripple structure in the $\text{Co}_{75}\text{Cr}_{25}$ film deposited at this temperature. Figure 5.8 b) is an in-focus image of the same area. The fact that there is magnetic structure in this film suggests that there are some areas of the film in which the Cr content is less than 25% and in which, therefore, the saturation magnetisation is non-zero. Hence, either the entire film has a different composition from the alloy target, or there are Co-rich regions within the film as proposed by Smits *et al* (1984).

In the $\text{Co}_{77}\text{Cr}_{23}$ film deposited at 300°C, the ripple structure appears most pronounced in the vicinity of the amplitude contrast in the film, as can be seen from figure 5.9 a). Once again figure b) is an in-focus image of the same area. Between the regions in which the ripple is prominent, there is magnetic structure on a much smaller scale. This is similar to the magnetic structure observed by Ohkoshi and Kusuda (1983) in a 100nm thick CoCr film. They deduced that this contrast corresponded to the perpendicular magnetic structure shown in figure 5.10. Although this structure does not extend over the entire

a)



b)



20 μ m

Figure 5.8: a) Fresnel image showing the magnetic structure in a $\text{Co}_{75}\text{Cr}_{25}$ film deposited at 300°C , b) infocus image of the same area.



20 μ m

Figure 5.9: a) Fresnel image of the magnetic structure in a $\text{Co}_{77}\text{Cr}_{23}$ film deposited at a substrate temperature of 300°C , b) infocus image of the same area.

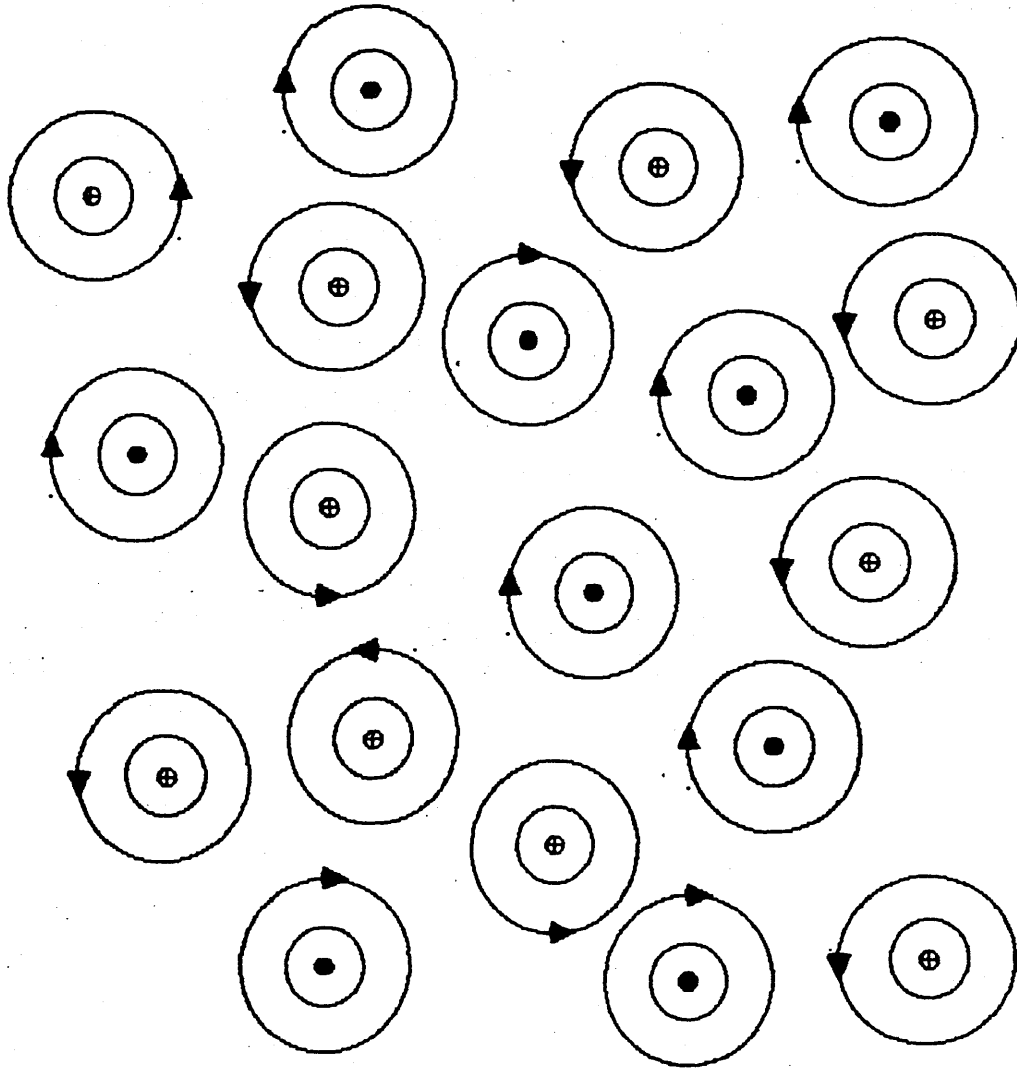


Figure 5.10 Magnetisation distribution proposed by Ohkoshi and Kusuda to explain the type of contrast seen in the Fresnel image in figure 5.9.

film surface, its presence in some areas indicates that there is a strong out of plane anisotropy in this film.

5.4 Summary And Conclusions:

Co-Cr artificial superstructure films:

The artificial superstructure films studied in this work were seen to be composed of separate layers of hcp Co and bcc Cr. The Co layers had a preferential c-axis orientation along the film normal, giving rise to weak or missing (002) and (004) reflections in the selected area electron diffraction patterns. The only magnetic structure observed in these films was magnetisation ripple, which for the film with 7 layers had a strong out of plane component. The layered structure does, therefore, produce a perpendicular anisotropy which is probably due to the c-axis orientation. However, to produce a strong anisotropy, the magnetic layers must remain very thin, Therefore, considerably more than 7 alternate layers will be required if the films are to have a strong anisotropy and a significant magnetic moment.

CoCr alloy films:

No magnetic structure was observed in either of the alloy films deposited at room temperature, although these films did have the crystal structure of polycrystalline hcp Co. It has been suggested that the observed increase in saturation magnetisation in some CoCr thin films, compared to bulk CoCr of the same composition, is due to Cr segregation within the films (Sugita *et al*/1981). Therefore in sputtered CoCr films in which there is very little Cr segregation, the saturation magnetisation should be close to the bulk value for the composition of the sputter target used. Smits *et al* (1983) have proposed that Cr segregation is less pronounced in films produced at low substrate temperatures than in films produced at high substrate temperatures. Thus the reason for the lack of magnetic structure in the films deposited at room temperature may be that there is very little Cr

segregation within these films. As the Cr content of the sputter targets used to produce these films was between 23% and 25% in, the saturation magnetisation within them will be close to zero.

In the films deposited at 200 and 250°C there was a strong in-plane domain structure. An in-plane component perpendicular to the domain walls was present over the entire film and strongest at the domain walls themselves. This led to a complicated 180° domain wall structure. The in-plane component of magnetisation rotates on either side of the domain wall and reduces the angle through which it has to rotate at the wall itself. From figure 5.7 it can be seen that the wall width is of the same order of magnitude as the crystallite size, and therefore the wall may not be a smooth rotation of the magnetisation. Instead the in-plane component of magnetisation may change discontinuously between crystallites on either side of the domain wall. This is in contrast to 180° and 90° domain walls in soft magnetic polycrystalline materials such as permalloy, in which the magnetisation in the domain wall can rotate through a number of crystallites (McVitie and Chapman 1986). If the magnetisation does rotate discontinuously then the exchange coupling between the individual crystal grains must be quite weak compared to the exchange coupling of magnetic moments within the grains. In the next chapter, evidence for the existence of a Cr-rich regions within thicker CoCr films will be presented.

In the films deposited at 300°C only magnetisation ripple was observed. For thin magnetic films, 40 to 80nm thick, magnetostatic considerations alone would produce an easy axis in the plane of the film. The absence of a large scale domain structure, in either of the films deposited at 300°C, indicates that there were no prominent in-plane easy axes in these films. The contrast observed in areas of the film in figure 5.9 a), indicates that there is an out of plane

component of magnetisation, and that in the areas of the film which are free from cracks, folds and other topographic features, the magnetisation lies mainly out of the plane of the film.

The strongest c-axis texture existed in those films deposited at low temperatures; the films deposited at the highest temperatures exhibited the least c-axis texture. Perpendicular magnetic structure, on the other hand, was strongest in the films deposited at the higher temperatures. Therefore, in these films it appears that the anisotropy is more dependent on the substrate temperature, and hence the proposed Cr segregation, than on the c-axis texture.

The films studied here were much thinner than the films which are of most interest in perpendicular magnetic recording, and it is likely that the columnar structure and c-axis texture is not as well developed in these films as it is in the thicker films. A number of authors have proposed that the initial layer of a CoCr sputtered film consists of randomly oriented equiaxed crystal grains (Ouchi and Iwasaki (1984); Futamoto *et al* (1985)). The columnar microstructure which develops is thought to be due to the preferential growth of the grains in which the c-axis is perpendicular to the film normal. Ouchi and Iwasaki propose that by the time the c-axis texture and columnar microstructure has fully developed, the grain size should have increased to ~70nm or more. In the films studied here the average grain size was ~25nm suggesting that the columnar microstructure had not yet developed in these films. As the grain size is much less than the film thickness there is probably more than one crystallite through the thickness of the film.

Films in which the columnar microstructure is fully developed generally have a thickness of 400nm, or more, which is far too thick for investigation by 100keV transmission electron microscopy. In chapters 6 and 7 the physical and magnetic microstructures of transverse sections of 400nm to 1500nm thick CoCr films are investigated.

CHAPTER 6

ELEMENTAL SEGREGATION IN CoCr PERPENDICULAR MAGNETIC RECORDING MEDIA

6.1 Introduction

The origin of the perpendicular anisotropy in sputtered CoCr thin films has been discussed greatly in the literature (Ohkoshi and Kusuda 1983; Grundy and Ali 1983; Futamoto *et al* 1985). The two main possibilities which have been investigated are i) magnetocrystalline anisotropy due to the alignment of the hcp c-axis with the film normal (see for example Ouchi and Iwasaki 1984) and ii) shape anisotropy due to the columnar microstructure present within the sputtered films (Ohkoshi and Kusuda 1983). In the latter, Cr-rich column boundaries, in which the saturation magnetisation is less than that in the columns, are thought to magnetically isolate the individual columns from one another.

Much work has been done on this problem and it is now generally accepted that the perpendicular anisotropy is, in the main, due to the c-axis alignment. However, the presence of Cr-rich, and perhaps non-magnetic, column boundaries would play an important role in the magnetisation reversal process within the CoCr film. If the boundaries between columns were Cr-rich, then the exchange coupling between columns would be reduced and the individual columns could be magnetically isolated from each other. This would affect the recording process in the film, since information is stored in a magnetic recording system as a reversal of the direction of magnetisation within the recording media. Furthermore, if the column boundaries were non-magnetic, there might not be magnetic domain walls between oppositely magnetised domains. Instead the domains could be separated by non-magnetic column boundaries (Ouchi and Iwasaki 1984). Therefore, the existence and extent of any Cr segregation within sputtered CoCr thin films is of great interest if the magnetisation

reversal process is to be understood.

A number of different methods have been used to investigate elemental segregation within CoCr thin films. Hoffmann *et al* (1986) studied surface replicas of sputtered CoCr thin films, before and after etching the film surface with concentrated nitric acid. They found that the columns were preferentially etched with respect to the column boundaries. Since nitric acid dissolves cobalt but not chromium they concluded that the column boundaries consisted mainly of chromium. Jhingan (1986) investigated the variation in Cr content across grain boundaries in a planar CoCr thin film using a fine electron probe in a transmission electron microscope and found variations of 2 wt. % with both Cr-rich boundaries and Co-rich boundaries. This corresponded to a real variation of >2 wt. % as the electron probe was much larger than the grain boundaries.

Both of the above studies involved planar CoCr films, the method used by Hoffmann *et al* investigates segregation at the film surface, as this is where the acid etch is carried out, and does not give information on any segregation within the film. Furthermore the technique is qualitative not quantitative. Jhingan used an electron probe directed along the grain boundaries. To minimise beam spreading using this technique the film has to be about 100nm thick, or less. Hence the films investigated by him had either to be thin to start with, or had to be back thinned. This type of thinning was unsuitable for our purposes as is explained below.

In order to sustain a perpendicular magnetic domain structure, CoCr films must be over a certain critical thickness of around 200nm. The films studied in this work had CoCr layers 400–500nm thick and, in addition, some had a soft magnetic underlayer consisting of 450–900nm of NiFe. Therefore to be able to study elemental segregation within these films, using EDX in the HB5 STEM, it was necessary to thin the films in some way. As the magnetic structure within the films was also to be investigated, the films were sectioned transversely rather than back thinned. This transverse sectioning, as well as producing

specimens thin enough for quantitative EDX microanalysis, allows the columns in the CoCr to be oriented perpendicular to the electron beam in the microscope thus allowing components of magnetisation along the film normal to be observed using DPC imaging.

As was shown in chapter 2, the electron beam profile within the sample can be calculated as a function of the specimen thickness. Therefore it is important to know the local specimen thickness in order to calculate what proportion of the volume analysed is column boundary, and what proportion is column matrix. Also required is a knowledge of the width and shape of the column boundary. It will be shown that an estimate of the boundary width, although not its shape, can be obtained using EDX. The local specimen thickness was determined by electron energy loss spectroscopy (EELS) using the formula derived in chapter 2.

6.2 Specimen Preparation

The CoCr films investigated here were prepared by Philips Research Laboratories by R.F. sputtering onto polyester (PET) foils using $\text{Co}_{78.5}\text{Cr}_{21.5}$ alloy targets. In some cases a soft magnetic underlayer of either NiFe or CoZrNb, together with a thin layer of Ti, were deposited on the polyester before the CoCr layer. This was to improve the magnetic recording characteristics of the CoCr media. Full details of the sputtering parameters are given in Luitjens *et al* (1985).

Once the thin films had been produced they were cut into transverse sections by embedding them in resin and microtoming the resulting sandwich. This produced long, straight sections of material of around 100nm in thickness. The magnetic structure of these sections will be discussed in chapter 7. Although the microtomed samples investigated were thin enough for 100keV electrons to travel through them, the beam spreading within a sample of this thickness is quite marked (see figure 2.16). Therefore thinner samples, prepared by ion beam milling, were also investigated. Ion beam milling produces

wedge-shaped samples and only very small areas of these samples were thin enough to study. These areas were $\leq 60\text{nm}$ in thickness, and therefore the effects of beam spreading within them was very much less than in the microtomed samples. There was very strong non-magnetic contrast from the crystallites in the cross-sections, which made magnetic contrast difficult to see. Therefore, long thin sections of sample were necessary in order to identify magnetic contrast by its periodic nature. For this reason the ion beam thinned samples were unsuitable for studying the magnetic structure.

6.3 General Observation Of CoCr Transverse Sections

Figure 6.1 shows a typical microtomed section studied in this work; a) is a brightfield image and b) is a darkfield image of a 130nm thick cross-section. This was the local thickness of the cross-section, measured, using EELS, at the points where the x-ray microanalysis was carried out. The columnar microstructure can be easily seen in both a) and b) and the column diameter is $\sim 70\text{nm}$. It can be seen from this figure, that some column boundaries are much more prominent than others. The reason for this is that some boundaries are lying along the beam direction; therefore there is a sharp transition from one crystallographic orientation to another across these boundaries, while others are at an angle to it. Figure 6.2 illustrates how this occurs.

Figure 6.2 a) shows a view looking down onto the surface of a film with a columnar microstructure, in which the columns are perpendicular to the film surface, as is the case in the CoCr films studied here. It can be seen from figure 6.2 b), that when a transverse section of thickness t , where t is approximately equal to the column diameter, is cut from this film there are only a few column boundaries which extend through the entire section; A, B and C are examples of such boundaries. Furthermore, few, if any, of these are oriented perpendicular to the section edges, and therefore lie along the beam direction in an untilted sample. For this reason it was generally necessary to tilt the section in the microscope so that some of the

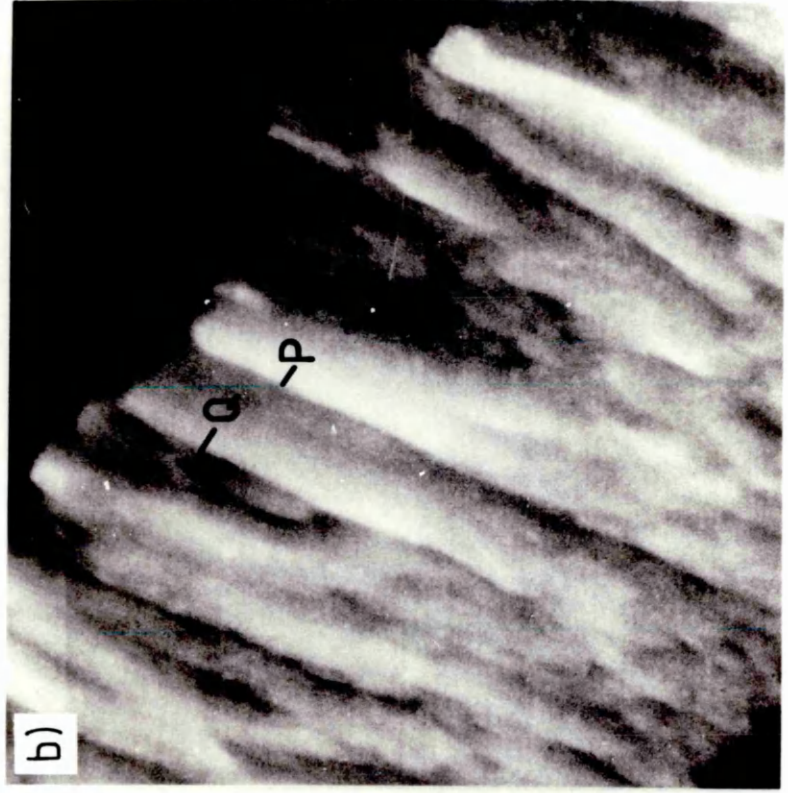
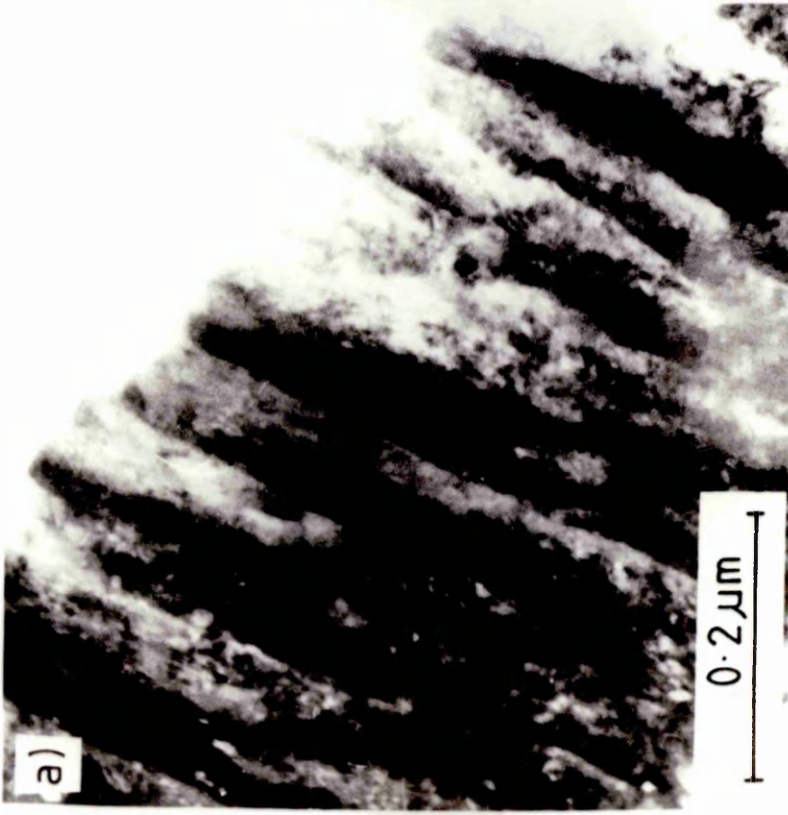
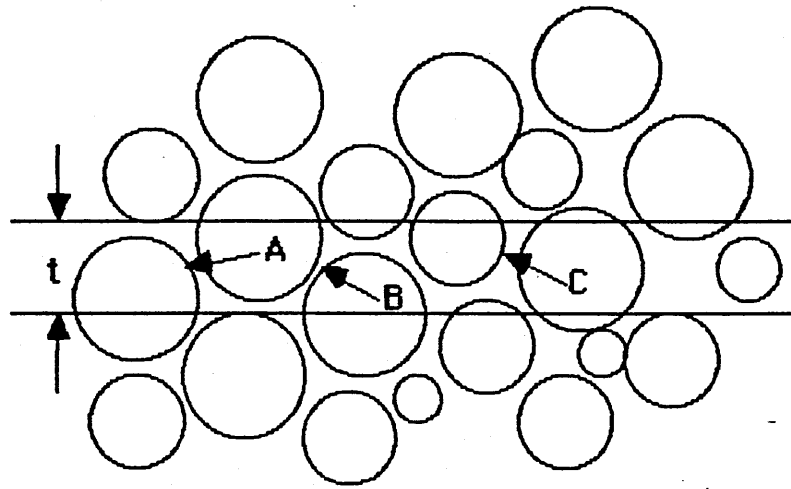


Figure 6.1: a) Bright field and b) annular dark field images of a 130nm thick transverse section through a CoCr film. P and Q are two boundaries which are thought to be well oriented for elemental analysis.

a)



b)

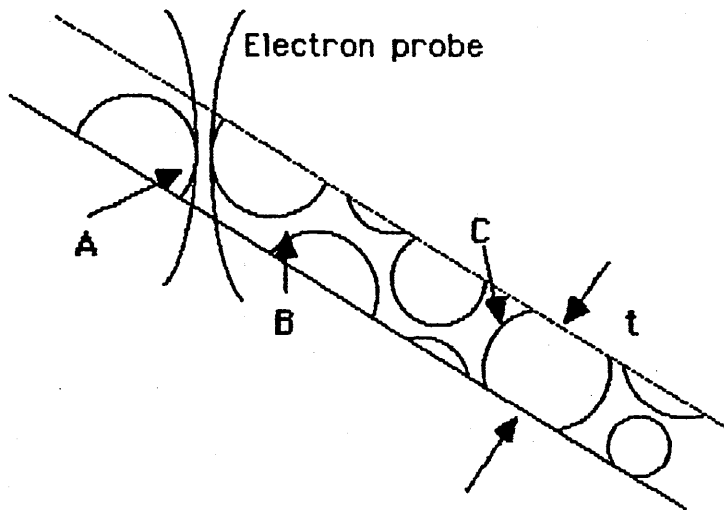


Figure 6.2 a) schematic representation of taking of a transverse section from a thin film with a columnar microstructure
b) Orientation of section to allow electron probe to remain in boundary region through entire section thickness.

column boundaries were aligned with the beam direction, as boundary A is in figure 6.2 b).

From figure 6.1 it can be seen that there is strong contrast in the bright field image from within the columns themselves as well as at the column boundaries. This is due to diffraction from the crystallites within the columns. The dark field image, on the other hand, has much less contrast within the columns and the boundaries stand out more clearly in it. The dark field image was therefore used to locate well oriented boundaries within the sections. Moreover, only those boundaries which had strong contrast in both the bright field and the dark field images were taken to be aligned with the electron beam. Boundaries P and Q are examples of the type of boundaries which were judged to be well oriented for elemental analysis.

6.4 Spectrum Acquisition Conditions

The column boundaries in CoCr occupy a very small volume compared to the columns. Therefore to be able to detect Cr-segregation to the column boundaries it is necessary to be able to ascertain the chemical composition of very small volumes within the samples. When acquiring EELS and x-ray spectra from a small volume in the HB5, the raster scan is disabled. This holds the electron probe stationary on the specimen surface at a point which has been previously determined by moving an illuminated marker to the position of interest on the bright field and dark field images. The positioning of the marker was done at magnifications of 1 or 2×10^6 ; this gives an accuracy in positioning the probe of $\sim 1\text{nm}$.

The spectra from these cross-sections were acquired using the conditions described in table 2.1. These conditions give a probe diameter of $\sim 2\text{nm}$ and a probe current of $\sim 0.2\text{nA}$. Smaller probe diameters are available in the HB5, but beam spreading within the sample increases the area irradiated by the probe to much more than that set by the diameter of the probe on the specimen. Furthermore the loss in probe current associated with the decrease in probe diameter

increases the acquisition time required for each spectrum, and subsequently the amount of specimen drift that occurs. Hence there is no real gain in decreasing the probe diameter to less than that used.

The x-ray spectra from the boundaries were acquired for ~60 seconds each, and the acquisition was halted every 15 seconds to ensure that excessive specimen drift did not occur during the acquisition time. If a small amount of specimen drift occurred during the 15 seconds, the probe was repositioned on the column boundary before acquisition was resumed. However, if a large drift, i.e. >1nm, occurred within the 15 seconds, the spectrum being acquired was discarded and the specimen was left to stabilise before the next spectrum was acquired.

For a 60 seconds acquisition time the number of counts in the Cr K_{α} peak varied between 400 and 1000. As x-ray production within a sample is a random process governed by Poisson statistics this gave an uncertainty of between 5 and 3% in the number of counts in the Cr K_{α} peak for each spectrum. The ratio of Co to Cr in the samples was approximately 4:1, and as the cross-sections for production of Co K_{α} and Cr K_{α} photons are approximately equal, the number of counts in the Co K_{α} and Cr K_{α} peaks were also approximately in the ratio 4:1. The uncertainty in the ratio of Co to Cr within the samples is, therefore, only slightly greater than the uncertainty in the number of counts in the Cr K_{α} peak.

If a small volume of the specimen is to be analysed, beam spreading within the sample has to be minimised. While the probe is stationary, carbon contamination builds up on the surface of the specimen. This is because hydrocarbons are present, either in the microscope or, more likely, on the specimen itself. These are free to move about the specimen surface until polymerised by the electron beam at which point they are immobilised. If the electron probe is stationary for a long period of time, as in spectrum acquisition, a contamination spot builds up and, because carbon has a low atomic number, the spot can be very thick before it is obvious in the bright

field or dark field images. The thicker the contamination spot, the more the beam spreads and therefore the greater the volume of sample being irradiated. For this reason short acquisition times of 60 seconds were used.

The spectra from the columns were also acquired for 60 seconds, and for these the electron probe was positioned in the centre of the columns. A number of spectra were acquired for a longer period of time, and these were used to determine the extent of self-absorption and the Bremsstrahlung background in the spectra being analysed.

6.5 Results Of Microanalysis

Raw data from x-ray spectra:

Figure 6.3 shows two typical x-ray spectra from the CoCr layer of a transverse section (TS2) from a film composed of 400nm CoCr; 15nm Ti; 900nm NiFe. The dashed spectrum was taken from a well oriented column boundary, and the solid spectrum was taken from the centre of a column. The Co peaks in these spectra have been scaled so that they are the same height and from this figure it appears that the column boundary is Cr-rich compared to the column matrix. However the statistics in these two individual spectra are such that the difference between the cobalt to chromium ratios from the two spectra is less than the error in the individual ratios. To obtain statistically significant results, a further 19 spectra were taken from well oriented boundaries and a further 36 from the column matrix around these boundaries.

In addition to the 60 second spectra, one spectrum was acquired for 200 seconds. The statistics in this spectrum were far better than those in the 60 second spectra, and this spectrum was used to calculate what percentage of the gross counts in the Co and Cr windows corresponded to actual characteristic x-rays and what percentage corresponded to background signal. A background fit of the form $D(a/E+b+cE)$ was used and it was found that 97.6% of the gross counts in the window containing the Co K_{α} peak were due to characteristic

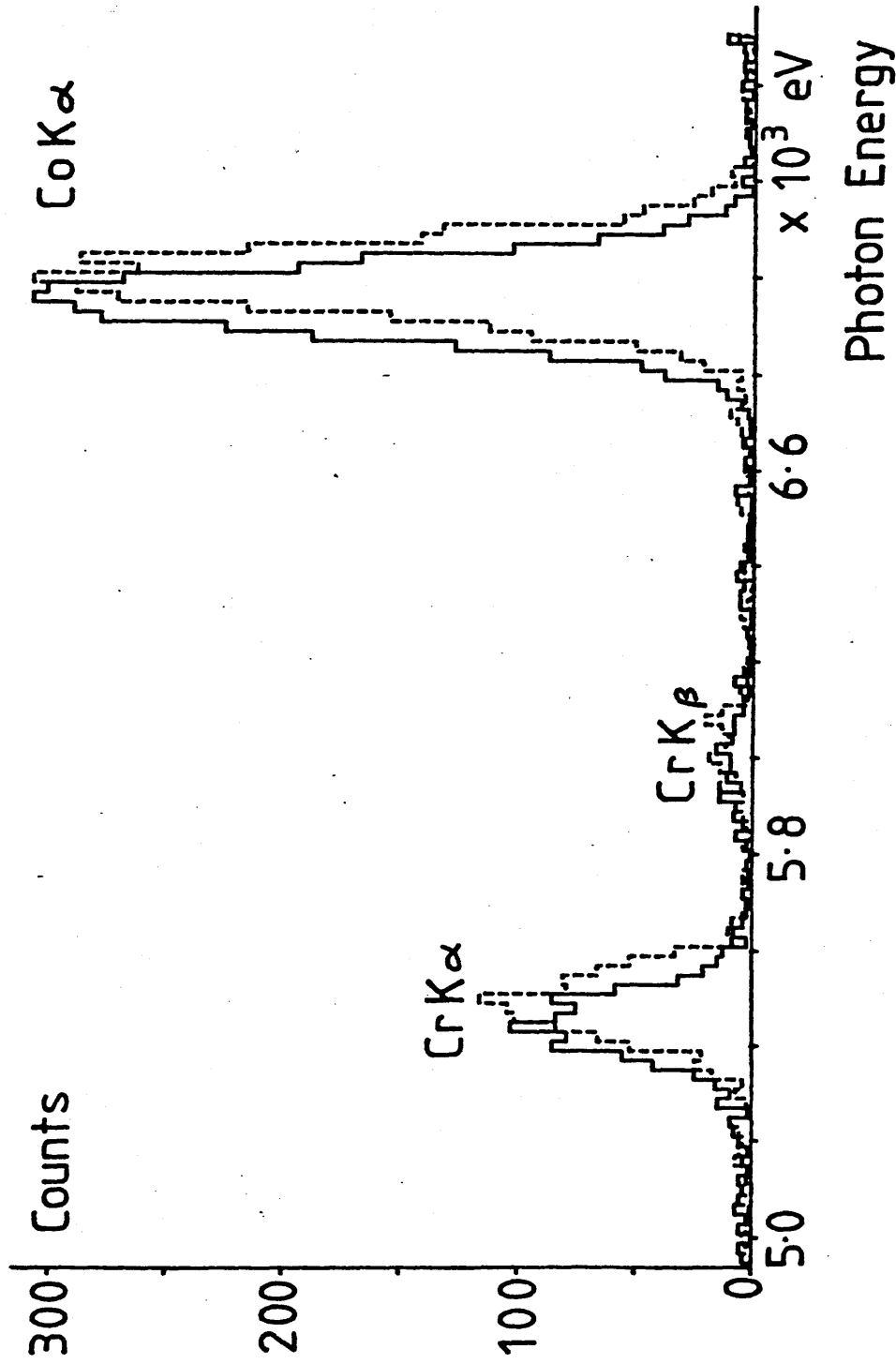


Figure 6.3: Two typical x-ray spectra from the CoCr layer of cross-section T52.

The dashed spectrum is from a well oriented column boundary and the solid spectrum is from within a column. The spectra are slightly displaced for clarity

x-rays, and the corresponding percentage for the Cr K_{α} peak was 91.3%. (Justification for the use of this background model is given in Chapman *et al* 1984). The computer programs used in this analysis are explained in more detail by Crozier (1986).

Figure 6.4 shows two histograms of the ratio of the number of characteristic Co K_{α} photons to Cr K_{α} photons, P_{Co}/P_{Cr} , given by:

$$P_{Co}/P_{Cr} = 0.975 N_{Co}/0.913 N_{Cr} = 1.07 N_{Co}/N_{Cr}$$

where N_{Co}/N_{Cr} is the ratio of the gross counts in the Co and Cr K_{α} windows. The solid histogram corresponds to spectra taken from within the columns and the dashed histogram corresponds to those from the column boundaries. The mean of P_{Co}/P_{Cr} at the column boundaries is 3.32 with a standard deviation of 0.13 while in the column matrix P_{Co}/P_{Cr} is significantly higher with a mean of 3.65 and a standard deviation of 0.19. The standard error in these two means is 0.03 therefore it can be seen that there is a statistically meaningful increase in Cr content between the column matrix and the column boundary.

Figure 6.5 is a similar histogram for a transverse section (TS1) from a 450nm thick CoCr film. Once again there is evidence for an increase in Cr content in this film between matrix and boundary. Table 6.1 is a summary of the information from these two histograms. Also given in this table is the local thickness of the cross-sections as calculated from EELS spectra using equation (2.39). This is important if the effect of beam broadening is to be taken into account.

The ratio of the number of atoms of Co (n_{Co}) to the number of atoms of Cr (n_{Cr}) in the irradiated volume of the cross-section is given by equation (2.41) i.e.

$$n_{Co}/n_{Cr} = P_{Co}/P_{Cr} \cdot \sigma_{Cr}/\sigma_{Co}$$

where σ_{Cr}/σ_{Co} is the ratio of the cross-sections for production of K_{α}

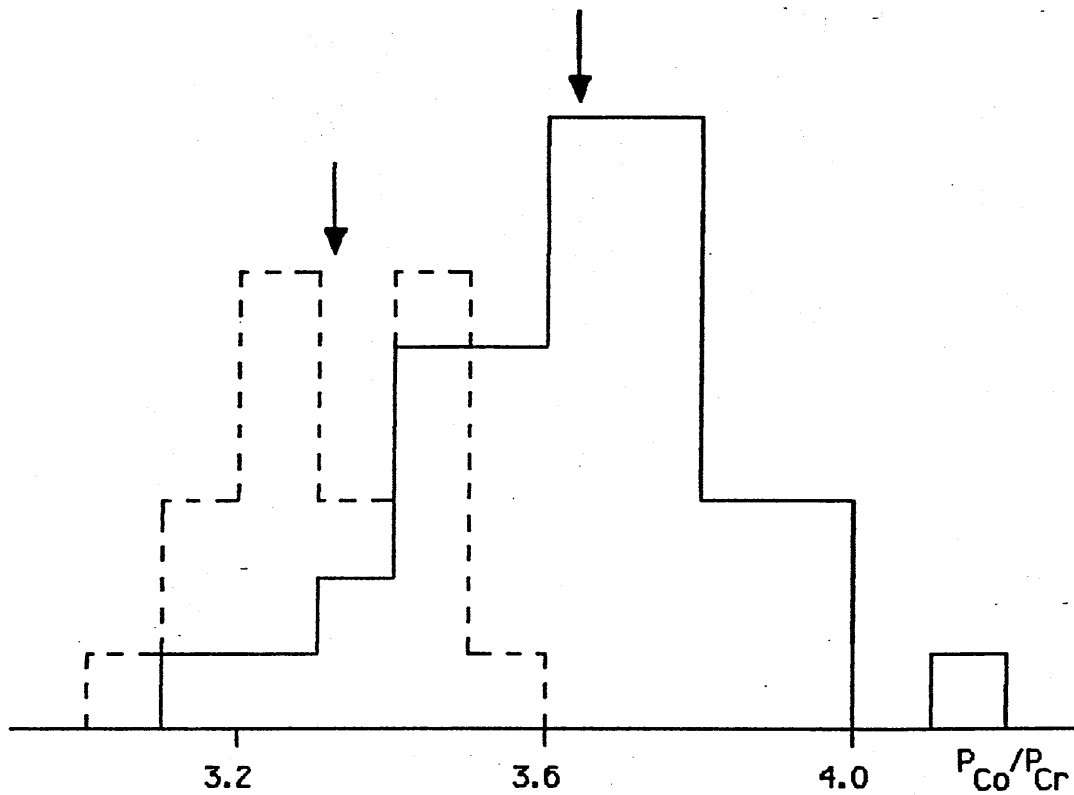


Figure 6.4: Histogram of P_{Co}/P_{Cr} for a 450nm thick CoCr film the dashed histogram corresponds to spectra from the column boundaries, and the solid histogram corresponds to spectra from within the columns

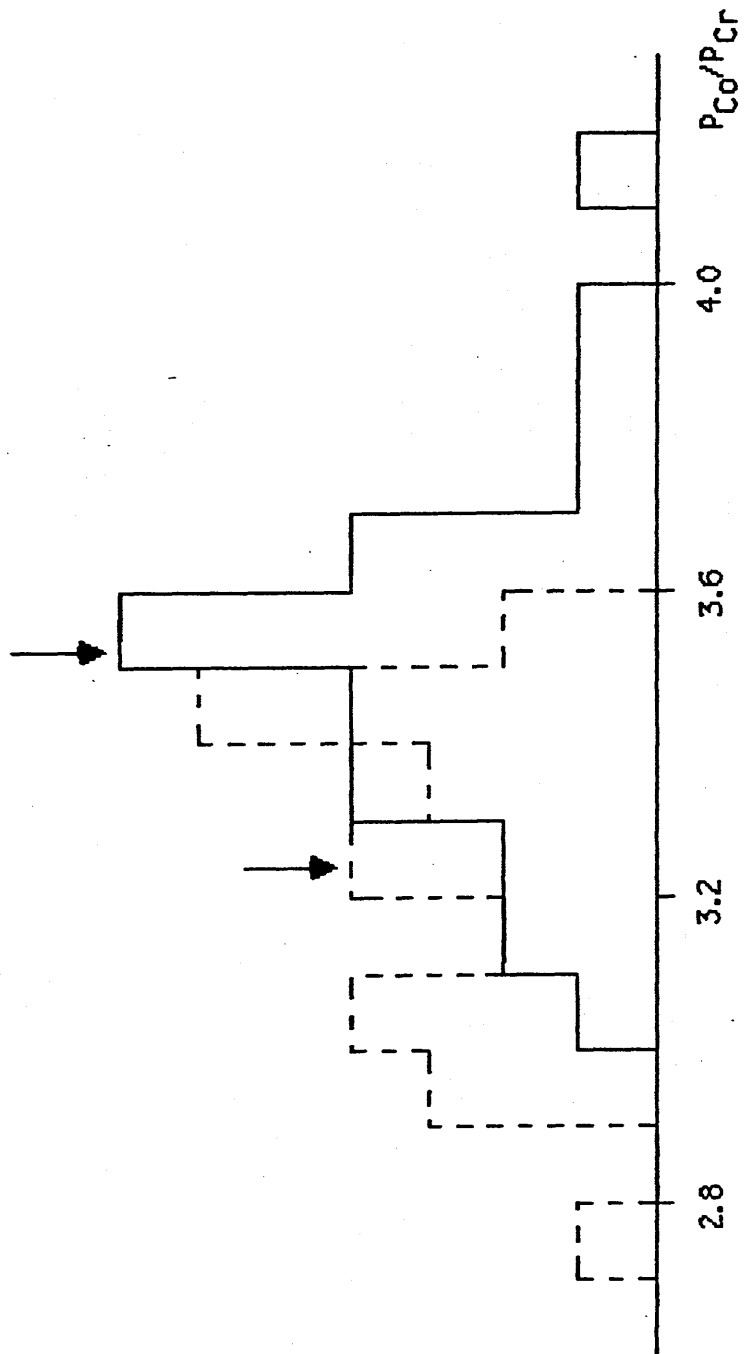


Figure 6.5: Histogram of P_{Co}/P_{Cr} ratio for section TS1, the solid histogram corresponds to spectra from within the columns, the dashed histogram corresponds to spectra from the column boundaries.

photons from the two elements. Using data from Chapman *et al* (1984) gives a value for σ_{Cr}/σ_{Co} of 1.07 ± 0.03 . Therefore the atomic percentage of Cr (x) can be written as

$$x = 100 n_{Cr}/(n_{Co}+n_{Cr}) = 100 \{1.07(P_{Co}/P_{Cr}) + 1\}^{-1} \quad (6.1)$$

Table 6.3 gives, for samples TS1 and TS2, the values of x when the probe was in the middle of a column (x_c) and when the probe was centred on a well oriented column boundary (x'). In both cases the column boundaries have an apparent Cr enrichment of ~ 1.5 at.%. This however must be considered a lower bound to the actual Cr enrichment as the volume analysed by the probe will include both boundary and matrix regions. To calculate the atomic percentage of Cr in the boundary region (x_b), the fraction $f = V_b/V_T$ has to be known, where V_T is the total volume irradiated by the probe, and V_b is the volume of boundary region irradiated by the probe.

Calculation of volume fraction, f:

As stated in section 2.8, the total volume irradiated by the electron probe is given by the probe diameter, the thickness of the sample, and the amount the beam broadens as it passes through the section. A good approximation to the total volume irradiated by the probe is given by the following integral:

$$V_T = \int_0^t \pi r^2 dz = \pi r_2^2 z_0 + \pi \int_{z_0}^t r_1^2(z) dz \quad (6.2)$$

where t is the specimen thickness, r_2 is the probe radius due to the microscope aberrations, and $r_1(z)$ is the probe radius due to beam broadening within the specimen. z_0 is the specimen thickness at which $r_1 = r_2$. $r_1(z)$ is given by equation (2.45) as

$$r_1(z) = \frac{1}{2} 6.25 \times 10^5 \frac{Z}{E_0} \left[\frac{\rho}{A} \right]^{1/2} z^{3/2} \text{ cm}$$

where Z is the average atomic number of the specimen, A is the average atomic weight, and ρ is the density of the specimen in gcm^{-3} . This, analytical, expression for the radius of the area irradiated by the probe has, as was stated in chapter 2, been shown to be in good agreement with Monté Carlo type calculations of the electron trajectories in this material. Putting in the values for $\text{Co}_{80}\text{Cr}_{20}$ gives $r_1(z) = 31.77 z^{3/2} \text{ cm}$.

Table 6.2 gives the volume, V , of sample irradiated by a 2nm diameter probe in three samples investigated in this work. Samples TS1 and TS2 are the two mentioned above which were both produced by microtoming, and sample TS3 was produced by ion beam thinning. From this table it can be seen that the volume of sample irradiated increases very rapidly with specimen thickness. The parameter d in the table is the diameter a cylinder, of length equal to the sample thickness, would have if its volume were to equal V . This can be taken as an approximate measure of the spatial resolution of the microanalysis.

The volume of boundary region irradiated by the probe can be calculated by considering the diagram in figure 6.6. It can be seen from this diagram that if the probe radius is larger than w , the boundary width, the area irradiated is approximately a rectangle of width w and length $2r$, and the volume irradiated can then be calculated by evaluating the integral

$$V_b = \int_0^t w 2r dz = w 2r z_0 + w \int_{z_0}^t r_1(z) dz \quad (6.3)$$

Since the probe radius increases very rapidly in the specimen due

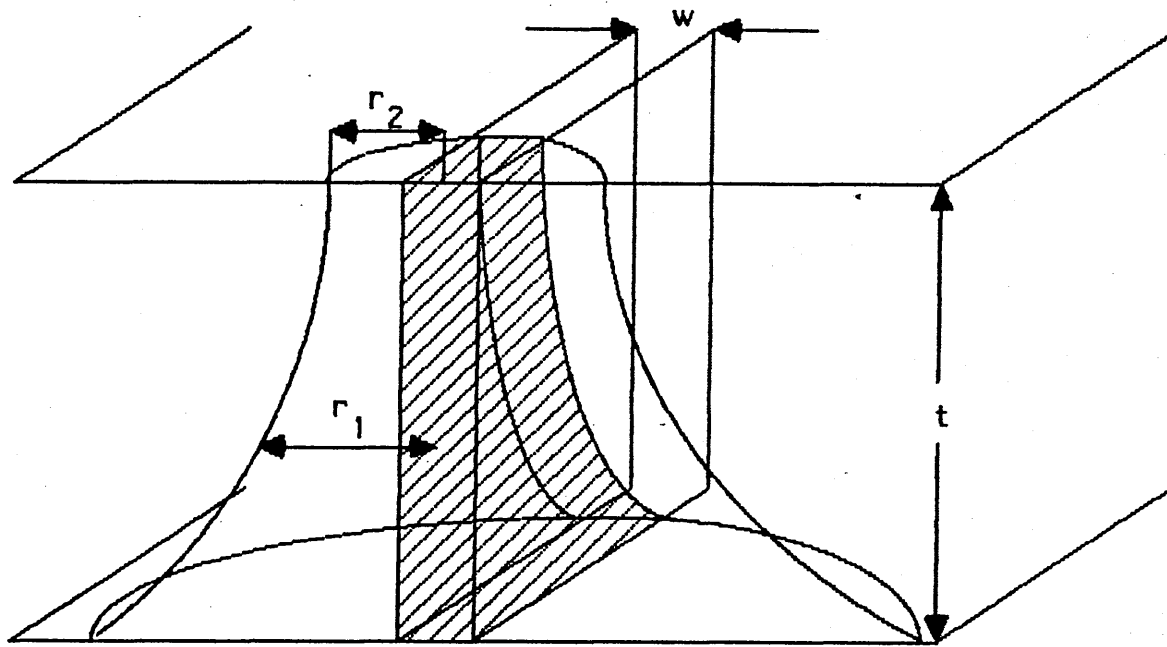


Figure 6.6: Illustration for calculation of volume of matrix and boundary region irradiated by probe: t is the sample thickness; w is the width of the boundary region; r_2 is the initial radius of the probe; and r_1 is the radius of the broadened beam in the sample.

to beam broadening, this equation gives a good approximation even if the initial probe diameter is less than the boundary width, w .

Figure 6.7 is a graph of the ratio $f = V_b/V_T$ against boundary width, w , for various specimen thicknesses, t . The straight lines were calculated using the above equations for V_b and V_T . The intercepts marked on the locus $f=1$, correspond to the value of w given by $w=r_1(t)$. Therefore the above method of calculating f can be seen to be valid for values of f up to ~ 0.95 .

In order to calculate f an estimate of the boundary width has to be obtained.

Estimation of boundary width:

Figure 6.8 shows two traces of the ratio P_{Co}/P_{Cr} across column boundaries in section TS3. These traces were obtained by moving the electron probe across the sample and taking x-ray spectra every 1.2nm. The spectra were acquired for ~ 60 seconds each and, even with the large error bars due to the poor statistics in the individual spectra, the boundary region can be clearly seen. The ratio N_{Co}/N_{Cr} is 10% lower in the boundary region than in the columns and the width of this region can be seen to be of the order of 5nm. When it is considered that the probe diameter is 2nm and that beam spreading reduces the spatial resolution to ~ 5 nm in a 60nm thick sample, this value can be taken as an upper limit of the boundary width. The well oriented boundaries in the annular dark field image are very sharp and indicate that the boundaries could be as narrow as 2nm. Although a measure of the boundary width can be obtained, it is not possible to determine the shape of, or the variation of the Cr content within, the boundary region. In the following discussion the boundary will be assumed to have a uniform Cr concentration and to be of width w through the entire thickness of the section.

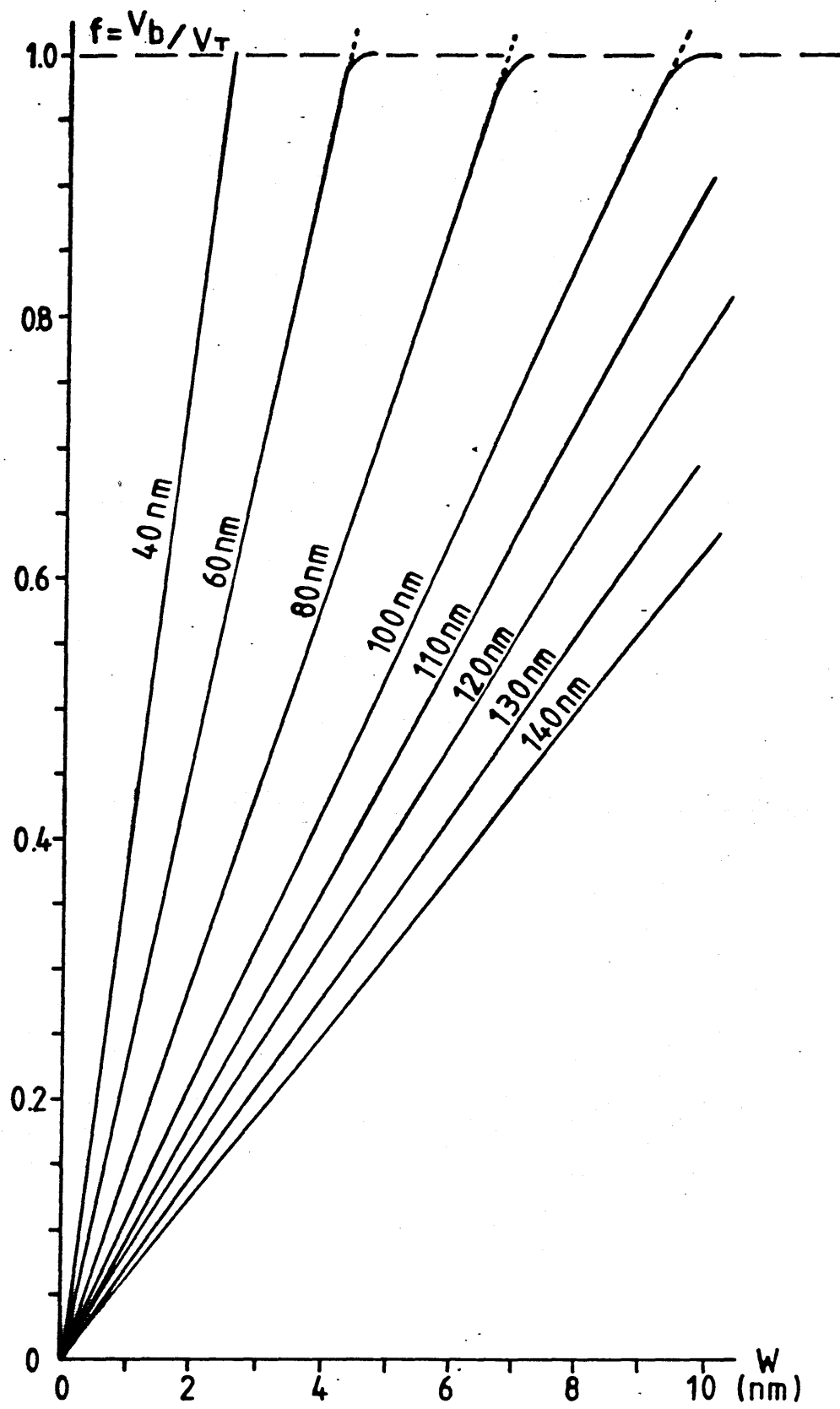


Figure 6.7: Graph of the ratio $f = V_b/V_T$ against boundary width, w , for various specimen thicknesses, t .

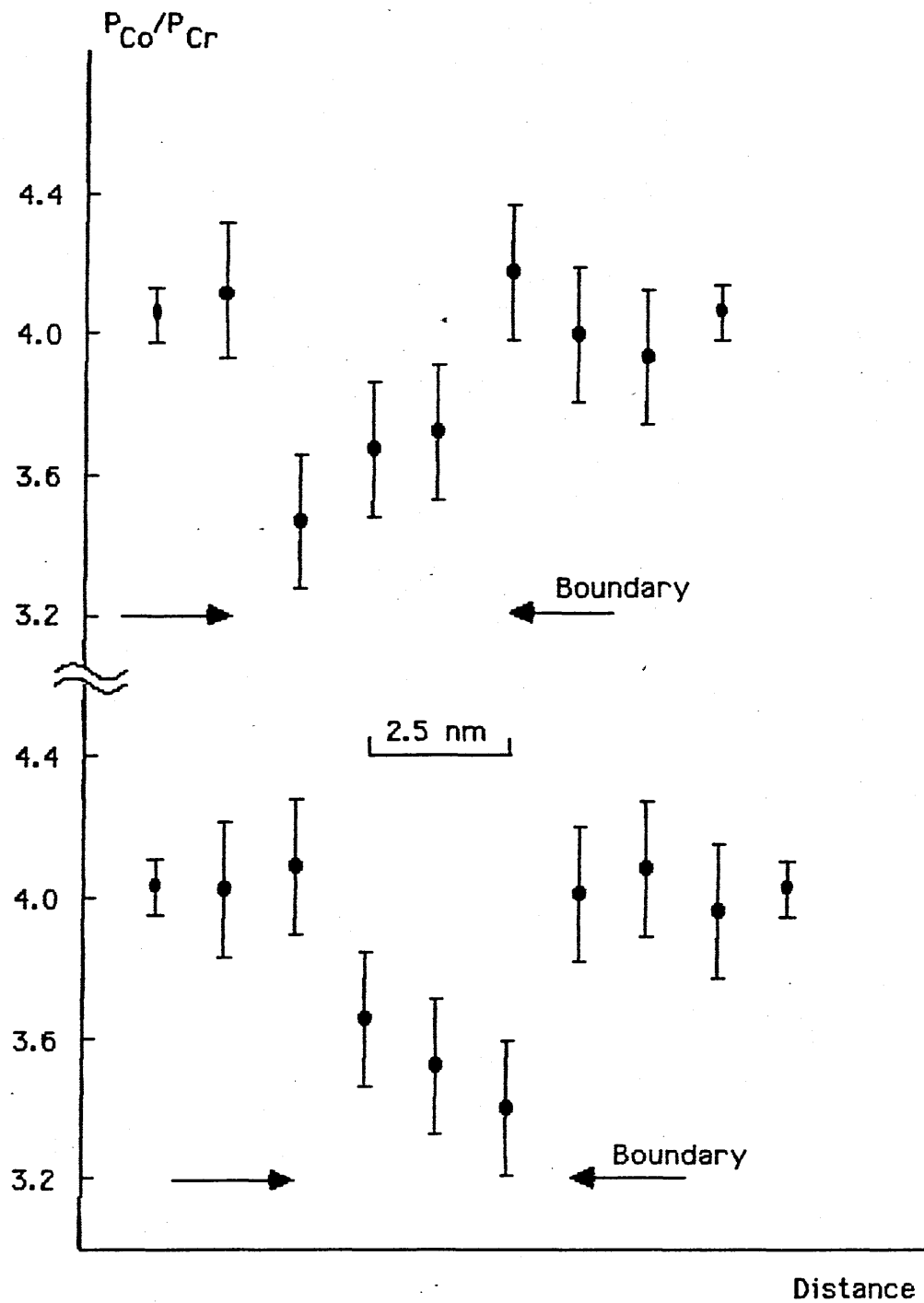


Figure 6.8: Two traces of the ratio P_{Co}/P_{Cr} across column boundaries in section TS3.

Effects of beam spreading and boundary width:

The atomic percentage of Cr deduced from x-ray spectra from the boundaries is given by

$$x' = x_b f + x_c (1-f)$$

Therefore if f and x_c are known, the atomic percentage of Cr in the boundary region can be calculated using the equation:

$$x_b = x'/f - x_c(1-f)/f \quad (6.4)$$

Assuming a boundary width of 2nm, the Cr enrichment at the column boundaries in samples TS1 and TS2 were found to be 10.1 at. % and 7.7 at. %-respectively, as shown in table 6.3. Therefore the actual Cr enrichment at the boundary region is very much greater than the 1.5 at. % apparent from the raw x-ray data.

The value of x_b is very dependent on the value of f , which in turn, is dependent on the particular model used for the boundary region. However, the 2nm width assumed in the analysis agrees well with the measured boundary width in the ion beam thinned sample, and with the sharpness on the boundaries in the dark field images.

6.6 Summary and Discussion

It has been shown that it is possible to measure local variations in the elemental composition of thin film specimens using energy dispersive x-ray microanalysis in the HB5 STEM. This microanalysis can be carried out at a very high spatial resolution, which is limited in most cases, not by instrumental factors, but by electron scattering in the specimen itself. For very thin specimens, in which beam broadening is not significant, the spatial resolution available is set by the probe diameter; under optimum imaging conditions this can be less than 1nm. The ability to use EELS to measure the local specimen thickness at the positions where EDX microanalysis has been carried out allows the effects of beam broadening within the sample to be taken into account.

The HB5 therefore, is capable of providing not only very high resolution information on the magnetic and crystallographic structures of thin film specimens, as shown in chapter 3 , but can also provide information on the variation of elemental composition across these samples on the scale of a few nm.

In the CoCr sections studied here, a Cr enrichment of at least 1.5 at. % was measured at the column boundaries. This Cr enrichment will decrease the saturation magnetisation at the column boundaries and reduce the exchange coupling between the individual columns. If the model assumed for the extent of this boundary region is valid, then the Cr content in the boundary region is greater than 25%, in which case the boundary will be non-magnetic. A trace of the P_{Co}/P_{Cr} ratio across a boundary gave the boundary width as $<5\text{nm}$; from the dark field images of the samples studied, the column boundaries appear to have a width of $\sim 2\text{nm}$, therefore the boundary width assumed in the analysis seems justified. The precise shape of the boundary is, however, not so easy to determine, and this means that the exact extent of the Cr enrichment at the column boundaries cannot be ascertained.

There are a number of possible reasons for the segregation of the Cr atoms within this type of specimen:

- 1) precipitation of a separate, Cr-rich phase;
- 2) formation of Cr oxide during film growth;
- 3) segregation of Cr for thermodynamic reasons.

The first possibility is ruled out as the temperatures required are too high. The second possibility was investigated by Philips at Eindhoven using Auger electron spectroscopy on the films studied here (Chapman *et al* 1986). No oxygen was detected in the films, indicating that the oxygen content was below the detection limit of the technique used. This limit is 0.5 at. %. If the assumption is made that a Cr to O ratio of 1:1 is required for oxide segregation, then at least 1.5 at. % O would need to be present to explain the Cr segregation; therefore this possibility is also ruled out. As for the third possibility, if surface bond breaking, and bulk elastic strain energy are considered to be the main factors

behind the driving force for segregation (Abraham and Brundle 1981), then CoCr is indeed an alloy in which the minority component segregates.

Table 6.1 Summary Of Results Of X-ray Microanalysis

Sample	Thickness (nm)	P_{Co}/P_{Cr} (Columns)	P_{Co}/P_{Cr} (Boundaries)
TS1	130	3.52 ± 0.04	3.24 ± 0.04
TS2	100	3.65 ± 0.03	3.32 ± 0.03

Table 6.2 Effect Of Sample Thickness On Volume Analysed

Sample	Thickness (nm)	V_T (nm ³)	d (nm)
TS1	130	22500	15
TS2	100	8000	10
TS3	60	1100	5

Table 6.3 Percentage Cr Content Of Sections

Sample	x_c	x'	f	x_b
TS1	20.9	22.3	0.14	31
TS2	20.3	21.9	0.21	28

CHAPTER 7

INVESTIGATION OF MAGNETIC STRUCTURE IN CROSS-SECTIONS OF PERPENDICULAR MAGNETIC RECORDING MEDIA

7.1 Introduction

As stated in chapters 5 and 6, sputtered CoCr films with a strong c-axis texture and columnar microstructure are of interest to the magnetic recording industry as suitable media for perpendicular recording. These films generally require to be >200nm thick if they are to sustain a perpendicular magnetic domain structure. Furthermore, it has been found that the read and write characteristics of the CoCr media are improved if a soft magnetic underlayer, such as permalloy, is deposited on the disk substrate prior to the deposition of the CoCr layer (Iwasaki *et al* 1979). This soft magnetic underlayer is thought to act as a magnetic keeper, as shown in figure 7.1, and is usually at least as thick as the CoCr layer. Thus on a perpendicular magnetic recording disk, the total thickness of magnetic material is of the order of 400nm or more.

The reason for interest in perpendicular recording is that it should increase the information storage densities available with magnetic recording. Therefore the size of reverse domains in a perpendicular magnetic recording medium should be substantially smaller than those in a longitudinal medium, in which case the domain size will be

$\ll 1000\text{nm}$. The only techniques which have a high enough resolution for detailed investigation of the bit patterns in these high density media are electron microscopical techniques. These include type I contrast and electron spin analysis, in the SEM, which are sensitive to stray fields and surface magnetism respectively, and Lorentz transmission electron microscopy which was the technique used here. The major drawback with this technique is the fact that, even using 100keV electrons, the maximum thickness of polycrystalline specimen that can be examined in the transmission electron

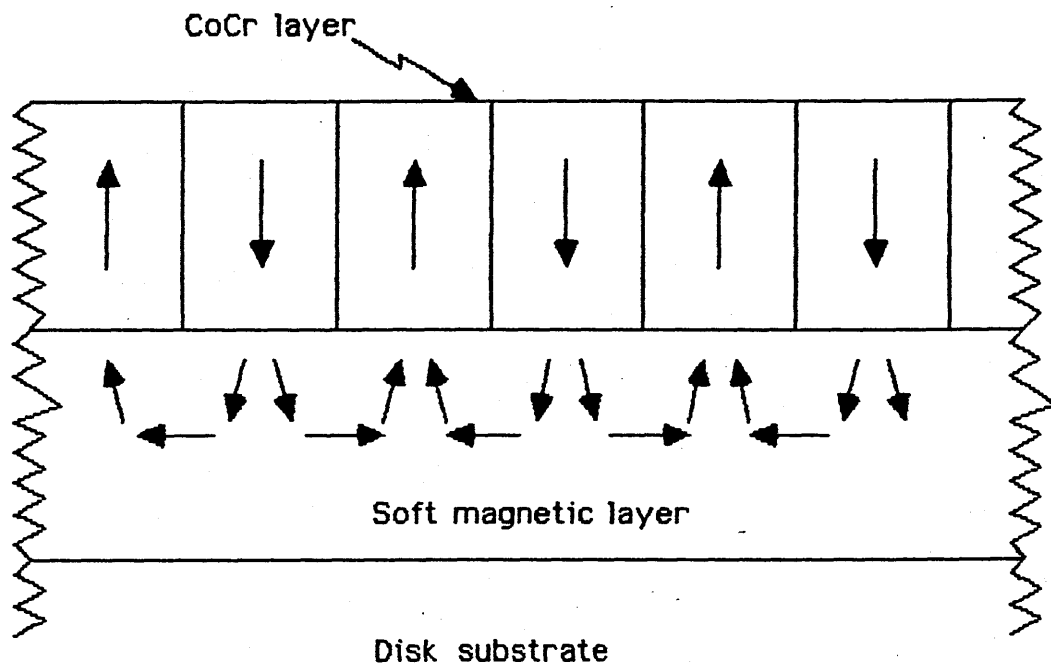


Figure 7.1: Proposed magnetic keeper structure of soft magnetic underlayer of double layer perpendicular recording medium

microscope is ~150nm. Therefore, in order to investigate the magnetic structure in a typical perpendicular magnetic recording medium, consisting of perhaps 400nm of CoCr on top of 400-900nm of a soft magnetic material, using Lorentz microscopy, the medium has to be thinned in some way.

Reasons for transverse sectioning of films:

There are two basic ways in which a single or double layer perpendicular magnetic recording film can be thinned:

- i) back thinning in which layers from the bottom (and/or top) surface are removed by mechanical, or ion beam, polishing, or by etching;
- or ii) transverse sectioning, in which the recording material is sandwiched between two layers of epoxy resin and sectioned perpendicular to the film surface with a microtome; this can provide sections <100nm in thickness. If thinner transverse sections are required, they can be produced by ion beam thinning of microtomed sections in which silicon, rather than epoxy, has been used as the sandwich material.

Back thinning, sufficient for observation in the TEM, would substantially reduce the thickness of the CoCr layer and would remove any soft magnetic layer completely. The reduction in the thickness of the CoCr layer would require either the removal of the initial growth layer, and/or of some of the well developed columnar structure. In neither case could the magnetic structure of the resulting film be expected to bear a strong resemblance to the magnetic structure of the original film. Transverse sectioning, on the other hand, would retain any soft magnet underlayer, and would not reduce the thickness of the CoCr layer. Therefore, as the film thickness along the expected easy axis direction remained unchanged, the magnetic structure in the cross-sections would be expected to be similar to that of the initial

film. Moreover, to be able to observe magnetic structure in the electron microscope the magnetisation must have a component perpendicular to the beam direction. A back thinned specimen, if it did retain the magnetic structure of the original film, would have to be tilted in the electron microscope before the magnetisation within the domains had any effect on the electron beam, although the domain walls should be visible. With transverse sectioning, the magnetisation in both the CoCr and any soft magnetic underlayer would be perpendicular to the electron beam without the specimen having to be tilted. Ouchi and Iwasaki (1982) have successfully used this technique to obtain Fresnel images of perpendicular magnetic domains in a 1 μ m thick CoCr film.

For the above reasons, transverse sectioning was chosen as the method of preparation for both the single layer and the double layer perpendicular magnetic recording films investigated here.

The specimens investigated:

The magnetic structures associated with three different films were investigated in this chapter and the three films had the following nominal layer thicknesses:

- 1) 900nm NiFe ; 15nm Ti ; 400nm CoCr
- 2) 200nm Ti ; 450nm CoCr
- 3) 500nm CoZrNb ; 500nm CoCr

The CoCr layers were R.F. sputtered using alloy targets of composition 78.5% Co, 21.5% Cr, and the NiFe layer was sputtered using a target of composition 79% Ni, 21% Fe. The composition of the CoZrNb layer is not known. The films were produced by Philips Research Laboratories in Eindhoven, and the cross-sectioning was also carried out by Philips. The specimen preparation is discussed in more detail by Luitjens *et al* (1985). Film 1 corresponds to sample TS2 in chapter 6, and in that chapter it was shown that the column boundaries in the CoCr layer of this film are Cr-rich. The other two films were produced by the

same R.F. sputtering technique as 1 and therefore it is assumed that Cr segregation to the column boundaries also occurs in these two films.

Requirements for preliminary investigation:

Preliminary studies of the cross-sections investigated in this work were carried out on a JEOL 1200EX conventional transmission electron microscope (CTEM). As the widths of the cross-sections studied were between 650nm and 1300nm it was necessary to use magnifications of the order of 5000x if structure within the sections was to be seen. However, it was also essential that the specimens were not subjected to a magnetic field in the electron microscope, if the magnetic structure was to be investigated. These two constraints of high magnification and zero magnetic field are usually mutually exclusive using the set magnifications available in conventional transmission electron microscopes, as magnifications of greater than ~1000x generally require the objective lens, in which the specimen sits, to be excited. However, the 1200EX is fitted with a free lens controller which allows the individual lens currents to be set by the user to values of his, rather than the manufacturer's, choosing. Using the free lens controller, magnifications of up to 5300x are available without the objective lens having to be used. A fuller description of magnification range available using the free lens controller, on this microscope, is given in appendix C.

Once suitable cross-sections had been identified in the 1200EX, the magnetic structure was investigated using DPC imaging in the HB5 STEM. This allowed any magnetic structure within the CoCr and soft magnetic layers, together with the stray fields from the cross-sections, to be studied at magnifications of up to 100kx.

7.2 Preliminary Observations In The CTEM

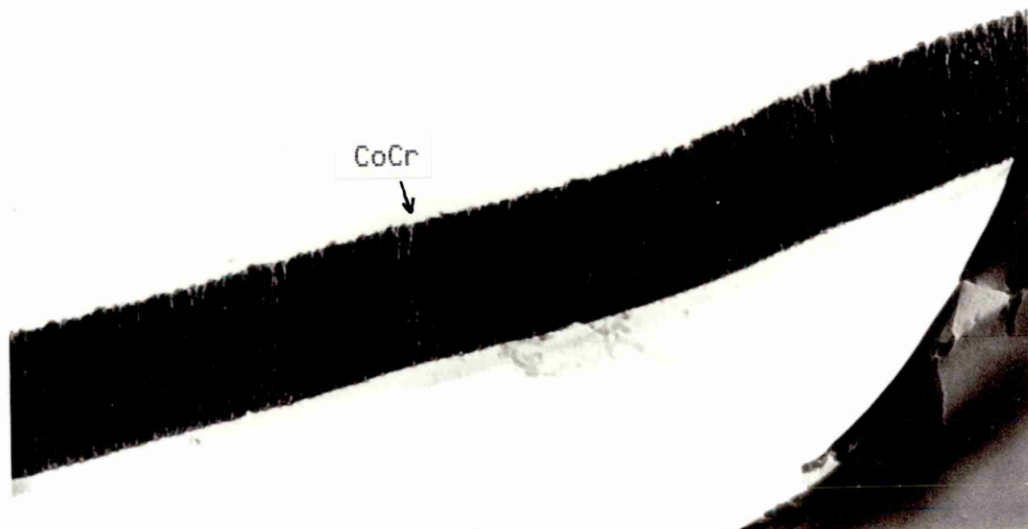
Importance of specimen thickness:

Figure 7.2 shows two cross-sections, a) is from film 1 and b) is from film 3. Both of these micrographs were taken in the 1200EX CTEM operated at an accelerating voltage of 120keV which is 20keV higher than that available on the HB5. These two cross-sections demonstrate the major problem involved in investigating transverse cross-sections; that of obtaining thin, self supporting sections. The cross-section from film 1 is long and straight but is near the thickness limit for imaging with 100keV or 120keV electrons. The cross-section from film 3, on the other hand, is quite thin and therefore can easily be investigated using 100keV electrons but, because it is so thin, it has a number of bends and folds in it. Cross-sections thicker than that in figure 7.2 a), although usually long and straight, were generally too thick for investigation in the HB5 STEM, while those thinner than that in figure 7.2 b) tended to curl up. Cross-sections of a total of 12 different films were prepared by Philips, but only those from the above three films were long enough, straight enough, and thin enough for investigation in the HB5 at 100keV.

Physical microstructure:

From figure 7.2 it can be seen that the CoCr layers in films 1 and 3 have a columnar structure. The columns lie along the film normal, and have a diameter of between 40 and 70nm. The same physical structure was observed in the CoCr layers of all of the cross-sections investigated here. From the low magnification image of figure 7.2 a) it is difficult to tell if the columns in film 1 are composed of one or more crystallites, because the cross-section is quite thick and the contrast level is subsequently low. However, from figure 7.2 b), where the section is much thinner, it can be seen that, in general, the columns are composed of a number of crystallites near the bottom of the CoCr layer, while at the top of the layer they consist of one crystallite. This

a)



b)

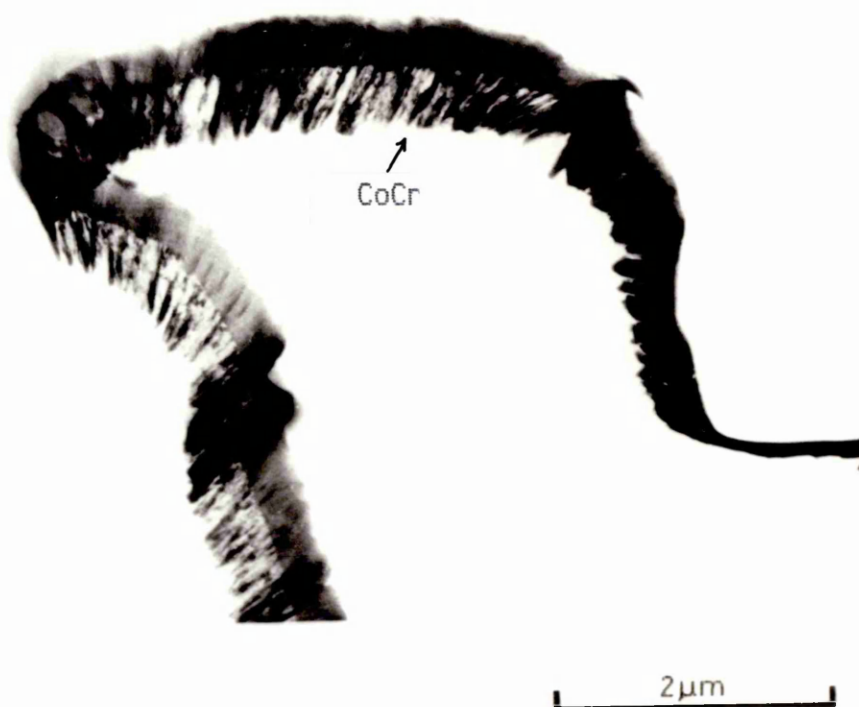


Figure 7.2: Low magnification bright field images of transverse sections a) from film 1 and b) from film 3

indicates that in the initial growth layer of the film the columnar microstructure is not well developed. As the film thickness increases, the well oriented crystallites grow at the expense of the less well oriented crystallites and therefore eventually each column consists of one, well oriented, crystallite (as proposed by Ouchi and Iwasaki 1984).

The columnar microstructure in these two films takes between 100 and 200nm to develop to the stage where each column is composed of only one crystallite. Due to the different contrast levels from the cross-sections under investigation, which is a result of the large difference in the section thicknesses, it is difficult to tell in which, if either, of these two films the columnar microstructure develops earlier.

The microstructure of the two different soft magnetic underlayers used in this work is also shown in figure 7.2. The NiFe underlayer, in figure 7.2 a), is polycrystalline, with a columnar microstructure similar to, but not as pronounced as, that of the CoCr layer. The CoZrNb layer in figure 7.2 b), on the other hand, has very little contrast and selected area diffraction showed it to be amorphous.

Figure 7.3 shows a cross-section of film 2, where the CoCr was deposited onto a 200nm thick Ti layer. The Ti layer is polycrystalline and has a columnar microstructure similar to that of the CoCr layer. Many of the columns in the CoCr layer of this film appear to be a continuation of the crystallites in the Ti layer. This indicates that the columnar structure of the CoCr layer develops very easily on top of the Ti layer. Between the NiFe and the CoCr of film 1 there is a thin layer of Ti which is easily visible in figure 7.2 a). This was deposited between these two layers to aid the development of the columnar microstructure in the CoCr layer.

Preliminary investigation of magnetic structure:

The magnetic structure of the cross-sections was investigated using the Fresnel mode of Lorentz microscopy in the 1200EX CTEM. Once again the maximum magnification available without subjecting the

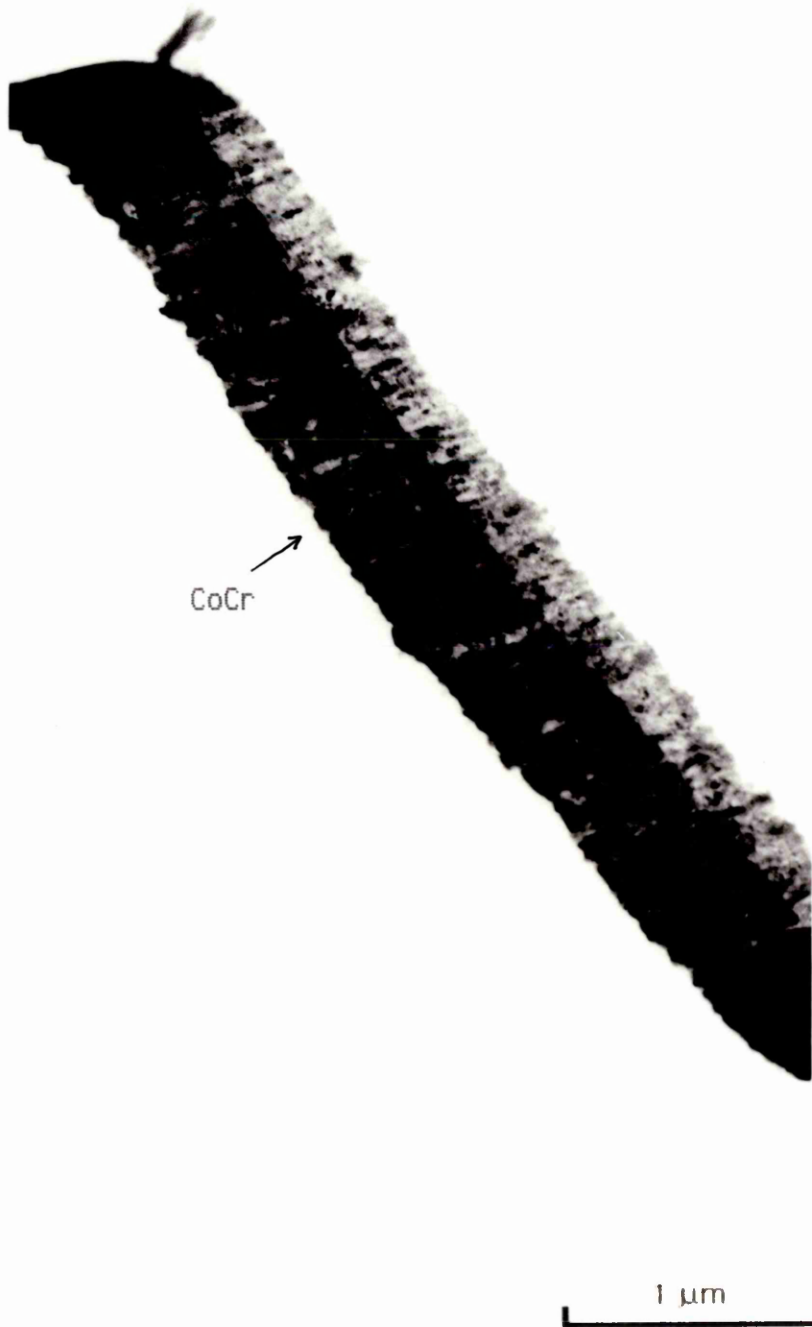


Figure 7.3: Low magnification bright field image of a transverse section from film 2

specimen to a magnetic field was the 5300x obtainable using the free lens controller. This is quite a large magnification for conventional Lorentz microscopy on an electron microscope with a side entry goniometer in which the specimen height is not easily varied. Even at this magnification, however, no magnetic structure was observed in either the CoCr layers or the soft magnetic layers of these cross-sections using this technique. This was surprising as investigation of the macroscopic magnetic properties of these film by Philips had indicated that all of these layers were magnetic.

The lack of magnetic contrast in these cross-sections could be due to the technique used not having a high enough resolution to detect the magnetic structure present. The magnification used was obtained by setting the intermediate lens currents to values at which they are not normally operated. Furthermore, only the weaker, intermediate stigmator was available in this mode of operation, not the main objective stigmator. Hence it was found that the astigmatism could not be fully corrected at this magnification leading to a reduction in resolution. In order to investigate whether or not there was magnetic structure in these cross-sections, they were put into the HB5 STEM for investigation using DPC imaging.

7.3 Investigation Of The Soft Magnetic Underlayers

As it was expected that the magnetic structure in the soft magnetic layers would be easier to detect than that in the CoCr layer, these were investigated first:

CoZrNb underlayer:

The cross-sections of film 3 were found to be very thin and subject to folding and curling. Subsequently there were very few long, straight sections of specimen, in which the cross-section was not folded over on itself, and which were therefore suitable for observation using DPC imaging. Those areas that did consist of a single thickness of cross-section were very short ($\sim 2\mu\text{m}$) and no magnetic structure was

seen in either the CoZrNb or the CoCr layer in these regions. Although no magnetic structure was seen in either layer, stray fields were seen beyond the edges of the cross-sections and these will be discussed in section 7.4

NiFe underlayer:

Three distinct magnetic structures were observed in the NiFe soft magnetic underlayer of film 1 using DPC imaging in the HB5 STEM. These are shown in figures 7.4 to 7.6. In each of these figures a) and b) are DPC images, of the cross-section, sensitive to two orthogonal components of magnetic induction; c) is a schematic of the magnetic structure seen in the two DPC images; and d) is an incoherent bright field image of the section.

Figure 7.4 shows the simplest magnetic structure seen in the soft magnetic underlayer of this film. The NiFe layer, in the part of the section imaged here, is uniformly magnetised along its length. This is what would be expected of a long, thin strip of a soft magnetic material such as NiFe. This uniformly magnetised strip illustrates one advantage of DPC imaging over Fresnel Lorentz microscopy. A uniformly magnetised area can be identified using DPC imaging; the Fresnel mode, on the other hand, can only detect changes in the magnetisation within a film.

The small scale contrast within the NiFe and CoCr layers is non-magnetic contrast from the crystallites within these layers. If there is any magnetic structure within the CoCr layer, it is on a scale comparable to the crystallite size and is hidden by the strong contrast from the crystallites.

The uniform magnetic structure seen here was typical of a number of areas in the cross-sections of film 1. However, more complicated magnetic structures were also seen in these same cross-sections.

Figure 7.5 shows the second type of magnetic structure seen in the NiFe layer of film 1. This consists of a series of small domains with approximately 90° walls between them.

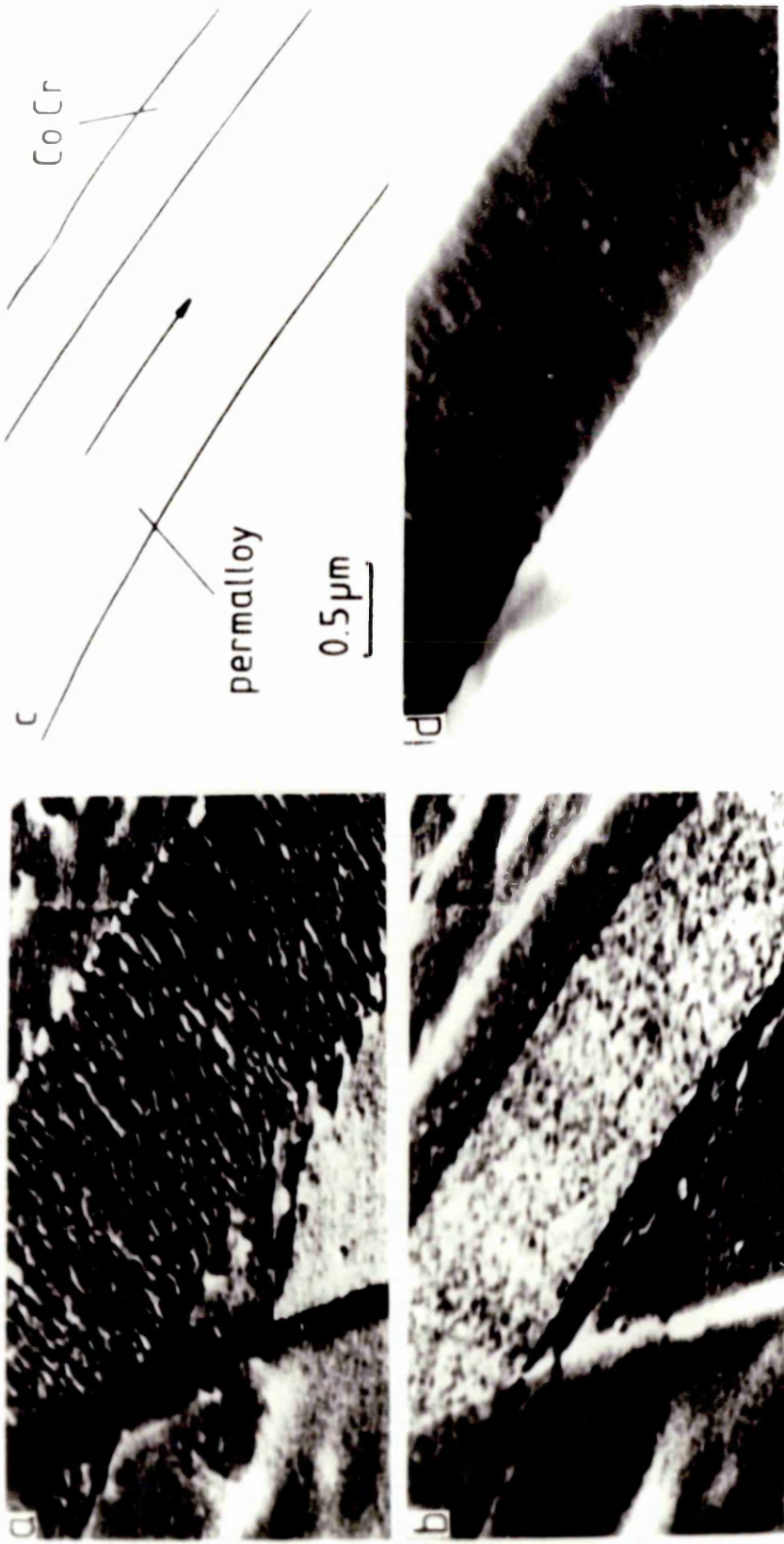


Figure 7.4: Simplest magnetic structure seen in the NiFe layer of film 1. a) and b) are DPC images sensitive to the components of magnetisation shown, c) is a schematic of the magnetic structure deduced from a) and b), and d) is an incoherent bright field image of the same area.

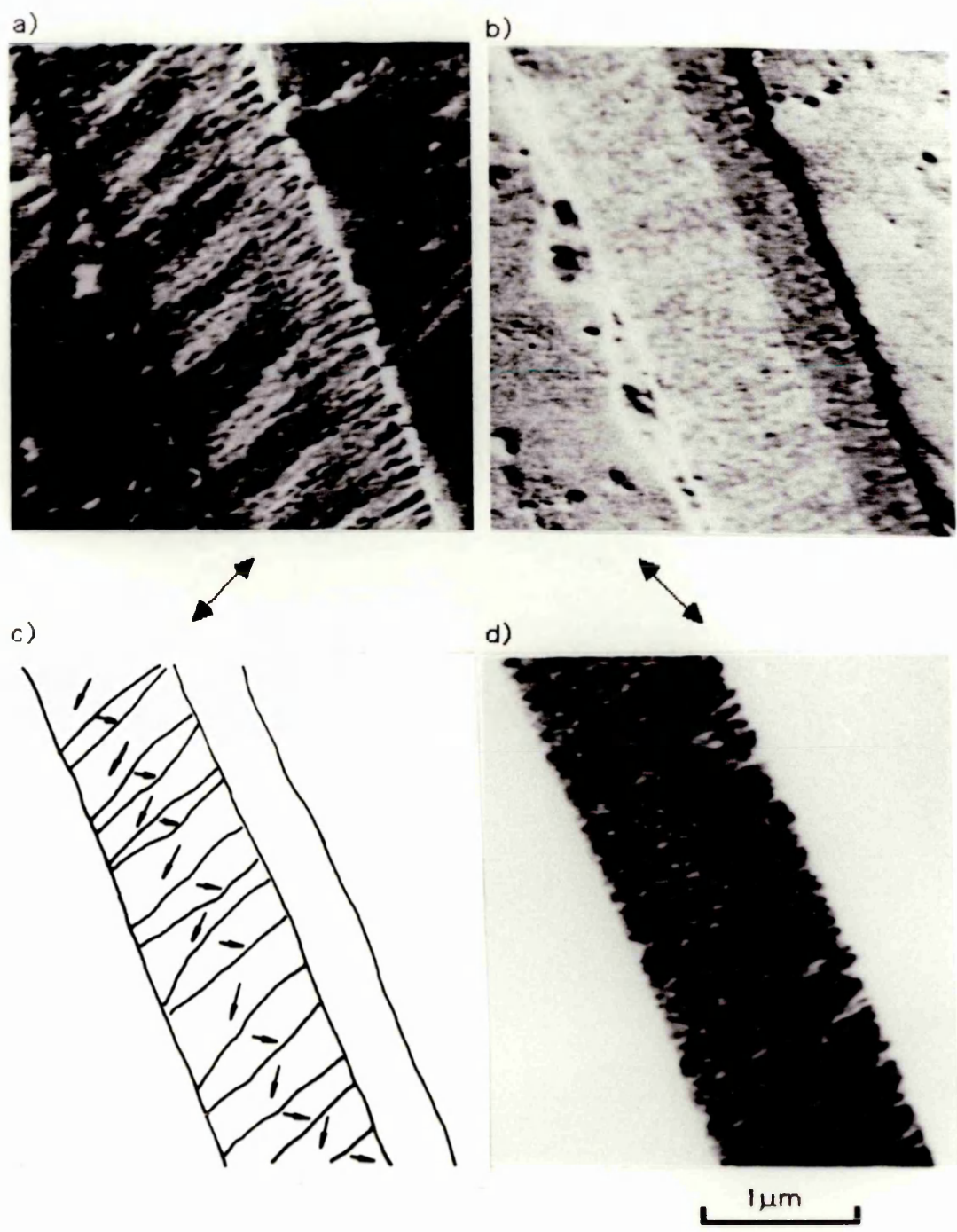


Figure 7.5: Second type of magnetic structure seen in the NiFe layer of film 1; a) and b) are DPC images sensitive to the components of magnetisation shown; c) is a schematic of the magnetic structure and d) is an incoherent bright field image.

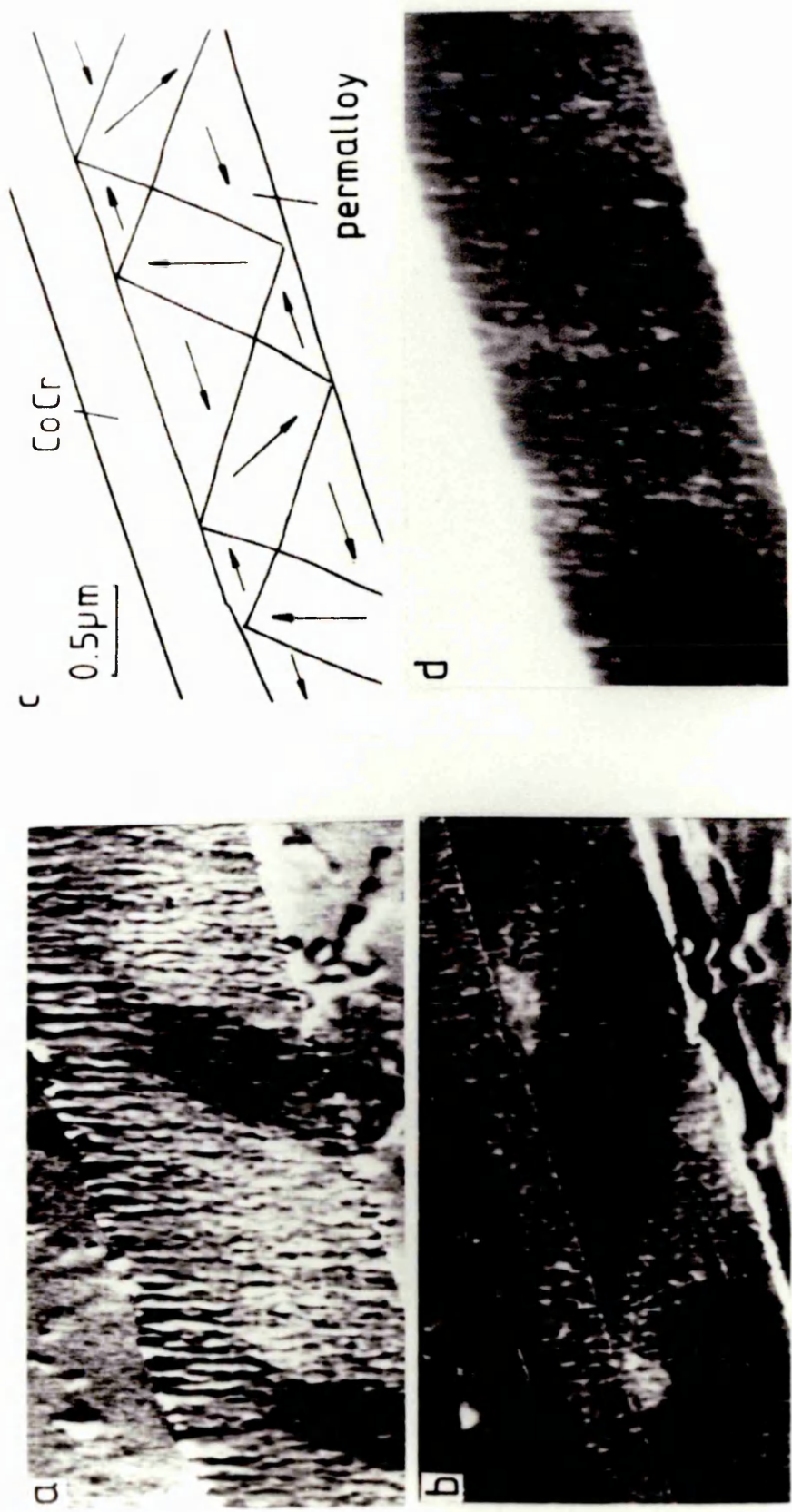


Figure 7.6: Third type of magnetic structure seen in the NiFe layer of film 1. a) and b) are DPC images sensitive to the components of magnetisation shown, c) is a schematic of the magnetic structure deduced from a) and b), and d) is an incoherent bright field image of the same area.

The average domain width in this part of the cross-section is $<300\text{nm}$. At the highest magnification used in the CTEM, the domain walls would have been less than 2nm apart, and although this would not be obvious on the viewing screen, it should have been recorded on the photographic film used. However, strong diffraction contrast from the crystallites, on the same scale as the domains would tend to obscure the domain wall contrast. The result, therefore, was that, even although the crystallite contrast was somewhat reduced because of the large defocus, no magnetic structure was observed.

The domain structure in this part of the NiFe layer is similar to that observed in the Co film discussed in chapter 4, although the magnetisation in this sample is at approximately 45° to the sample edge. In the case of the Co film there were large stray fields beyond the edge of the film; here, there do not appear to be any stray fields, at least, on the NiFe side of the cross-section. This may be because the domains are very small and therefore any stray fields from them will be very limited in extent, in which case, the strong contrast from the backing material at the edge of the section would obscure them. There is an indication of stray fields on the CoCr side of the cross-section although the contrast is not very strong.

The third type of domain structure observed in the NiFe layer of this film is shown in figure 7.6. This structure is more complicated than that in figure 7.5, and there is a degree of flux closure within the NiFe layer of the film. There also appear to be some stray fields from this part of the cross-section, on both the NiFe side, and the CoCr side of the film.

The reason for the different types of magnetic structure is not known. One possibility is that the thickness varies markedly within the cross-sections. However, variations in thickness between the sections should be more marked than variations within individual sections. Therefore it would be expected that the magnetic structure would be constant within any given cross-section and would vary between the different cross-sections of film 1. This was not the case, all three

magnetic structures were seen in a number of different cross-sections and the structure was seen to vary from place to place within a given cross-section. Figure 7.7 shows such an area of cross-section in which the magnetic structure changes from small domains lying along the film normal, similar to those in figure 7.5, to the more complicated structure seen in figure 7.6. It does not, therefore, appear that the different magnetic structures correspond to different section thicknesses. The possibility that there are marked local thickness variations within the cross-sections could be investigated using EELS; however, time did not permit this to be done in this work. Another possible reason for the change in magnetic structure is that the magnetic properties or structure of the CoCr layer change, or that the coupling between the CoCr and NiFe layers changes, although no evidence has been found to support this. Whatever the reason, the CoCr layer must be having a strong effect on the NiFe layer, as the structures in figure 7.5 and 7.6 are expensive in terms of wall energy and, to some extent magnetostatic energy, compared to the uniformly magnetised structure seen in figure 7.4.

The magnetic structures seen in the soft magnetic layer of these cross-sections may be artifacts produced by the cross-sectioning process. However, although the structure in the NiFe layer of the sectioned film may be quite different from that in an unsectioned film, it is unlikely that the magnetic structure of the CoCr layer has been greatly changed by the sectioning process as CoCr is a much harder magnetic material than NiFe. Therefore although no magnetic structure can be seen in the CoCr layer, the magnetic structure in the NiFe layer indicates that the CoCr layer does, indeed, have a small scale magnetic structure, which is probably similar to that which existed in the original film. If stray fields from the CoCr layer could be observed, this would give an indication of the size of these magnetic structures, therefore in the next section the stray fields from these cross-sections are discussed.

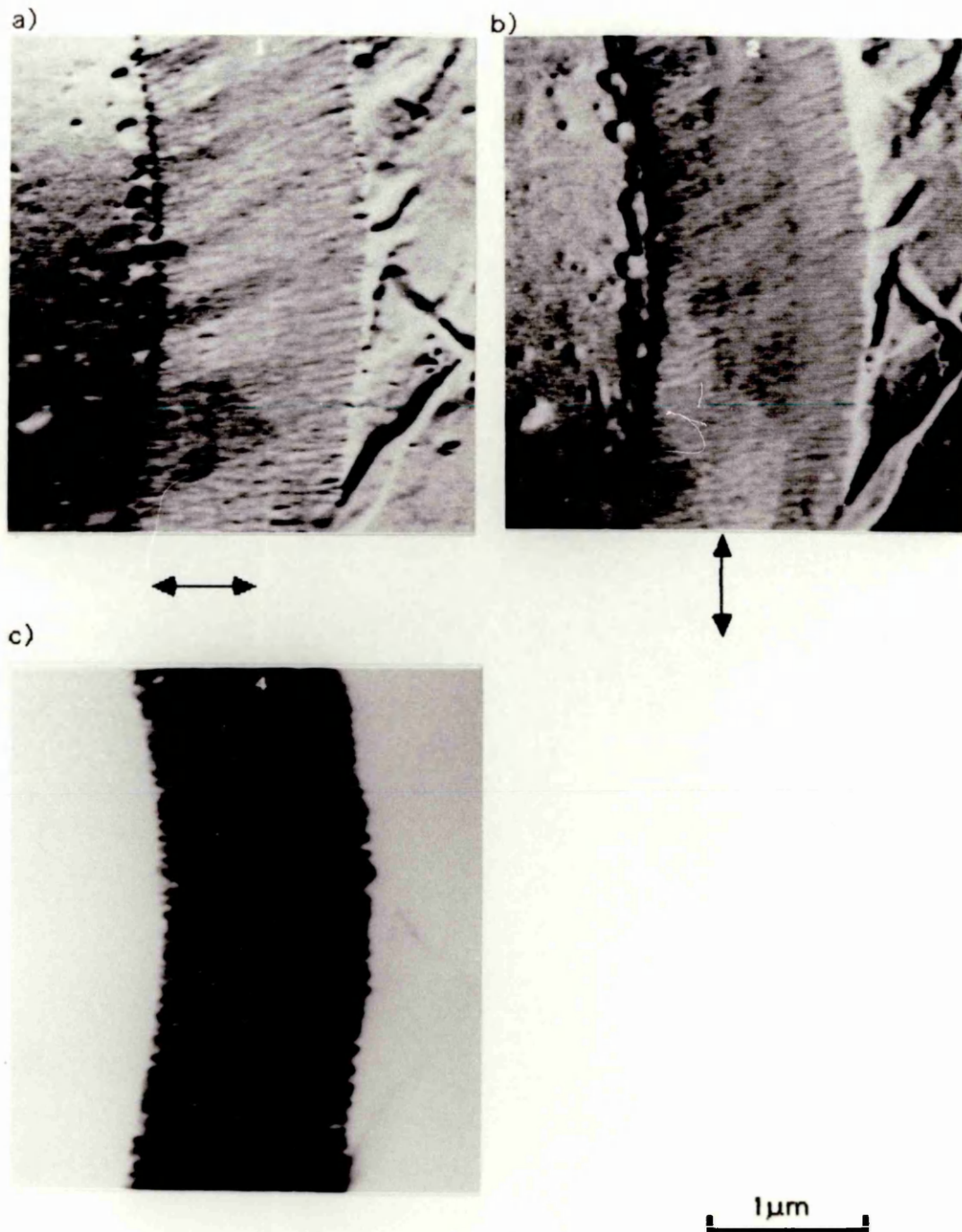


Figure 7.7: a) and b) are DPC images showing the magnetic structure within the soft magnetic underlayer of film 1 changing from type 2 to type 3, c) is an incoherent bright field image of the same area.

7.4 Stray Fields From Single And Double Layer Films

As stated above, stray field distributions were observed beyond the edges of the cross-sections of films 1 and 3, in which there were soft magnetic layers. They were also seen beyond the edges of the cross-sections of film 2, in which the backing material was non-magnetic. In none of the films studied was any unambiguous magnetic structure observed in the CoCr layer; therefore the presence of stray fields from the film with the non-magnetic backing layer was the only direct indication that the CoCr layer was indeed magnetic.

Figure 7.8 shows an area of cross-section, from film 1, in which the magnetic structure in the NiFe layer changes from a uniform magnetisation, to a zig-zag domain structure, similar to that in figure 7.6, and back again. At this point, stray field from the bottom of the NiFe can be seen and it extends for approximately 400nm beyond the bottom of the NiFe layer before the contrast level, and therefore the integrated induction, decreases markedly. This gives an indication of the size of the stray fields which these small domain structures can produce, and which could be expected from the CoCr layers if they had a similar magnetic structure. The stray field from this film originates in the magnetic structure of the NiFe layer rather than in the CoCr layer, although the structure in the NiFe is probably a consequence of the magnetic structure of the CoCr.

An example of the stray fields from cross-sections of film 3 is shown in figure 7.9; once again a) and b) are DPC images sensitive to two orthogonal components of magnetic induction and in this case, c) is the incoherent bright field image. The stray fields appear to be on the CoCr side of this cross-section rather than on the side of the soft magnetic layer. These stray fields have a width of >1000nm indicating that the magnetic structure in this film is slightly larger scale than that in film 1. However, the cross-section shown here has the characteristic folded and curled nature of all of the cross-sections of this film that were studied. Therefore, it is difficult to determine the relationship between the stray fields and the cross-section itself.

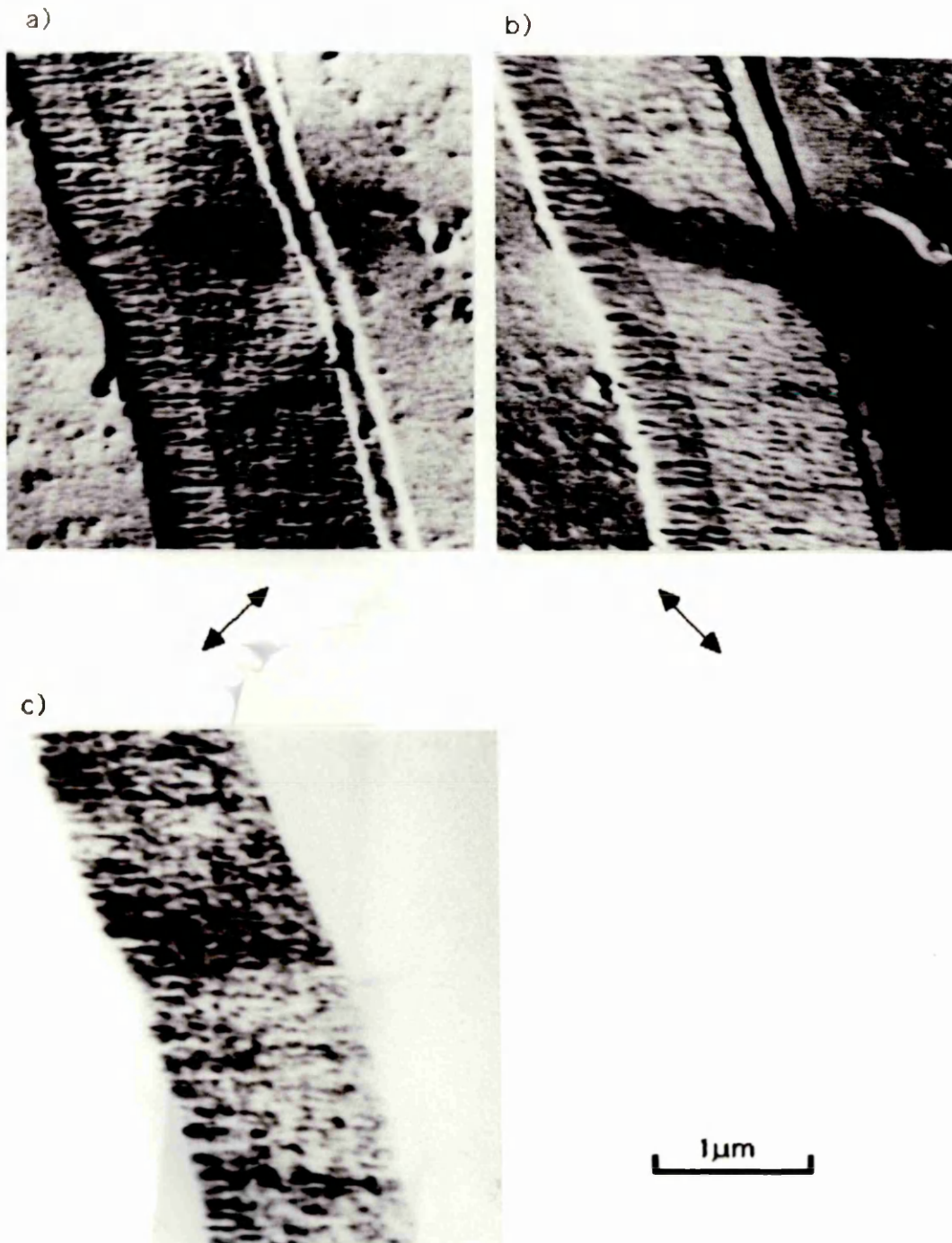


Figure 7.8: Illustration of two different magnetic structures seen within the NiFe layer of film 1; a) and b) are DPC images sensitive to the two directions of magnetisation shown and c) is an incoherent bright field image of the same area. Also seen are the stray fields from the zig-zag domain.

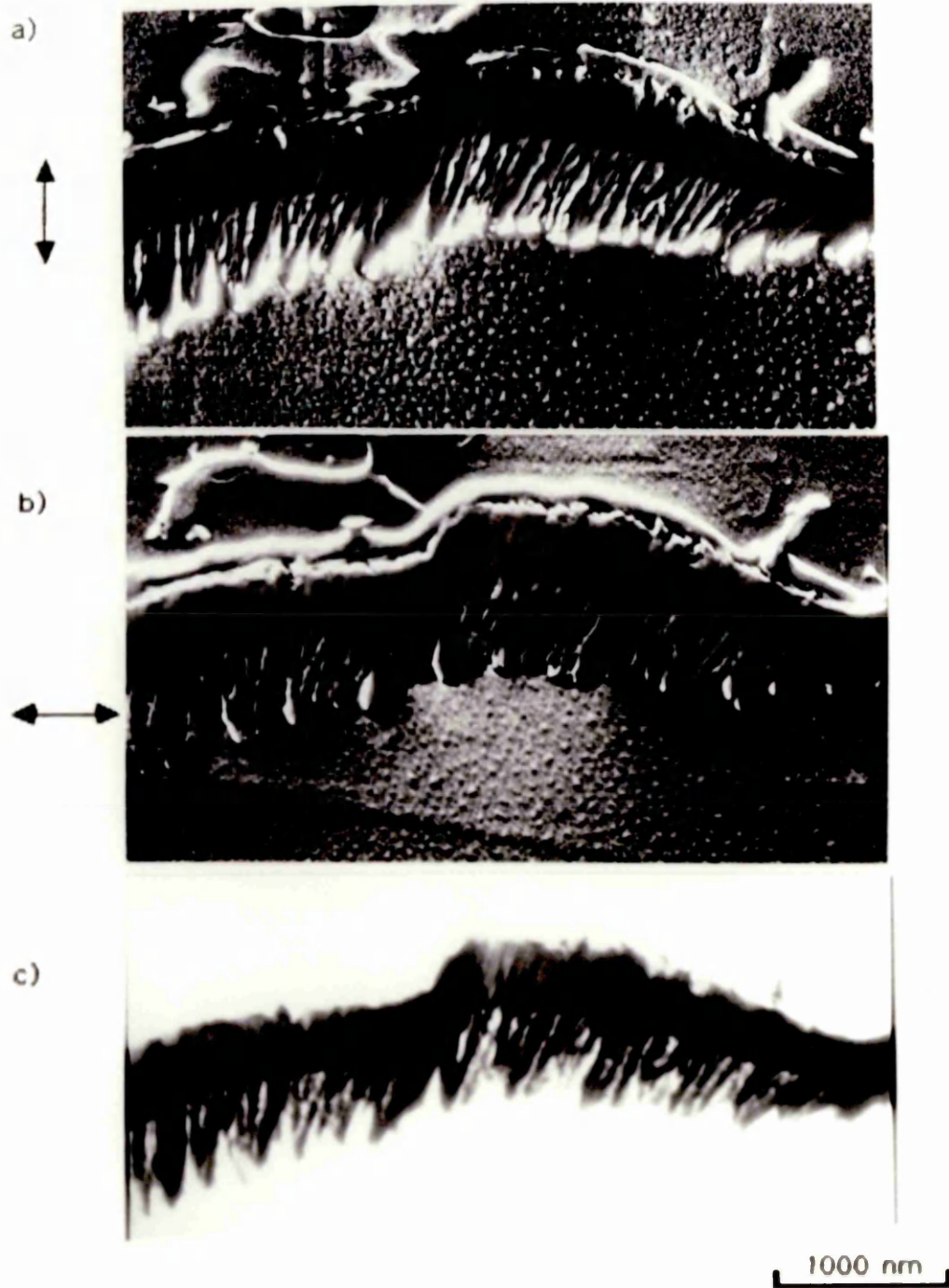


Figure 7.9: a) and b) DPC images showing stray fields from film 3. The arrows indicate which direction of magnetisation each image is sensitive to, c) is an incoherent bright field image of the same area.

The cross-sections which showed the best stray fields from the CoCr layer were those of film 2. The cross-sections of this film were thick enough to be long, straight and self supporting but thin enough for investigation using 100keV electrons. Moreover, the backing layer in this film was non-magnetic Ti and therefore the magnetic contrast seen was due entirely to the CoCr. Figure 7.10 illustrates the type of stray field distributions which were seen from these cross-sections in their as prepared state; a) and b) are DPC images showing the magnetic structure, c) is an incoherent bright field image of the same area. The stray field mapping programs used in chapter 4 were of no use with these stray field distributions, as the stray fields were not extensive enough to allow a sufficiently large sampling area for the pixel averaging routines used to suppress random noise in the image.

The stray field distributions seen in this figure range, in width, from ~130 nm to ~650 nm. There may be areas of stray field less than 130 nm in width; however, if there are the contrast from them is swamped by the very strong contrast from the cross-section edge. From the size of these stray fields it can be deduced that the average domain width in the CoCr of this film is approximately 300 nm. This agrees well with the domain sizes seen in the soft magnetic underlayer of film 1.

In order to make sure that the contrast seen beyond the edges of this section was indeed magnetic, the section was subjected to the magnetic field of the objective lens of the microscope. Figure 7.11 shows the magnetic structure which was observed in the cross-section after the objective lens had been applied. This is the same area of the section as is shown in figure 7.10, and once again a) and b) are complementary DPC images, and c) is an incoherent bright field image. The stray field distribution has changed completely from that in figure 7.10, and the average width of the stray fields from the section in this remanence state appears to be substantially larger than that in the as prepared

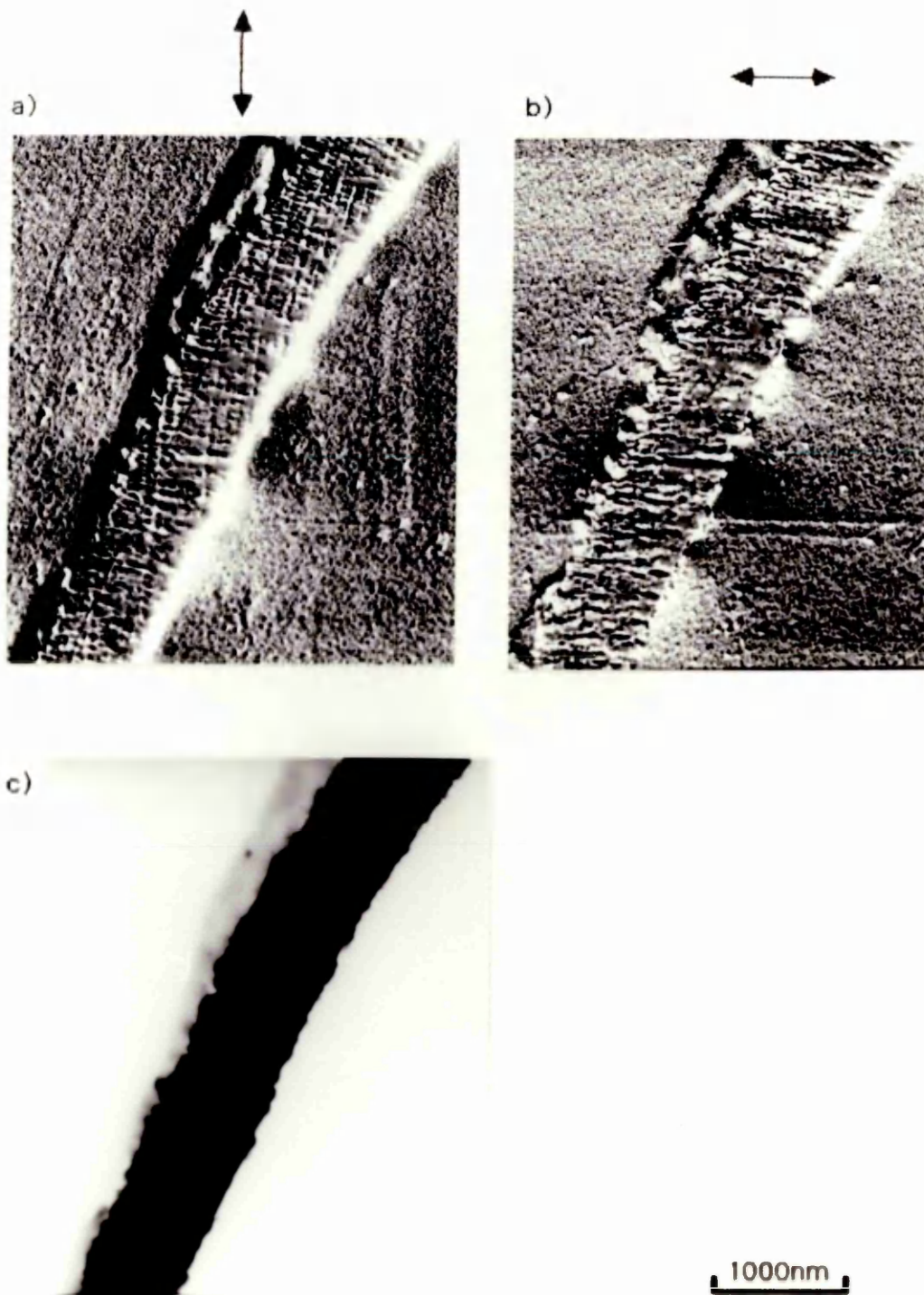


Figure 7.10: Stray fields from a transverse section of film 2 in the as-grown state. a) and b) are DPC images sensitive to the components of magnetisation shown, c) is an incoherent bright field image of the same area.

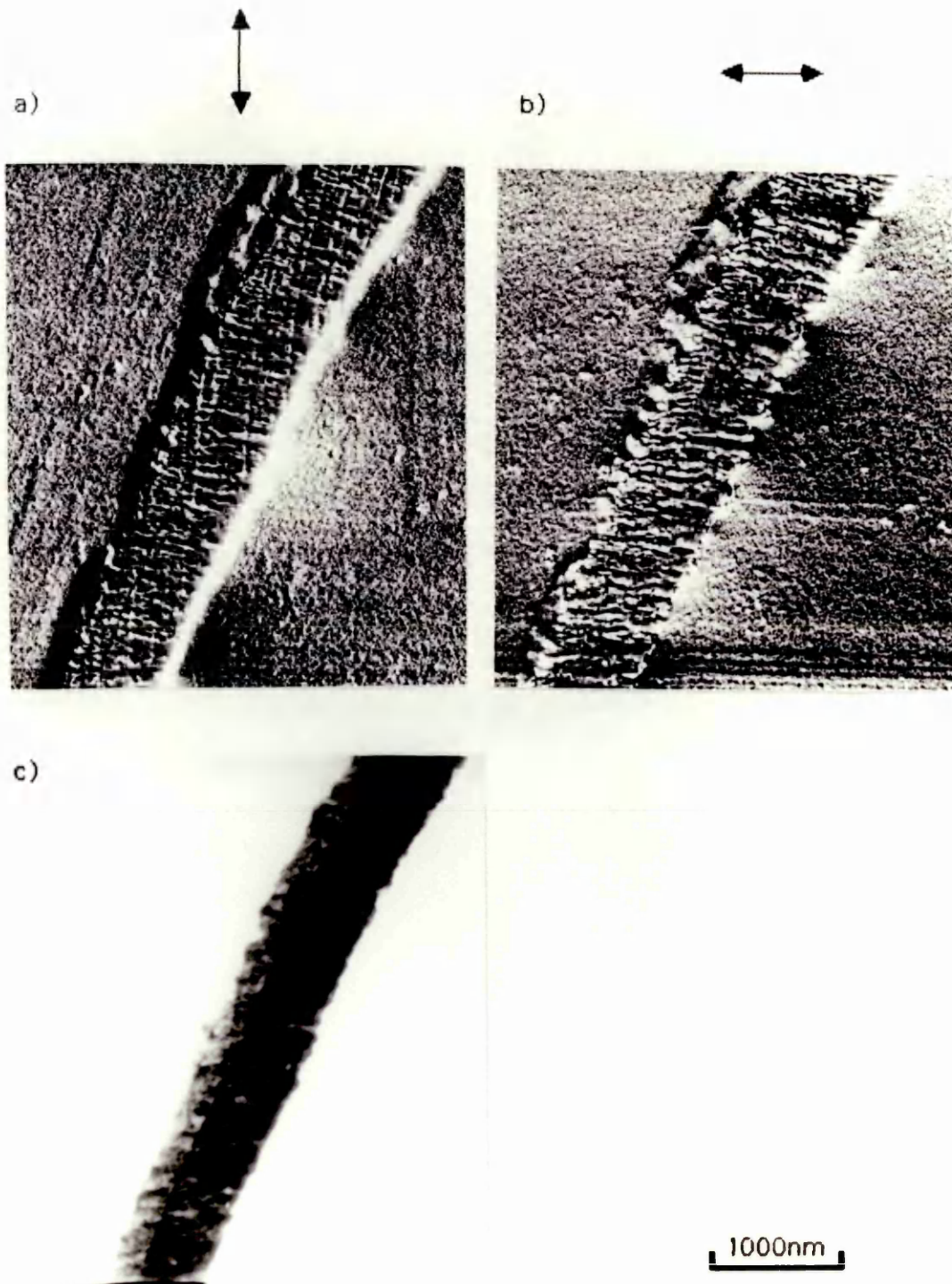


Figure 7.11: Stray fields from a transverse section of film 2 after a strong magnetic field has been applied perpendicular to the plane the section is in. a) and b) are DPC images sensitive to the components of magnetisation shown, c) is an incoherent bright field image of the same area.

state. The average width of the stray field distributions in figure 7.11 is ~ 1000 nm.

7.5 Magnetic Structure Within The CoCr Layer

In figures 7.10 and 7.11 the stray fields from the CoCr layer are easily seen, and therefore it is certain that there is some sort of magnetic structure in the CoCr layer. However, no obvious magnetic domain contrast can be seen in the CoCr layer of any of the images so far presented. This may be because the contrast from the physical structure within this layer is very strong and is obscuring contrast from the magnetic domains. To investigate if this was the case, very high amplifier gains were used to try and bring out any magnetic domain contrast that might be present in the CoCr layer. Figure 7.12 shows the type of images which were produced by this technique; a) and b) are DPC images sensitive to the two orthogonal components of induction shown; and c) is an incoherent bright field image of the same area. There is no contrast from the area outside the cross-section because the material here has a much lower density than the cross-section and the amplifiers have been driven into saturation by the high signal from this area. The material at the top of the cross-section is the polyester substrate on which the metal layers were deposited; this is quite thick and therefore does lead to contrast in the DPC images. In b), which is sensitive to the component of magnetisation along the length of the cross-section, there is no magnetic structure. The structure which can be seen in this image is the interface between the Ti layer and the CoCr layer, and the striations caused by the microtoming process. In figure 7.12 a), however, there is contrast running across the CoCr layer which does not extend into the Ti layer; this contrast is on a slightly larger scale than the contrast from the columns and it is assumed that this is due to magnetic

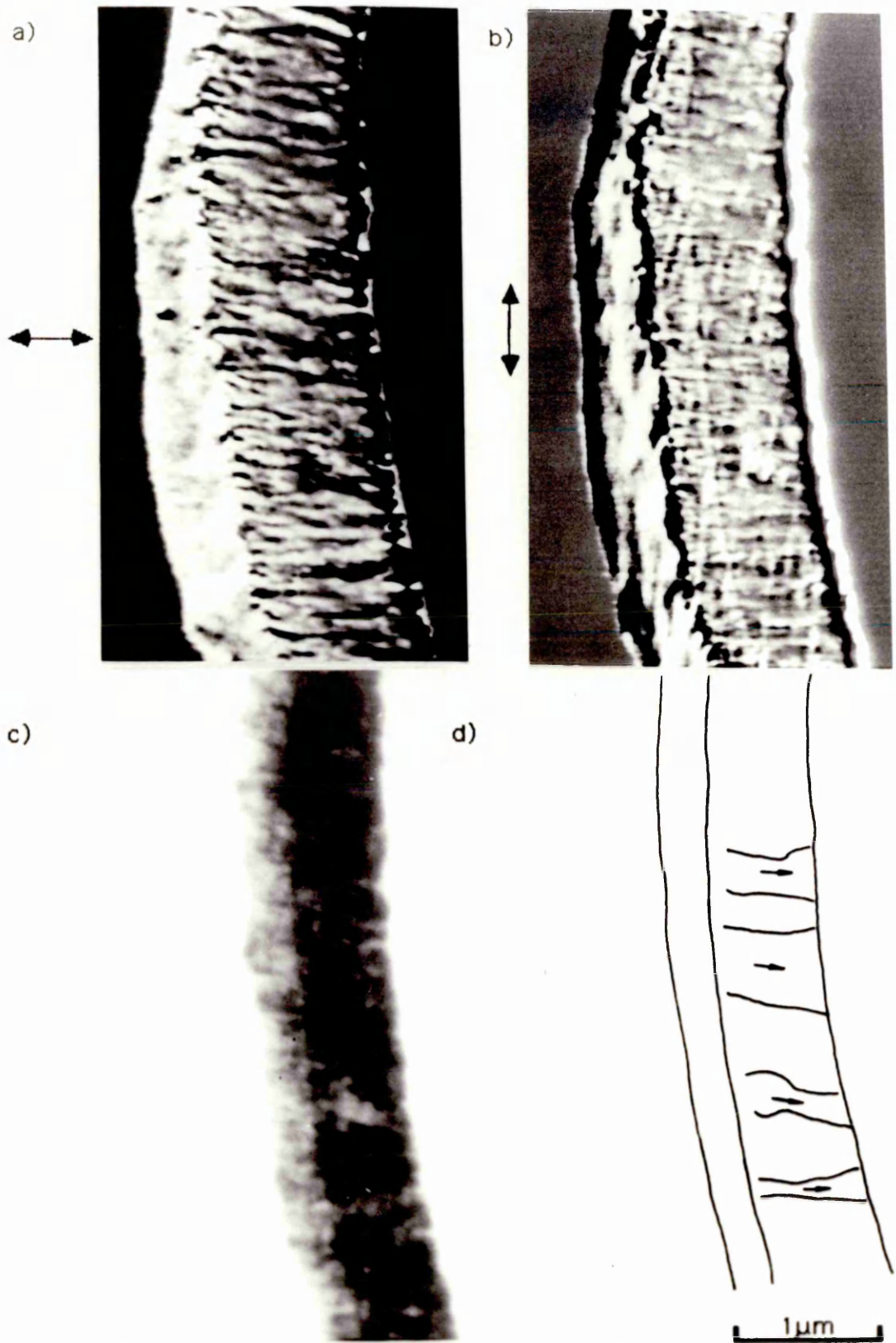


Figure 7.12: a) and b) are DPC images sensitive to the components of magnetisation shown, c) is an incoherent bright field image of the same area of film 2, and d) is a schematic of the possible magnetic structure in the CoCr layer of this film.

structure in the CoCr layer. It is very difficult to distinguish between this magnetic contrast and the strong contrast from the physical structure of the cross-section. Figure 7.12 d) is a schematic of the magnetic structure that can be seen in figure a). The magnetic domains in this figure range from ~80 nm to ~270nm wide, which is in general agreement with the size of the smaller stray fields seen in this sample. From these two images it can be seen that, even with the high resolution available using DPC imaging, the magnetic structure in the CoCr layer is very difficult to detect. This is due to a combination of the strong contrast from the columns within the CoCr, and the limited size and random distribution of the magnetic domains.

7.6 Summary And Conclusions

In this chapter it has been shown that very small magnetic structures can be investigated using Lorentz transmission electron microscopy, in particular the DPC mode of Lorentz microscopy. The technique was applied to cross-sections of single and double layer CoCr perpendicular magnetic recording media, and, although the results from the CoCr itself were disappointing, the stray fields from the cross-section and the structure within the soft magnetic NiFe underlayer were easily detected. The technique requires a sample thickness of ≤ 150 nm; therefore the films under investigation, which were initially ≥ 400 nm thick had to be thinned in some way. The most suitable technique found for thinning these films was transverse sectioning using a microtome. Not only is transverse cross-sectioning capable of providing samples thin enough for investigation using 100keV electrons, it has the added advantage that the magnetic structure within the CoCr layer and any soft magnetic underlayer can be studied simultaneously without the need to tilt the sample in the microscope.

Preliminary investigation of the cross-sections were carried out on a JEOL 1200EX CTEM which was fitted with a free lens controller, allowing magnifications of up to 5300x to be used without subjecting the cross-sections to a magnetic field. The high magnifications available

using the free lens controller were found to be a great help in this work as the cross-sections under investigation were generally ~ 1000 nm wide. Using the 1200EX, the CoCr layers in these films were found to have a columnar microstructure with the columns, of diameter 40 to 70 nm, running along the original film normal. However, as was shown in section 7.2, even at a magnification of 5000x the magnetic structure within the cross-sections could not be seen. Therefore, DPC imaging in the HB5 STEM was used to investigate the magnetic structure of these cross-sections; this allowed magnifications of up to 10^5 to be used without subjecting the specimen to a magnetic field.

Some contrast was seen within the CoCr layer of film 2 which may have been due to magnetic domains in the CoCr. However, the contrast observed was very similar to the non-magnetic contrast from the columns of this film and could not be definitely identified as magnetic. Although no unambiguous magnetic structure was seen in the CoCr layer of these cross-sections, the stray fields from the cross-sections, and the domain structures seen in the soft magnetic layer of film 1, indicated that the CoCr layer was, indeed, magnetic. From the width of the domains and stray field distributions it can be deduced that the magnetic structure within the CoCr layer must be on the scale of a few hundred nanometres. Therefore this material is capable of sustaining the very small domain sizes necessary for high density magnetic recording. Furthermore the magnetic structures observed indicated that the easy direction of magnetisation within the CoCr layer is along the film normal, which is the desired direction for a perpendicular magnetic recording material.

Differential Phase Contrast electron microscopy in the HB5 STEM can, therefore, be seen to be a powerful technique for investigating the very small magnetic domain structures. The use of microtoming to produce thin transverse cross-sections of sample which would otherwise be too thick for investigation in 100keV electron microscopes has also been shown to be a very useful technique. The use of these two techniques together allows the simultaneous investigation of the

magnetic structure in the individual layers of a double layer magnetic recording medium, composed of one hard magnetic material, such as CoCr, with an easy axis along the film normal and one soft magnetic material, such as NiFe, with an easy axis in the film plane. More information on the domain structure in the CoCr layers of these films is likely to be obtained if it becomes possible to investigate cross-sections of films on which a magnetic recording head had written a signal. The regular domain structure of a written pattern should allow the definite identification of magnetic contrast in the CoCr layer. A comparison of the domain structures in written CoCr recording media, with and without soft magnetic backing layers, should allow the effect of these soft magnetic layers to be studied. However, during the period of this work cross-sections from written films were not available, and so these investigations have not been carried out.

CHAPTER 8

CONCLUSIONS AND FUTURE WORK

8.1 General Conclusions

In this thesis it has been shown that a dedicated scanning transmission electron microscope, such as the V.G. Microscopes HB5 STEM at Glasgow, can provide a complete description of the magnetic and physical microstructure of a thin electron microscope specimen.

The crystal structure and orientation of a thin film sample can be ascertained by selected area electron diffraction in almost any transmission electron microscope. Furthermore, details of grain shape and size and the general film morphology can be easily obtained using high resolution imaging in a modern transmission electron microscope. However, although it is possible to carry out the above investigations of the physical microstructure of thin films using a CTEM, the use of a dedicated STEM, such as the HB5, has a number of added advantages, especially for high spatial resolution microanalysis and magnetic imaging:

1) The field emission tip in the HB5 acts as a very small virtual source, less than 10 nm in diameter, which means that a very small area on the specimen can be irradiated without having to greatly demagnify the image of the source. This allows relatively high resolution imaging without the need for the specimen to be situated in the magnetic field of the objective lens.

2) Simultaneous energy dispersive x-ray microanalysis (EDX) and electron energy loss spectroscopy (EELS) can be carried out on the HB5 with a spatial resolution of ~ 1 nm, when the specimen is situated in the magnetic field of the objective lens. In this case the limit on how small a volume of specimen can be analysed is set by fundamental electron scattering within the specimen rather than by instrumental factors.

3) Non-standard detector response functions can be used to

extract the information of interest from the electron distribution emerging from the specimen. For example the antisymmetric response function of the quadrant detector used in this work allows information on the phase of the electron wave to be obtained.

4) The sequential nature of signal acquisition in a STEM allows digital image and spectrum acquisition and immediate on-line computer processing of these images and spectra.

High resolution without a magnetic field:

All of the materials investigated in this work were magnetic and the magnetic microstructure was of more interest than the physical microstructure. Therefore the ability to obtain high resolution images of the magnetic and physical microstructure without applying a magnetic field to the specimen was of great importance, as any strong external magnetic field would be likely to alter the magnetic structure within the specimen. This was of most use in the work reported in Chapter 5 where the physical microstructure of the films was very small scale with crystal grains ~25 nm in diameter. The columnar microstructure of the cross-sections in Chapter 7 was also very small with an average column diameter of < 100 nm.

Simultaneous EELS and EDX:

The use of EELS and EDX microanalysis to measure localised composition variations on the scale of a few nm was demonstrated in Chapter 6. The EDX spectra from the CoCr cross-sections investigated in this Chapter showed that there was Cr segregation to the boundaries of individual columns in the columnar microstructure. The EELS spectra obtained from the CoCr cross-sections allowed the local specimen thickness and, consequently, the total volume irradiated by the electron probe, to be estimated. This, together with a plausible model for the shape and size of the Cr-rich region in these samples, resulted in the conclusion that the column boundaries in the films analysed had a Cr content >25%at. which would make them

non-magnetic. It was seen, therefore, that the simultaneous EDX and EELS acquisition capabilities of the HB5 could provide very high spatial resolution information on composition variations in a thin film sample. This high spatial resolution was necessary if any Cr segregation was to be measured at all, because of the very small volume within which the Cr segregation took place.

Novel detector response function:

Conventional transmission electron microscopes can provide much information on the magnetic structure of thin films, the Fresnel mode of Lorentz microscopy being the most common imaging mode used to obtain this information. However, all of the normal imaging modes used in the CTEM to investigate magnetic structure tend to be non-linear (Chapman 1984). In this thesis, a linear mode of Lorentz microscopy has been used; this was differential phase contrast (DPC) imaging. As was shown in Chapter 2, this mode of Lorentz microscopy requires a detector with an antisymmetric response function. In this work the detector used was a quadrant detector, the use of which allows two orthogonal in-plane components of magnetic induction, integrated along an electron trajectory, to be mapped.

In Chapter 3 it was seen that this mode of electron microscopy allows the direction of the in-plane component of induction within magnetic domains to be obtained. Moreover it was shown in Chapter 3 that a DPC image is a high resolution in-focus map of the variation of magnetic induction across a specimen convolved with a source intensity distribution. Therefore, if the source size is small enough, a line trace across a domain wall in a DPC image can be considered as an experimentally determined domain wall profile. Another technique which is available in the HB5 when it is configured for DPC imaging is the split spot technique, which involves replacing the quadrant detector with a fluorescent screen as described in Chapter 3. By using the split spot technique at a number of specimen tilts the angle between the direction of magnetisation within a domain and the film normal can be

obtained. Therefore, DPC imaging and the split spot technique available in the HB5 can provide a complete description of the magnetic domain structure and the direction of magnetisation within each domain in a thin film sample. This, however, requires that non-magnetic contrast in the DPC images does not obscure any magnetic contrast which is present as happened with the CoCr cross-sections discussed in Chapter 7.

The fact that the contrast in a DPC image is directly proportional to an in-plane component of induction means that stray fields beyond the edges of magnetic materials can be mapped with a spatial resolution of ~ 10 nm and a sensitivity of 2.2 Tnm which is equivalent to the integrated induction through 1.2 nm of cobalt. This was demonstrated in Chapter 4 using a thin cobalt foil. Also investigated in Chapter 4 were the stray fields from a longitudinal magnetic recording medium. It was seen that the stray field distribution was asymmetric, the stray fields from the small reverse domains having a smaller linear extent than those from the uniformly magnetised areas of the film. This agreed with the asymmetric readback pulses obtained from this medium by Tong *et al* (1984). In Chapter 7 the stray fields from the cross-sections of CoCr investigated gave information on the scale of the magnetic structure within the CoCr layer which was not otherwise available. This was because the non-magnetic contrast from the physical microstructure of these cross-sections was so strong.

Digital acquisition:

The on-line computer processing, which is available using the Toltec computer system connected to the HB5, allowed the DPC images of magnetic stray fields acquired on the STEM to be turned into vector plots of the stray fields from these films. These were shown in Chapter 4 and the plots from the Co sample agreed well with theoretical computer calculations of the stray fields which should be present at the edges of the domain structure observed.

The ability to use image processing techniques on the images

acquired by the Toltec computer system allows crystallite and other random non-magnetic contrast to be removed from the magnetic domain wall profiles. This was done by averaging the image intensity along the domain wall. As discussed in Chapter 3 the contrast from the domain wall is enhanced by this technique and random non-magnetic contrast is reduced.

8.2 Future Work

Computer acquisition and analysis:

Currently, images can only be acquired sequentially using the computer programs available on the Toltec computer system. The ability to acquire both sum (incoherent bright field) and difference (DPC) signals from the quadrant detector simultaneously should allow much of the non-magnetic contrast in the DPC images to be removed. As discussed by Morrison (1981), contrast in DPC images due to fluctuations in the probe current, and to scattering by the specimen itself, can be removed, to some extent, by normalising the DPC image using the sum image. As the fluctuation of the probe current is a random process, the sum image has to be acquired at the same time as the DPC image it is to be used to normalise. Most of the hardware required to do this already exists in the HB5-Toltec system, and although it may be necessary to buy an additional analogue to digital converter, such as that on the Data Translation board mentioned in Chapter 2, the problem is basically a software one. The programs which drive the image acquisition hardware are written in assembler and it is these that will have to be modified and adapted if multiple simultaneous image acquisition is to be achieved.

As stated, most of the unwanted amplitude contrast in DPC images is due to crystallites and noise from the field emission tip. This is mainly high frequency noise. A standard means of removing unwanted high spatial frequency noise, such as crystallite noise, from an image is to apply a high frequency filter to the Fourier transform of the

image. Although some work has already been done on this, and is reported in Appendix D, much work still remains to be undertaken. With the present program approximately 12 minutes are required for each frequency filter. This includes 4 minutes for a fast Fourier transform (FFT) of the original image and 4 minutes for an inverse FFT. If the initial FFT could be stored once it has initially been calculated, and recalled from disk rather than recalculated, this could reduce by 1/3 the time required for each calculation.

A much faster method of performing a high frequency filter is available: the frequency filter normally used in Fourier space is a Gaussian filter as this leads to the minimum "ringing" in the inverse Fourier transform image. The Fourier transform of a Gaussian, however, is another Gaussian. Therefore convolution of the original real space image with an appropriately scaled Gaussian should produce the same effect as multiplication of its Fourier transform by the desired Gaussian. This would remove the need for the two FFT's and, as each image occupies 1/4 of the memory used for its Fourier transform, the convolution in real space should take less time than the multiplication in Fourier space. This method of filtering should take less than 1/3 of the time required for the Fourier transform method. However, the real space Gaussians required would probably be non-zero only over a small region and therefore necessarily be piecewise defined functions. If this does cause a problem with ringing in the image then the slower FFT system could be used to produce a final filtered image. The size of the Gaussian in Fourier space would be appropriately scaled Fourier transform of the real space Gaussian that was found to produce the best results.

The vector maps discussed in Chapter 4 are not "snap-shots" of the in-plane induction at a given plane in space, but represent an averaged in-plane induction along an electron trajectory as described in Chapter 2. It may be possible to use computer tomography to construct a 3-dimensional map of the magnetic induction beyond the edge of the specimen by using a number of images taken at different

specimen tilts. Computer tomography is commonly used in medical scanning systems such as whole body scanners, and the technique has recently been applied by Elsbrock *et al* (1985) to images, obtained in an SEM, of the stray field from a magnetic recording head. This however, would probably require a larger image storage capacity and on-line memory than that which is currently available on the Toltec computer system.

CoCr recording materials:

Artificial superstructure films:

The artificial superstructure films investigated in this work had good c-axis texture and a degree of perpendicular anisotropy. However, the number of alternate layers in the films studied was quite small, and it would be interesting to see how the magnetic properties of these films changed as the number of alternate layers was increased. The initial studies carried out in this work seem to indicate that the layered structure did produce a perpendicular anisotropy which increased as the number of alternate layers increased. Transverse cross-sectioning may be a useful technique in the study of these films as it would allow the layered structure to be investigated, both in terms of the magnetic structure in each layer and the coupling between layers, and with regard to the sharpness of the boundaries between the alternate layers.

Alloy films:

The magnetic domain wall structures seen in the planar CoCr alloy films discussed in Chapter 5 require more analysis to ascertain whether the magnetisation in the domain wall rotates continuously across one or more crystal grains or if the magnetisation switches discontinuously across a grain boundary. This analysis may require extensive image processing to reduce the crystallite contrast as this was very strong in these films. The results should help in the

understanding of the magnetisation reversal process in CoCr as these films represent the initial growth layers of the thicker films used for perpendicular magnetic recording.

As stated in Chapter 7 the results from the study of the magnetic structure of the CoCr layer in the cross-section specimens were disappointing. The stray fields observed indicated that the CoCr layers were magnetic; however, no unambiguous magnetic contrast was seen in these layers. The study of cross-sections of films on which a signal has been written may shed more light on the magnetic structure of these layers. A film which has been magnetised using a periodic write signal, would have a regular magnetic domain structure with a regular, well defined stray field pattern. This stray field pattern should allow the magnetic domains to be identified and the contrast from them separated from that due to the columnar microstructure. An obvious domain pattern within written cross-sections would permit the magnetisation transitions in these films to be investigated. It should be possible to discover whether the magnetisation transition takes place discontinuously at a Cr-rich column boundary or if it takes place within a column. This information may be more easily obtained from cross-sections than from the planar films discussed earlier, as the stray fields from the cross-sections would aid in the identification of the magnetisation transitions.

Elemental segregation:

Most models for elemental segregation within CoCr alloy films involve the diffusion of Cr to the column boundaries. Recently however Maeda *et al* (1985) have suggested a new model in which the Co segregates to wall-like structures parallel to the film normal and arranged radially in each column. So far these so called "chrysanthemum-like" structures have only been seen by this one group using a preferential etching technique. It may be possible to verify that the structures seen by them are due to the segregation model they suggest using the microanalysis techniques used in this

work. The etching technique used by Maeda *et al* has provided a definite size and shape for the Co- and Cr-rich regions and this should allow accurate values for the Co to Cr ratio to be obtained.

APPENDIX A

STRAY FIELD MAPPING PROGRAMS

This Appendix contains computer listings of the programs used to produce the stray field vector maps shown in Chapter 4. The first program is VMAP, together with the subroutines used in it. This program uses two DPC images of the same area, but sensitive to two different orthogonal components of induction, to calculate x- and y-components of induction at points on a regular grid as described in Chapter 4. The second program is DRMP (with its associated subroutines) which uses the x- and y-components calculated by VMAP to produce a vector map on the Hewlett Packard A3 plotter attached to the Toltec computer system. The third program, LOG1, is used to obtain the logarithms of the x- and y-components calculated by VMAP to allow these to be plotted by DRMP.

Below is a list of the programs and associated subroutines given in this Appendix. As the programs listed here are intended for use, and perhaps further development, on the Toltec computer system at Glasgow, the subroutine libraries which need to be linked with these programs are given also.

<u>Main prog</u>	<u>Subroutines</u>	<u>Libraries</u>
VMAP	MAP; XMAP; ARROW; AVE	5 GIRL; GUTS
	BUFFAV; PSETI; PLEFT; PRIGHT	1 ALB8; GMRL;
	PTOP; PBOTM; BFILE	1 GM2F
DRMP	RANGE; PAPER; SCALE; AROHED	5 GUTS;
		1 E488
LOG1		

The number before each Library refers to the hard disk drive on which that library normally resides.


```

C Set up terminal in PAGE mode.
  CALL OPCH (1,:9BAØ)
  CALL OPCH (1,'S')
  CALL OPCH (1,:9BAØ)
  CALL OPCH (1,'A')
C
  CALL ENG
  CALL INIT ('LB')
C Set up GEMS screen offsets
  CALL GEMSYX
C This initialises the labelled common block /OFFSET/ correctly.
C Set NC = Number of Commands in current menu
  NC=13
C Set MTX = Menu Table X-offset
  MTX=2
C
5  CALL NEWPAGE (1)
  WRITE (2,1Ø)
1Ø  FORMAT (' Magnetisation Vector Map, Parameter Selection Menu ',/,
&      ' V1.1 (IRM;24/4/85)')
  CALL PTEXT (1,MTX,4)
  WRITE (1,2Ø)
2Ø  FORMAT (1X,'x      x-component buffer      P',/,
&      1X,'y      y-component buffer      P',/,
&      1X,'m      map display buffer      P',/,
&      1X,'G      Grid size: N*N          N=',/,
&      1X,'Z      Zero flux intensity: Auto average of whole picture
& buffer',/,
&      1X,'          x-buffer ave =          y-buffer ave =',/,
&      1X,'B      Black / white range in pixels =',/,
&      1X,'P      Produce vector map:  x-component',/,
&      1X,'          y-component',/,
&      1X,'          both components',/,
&      1X,'F      File components',/,
&      1X,'p      quit to PCTG',/,
&      1X,'r      quit to RASP',/,
&      1X,'i      quit to IGET',/,
&      1X,'X      quit to user-defined program',/,
&      1X,'Q      quit to SPRAT')
C

```

```

CALL PWRT (MTX+29,MY(1),NPX)
CALL PWRT (MTX+29,MY(2),NPY)
CALL PWRT (MTX+29,MY(3),NPM)
CALL PTEXT (1,MTX+36,MY(4))
WRITE (2,25) N
25 FORMAT (I2)
CALL PTEXT (1,MTX+36,MY(6))
WRITE (2,26) IBW
26 FORMAT (I3)
30 NR=0
C Carry out the instructions in the menu.
CALL MENACT (MC,MTX,MY,NC,NR)
C Check that RETURN has been pressed after selection
CALL IPCH (6,IK)
IF (IK.NE.:8DA0) GOTO 30
C
IF (NR.EQ.0) GOTO 5
IF (NR.EQ.1) CALL PSETI (NR,NPX)
IF (NR.EQ.2) CALL PSETI (NR,NPY)
IF (NR.EQ.3) CALL PSETI (NR,NPM)
IF (NR.EQ.4) CALL IVALIN (MTX+32,MY(NR),N)
IF (NR.EQ.5) CALL AVE (NR)
IF (NR.EQ.6) CALL IVALIN (MTX+36,MY(NR),IBW)
IF (NR.EQ.7) CALL MAP (NR)
IF (NR.EQ.8) CALL BFILE (NR,BX,BY)
IF (NR.EQ.9) CALL PQUIT (0,MTX+20,MY(NR),'PC','TG')
IF (NR.EQ.10) CALL PQUIT (0,MTX+20,MY(NR),'RA','SP')
IF (NR.EQ.11) CALL PQUIT (0,MTX+20,MY(NR),'IG','ET')
IF (NR.EQ.12) CALL PQUIT (1,MTX+34,MY(NR),'PC','TG')
IF (NR.EQ.13) GOTO 99
GOTO 30
99 CONTINUE
CALL EXIT
END

```

C*****

C

SUBROUTINE MAP (NR)

C

C

C

C

This subroutine is the main vector map subroutine, it produces a vector map of the x- and y-components of magnetisation

```
COMMON /ADDRS/ IOBASE, MBASE, ILN, IROW, ICOL, IWORD, IBYTE
COMMON /OFFSET/ IXO(6), IYO(6), IXPZ(6,2), IYPZ(6,2)
COMMON /MENU/ MC(24), MTX, MY(24)
COMMON /BUFFER/ NPX, NPY, NPM
COMMON /AVRAGE/ AVEX, AVEY, IBW
COMMON /GRID/ N
COMMON /INTENS/ INT(8)
COMMON /COMPS/ BX(1024), BY(1024)
```

C

5

CALL PTEXT (1, MTX+24, MY(NR))

CALL IPCH (6, IK)

C

C

Hitting RETURN will return control to main menu program.

IF (IK.EQ.:8DA0) RETURN

IF ((IK.EQ.'X').OR.(IK.EQ.'x')) GOTO 10

IF ((IK.EQ.'Y').OR.(IK.EQ.'y')) GOTO 20

IF ((IK.EQ.'B').OR.(IK.EQ.'b')) GOTO 30

GOTO 5

C

10

CALL PTEXT (1, MTX+26, MY(NR))

CALL XMAP (1)

GOTO 5

20

CALL PTEXT (1, MTX+26, MY(NR)+1)

CALL XMAP (2)

GOTO 5

30

CALL PTEXT (1, MTX+26, MY(NR)+2)

CALL XMAP (1)

CALL XMAP (2)

GOTO 5

END

C Subroutine XMAP(NDIR)

15/11/84 file xmap

C*****

C

SUBROUTINE XMAP (NDIR)

C

C

C

C

C

This subroutine will produce a set of arrows lying along the x-axis, the length of the arrows being proportional to the value of the magnetisation in the x-direction.

COMMON /ADDRS/ IOBASE, MBASE, ILN, IROW, ICOL, IWORD, IBYTE
COMMON /OFFSET/ IXO(6), IYO(6), IXPZ(6,2), IYPZ(6,2)
COMMON /BUFFER/ NPX, NPY, NPM
COMMON /AVRAGE/ AVEX, AVEY, IBW
COMMON /GRID/ N
COMMON /INTENS/ INT(8)
COMMON /COMPS/ BX(1024), BY(1024)

C

DIMENSION ABUF(1024), IBUF(1024)

C

NP=NPX
IF (NDIR.EQ.2) NP=NPY
N1=256/N
IPOINT=N*N
POINTS=FLOAT(IPOINT)

C

CALL ENG
DO 10 J=1, N1
DO 20 I=1, N1
SUM=0
DO 25 L=1, N
CALL SETWIN(0, IROW, IXO(NP+1)+(J-1)*N, IYO(NP+1)+(I-1)*N
&+(L-1), IOBASE, MBASE)
CALL MOVEDN (IWORD, IBUF(1), 1, MBASE, 1, N)
DO 30 K=1, N
ABUF(K)=FLOAT(IBUF(K))
SUM=SUM+ABUF(K)

30

CONTINUE

25

CONTINUE

AVE=SUM/POINTS

CALL ARROW(J, I, AVE, NDIR)

20

CONTINUE

10

CONTINUE

RETURN

END

C SUBROUTINE ARROW (IX,IY,AVE,ICOMP)

C This subroutine calculates the length and direction of the
C required vector arrow, for a give grid square and displays
C it in the appropriate square.

C COMMON /ADDRS/ IOBASE, MBASE, ILN, IROW, ICOL, IWORD, IBYTE
C COMMON /OFFSET/ IXO(6), IYO(6), IXPZ(6,2), IYPZ(6,2)
C COMMON /BUFFER/ NPX, NPY, NPM
C COMMON /AVRAGE/ AVEX, AVEY, IBW
C COMMON /GRID/ N
C COMMON /INTENS/ INT(8)
C COMMON /COMPS/ BX(1024), BY(1024)

C INT holds the values which are to be written to the GEMS to
C produce the arrows on the screen.

C Set up which element of Bx or By is being calculated.

C NGRID=256/N
C I=IY+(IX-1)*NGRID

C For x-component ICOMP=1
C For y-component ICOMP=2

C IF (ICOMP.EQ.1) TSTAVE=AVEX
C IF (ICOMP.EQ.2) TSTAVE=AVEY

C TSTAVE is the zero flux pixel intensity
C AVE is the average pixel intensity of the current grid square.
C DIF is a measure of the size magnetisation.

C DIF=TSTAVE-AVE

C If DIF is -ve -bright region-left to right arrow for x-comp,
C or bottom to top for y-comp.
C If DIF +ve -dark region- right to left arrow for x-comp,
C or top to bottom for y-comp.

C ICENT gives location of the blunt end of the arrow wrt
C the top left hand corner of the grid square

C ICENT=(N/2-1)

C MAXLEN=N/2

C MAXLEN is the maximum length of the arrow in pixels.

C IF (ABS(DIF).LT.1) RETURN

C SCaLe DIF for black to white pixel range.

C BW=FLOAT(IBW)
C SCLDIF=MAXLEN*DIF*2/BW

C ILENTH is the length of the arrow to be drawn.

```

ILENTH=IFIX(ABS(SCLDIF))
IF (ILENTH.GT.MAXLEN) ILENTH=MAXLEN
IF (ILENTH.EQ.0) RETURN

```

```

C
C
C If y-comp being mapped jump over x map section.

```

```

IF (ICOMP.EQ.2) GOTO 10

```

```

C
C
C Store Bx component

```

```

BX(I)=SCLDIF

```

```

C
C
C IF (DIF.GT.0) GOTO 20
+ve x-comp

```

```

CALL SETWIN (0, IROW, IXO(NPM+1)+(IX-1)*N+ICENT,
&
IYO(NPM+1)+(IY-1)*N+ICENT, IOBASE, MBASE)
CALL MOVEUP (IWORD, INT(1), 1, MBASE, 1, ILENTH)
CALL PRIGHT (IXO(NPM+1)+(IX-1)*N+ICENT+(ILENTH-1),
&
IYO(NPM+1)+(IY-1)*N+ICENT)

```

```

GOTO 50
-ve x-comp

```

```

C
C
C 20 CALL SETWIN (0, IROW, IXO(NPM+1)+(IX-1)*N+ICENT-(ILENTH-1),
&
IYO(NPM+1)+(IY-1)*N+ICENT, IOBASE, MBASE)
CALL MOVEUP (IWORD, INT(1), 1, MBASE, 1, ILENTH)
CALL PLEFT (IXO(NPM+1)+(IX-1)*N+ICENT-(ILENTH-1),
&
IYO(NPM+1)+(IY-1)*N+ICENT)

```

```

GOTO 50

```

```

C
C
C Store By component

```

```

C
C
C 10 BY(I)=SCLDIF

```

```

C
C
C IF (DIF.LT.0) GOTO 30
+ve y-comp

```

```

CALL SETWIN (0, ICOL, IXO(NPM+1)+(IX-1)*N+ICENT,
&
IYO(NPM+1)+(IY-1)*N+ICENT-(ILENTH-1), IOBASE, MBASE)
CALL MOVEUP (IWORD, INT(1), 1, MBASE, 1, ILENTH)
CALL PTOP (IXO(NPM+1)+(IX-1)*N+ICENT,
&
IYO(NPM+1)+(IY-1)*N+ICENT-(ILENTH-1))

```

```

GOTO 50
-ve y-comp

```

```

C
C
C 30 CALL SETWIN (0, ICOL, IXO(NPM+1)+(IX-1)*N+ICENT,
&
IYO(NPM+1)+(IY-1)*N+ICENT, IOBASE, MBASE)
CALL MOVEUP (IWORD, INT(1), 1, MBASE, 1, ILENTH)
CALL PBOTM (IXO(NPM+1)+(IX-1)*N+ICENT,
&
IYO(NPM+1)+(IY-1)*N+ICENT+(ILENTH-1))

```

```

C
C
C IXO and IYO hold the buffer coordinates.
C (IX-1)*N and (IY-1)*N give the grid within this buffer
C +ICENT goes to the center of this grid (arrow may start here)
C and if ILENTH is used this goes to where the arrow is
C to be written to (remembering that INC is positive).

```

```

C
C
C 50 RETURN

```

```

END

```

C*****

C
C SUBROUTINE AVE (NR)C
C This subroutine allows the user to automatically obtain
C the average pixel intensity in picture buffers NPX and
C NPY or to enter alternative values of average intensity.
CCOMMON /ADDRS/ IOBASE, MBASE, ILN, IROW, ICOL, IWORD, IBYTE
COMMON /OFFSET/ IXO(6), IYO(6), IXPZ(6,2), IYPZ(6,2)
COMMON /MENU/ MC(24), MTX, MY(24)
COMMON /BUFFER/ NPX, NPY, NPM
COMMON /AVRAGE/ AVEX, AVEY, IBWC
30 CALL PTEXT (1, MTX+25, MY(NR))
CALL IPCH (6, IK)C Hitting RETURN will return control to the main menu program.
CIF (IK.EQ.:8DA0) RETURN
IF (IK.EQ.'A') GOTO 10
IF ((IK.EQ.'X').OR.(IK.EQ.'x')) CALL VALIN (MTX+20, MY(NR)+1, AVEX)
IF ((IK.EQ.'Y').OR.(IK.EQ.'y')) CALL VALIN (MTX+45, MY(NR)+1, AVEY)
GOTO 30C
10 CALL PTEXT (1, MTX+26, MY(NR))
CALL BUFFAV (NPX, AVEX)
CALL BUFFAV (NPY, AVEY)
CALL PTEXT (1, MTX+20, MY(NR)+1)
WRITE (2, 20) AVEX
CALL PTEXT (1, MTX+45, MY(NR)+1)
WRITE (2, 20) AVEY
20 FORMAT (1PE10.2)
GOTO 30
END

C Subroutine BUFFAV (NP,AVE) 4/10/84 file bfav

C*****

C
C SUBROUTINE BUFFAV (NP,AVE)

C
C This subroutine calculates the average pixel intensity
C within picture buffer NP.

COMMON /ADDRS/ IOBASE,MBASE,ILN,IROW,ICOL,IWORD,IBYTE
COMMON /OFFSET/ IXO(6),IYO(6),IXPZ(6,2),IYPZ(6,2)
COMMON /MENU/ MC(24),MTX,MY(24)
COMMON /BUFFER/ NPX,NPY,NPM

C
C DIMENSION IBUF(512),ABUF(512)

C Set size to whole buffer.

NROW=256

NCOL=256

C If P0 set to 512 by 512

IF (NP.EQ.0) NROW=512

IF (NP.EQ.0) NCOL=512

C Zero sum.

SUM=0.0

C Set up GEMS for access, and set window in column mode.

CALL ENG

DO 20 J=1,NCOL

CALL SETWIN (0,ICOL,IXO(NP+1)+J-1,IYO(NP+1),IOBASE,MBASE)

CALL MOVEDN (IWORD,IBUF(1),1,MBASE,1,NROW)

DO 10 I=1,NROW

ABUF(I)=FLOAT(IBUF(I))

SUM=SUM+ABUF(I)

10 CONTINUE

20 CONTINUE

C
C POINTS=FLOAT(NROW)*FLOAT(NCOL)

AVE=SUM/POINTS

RETURN

END

C Subroutine PSETI (NP,NPNEW) 15/10/84 file psti

C*****

C
C SUBROUTINE PSETI (NR,NPNEW)

C
C This subroutine reads in the value of NPNEW at the position
C defined by NR and then rewrites it at this position.

COMMON /MENU/ MC(24),MTX,MY(24)

C Read in the value of NPNEW from the screen.

CALL PRD (MTX+29,MY(NR),NPNEW)

C Rewrite this value to the screen.

CALL PWRT (MTX+29,MY(NR),NPNEW)

RETURN

END

C Subroutine PLEFT (IX,IY) IRM 12/11/84 file plft

C*****

C
C SUBROUTINE PLEFT (IX,IY)

C
C This subroutine puts an arrow head pointing to the left
C at the position (IX,IY) on the GEMS screen

C
C COMMON /ADDRS/ IOBASE,MBASE,ILN,IROW,ICOL,IWORD,IBYTE
C COMMON /GRID/ N
C COMMON /INTENS/ INT(8)

C
C CALL SETWIN (0,ICOL,IX+1,IY-1,IOBASE,MBASE)
C CALL MOVEUP (IWORD,INT(1),1,MBASE,1,3)

C
C If grid size is too small do not draw any more of arrow

C
C IF (N.LE.8) GOTO 10

C
C CALL SETWIN (0,ICOL,IX+2,IY-2,IOBASE,MBASE)
C CALL MOVEUP (IWORD,INT(1),1,MBASE,1,5)

10
C RETURN
C END

C Subroutine PRIGHT (IX,IY) IRM 12/11/84 file prit

C*****

C
C SUBROUTINE PRIGHT (IX,IY)

C
C This subroutine puts an arrow head pointing to the right
C at the position (IX,IY) on the GEMS screen

C
C COMMON /ADDRS/ IOBASE,MBASE,ILN,IROW,ICOL,IWORD,IBYTE
C COMMON /GRID/ N
C COMMON /INTENS/ INT(8)

C
C CALL SETWIN (0,ICOL,IX-1,IY-1,IOBASE,MBASE)
C CALL MOVEUP (IWORD,INT(1),1,MBASE,1,3)

C
C If grid size is too small do not draw any more of arrow

C
C IF (N.LE.8) GOTO 10

C
C CALL SETWIN (0,ICOL,IX-2,IY-2,IOBASE,MBASE)
C CALL MOVEUP (IWORD,INT(1),1,MBASE,1,5)

10
C RETURN
C END

```

C Subroutine PTOP (IX,IY) IRM 12/11/84 file ptop
C*****
C
C SUBROUTINE PTOP (IX,IY)
C
C This subroutine puts an arrow head pointing to the top
C at the position (IX,IY) on the GEMS screen
C
C COMMON /ADDRS/ IOBASE, MBASE, ILN, IROW, ICOL, IWORD, IBYTE
C COMMON /GRID/ N
C COMMON /INTENS/ INT(8)
C
C CALL SETWIN (Ø, IROW, IX-1, IY+1, IOBASE, MBASE)
C CALL MOVEUP (IWORD, INT(1), 1, MBASE, 1, 3)
C
C If grid size is too small do not draw any more of arrow
C
C IF (N.LE.8) GOTO 1Ø
C
C CALL SETWIN (Ø, IROW, IX-2, IY+2, IOBASE, MBASE)
C CALL MOVEUP (IWORD, INT(1), 1, MBASE, 1, 5)
1Ø RETURN
END

```

```

C Subroutine PBOTM (IX,IY) IRM 12/11/84 file pbtm
C*****
C
C SUBROUTINE PBOTM (IX,IY)
C
C This subroutine puts an arrow head pointing to the bottom
C at the position (IX,IY) on the GEMS screen
C
C COMMON /ADDRS/ IOBASE, MBASE, ILN, IROW, ICOL, IWORD, IBYTE
C COMMON /GRID/ N
C COMMON /INTENS/ INT(8)
C
C CALL SETWIN (Ø, IROW, IX-1, IY-1, IOBASE, MBASE)
C CALL MOVEUP (IWORD, INT(1), 1, MBASE, 1, 3)
C
C If grid size is too small do not draw any more of arrow
C
C IF (N.LE.8) GOTO 1Ø
C
C CALL SETWIN (Ø, IROW, IX-2, IY-2, IOBASE, MBASE)
C CALL MOVEUP (IWORD, INT(1), 1, MBASE, 1, 5)
1Ø RETURN
END

```

C Subroutine BFILE 25/4/85 file bfil

C*****

C

SUBROUTINE BFILE (NR, BX, BY)

C

C

C

C

C

This subroutine will put calculated components of Bx, By, Btotal, and THETA (the angle that Btotal makes with the +ve x-axis) into a file defined by the user.

COMMON /MENU/ MC(24), MTX, MY(24)
COMMON /ADDRS/ IOBASE, MBASE, ILN, IROW, ICOL, IWORD, IBYTE
COMMON /GRID/ N

C

DIMENSION NAMEST(3), IA(10), BX(1024), BY(1024),
& BT(1024), THETA(1024)

C

C

C

C

To be consistent with VMAP, and DRMP, must output (256/N)**2 points. NGRID is the number of grids along x.

NGRID=256/N
IPOINT=NGRID*NGRID
IDRV=0
10 CALL PTEXT (1, MTX+27, MY(NR))
WRITE (2, 15)
15 FORMAT (32X)
CALL PTEXT (1, MTX+27, MY(NR))
WRITE (2, 20)
20 FORMAT ('Enter filename ')
CALL GETNAM (IDRV, IDRV, NAMEST, NCHAR, ITERM)
IF ((ITERM.EQ.:DFA0).AND.(NCHAR.EQ.0)) RETURN
IF (ITERM.EQ.:DFA0) GOTO 10
NAMEST(3)=' S'

C

C

C

Check to see if this file already exists on IDRV

C

C

C

C

C

C

C

WRITE (99, 30) IDRV, NAMEST
30 FORMAT ('?', I1, 3A2)
READ (99) IA
IF (IA(3).NE.0) GOTO 90

If IA(3)=0 then this file does not yet exist.

```

WRITE (99,40) IDR,NAMEST
40  FORMAT ('W',I1,3A2)
    DO 50 I=1,IPOINT
        BT(I)=SQRT(BX(I)**2+BY(I)**2)
        IF (BX(I).NE.0) GOTO 45
        IF (BX(I).EQ.0) THETA(I)=3.14/2
        IF ((BX(I).EQ.0).AND.(BY(I).EQ.0)) THETA(I)=99.99
        GOTO 50
45  THETA(I)=ATAN(BY(I)/BX(I))
50  CONTINUE
    WRITE (4,60) (BX(I),BY(I),BT(I),THETA(I),I=1,IPOINT)
60  FORMAT (4F10.5)
    WRITE (4,70)
70  FORMAT (/,4X,'BX',8X,'BY',8X,'BT',6X,'THETA')
    END FILE 4
    CALL PTEXT (1,MTX+27,MY(NR))
    WRITE (2,75)
75  FORMAT (32X)
    CALL PTEXT (1,MTX+30,MY(NR))
    WRITE (2,80)
80  FORMAT ('    OK')
    RETURN
90  CALL PTEXT (1,MTX+27,MY(NR))
    WRITE (2,75)
    CALL PTEXT (1,MTX+27,MY(NR))
    WRITE (2,100) NAMEST,IDR
100 FORMAT (3A2,'already exists on drive ',I1)
    GOTO 10
    END

```

```

C Source program DRAMAP IRM 31/5/85 file drmp
C*****
C
C This program will plot out a vector map on the HP plotter
C using the components of Bx and By generated by VMAP
C
C INTEGER XMIN,XMAX,YMIN,YMAX
C DIMENSION BX(1024),BY(1024),NAMEST(3),IA(10)
C COMMON /ARO/ BLEN,N
C DATA IDRV /0/
C DATA XMIN,XMAX,YMIN,YMAX/0,12800,0,12800/
C
C Identify program
C WRITE (1,10)
10 FORMAT (' DRAMAP IRM ')
C
C Find out grid size N
C WRITE (1,20)
20 FORMAT (//,'How many grid squares in x direction ? ')
C READ (1,15) N
15 FORMAT (I2)
C
C Total number of grid squares is N2=N*N
C N2=N*N
C
C Get data set name
C WRITE (1,30)
30 FORMAT (/, 'Enter name of data set to be plotted ')
C CALL GETNAM (IDRV,IDRV,NAMEST,NCHAR,ITERM)
C IF ((ITERM.EQ.:DFA0).AND.(NCHAR.EQ.0)) CALL EXIT
C IF (ITERM.EQ.:DFA0) GOTO 25
C NAMEST(3)=' S'
C
C Check to see if this file exists on IDRV
C WRITE (99,40) IDRV,NAMEST
40 FORMAT ('?',I1,3A2)
C READ (99) IA
C IF (IA(3).EQ.0) GOTO 900
C
C If IA(3) does not equal zero then file exists and can be read
C
C Open file for reading
C WRITE (99,50) IDRV,NAMEST
50 FORMAT ('R',I1,3A2)
C
C Read in data set. BT and THETA are not needed by this program
C but are included here to be consistant with data set from VMAP
C DO 66 I=1,N2
C READ (4,60) (BX(I),BY(I),BT,THETA)
60 FORMAT (4F10.5)
66 CONTINUE
C
C Scale Bx and By so that B(x or y)max = BLEN
C BLEN=FLOAT(6400/N)
C CALL RANGE(BX,BY,N2,BLEN)
C

```

```

C Find out which size of paper is being used
WRITE (1,70)
70 FORMAT (/, ' Is paper A4 or A3 ? ')
READ (1,80) IPAPER
80 FORMAT (I1)
C
C Set scaling points for this size of paper
CALL PAPER (IP1X,IP1Y,IP2X,IP2Y,IPAPER)
C
C Find out which part of map is to be plotted out and with
C which pen.
85 WRITE (1,90)
90 FORMAT (/, 'Which pen is to be used ? ')
READ (1,80) IPEN
WRITE (1,100)
100 FORMAT (/, 'Select area of map to be plotted '
&          /, 'Input first and last column '
&          /, ' and first and last row in I2 format')
READ (1,110) ICLF,IPLL,IRWF,IRWL
110 FORMAT (4I2)
C Echo these
115 WRITE (1,120) ICLF,IPLL,IRWF,IRWL
120 FORMAT (/, 'First col = ',I2,
&          /, 'Last col = ',I2,
&          /, 'First row = ',I2,
&          /, 'Last row = ',I2,
&          /, 'Press RETURN to start, RUB to reset, Q to quit ')
C
CALL IPCH (6,IK)
IF (IK.EQ.:DFA0) GOTO 85
IF (IK.EQ.'Q') CALL EXIT
IF (IK.NE.:8DA0) GOTO 115
C
C Start plot
C
C Initialise plotter
CALL PLINIT
C
C Set PEN velocity
WRITE (25,155)
155 FORMAT ('VS7;')
C
C Set up scaling points P1 and P2 in plotter coordinates
WRITE (25,130) IP1X,IP1Y,IP2X,IP2Y
130 FORMAT ('IP',I5,',',I5,',',I5,',',I5,',;')
C
C Set scaling limits in user coordinates
WRITE (25,140) XMIN,XMAX,YMIN,YMAX
140 FORMAT ('SC',I5,',',I5,',',I5,',',I5,',;')
C
C Get selected pen
WRITE (25,150) IPEN
150 FORMAT ('SP',I1,',;')

```


C Subroutine RANGE (BX, BY, NMAX, BLEN) IRM 31/5/85 file rng
C*****

C This subroutine find BMAX from BX and BY and then scales this
C to BLEN. It scales all of BX and BY by the same factor
C

SUBROUTINE RANGE (BX, BY, NMAX, BLEN)
DIMENSION BX(NMAX), BY(NMAX)

C Find BMAX
BMAX=BX(1)
DO 10 I=1, NMAX
IF (ABS(BX(I)).GT. BMAX) BMAX=ABS(BX(I))
IF (ABS(BY(I)).GT. BMAX) BMAX=ABS(BY(I))
10 CONTINUE

C Scale BX and BY
DO 20 I=1, NMAX
BX(I)=BX(I)*BLEN/BMAX
BY(I)=BY(I)*BLEN/BMAX
20 CONTINUE
RETURN
END

C Subroutine PAPER (IP1X, IP1Y, IP2X, IP2Y, IPAPER) IRM 31/5/85 file pap
C*****

C This subroutine will set up the scaling parameters IP1X, IP1Y, IP2X, IP2
C depending on whether the paper being used is A4 or A3
C

SUBROUTINE PAPER (IP1X, IP1Y, IP2X, IP2Y, IPAPER)

C IP1X IP1Y IP2X IP2Y
C A4 1200 4640 7200 10640
C A3 3360 740 13760 11140

C Usually paper is A4
C

IP1X=1200
IP1Y=4640
IP2X=7200
IP2Y=10640

C IF (IPAPER.EQ.3) GOTO 10
RETURN
10 IP1X=3360
IP1Y=740
IP2X=13760
IP2Y=11140
RETURN
END

C Subroutine SCALE (A1,A2,AMAX) IRM 31/5/85 file scl
C*****

C
C This subroutine will scale ABS(A1) to AMAX and also scale
C A2 by the same factor
C

SUBROUTINE SCALE (A1,A2,AMAX)
A2=A2*AMAX/ABS(A1)
A1=A1*AMAX/ABS(A1)
RETURN
END

C This subroutine draws an arrowhead at the current pen
C position, the size of the arrowhead and its direction
C are determined by the values of BX and BY

C SUBROUTINE AROHED (BX, BY)

C COMMON /ARO/ BMAX, N

C Determine RUN and RISE to give slope of line on which
C arrowhead (which is in fact a user defined character)
C is drawn.

C IF (BX.EQ.0.0) GOTO 10
C RISE=10.0*BX/ABS(BX)
C RUN=(BY*RISE/BX)

C IF (ABS(RISE).GT.ABS(RUN)) CALL SCALE (RISE, RUN, 127.0)
C IF (ABS(RUN).GT.ABS(RISE)) CALL SCALE (RUN, RISE, 127.0)

C GOTO 15
10 RUN=127.0
RISE=0.0
IF (BY.NE.0.0) RUN=RUN*BY/ABS(BY)

C Scale size of arrowhead to length of arrow

15 B=SQRT(BX**2+BY**2)
HEIGHT=(B*18.0)/(BMAX*N)

C If HEIGHT is less than 0.004 then the plotter will register
C an error and plot using the previous (or the default) height
C if HEIGHT is less than 0.004 then plotted it would be too
C small to see anyway so do not draw arohed just RETURN.

C IF (HEIGHT.LT.0.004) RETURN

C Set arrowhead size

20 WRITE (25, 20) HEIGHT, HEIGHT
FORMAT ('SR', F8.3, ', ', F8.3, ';')

C Set arrow direction

30 WRITE (25, 30) RUN, RISE
FORMAT ('DR', F8.3, ', ', F8.3, ';')

C Draw arrowhead

C40 WRITE (25, 40)
FORMAT ('LBA')
40 FORMAT ('UC99, 2, -6, -4, 0, 2, 6, -99;')
C WRITE (5, 50) HEIGHT, RUN, RISE, B, BMAX, N
50 FORMAT (5F8.3, 12)
RETURN
END

```

C      Source program LOG1                      IRM (10/8/85)  file log1
C*****
C
C      This program reads in a file produced by VMAP in format 4F10.5
C      and takes the log of this file and outputs it in format 4F10.5
C
C      DIMENSION NAMEST (3), IA(10), BX(1024), BY(1024),
C      &          BT(1024), THETA(1024), BTL(1024)
C      DATA IDRV / 2/
C
C      Read in number of data points in set
C      WRITE (2,10)
10     FORMAT (/, '  IRM LOG1 PROGRAM ', //)
C      WRITE (2,20)
20     FORMAT ( '  How many data points in x-direction ? ')
C      READ (1,30) N
30     FORMAT (I2)
C
C      Total number of points is N2=N*N
C      N2=N*N
C
C      Get data set name
35     WRITE (1,40)
40     FORMAT (/, 'Enter name of data set ')
C      CALL GETNAM (IDRV, IDRV, NAMEST, NCHAR, ITERM)
C      IF ((ITERM.EQ.:DFA0).AND.(NCHAR.EQ.0)) CALL EXIT
C      IF (ITERM.EQ.:DFA0) GOTO 35
C      NAMEST(3)=' S'
C
C      Check to see if this file exists of IDRV
C      WRITE (99,50) IDRV,NAMEST
C      WRITE (1,50) IDRV,NAMEST
50     FORMAT ('?', I1, 3A2)
C      READ (99) IA
C      IF (IA(3).EQ.0) GOTO 900
C
C      If IA(3) does equal 0 then file does not exist and cannot be read.
C
C      Open file for reading
C      WRITE (99,60) IDRV,NAMEST
60     FORMAT ('R', I1, 3A2)
C
C      Read in data set.
C      DO 80 I=1,N2
C      READ (4,70)(BX(I),BY(I),BT(I),THETA(I))
C      WRITE (1,70)(BX(I),BY(I),BT(I),THETA(I))
70     FORMAT (4F10.5)
80     CONTINUE

```

```

C   Take log of BX, BY and BT
      DO 90 I=1,N2
      IF (BT(I).NE.0) GOTO 85
      BTL(I)=BT(I)
      GOTO 90
85   BTL(I)=ALOG(ABS(BT(I)))*BT(I)/ABS(BT(I))
      BX(I)=BX(I)*BTL(I)/BT(I)
      BY(I)=BY(I)*BTL(I)/BT(I)
90   CONTINUE
C
C   Find out name of data set to which file is to be written
95   WRITE (1,100)
100  FORMAT (/, 'Enter name of output file ')
      CALL GETNAM (IDRV, IDRV, NAMEST, NCHAR, ITERM)
      IF ((ITERM.EQ.:DFA0).AND.(NCHAR.EQ.0)) CALL EXIT
      IF (ITERM.EQ.:DFA0) GOTO 95
      NAMEST (3)=' S'
C
C   Check to see if this file exists on IDRV
      WRITE (99,110) IDRV,NAMEST
110  FORMAT ('?',I1,3A2)
      READ (99) IA
      IF (IA(3).NE.0) GOTO 990
C
C   If IA(3) is not equal to zero then file does not exist yet on IDRV
C   and can therefore be written.
C
C   Open file for writing
      NAMEST (3)=' S'
      WRITE (1,121) NAMEST (3)
121  FORMAT (A2, 'FILE EXTENSION')
      WRITE (99,120) IDRV,NAMEST
      WRITE (1,120) IDRV,NAMEST
120  FORMAT ('W',I1,3A2)
C
C   Write data set out
      WRITE (4,130) (BX(I),BY(I),BTL(I),THETA(I),I=1,N2)
      WRITE (1,130) (BX(I),BY(I),BTL(I),THETA(I),I=1,N2)
130  FORMAT (4F10.5)
      END FILE 4
      CALL EXIT
900  WRITE (1,901) IDRV
901  FORMAT (/, 'This file does not exist on drive ',I1)
      GOTO 35
990  WRITE (1,991) IDRV
991  FORMAT (/, 'This file already exists on drive ',I1)
      GOTO 95
      END

```

APPENDIX B

ALIGNMENT ROUTINES AND ASSOCIATED PROBLEMS

B.1 Introduction

As stated in Chapter 3, a line trace across a domain wall in a DPC image can be considered to be an experimentally determined domain wall profile. For a region of thin single crystal with no bend contours a single line trace can give a good indication of the domain wall profile. However, some non-magnetic signal is normally apparent in a single line trace, due to, for example, variations in surface roughness. This non-magnetic signal is usually uncorrelated with the magnetic structure, and therefore by summing a number of line traces together, the magnetic contrast can be reinforced while the non-magnetic contrast is reduced. The ability to sum a number of line traces is essential when dealing with polycrystalline materials as the contrast from the individual crystallites can swamp the magnetic contrast in a single line trace, as shown in figure B.1. In order to sum individual line traces, such that the magnetic contrast is reinforced, the magnetic feature in the line traces must be in registration. This is achieved on the Toltec computer system by aligning successive rows, within a chosen area of a digital image, to a model of the feature of interest.

B.2 Alignment Of Well Defined Magnetic Domain Walls

Well defined magnetic domain walls are considered to be those which can be identified easily in a single line trace, and correspond to images in which the contrast from other objects is weak. The same technique can be used to align most well defined linear features provided the feature runs in a reasonably straight line down the image.

The alignment is carried out in two "passes": For the first pass the model used for alignment is a running average of the rows so far aligned. For the second pass the sum of all the rows as aligned at the

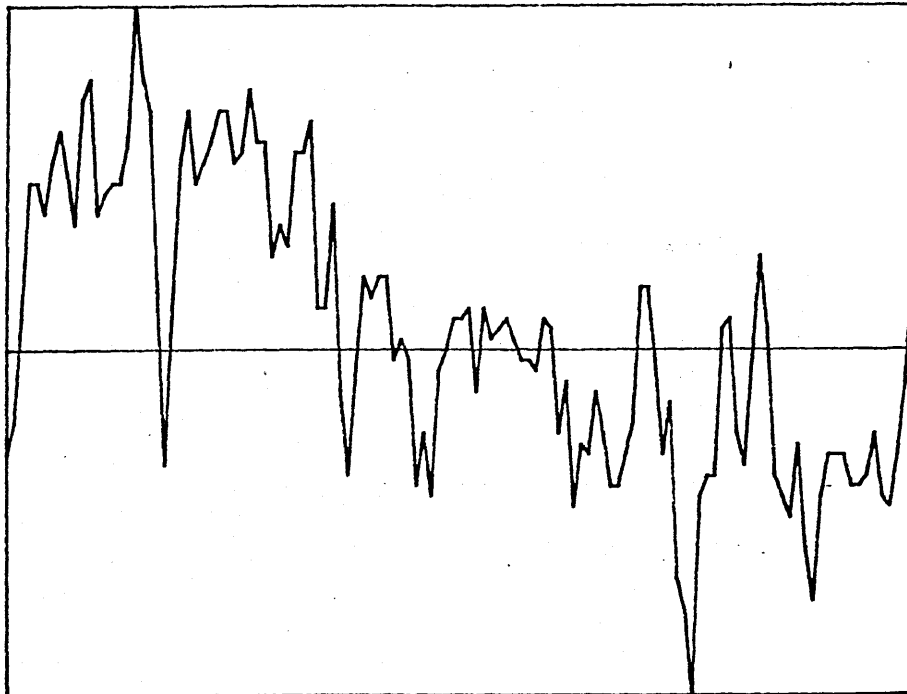


Figure B.1: Line trace across a domain wall in a film with strong crystallite contrast

end of the first pass is used throughout. This two pass system is used because it was found that the first few rows in the first pass sometimes aligned to non-magnetic features which they had in common rather than the magnetic feature. These non-magnetic features were generally averaged out by the end of the first pass.

Some sort of arithmetic test has to be used to ascertain when successive rows are in alignment; two different tests have been used on the Toltec:

- 1) maximising the covariance function, $C(x,y) = \langle xy \rangle - \langle x \rangle \langle y \rangle$
- 2) minimising the function $\sum \{x(J) - y(J)\}^2$, i.e. a least square fit.

where x is the model feature, y is the row to be aligned, $\langle \rangle$ implies a mean value and J is the pixel number which runs from 1 to $NPIX$, the number of pixels in the row to be aligned.

Problems with covariance as an alignment test:

The covariance is maximised when large x implies large y and small x implies small y , and is generally used to measure the correlation between two functions or distributions. This was the test initially used to align magnetic features and it was found to work when the profile to be aligned was reasonably smooth and monotonic. However, for this alignment routine to function as desired the profile has to have appreciable areas in which the value of x (and y) is high, and appreciable areas in which it is low, i.e. flat areas at either side of the domain wall as shown in figure B.2 a). If the value of x (and y) varies monotonically across most of the profile the covariance technique is liable to fail as an alignment routine; this is because the covariance of two line segments with the same slope is independent of the distance between them vertically. This can be seen by considering a line, x , of constant slope, and the same line displaced by n units vertically, y , as shown in figure B.2 b): The covariance of x with itself

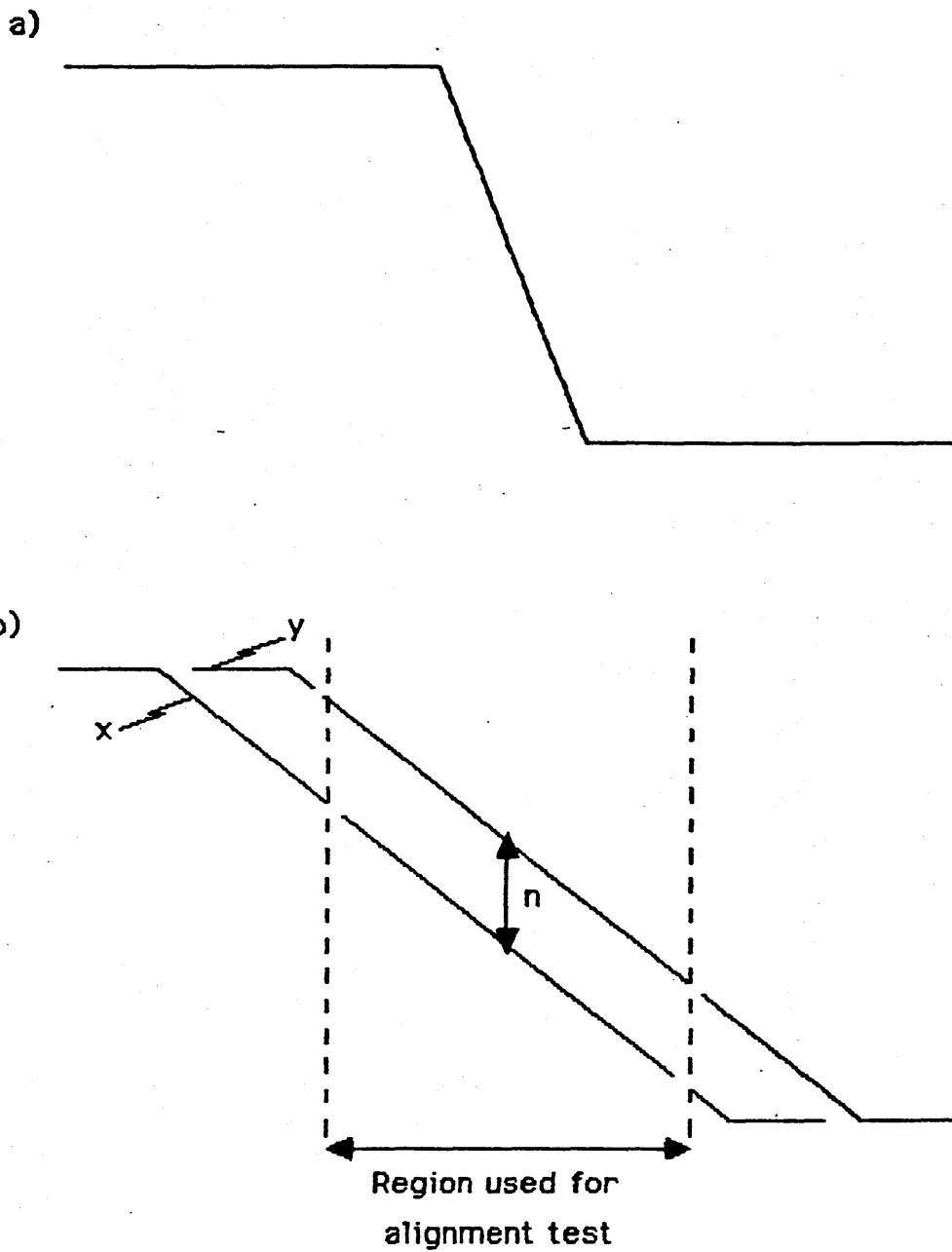


Figure B.2: a) illustration of the type of feature required by covariance alignment routine. b) Illustration of the type of smooth feature that cannot be aligned by the covariance technique but which can be aligned by the least square fit technique.

is:

$$C(x, x) = \langle xx \rangle - \langle x \rangle \langle x \rangle = \langle x^2 \rangle - \langle x \rangle^2$$

The covariance of x with y is:

$$\begin{aligned} C(x, y) &= \langle x(x-n) \rangle - \langle x \rangle \langle x-n \rangle = \langle x^2 - nx \rangle - \langle x \rangle (\langle x \rangle - n) \\ &= \langle x^2 \rangle - n \langle x \rangle - (\langle x \rangle^2 - n \langle x \rangle) \\ &= \langle x^2 \rangle - \langle x \rangle^2 \end{aligned}$$

Therefore $C(x, x) = C(x, y)$. In most cases the digital images acquired on the HB5 STEM contain non-magnetic contrast, such as bend contours, which restrict the area of the image which can be used for alignment to a narrow strip either side of the domain wall. Therefore, the covariance technique cannot always be considered reliable. For this reason the least squares fit technique is now used for aligning wall profiles on the Toltec. This technique works well for reasonably well defined wall profiles whether or not they have appreciable flat areas at either side of the transition. However, neither of the two above techniques are very successful in aligning domain walls in images in which there was strong crystallite contrast.

B.3 Alignment Of Magnetic Domain Walls In Images With Strong Crystallite Contrast

In order to align magnetic feature in images with strong crystallite contrast, the crystallite contrast has to be suppressed in some way. The following are ways in which this can be done.

Median filter:

This filter replaces the value associated with each pixel by the median value of a group of pixels around it. This is a 1D filter, where the group of pixels are all in the same row. The effect of this filter is to remove local spikes and dips without degrading the sharpness of edges in the image. Therefore domain walls are not smeared out by this filter. In cases where the crystallite noise is much reduced, the least squares alignment routine discussed above can be used to align

the domain wall. However, when the crystallite contrast is of the same order of magnitude as the magnetic contrast this filter does not sufficiently reduce the crystallite noise to allow the use of the alignment routines.

Spatial frequency filter:

Appendix D explains another means by which the crystallite noise can be suppressed. This involves using spatial frequency filters in the Fourier plane to remove the higher frequency components from an image. The problem with this is that, although this can markedly reduce the crystallite noise, it also smears out the domain wall to some extent, the sharper the domain wall, the more it is smeared out. Therefore, the domain wall profiles obtained from these filtered images are broader than the true domain wall profile. However, by storing the shift require to align each row in the spatially filtered image, and applying these shifts to the original image, the domain wall in the original image can be successfully aligned. This technique does not work for very sharp domain walls.

Alignment to a standard test pattern:

In cases where the crystallite noise cannot be removed, without almost completely removing the domain wall, another technique can be used. This technique relies on the fact that the human eye can pick out an underlying linear feature, such as the dark bright transition across a domain wall, even if there is stronger small scale contrast superimposed upon it. If the domain wall runs in a straight line across the image the operator can measure, or estimate, the slope of the domain wall to the vertical. A strong contrast pattern can then be generated, with the same slope as the feature of interest, using the image acquisition program, PCTG (This is a lengthy procedure and would be made much easier if an image rotation algorithm were available on the Toltec). The pattern, once generated can then be aligned as if it were a well defined domain wall, and the shift for each

row stored and applied to the image of interest.

B. 4 Implementation Of Alignment Techniques On The Toltec

All alignments of domain walls on the Toltec were done using the programs IGET and RASP. IGET allows the areas of interest in individual images to be selected, and RASP contains the alignment routines. Two different alignment commands can be selected in RASP: ALIGN and BRING INTO REGISTRATION.

The ALIGN command aligns the selected image segment using the least squares fit and also stores the shifts needed to achieve this alignment. This routine is therefore used to align well defined domain walls, filtered images and test patterns. The BRING INTO REGISTRATION command uses the shifts stored by the last ALIGN command to align the selected image segment. Therefore this routine is used to align a domain wall, in an image which has a lot of crystallite noise, using a filtered image or a test pattern as a model.

The median filter program is called MEDN, and the spatial frequency filtering program is called SFF; the latter is discussed more fully in Appendix D.

As stated above, test patterns can be generated using PCTG. This is done using the $P_n = rpx, 255$ and $P_m = rpy, 255$ commands, these generate intensity ramps from pixel intensity 0 to 255 in the picture buffers P_n and P_m , in the x- and y-directions respectively. When two picture buffers are added together the intensity in each buffer is first halved, therefore $P_n + P_m$ gives an intensity ramp at 45° to both x and y, while $(P_n + P_m) + P_n$ gives an intensity ramp at 22.5° to the x-direction. By adding buffers in suitable combinations ramps in any direction can be obtained. Once a ramp in the desired direction has been obtained, it can be turned into two ramps of half the original width with a sharp transition between them by carrying out a logical AND with the number 127 (three transitions can be introduced using 63 instead of 127). The command to perform a logical AND of P_m with 127 and store the result in P_n is $P_n = bcm, 127$.

APPENDIX C

JEOL 1200EX FREE LENS CONTROLLER - LOW MAG SETTINGS

Introduction

As the lens settings described in this appendix are mainly intended for use with magnetic specimens, it is important that the user realise that the objective lens can be accidentally switched on when using the Free Lens Controller, thereby subjecting the specimen to a magnetic field. The reason for this is the following: The Low Mag settings on the JEOL 1200EX come in two groups:

- 1) Those with a magnification of less than 300x in which the objective lens is WEAKLY EXCITED.
- 2) Those with a magnification of 300x or more in which the objective lens is OFF.

The microscope "remembers" what mode it is in even when the Free Lens Controller (FLC) is being used. For example if the FLC is used from an initial magnification of less than 300x the objective lens will automatically be set to its weakly excited condition (a value of 0.44 Amps at 120 keV) every time the focus control is used irrespective of what it was set to using the free lens controller. To prevent the objective lens from being accidentally excited when using the FLC to look at magnetic specimens, the FLC should be operated from an initial magnification of 300x or more.

Magnifications of > 1000x with the objective lens OFF

Magnifications of > 1000x are most easily obtained on the 1200EX by the following method:

- 1) Start at an initial Low Mag setting of 1000x
- 2) Switch on the FLC
- 3) Increase the current through intermediate lens 2 (Int2)
- 4) Decrease the current through Int1 and Int3.

The maximum magnification available is obtained by switching Int1 and Int3 off, and putting Int2 to maximum excitation; this gives a magnification of ~5000x with the projector lens at its normal setting, and ~5300x with the projector at its maximum setting.

To return to the ordinary low magnification settings merely requires switching the FLC off.

Obtaining a desired magnification

Table C.1 lists a series of lens settings and the magnifications available with the FLC. The magnifications were calculated using micrographs of a standard cross-grating, and for those up to 4840x the effect of reducing Int3 as Int2 is increased is to keep image rotation to a minimum.

Graph C.1 allows magnifications not listed in table C.1 to be obtained: To use this graph the desired magnification is found on the ordinate axis and from the graph at this point the required currents through Int2 and Int3 are obtained. The magnifications listed correspond to Int1 being set to 0.13 and the projector being set to 7.49.

Stigmating when using the FLC

The stigmator used in the above mode is the intermediate stigmator which is controlled through objective stigmator channel 2. This stigmator is not generally strong enough to fully correct the astigmatism in the image; however the following mode of operation has been found to be adequate:

- 1) With the x-image wobbler on, focus using the focus control.
- 2) Switch the x-image wobbler off and the y-image wobbler on.
- 3) Use the y-def knob to reduce the image movement as much as possible.
- 4) Switch the y-image wobbler off and the x-image wobbler on.
- 5) Use the x-def knob to reduce the image movement as much as possible.

Repeat steps 2 to 5 until no further improvement is possible.

Storing FLC settings in memory

Once the FLC has been used once to obtain a given magnification, the lens settings together with the settings on the deflection coils in the microscope can be stored in one of ten memories available to the user and recalled at any time. This is done by typing "UF IN <rt>" on page 1 of the VDU. The microscope replies by putting up on the screen the message "UF No =" at which point any number between 0 and 9 inclusive can be entered followed by <rt>. To recall the settings the user types "UF OUT <rt>" the "UF No =" message is again put up on the screen. Any number between 0 and 9 can then be entered, followed by <rt>; this recalls both the lens settings and the deflection coil settings. If only the lens settings are required then the desired memory number is typed followed by "L <rt>"; for deflection coils only, a "D" is typed instead of an "L".

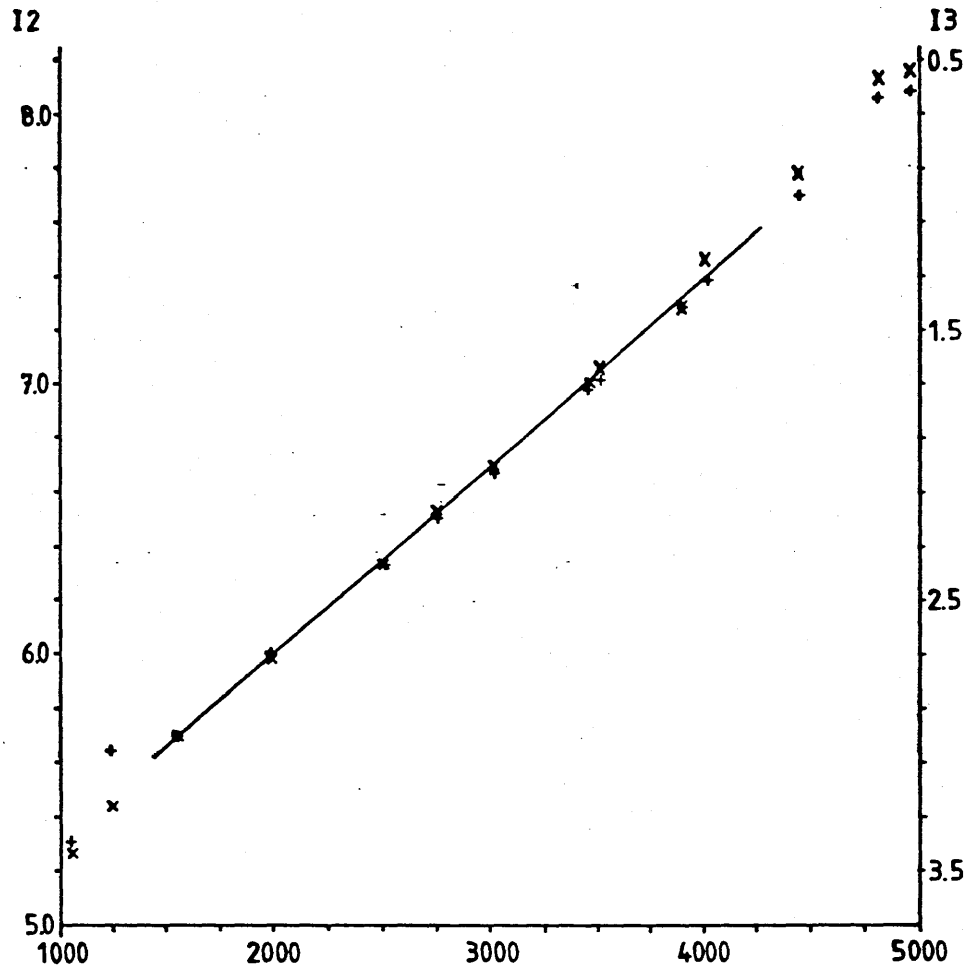
In table C.1 the column headed UF gives the user function memories in which the given magnification settings are usually stored. These are 1 for 1000x up to 5 for 5000x. The standard 1200EX 1000x setting is stored as this allows for an easy return from the user function settings to standard settings.

TABLE C.1 OF LENS SETTINGS AND CORRESPONDING MAGNIFICATIONS

<u>Magnification</u>	<u>Int1 (A)</u>	<u>Int2 (A)</u>	<u>Int3 (A)</u>	<u>Proj(A)</u>	<u>OM (A)</u>	<u>UF</u>
860	0.13	5.17	3.56	7.49	7.09	1 *
1030	0.13	5.30	3.43	7.49	7.08	
1230	0.13	5.64	3.26	7.49	7.08	
1550	0.13	5.70	3.00	7.50	7.08	
1980	0.13	6.00	2.71	7.49	7.07	2
2490	0.13	6.34	2.36	7.49	7.07	
2740	0.13	6.52	2.17	7.49	7.07	
3010	0.13	6.68	2.01	7.49	7.07	3
3460	0.13	6.99	1.70	7.49	7.06	
3510	0.13	7.02	1.64	7.49	7.06	
3890	0.13	7.29	1.41	7.49	7.07	
4040	0.13	7.38	1.24	7.49	7.05	4
4450	0.13	7.70	0.92	7.49	7.05	
4820	0.13	8.06	0.57	7.49	7.05	
4840	0.13	8.09	0.52	7.49	7.06	
4970	0.02	8.11	0.02	7.50	7.06	5
5340	0.02	8.11	0.02	8.12	7.05	

* JEOL 1200EX Low Mag 1000x setting.

The lens current values are obtained by measuring the voltages across standard 1 Ohm resistors and are displayed on page 4 of the microscope CRT display.



Graph C.1: JEOL 1200EX Free Lens Controller magnifications as a function of the current through intermediate lenses 2 and 3

APPENDIX D

HIGH FREQUENCY FILTERING OF DIGITAL IMAGES

D.1 Introduction

In many of the DPC images of polycrystalline materials acquired on the HB5 there is unwanted crystallite contrast, which makes the extraction of magnetic information more difficult. Where the average size of the crystallites in the film under investigation is much smaller than the size of the magnetic structures, the crystallite contrast can be considered to be random high spatial frequency noise. If this is the case, the crystallite contrast can be reduced by applying a low-pass spatial frequency filter to the DPC image. This can be accomplished by taking the Fourier transform of the DPC image, multiplying this by a low-pass filter, and taking the inverse Fourier transform of the resulting frequency space distribution. The following explains how this is implemented on the Toltec computer system (hereafter called the Toltec).

D.2 Fourier Transforms On The Toltec Computer

A suite of Fast Fourier Transform (FFT) programs, called FFFT, was provided with the Toltec, and this was used to calculate both the forward and the reverse Fourier transforms required by the frequency filtering routines. As computer memory space is very limited on the Toltec, the GEMS image memory is used by the FFT program to store information both during and after the FFT operation.

The GEMS image memory is 1024×512 pixels, half of which is used to display up to four 256×256 images. The remaining 512×512 pixels, referred to as hidden GEMS memory, are used by the FFT program to store the real and imaginary parts of the FFT. The way in which the FFT program packs the Fourier transform into this memory is dealt with in much greater detail in the user notes provided with the program. All that is of interest here is that the data can be accessed by the user as

if it were only one half of the Fourier image that was stored in a 129 x 256 array using fortran code supplied with the FFT suite. Using this code, the modification of the Fourier transform is accomplished by the following DO loop:

```
DO 1 I = 1, N3
  CALL CMLXI (I)
  CALL ALTER (I)
  CALL FTSAVE (I)
1 CONTINUE
```

CMLXI and FTSAVE are subroutines provided with the FFT suite, CMLXI is used to call down and unpack the Fourier transform, and FTSAVE packs and restores the filtered transform. N3 is the number of columns of data that have to be called down (usually 129). ALTER is a user written subroutine which modifies the data.

D.3 Frequency Filters Available:

Currently there are four different frequency filters available using the spatial frequency filtering program SFF on the Toltec, these are:

- 1) An aperture function: $DATA \rightarrow DATA$ for $k < k_0$
 $DATA \rightarrow 0$ for $k > k_0$
- 2) A Lorentzian filter: $DATA \rightarrow DATA * \exp(-k/\beta)$
- 3) A Gaussian filter: $DATA \rightarrow DATA * \exp(-k^2/2\sigma^2)$
- 4) A Band pass filter: $DATA \rightarrow DATA * (g_1 - g_2)$
where g_1 and g_2 are two Gaussians of the same amplitude, with standard deviations σ_1 and σ_2

In the above, k (the distance from the centre of the Fourier plane), k_0 (the radius of aperture), β (the scaling parameter for the Lorentzian), and σ , σ_1 , and σ_2 (the standard deviations of the Gaussians), are all in pixel units, and all, except k , can be set to any value by the user.

The aperture function is the crudest of the four filters, and leads to marked ringing in the final real space image. The Lorentzian also suffers from some ringing in the final image. The Gaussian has no ringing in the final image, since its Fourier transform is also a Gaussian, and is the filter that has been found to be most useful. The band pass filter, being a difference of Gaussians, does not suffer badly from ringing in the final image.

D.4 Relationship Between Fourier Space And Real Space

On the Toltec the real space sampling interval (pixel) is Δx , and the sampling window is $256 \cdot \Delta x$ square. The Fourier space sampling interval (pixel) is $\Delta k = 1 / (256 \Delta x)$, and extends, as far as the user is concerned, from $-128 \Delta k$ to $+128 \Delta k$. Therefore a real space object of periodicity $N \cdot \Delta x$ gives rise to intensity in the Fourier plane every $1 / (N \cdot \Delta x) = \Delta k \cdot 256 / N$ pixels from the centre of the Fourier plane. For example if a real space image is periodic every 4 pixels, the Fourier transform of it will have an intensity peak every $256 / 4 = 64$ pixels.

Table D.1 lists the relationship between the real and Fourier planes. This table may be of use in deciding what value to use for k_0 , β , or σ , to filter a particular image. For example, if the average crystallite diameter is 6 pixels in real space, this will give rise to intensity on the Fourier plane at a distance of 43 pixels from the centre. Therefore, any attempt to filter out the crystallite noise in this image should use a filter which has dropped markedly by the time $k = 43 \Delta k$

TABLE D.1 RELATIONSHIP BETWEEN THE REAL SPACE AND FOURIER PLANES

Real space coord.	Fourier space coord.
<u>Δx</u>	<u>Δk</u>
1	256
2	128
3	85
4	64
5	51
6	43
7	37
8	32
9	28
10	26
11	23
12	21
13	20
14	18
15	17
16	16
25	10

REFERENCES

CHAPTER 1:

- A. E. Berkowitz, R.P. Goehner, E.L. Hall, P.J. Flanders: J. Appl. Phys., 57, (1985) 3928-3930
- F. Bloch: Z. Physik, 74, 295 (1932)
- R. P. Ferrier, H. C. Tong, K. Parker, R. H. Geiss: Inst. Phys. Conf. Ser. No.68: Ch6 (1983) 193-196
- R. P. Ferrier: Private communication (1986)
- W. Heisenberg: Z. Physik, 49, 619 (1928)
- S. Iwasaki, Y. Nakamura: IEEE Trans. Magn., MAG-13 (1977) 1272
- S. Iwasaki, K. Takemura: IEEE Trans. Magn., MAG-11 (1975) 1173-1175
- S. B. Luitjens, C. P. G. Schrauwen, J. P. C. Bernards, V. Zieren: IEEE Trans. Magn., MAG-21 (1985) 1438-1440
- K. Ouchi, S. Iwasaki: in JARECT 15 Recent Magnetism For Electronics (1984) Y. Sakurai (ed) North-Holland
- T. Suzuki: IEEE Trans. Magn., MAG-20 (1984) 675-680
- P. Weiss: J. Phys., 6, 661 (1907)
- K. Yoshida, T. Okuwaki, N. Osakabe, H. Tanabe, Y Horiuchi, T. Matsuda, K. Shinagawa, A. Tonomura, H. Fujiwara: IEEE Trans. Magn., MAG-19 (1983) 1600-1604

CHAPTER 2

- P. F. Adams: Ph.D. Thesis, University of Glasgow (1986)
- Y. Aharonov, D. Bohm: Phys. Rev. Second Series Vol. 115(3) (1959) 485-491
- B. E. Argyle, F. Suits: ICMFS-11, paper AA-10 (1985)
- F. Bitter: Phys. Rev., 38, 1903 (1931)
- R. E. Burge, F. C. Dainty: Optik, 46 (1976) 229
- J. N. Chapman, G. R. Morrison: J. Magn. Magn. Mater., 35 (1983) 254-260
- M. S. Cohen, K. J. Harte: J. Appl. Phys., 40 (1969) 3597

- C. Colliex, C. Mory: in "Quantitative Electron Microscopy" proceedings of the 25th Scottish Universities Summer School in Physics 1983. eds. J. N. Chapman and A.J. Craven, SUSSP publications, Dept of Physics, Univ. of Edinburgh
- J. M. Cowley: Appl. Phys. Letts. 15 (2) (1969) 58-59
- A. J. Craven, T. W. Buggy: Ultramicroscopy 7 (1981) 27-37
- A. J. Craven, T. W. Buggy: J. Microscopy 136 Pt.2 (1984) 227-239
- P. A. Crozier: Ph.D. Thesis, University of Glasgow (1985)
- J. M. Cowley, A. Y. Au: Scanning Electron Microscopy /1978/ Vol.1 53-60
- N. H. Dekkers, H. de Lang: Optik 44 452-456 (1974)
- J. F. Dillon Jr.: J. Appl. Phys., 29, 1286 (1958)
- R. F. Egerton: in "Quantitative Electron Microscopy" proceedings of the 25th Scottish Universities Summer School in Physics 1983. eds. J. N. Chapman and A.J. Craven, SUSSP publications, Dept of Physics, Univ. of Edinburgh
- R. Eusemann, H. Rose, J. Dubochet: J. Microscopy 128, 239 (1982)
- R. P. Ferrier, R. H. Geiss, P. S. Alexopoulos: ICMFS-11, paper AA-09 (1985) (not in proceedings)
- D. Gabor: Nature 161, 777 (1948)
- J. I. Goldstein, J. L. Costley, G. W. Lorimer, S. J. B. Reed: SEM 1977, Ed. O. Johari, IIRTI, Chicago, 315 (1977)
- C. C. Gray, J. N. Chapman, W. A. P. Nicholson, B. W. Robertson, R. P. Ferrier: X-ray Spectrometry, 12 (4) (1983) 163-169
- J. M. Hastings, L.M. Corliss: J. Phys. Soc. Japan 17, Suppl. BIII, 43 (1962)
- P. W. Hawkes: in "Advances in Optical and Electron Microscopy" Vol 7, pp101-184, Eds. V. E. Cosslett, R. Barer, Academic Press: London (1978)
- K. Hemmes, J. C. Lodder, M. Th. Rekveldt, W. H. Kraan: J. Phys. D: Appl. Phys., 17 L157-L162 (1984)
- S. Kaya: Z. Physik. 89, 796 (1934)
- J. K. Kjems, P. Touborg, M. de Jong: J. Magn., 14, 277 (1979)

Physics Bullitin 36 (1985) 449

H. Rose: Optik 39, (1974) 416-436

H. Rose: Ultramicroscopy 2 251-267 (1977)

T. Suzuki, K. Hiraga: J. Magn. Mater., 54-57 (1986) 527-529

M. G. R. Thomson: Optik 39 (1) (1973) 15-38

A. Tonomura, T. Matsuda, J. Endo, T. Aarii, K. Mihama: Phys. Rev. Lett. 44, 1430-1433 (1980)

S. Tsukahara: in JARECT 15 Recent Magnetics For Electronics (1984)
Y. Sakurai (ed) North-Holland

J. Unguris, G. Hembree, R. J. Celotta, D. T. Pierce: J. Magn. Mater., 54-57 (1986) 1629-1630

R. H. Wade: J. Appl. Phys., 37 (1966) 366

CHAPTER 3

J. N. Chapman, G. R. Morrison: J. Magn. Mater., 35 (1983)
254-260

J. N. Chapman, I. R. McFadyen, J. P. C. Bernardis: submitted to the
Journal of Magnetism and Magnetic Materials, in press.

P. J. Grundy, M. Ali: J. Magn. Mater., 40 (1983) 154-162

Hirsch, Howie, Nicholson, Pashley, Whelan: "Electron Microscopy of
Thin Crystals" Butterworth Scientific Publications (1965)

J. P. Jakubovics: Phil. Mag. 14 (1966) 881-899

J. P. Jakubovics: Phil. Mag. B 37 (1978) 761-771

J. P. Jakubovics: in "Magnetism in Solids Some Current Topics"
proceedings of the 22nd Scottish Universities Summer School in
Physics 1981: eds. A. P. Cracknell and R. A. Vaughan

A. E. La Bonte: J. Appl. Phys. 40 (1969) 2450-2458

L. D. Landau, E. M. Lifshitz: Phys. Z. Sowjet 8 (1935) 135

T. Sekiguchi, D. Watanabe, K. Tsuno: Jpn. J. Appl. Phys. 24 (1985),
1229-1233

CHAPTER 4

J. B. Elsbrock, L. J. Balk: IEEE Trans. Magn., MAG-20 (1984) 866-868

- R. P. Ferrier, H. C. Tong, K. Parker, R. H. Geiss: Inst. Phys. Conf. Ser. No.68: Ch.6 193-196 (1983)
- R. P. Ferrier: Private communication (1986)
- J. P. Jakubovics: in "Electron Microscopy in Material Science" 1975, eds. E. Ruedl and U. Valdri pp1303
- P. Rhodes, G. Rowlands, Proc. Leeds Phil. Lit. Soc., 6, (1952-5) 191
- H. C. Tong, R. P. Ferrier, P. Chang, J. Tzeng, K. Parker: IEEE Trans. Magn., MAG-20 (1984) 1831-1833
- K. Yoshida, T. Okuwaki, N. Osakabe, T. Tanabe, Y. Horiuchi, T. Matsuda, K. Shinagawa, A. Tonomura, H. Fujiwara: IEEE Trans. Magn., MAG-19 (1983) 1600-1604

CHAPTER 5

- H. Futamoto, Y. Honda, H. Kakibayashi, T. Shimotsu, Y. Uesaka: Jpn. J. Appl. Phys. 24 (1985) L460-L462
- S. Iwasaki, Y. Nakamura: IEEE Trans. Magn., MAG-13 (1977) 1272
- J. C. Lodder, T. Wielinga: IEEE Trans. Magn., MAG-20 (1984) 57
- W. T. Maloney, C. D. Lustig: IEEE Trans. Magn., MAG-20 (1984) 521-522
- S. McVitie, J. N. Chapman: Proc. XIth Int. Cong. on Electron Microscopy, Kyoto (1986) 1735-36
- M. Ohkoshi, T. Kusuda: Jpn. J. Appl. Phys. 22 (1983) L130-L132
- K. Ouchi, S. Iwasaki: in JARECT 15 Recent Magnetism For Electronics (1984) Y. Sakurai (ed) North-Holland
- T. Shinjo, N. Hosoito, K. Kawaguchi, N. Nakayama, T. Takada, Y. Endo: J. Magn. Mater., 54-57 (1986) 737-742
- J. W. Smits, S. B. Luitjens, F. J. A. den Broeder, A. G. Dirks: J. Magn. Mater., 31-34 (1983) 920-922
- J. W. Smits, S. B. Luitjens, F. J. A. den Broeder: J. Appl Phys 55 (1984) 2260-2262
- R. Sugita, T. Kunieda, F. Kobayashi: IEEE Trans. Magn., MAG-17 (1981) 3172-3174
- T. Suzuki, H. Ichinose, E. Aoyagi: Jpn. J. Appl. Phys. 23 (1984)585-592

- K. Tsutsumi, H. Sugahara: Jpn. J. Appl. Phys. 23 (1984) L169-L171
S. Yoshino, H. Takagi, S. Tsunashima, M. Masuda, S. Uchiyama: Jpn. J. Appl. Phys. 23 (1983) 188-191

CHAPTER 6

- F. F. Abraham, C. R. Brundle: J. Vac. Sci. Technol., 18 (1981) 506-519
J. N. Chapman, W. A. P. Nicholson, P. A. Crozier: J. Microsc. 136 (1984) 179
J. N. Chapman, I. R. McFadyen, J. P. C. Bernardis: submitted to the Journal of Magnetism and Magnetic Materials; in press.
P. A. Crozier: Ph.D. Thesis, University of Glasgow 1985
H. Futamoto, Y. Honda, H. Kakibayashi, T. Shimotsu, Y. Uesaka: Jpn. J. Appl. Phys. 24 (1985) L460-L462
P. J. Grundy, M. Ali: J. Magn. Magn. Mater., 40 (1983) 154-162
H. Hoffmann, H. Mandl, Th. Schurmann: paper 5Ph06 at ICM'85 in San Francisco, not in proceedings.
A. K. Jhingan: J. Magn. Magn. Mater., 54-57 (1986) 1685-1686
S. B. Luitjens, C. P. G. Schrauwen, J. P. C. Bernardis, V. Zieren IEEE Trans. Magn., MAG-21 (1985) 1438-1440
M. Ohkoshi, T. Kusuda: Jpn. J. Appl. Phys. 22 (1983) L130-L132
K. Ouchi, S. Iwasaki: in JARECT 15 Recent Magnetism For Electronics (1984) Y. Sakurai (ed) North-Holland

CHAPTER 7

- S. Iwasaki, Y. Nakamura, K. Ouchi: IEEE Trans. Magn., MAG-15 (1979) 1456
S. B. Luitjens, C. P. G. Schrauwen, J. P. C. Bernardis, V. Zieren IEEE Trans. Magn., MAG-21 (1985) 1438-1440
K. Ouchi, S. Iwasaki: IEEE Trans. Magn., MAG-18 (1982) 1110-1112
K. Ouchi, S. Iwasaki: in JARECT 15 Recent Magnetism For Electronics (1984) Y. Sakurai (ed) North-Holland

CHAPTER 8

J. N. Chapman: J. Phys. D: Appl. Phys. 17 (1984) 623-647

J. B. Elsbrock, W. Schroeder, E. Kubalek: IEEE Trans. Magn., MAG-21
(1985) 1593-1595

Y. Maeda, M. Asahi, M. Seki: Jpn. J. Appl. Phys. 25 (1986) L668-L670

G. R. Morrison: Ph.D. Thesis, University of Glasgow (1981)

H. C. Tong, R. P. Ferrier, P. Chang, J. Tzeng, K. L. Parker: IEEE
Trans. Magn., MAG-20 (1984) 1831-1833

